Winter 11-20-2020

Band structure topology and spin transport in magnon systems

Bo Li
University of Nebraska - Lincoln, boliwalker@huskers.unl.edu

Li, Bo, "Band structure topology and spin transport in magnon systems" (2020). *Department of Physics and Astronomy: Dissertations, Theses, and Student Research*. 51.
https://digitalcommons.unl.edu/physicsdiss/51

Band structure topology and spin transport in magnon systems

by

Bo Li

A DISSERTATION

Presented to the Faculty of

The Graduate College at the University of Nebraska

In Partial Fulfilment of Requirements

For the Degree of Doctor of Philosophy

Major: Physics and Astronomy

Under the Supervision of Professor Alexey A. Kovalev

Lincoln, Nebraska

November, 2020

BAND STRUCTURE TOPOLOGY AND SPIN TRANSPORT IN MAGNON SYSTEMS

Bo Li, Ph.D.

University of Nebraska, 2020

Adviser: Professor Alexey A. Kovalev

As the spin excitation quanta in magnetic materials, the magnon is at the heart of the spintronics research because it plays a key role in magnetic dynamics, energy and spin transport, and even determining the ground state of magnetic systems. In this thesis, we will study the band-structure topology and transport properties of magnons in both collinear and noncollinear magnets. Inspired by the great success of topological insulators, exploring magnon topology can unveil the topological nature of bosonic particles and widen the zoo of topological materials. We propose a three-dimensional magnon topological insulator model protected by sublattice chiral symmetries, which realizes a surface Dirac cone in a magnonic system. On the other hand, magnons can facilitate angular momentum transport with low dissipation due to the absence of Joule heating. We explore the spin Nernst effect, a transverse spin current driven by a temperature gradient, in noncollinear magnetic systems by developing a new linear response theory. The theory will be applied to frustrated noncollinear antiferromagnets, antiferromagnetic skyrmion crystals, and an antiferromagnetic magnon topological insulator model. In particular, the antiferromagnetic magnon topological insulator model is featured by unconventional Landau levels and can be regarded as a magnon version of the quantum spin Hall effect. In addition to the magnon-mediated spin transport, magnons are also able to accumulate nonequilibrium net spin density in a sample under the driving of a temperature gradient. The latter effect is a magnon version of the Edelstein effect and can be also analyzed by the aforementioned linear response theory. Such an effect can be ideally realized in 2D and 3D noncollinear antiferromagnets that have a compensating ground state.

COPYRIGHT

ACKNOWLEDGMENTS

First and foremost, I would like to thank my advisor, Prof. Alexey Kovalev, for his guidance and support during my Ph.D. program. He is an insightful and patient mentor. I could not remember how many times I sat in his office to discuss our projects for several hours, and I usually gained new versions of seemingly unsolvable problems. He is always willing to share his previous Mathematica notebooks without any reservation, from which I learned lots of coding skills necessary for my research. I am deeply influenced by his prudent attitude on research, which will definitely benefit me in my whole career. He always encourages me to pursue the most transparent and elegant theory. He insists that every step of derivation must be solid and never let any flaws slide. All of these shaped my style and taste as a researcher. I also appreciate that Alexey gave me much freedom in choosing the research topics and tolerated my failure on several projects. Without his support, my published papers and this thesis would not have been possible.

I would like to thank other members of my committee: Prof. Kirill Belashchenko, Prof. Christian Binek, and Prof. Christos Argyropoulos for taking their precious time to discuss my Comprehensive exam topic, read my report and thesis, and give very nice comments on my presentations. Prof. Kirill Belashchenko also gave me a lot of help in my course work. I took three classes taught by him and I was always impressed by his sharp physics intuition and his skill of simplifying physical problems.

I would like to thank all my group mates: Shane Sandhoefner, Rabindra Nepal, Aldo Raeliarijaona, Sanjay Prabhakar, Utkan Güngördü, and Vladimir A. Zyuzin. I benefit a lot from their presentations and our discussions all the time, which broadens my view on different research fields. I enjoyed collaborations with Shane and Aldo; their hard work and valuable input are really nonnegligible ingredients of our coauthored projects.

I also would like to thank all my good friends in Lincoln. First, all our coffee team members: Shane Sandhoefner, Guanhua Hao, Prescott Evans, and Corbyn Mellinger. Our daily coffee and chat was really a salutary activity; we shared lots of interesting news and

funny stories, which really released me at the moment from tedious formula derivations and sometimes brought about some inspiration. I especially owe Shane for his patient help when I was seeking advice on some issues about life and study. Second, I am really grateful to meet Xuanyuan Jiang and Ming Li because they really provide me tremendous help on many aspects of my life in Lincoln. They really treated me like a family. I have to thank Dingfu Shao, who takes care of me as an elder brother and often invites me to his house to enjoy the delicious food made by his wife; I also benefit a lot from our discussion on many research topics. I also would like to thank all friends who shared happy Lincoln memories: Zilin Chen, Xiaojun Wang, Yi Yang, Tianlin Li, Yibo Wang, Wuzhang Fang, Yuanyuan Ni. Thanks to them for the help and happiness they brought to me.

Finally, I would like to say thank you to my parents and brother. There is no doubt that they are always my strongest supporters. Without their support, I cannot imagine how I could possibly have finished my Ph.D. program.

PREFACE

The results presented in Chapter 2 have been published in Physical Review B (Bo Li and Alexey A. Kovalev Phys. Rev. B 97, 174413 (2018))

The results in Chapter 3 have been published in Physical Review Research (Bo Li, Shane Sandhoefner, and Alexey A. Kovalev Phys. Rev. Research 2, 013079 (2020))

The results in Chapter 4 have been published in Physical Review B (Bo Li, Alexander Mook, Aldo Raeliarijaona, and Alexey A. Kovalev Phys. Rev. B 101, 024427 (2020))

The results presented in Chapter 5 were accepted for publication in Physical Review Letters. (Bo Li and Alexey A. Kovalev, “Magnon Landau Levels and Topological Spin Responses in Antiferromagnets" (accepted for publication in Phys. Rev. Lett., November 2020).)

Contents

List of Figures

List of Tables

Chapter 1

Introduction

Research on topology and relevant transport phenomena in electronic systems has greatly added to the richness of condensed matter physics in recent decades. The journey of these topological explorations was initiated by the discovery of the quantum Hall effect [1], where the quantum conductance is explained by a topological invariant [2,3]. Henceforth, the exploration of topological physics blossomed. Various Hall-type transport physics, including (quantum) anomalous Hall [4–6], (quantum) spin Hall [7–9], and thermal Hall [10, 11], have become the mainstream of condensed matter physics. The underlying connection between the band-structure topology of materials, the quantized conductance, and the edge-state physics was gradually recognized. Another breakthrough is the discovery of topological insulators and superconductors [12, 13], which greatly expanded the realm of topological physics in real materials. This development has improved our understanding of topology mainly in the sense of uncovering the important relationship between symmetries and topology. At the same time, other fascinating physics emerges, e.g., surface Dirac cone, topological magnetoelectric effect, Majorana zero modes, *etc.* Later, the focus was partially shifted from gapped (insulator, superconductor) systems to gapless systems, metals, which include topological Weyl and Dirac semimetals [14]. The rapid development of topological condensed matter physics does not only improves our understanding of fundamental physics, but also brings about a great potential for applications. For example, (quantum) spin Hall effect has been widely used as a spin source in the spintronics research [15], topological insulators can be used in photodetectors, magnetic devices, field-effect transistors, quantum computing, *etc.* [16, 17]

Stimulated by developments in electronic systems, there has been a surge of studying the topology of other systems, e.g., magnonic [18–24], acoustic [25, 26], and photonic [27] systems. The study of magnon topology started from the prediction and realization of the magnon thermal Hall effect in ferromagnets [28, 29]. The thermal Hall effect was quickly attributed to the Berry curvature induced anomalous velocity of magnons [30, 31]. There was subsequently investigation of the magnon analogy of Chern insulators and the corresponding edge states [20, 32–35]. Remarkably, a magnon version of the representative Haldane model was found in a honeycomb ferromagnet [36, 37]. In antiferromagnets, with collinear or noncollinear spin orders, the magnon spin Nernst effect [38, 39] and the magnon thermal Hall effect [40–44] have been discovered. Moreover, the realization of magnon Weyl and Dirac spectrum drew considerable attention [45–51]. All the progress does not only enrich the magnon physics from a fundamental level but also implies new opportunities for spintronics. For instance, the magnon spin Nernst effect suggests a new low-dissipation spin generation method; the thermal Hall effect offers a way to explore the topology of the excitation spectrum in insulators or even to detect the spin liquid materials [52].

In this work, we will study the rich physics of magnons in different kinds of magnetic insulators, including collinear ferromagnets and antiferromagnets, noncollinear antiferromagnets, and spin textures. The focus is mainly on the magnon band-structure topology and magnon-mediated spin transport and accumulation. In the rest of this chapter, we introduce necessary background knowledge that will be frequently used in subsequent chapters. First, we discuss the origin of spin-spin exchange interactions and briefly review several kinds of commonly considered interactions in magnetic materials. Second, we discuss the concept of magnons by reviewing the Holstein-Primakoff transformation. Next, we introduce the important concept of Berry curvature, and relevant topological physics. As an example, we discuss the famous Haldane model and its realization in magnon systems. This can be regarded as a warm-up for Chapter 2 where more involved topology will be discussed. We also discuss the real-space Berry curvature which induces an emergent gauge field for electrons or magnons in a spin-texture background. This lays down the foundation for exploring the magnon excitations in a skyrmion crystal, which is the topic of Chapter 5. Finally, we outline the linear response theory to prepare for our discussion on the temperature gradient induced linear response phenomena in Chapters 3 and 4.

1.1 Spin-spin interactions

The foundation of this thesis is a variety of spin-spin interaction models that describe different magnetic systems. In this section, we briefly review three types of common and important interactions: the exchange, magnetic anisotropies, and Dzyaloshinskii-Moriya interaction (DMI).

1.1.1 Exchange interaction

The simplest model commonly used to describe spin exchange is the Heisenberg model. We follow Ref. [53] to explain the origin of exchange interaction. In materials, the magnetism comes from the alignment or staggered ordering of the magnetic moments of electrons. The direct dipole-dipole interaction in which the spins of electrons are directly involved is too weak to explain the typical magnetism at high temperatures. It has been realized that the mechanism to explain the formation of local magnetization could come from the Coulomb interaction.

This picture can be explained by considering two orbitals ϕ_1, ϕ_2 with energy ϵ_1, ϵ_2. The electron fields can be described by $\phi_{1(2)}$

$$\psi_s^\dagger(\boldsymbol{x}) = \sum_i \phi_i^* c_s^\dagger, \qquad s = \uparrow, \downarrow, \tag{1.1}$$

where $c_s^\dagger$ is the creation operator for an electron of spin s. The Coulomb interaction is given by

$$U = \frac{1}{2} \int d\boldsymbol{x} d\boldsymbol{y} V(\boldsymbol{x}, \boldsymbol{y}) \sum_{s,s'} \psi_s^\dagger(\boldsymbol{x}) \psi_{s'}^\dagger(\boldsymbol{y}) \psi_{s'}(\boldsymbol{y}) \psi_s(\boldsymbol{x}) \tag{1.2}$$

where $V(\boldsymbol{x}, \boldsymbol{y})$ describes the Coulomb interaction potential between electrons at $\boldsymbol{x}$ and $\boldsymbol{y}$. Substituting Eq. (1.1) into the interaction above leads to

$$U = \sum_{i \neq j} U_{ij} n_i n_j + \sum_i U_{ii} \rho_{i,\uparrow} \rho_{i,\downarrow} + \sum_{i \neq j, ss'} J c_{i,s}^\dagger c_{j,s'}^\dagger c_{i,s'} c_{j,s} \tag{1.3}$$

where U_{ii}, U_{ij}, and J are overlap integrals of orbital function on the corresponding sites, and $n_i = \sum_s \rho_{i,s}$ with $\rho_{i,s}$ being the density of electron with spin s. In the full screening or no screening cases, the exchange integral J can be shown to be positive, which endows a ferromagnetic exchange between local spins in the following discussion. The Coulomb interaction finds minimum value in the situation where electrons are distributed on two orbitals, i.e., $n_i \simeq 1$, the interaction can be simplified to spin-spin exchange interaction on two sites. Note

$$\sum_{ss'} J c_{i,s}^\dagger c_{j,s'}^\dagger c_{i,s'} c_{j,s} = -2J(\boldsymbol{S}_i \cdot \boldsymbol{S}_j + \frac{1}{4} n_i n_j), \tag{1.4}$$

where $\boldsymbol{S}_i = \frac{1}{2} \sum_{ss'} c_{is}^\dagger \boldsymbol{\sigma}_{ss'} c_{i,s'}$. Up to a constant, the Coulomb interaction is reduced to

$$U = -J \sum_{i \neq j} \boldsymbol{S}_i \cdot \boldsymbol{S}_j. \tag{1.5}$$

To this point, we based the theory upon two assumptions: (i) the two orbitals are non-degenerate and are isolated from other orbitals in energy, (ii) the two orbitals are orthogonal to each other, which is usually true for two orbitals around the same atom. These assumptions limit the resultant coupling to be ferromagnetic. To gain antiferromagnetic exchange, a model of two electrons living on different sites would be more appropriate. Fix the ions on positions $\boldsymbol{R}_1$, $\boldsymbol{R}_2$ and two orbitals ϕ_1, ϕ_2 are centered at the corresponding atom position. The full Hamiltonian describing such a system is

$$H = \sum_{i=1,2} H_i^{(0)} + \delta H \tag{1.6}$$

where

$$\begin{aligned} H_i^{(0)} &= -\frac{\hbar^2}{2m}\nabla_i^2 - \frac{e^2}{|\boldsymbol{r}_i - \boldsymbol{R}_i|^2}, \\ \delta H &= \sum_{i \neq j} \frac{-e^2}{|\boldsymbol{r}_i - \boldsymbol{R}_j|^2} + \frac{e^2}{|\boldsymbol{r}_1 - \boldsymbol{r}_2|^2} + \frac{e^2}{|\boldsymbol{R}_1 - \boldsymbol{R}_2|^2}. \end{aligned} \tag{1.7}$$

Here, the two orbital wave functions obey

$$H_i^{(0)}\phi_i = E_0\phi_i, \qquad (i = 1, 2). \tag{1.8}$$

To avoid large on-site Coulomb interactions, electrons prefer spatially separated wave functions which can be constructed as

$$\begin{aligned} \psi_1 &= \phi_1(\boldsymbol{r}_1)\phi_2(\boldsymbol{r}_2), \\ \psi_2 &= \phi_1(\boldsymbol{r}_2)\phi_2(\boldsymbol{r}_1). \end{aligned} \tag{1.9}$$

By performing the variational calculation, it can be shown that the energy minimized wave function is either symmetric or antisymmetry under exchange of electron coordinates

$$\psi^{\pm} = \frac{1}{\sqrt{2}}(\psi_1 \pm \psi_2). \tag{1.10}$$

When the spin freedom of electrons is taken into account, the overall wave function should be composed of a spatial part and a spinor vector part, and the wave function should flip sign under the interchange of two electrons. Therefore, the full wave function is expressed by

$$\Psi^{\pm} = \psi^{\mp}(\boldsymbol{r}_1, \boldsymbol{r}_2)\chi^{\pm}(\boldsymbol{r}_1, \boldsymbol{r}_2) \tag{1.11}$$

where the spinor part is

$$\chi^{\pm} = \chi^{\uparrow}(\boldsymbol{r}_1)\chi^{\downarrow}(\boldsymbol{r}_2) \pm \chi^{\uparrow}(\boldsymbol{r}_2)\chi^{\downarrow}(\boldsymbol{r}_1). \tag{1.12}$$

Here, $\chi^{\pm}$ describes antiparallel spin states. It can be shown that the wave functions Ψ^{+}, Ψ^{-} are the triplet and singlet eigenstates of the total spin operator

$$\boldsymbol{S}_{\text{total}} = \sum_{i=1,2} \frac{1}{2} \sum_{ss'} c^{\dagger}_{is} \boldsymbol{\sigma}_{ss'} c_{i,s'}. \tag{1.13}$$

The corresponding eigenvalues $E^{\pm}$ are spaced by an energy gap

$$E^{+} - E^{-} = J > 0. \tag{1.14}$$

The system can be effectively presented as a Heisenberg antiferromagnet

$$H = J\boldsymbol{S}_1 \cdot \boldsymbol{S}_2 = J[\frac{1}{2}(\boldsymbol{S}_{\text{total}})^2 - \frac{3}{4}] = \begin{cases} \frac{1}{4}J, & S_{\text{total}} = 1 \\ -\frac{3}{4}J, & S_{\text{total}} = 0 \end{cases}. \tag{1.15}$$

Here, the relation $S_{1(2)}^2 = S(S+1)$ with $S = \frac{1}{2}$ is applied. Compared to the ferromagnetic exchange case, the model leading to the antiferromagnetic exchange involves two spatially separated non-orthogonal orbitals, which allows hopping of electrons between two sites. The anti-alignment of spins in an antiferromagnetic state can reduce the kinetic exchange energy.

In this thesis, we are mainly interested in the insulating antiferromagnet. The origin of antiferromangetic exchange in a ionic insulator can be easily understood by considering a two-site Hubbard model [54],

$$H = -t \sum_{s=\uparrow,\downarrow} c^{\dagger}_{1,s} c_{2,s} + \sum_{i=1,2} U \rho_{i,\uparrow} \rho_{i,\downarrow}, \tag{1.16}$$

where the first term describes the kinetic energy with exchange energy t, U is the on-site Coulomb interaction energy introduced in Eq. (1.3). The Hilbert space for this model is composed by six bases, $\{|\uparrow\downarrow, 0\rangle, |0, \uparrow\downarrow\rangle, |\uparrow, \downarrow\rangle, |\downarrow, \uparrow\rangle, |\uparrow, \uparrow\rangle, |\downarrow, \downarrow\rangle\}$, under which the Hamiltonian is written as a matrix

$$H = \left(\begin{array}{cccc|cc} U & 0 & t & -t & 0 & 0 \\ 0 & U & t & -t & 0 & 0 \\ t & t & 0 & 0 & 0 & 0 \\ -t & -t & 0 & 0 & 0 & 0 \\ \hline 0 & 0 & 0 & 0 & 0 & 0 \\ 0 & 0 & 0 & 0 & 0 & 0 \end{array}\right). \tag{1.17}$$

Transforming the sub-basis from $(|\uparrow, \downarrow\rangle, |\downarrow, \uparrow\rangle)$ onto $\{(|\uparrow, \downarrow\rangle - |\downarrow, \uparrow\rangle)/\sqrt{2}, (|\uparrow, \downarrow\rangle + |\downarrow$

$, \uparrow\rangle)/\sqrt{2}\}$ simplifies the above Hamiltonian to

$$H' = \left(\begin{array}{ccc|ccc} U & 0 & \sqrt{2}t & 0 & 0 & 0 \\ 0 & U & \sqrt{2}t & 0 & 0 & 0 \\ \sqrt{2}t & \sqrt{2}t & 0 & 0 & 0 & 0 \\ \hline 0 & 0 & 0 & 0 & 0 & 0 \\ 0 & 0 & 0 & 0 & 0 & 0 \\ 0 & 0 & 0 & 0 & 0 & 0 \end{array}\right). \tag{1.18}$$

The eigenvalues of the second sector are degenerated at 0. Their eigenstates form a triplet, $(|\uparrow,\downarrow\rangle + |\downarrow,\uparrow\rangle)/\sqrt{2}$, $|\uparrow,\uparrow\rangle$, and $|\downarrow,\downarrow\rangle$. The eigenvalues of the first sector are U, $(U \pm \sqrt{U^2 + 16t^2})/2$. For a ionic system with small kinetic energy, $t \ll U$, the lowest energy is

$$\frac{U - \sqrt{U^2 + 16t^2}}{2} \simeq -\frac{4t^2}{U} < 0. \tag{1.19}$$

In the limit $U/|t| \to \infty$, the corresponding eigenstate approaches to the singlet $(|\uparrow,\downarrow\rangle - |\downarrow,\uparrow\rangle)/\sqrt{2}$. Therefore, we found that the singlet (antiferromagnet) has a lower energy than the triplet (ferromagnet), which can be described as a antiferromagnetic Heisenberg exchange model

$$H_{eff} = J\boldsymbol{S}_1 \cdot \boldsymbol{S}_2 \tag{1.20}$$

with $J = 4t^2/U$. This mechanism is called kinetic exchange. It results from that the anti-parallel spin configuration reduces the kinetic energy between electrons. This result does not only hold for a two-site model, but can be generalized to lattice models.

1.1.2 Other interactions

In general, the interaction between spins can be written as

$$H = \sum_{ij} \boldsymbol{S}_i \hat{\mathcal{J}}_{ij} \boldsymbol{S}_j \tag{1.21}$$

where $\hat{\mathcal{J}}_{ij}$ is a 3×3 matrix that describes the coupling between different components of two spins. The Heisenberg model corresponds to a unit matrix $\hat{\mathcal{J}}_{ij} = J\mathbb{1}$. If the diagonal elements of the matrix take different values, i.e., $\hat{\mathcal{J}}_{ij} = \mathrm{Diag}\{J^x_{ij}, J^y_{ij}, J^z_{ij}\}$, it describes anisotropic exchange interactions. A famous example of this is the Kitaev model [55]. The coupling matrix also allows an antisymmetric part

$$\hat{\mathcal{J}}_{ij} = \begin{bmatrix} 0 & -D_{ij,z} & D_{ij,y} \\ D_{ij,z} & 0 & -D_{ij,x} \\ -D_{ij,y} & D_{ij,x} & 0 \end{bmatrix} \tag{1.22}$$

which describes the Dzyaloshinskii-Moriya exchange interaction (DMI)

$$H_{\mathrm{DMI}} = \sum_{ij} \boldsymbol{D}_{ij} \cdot (\boldsymbol{S}_i \times \boldsymbol{S}_j). \tag{1.23}$$

DMI between spins usually arises from the superexchange interaction mediated by a nonmagnetic atom in non-centrosymmetric environment. In Fig. 1.1, the direction of the DMI vector between two neighboring spins $\boldsymbol{S}_1$ and $\boldsymbol{S}_2$ is given by $\boldsymbol{D}_{12} \propto \boldsymbol{r}_1 \times \boldsymbol{r}_2$ with $\boldsymbol{r}_1$ and $\boldsymbol{r}_2$ respectively being the vector pointing from the nonmagnetic atom to the magnetic atoms. The strength of DMI is proportional to the energy scale of spin-orbit coupling. In magnetic thin films, DMI usually arises from the nonmagnetic atoms of the heavy metal substrates.

Apart from the two-ion interactions, there are systems that also have single-ion contributions. First, the spin orders are usually affected by the single-ion anisotropy due to

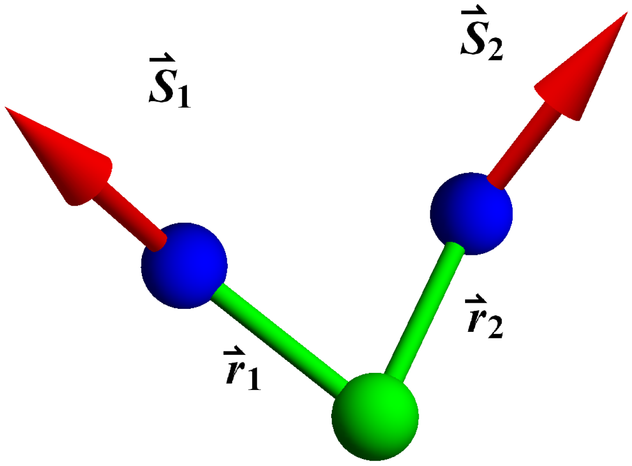

Figure 1.1: The Dzyaloshinskii-Moriya exchange interaction (DMI) between two neighboring spins is mediated by a non-magnetic atom. The DMI vector is pointing along the direction of $\boldsymbol{r}_1 \times \boldsymbol{r}_2$.

the crystalline field

$$H_A = K \sum_i (\boldsymbol{S} \cdot \hat{\boldsymbol{n}}_i)^2. \tag{1.24}$$

When $K < 0$, it is called easy-axis anisotropy with $\hat{\boldsymbol{n}}_i$ giving the preferred direction of spins; when $K > 0$, it describes the easy-plane anisotropy due to which spins are inclined to lie in the plane perpendicular to $\hat{\boldsymbol{n}}_i$. Typically, in collinear ferromagnets or antiferromagnets, $\hat{\boldsymbol{n}}_i$'s are given along a single direction for all spins. While for noncollinear antiferromagnets, e.g., the three-sublattice antiferromagnets, the situation will become more complicated.

In consideration of specific magnetic systems, it could also include Zeeman interactions between the external magnetic field and local magnetic moments, or dipole-dipole interactions with a strength inversely proportional to the cube of the distance between two

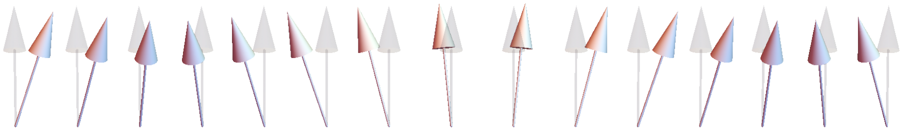

Figure 1.2: Spin waves. Here, the vertical arrows show the ground-state spin direction.

spins. The details will be given if necessary in the following discussion.

1.2 Magnons: Holstein-Primakoff transformation

In the last section, we introduced different types of spin interactions, which can fix the magnetic system to a certain ordered ground state in ferromagnets or antiferromagnets. At low temperatures, it is mainly the quantum fluctuation on top of the ground state that contributes to transport properties in insulating magnets. In the classical description, we call the fluctuation as spin wave. In a quantum mechanical frame, the spin waves are quantized as bosonic quasiparticles, magnons, which carry quantized spin $\hbar$. Fig. 1.2 schematically shows the spin waves or magnons upon a vertical ground state. The main focus of this thesis is the topology of magnon band structure and magnon-mediated spin transport. Therefore, in this section, we introduce the concept of magnons by reviewing the Holstein-Primakoff transformation.

In the ground state of a ferromagnet, all spins with magnitude S are aligned along a certain direction. One can assign this direction to be the z-axis, thus the spin state on a given site is labeled by the eigenvalues of the quantum operator $\hat{S}^2$, $\hat{S}^z$:

$$\begin{aligned} \hat{S}^2|S,S_z\rangle &= S(S+1)|S,S_z\rangle, \\ \hat{S}^z|S,S_z\rangle &= S_z|S,S_z\rangle. \end{aligned} \tag{1.25}$$

Here, S_z takes values $-S, -S+1, \cdots, S-1, S$. These successive states are distinguished by a quantized variation of S_z, which indicates a deviation of spins from the quantization axis. This deviation describes the excitation states. If one regards the ground state as a quantum vacuum state, all excited states can be built up through the following ladder operators

$$S^{\pm} = S_x + iS_y, \tag{1.26}$$

where S^{+}, S^{-} can respectively increase and decrease the value of S_z by one, i.e.,

$$S^{\pm}|S, S_z\rangle = \sqrt{(S \mp S_z)(S \pm S_z + 1)}|S, S_z \pm 1\rangle. \tag{1.27}$$

We see that the ladder operators realize the spin deviation from the ground state, which facilitates the description of the quantum fluctuation. In the second quantization language, the ladder operators are reformulated by magnon operators through the Holstein-Primakoff (HP) transformation

$$S^{+} = \sqrt{2S - n_b}b, \quad S^{-} = b^{\dagger}\sqrt{2S - n_b}, \quad S_z = S - n_b. \tag{1.28}$$

Here, b and $b^{\dagger}$ are magnon annihilation and creation operators, respectively. They respect the following commutation relations

$$[b, b^{\dagger}] = 1, \qquad [b, b] = [b^{\dagger}, b^{\dagger}] = 0. \tag{1.29}$$

The magnon number operator is $n_b = b^{\dagger}b$. A way to confirm the validity of these relations is by checking the agreement between magnon commutators and the commutator between quantum spin operators $[S_i, S_j] = i\epsilon_{ijk}S_k$. When dealing with magnons, one needs to be aware of their unphysical aspects. The bosonic nature of magnons implies that the magnon number n_b corresponding to a given spin can take any nonnegative integer value. This obviously contradicts the HP transformation regarding the requirement $2S - n_b \geq 0$. Therefore, to be physical, the system has to be restricted to the regime $n_b \leq 2S$.

Magnon picture is an effective tool in the low-temperature region where the magnon number is small: $n_b \ll 2S$ (this requires $S \gg 1$). In this case, the HP transformation can be kept to the lowest order, $S^+ \approx \sqrt{2S}b$, $S^- \approx \sqrt{2S}b^\dagger$, and $S^z = S - b^\dagger b$, thus we can obtain a bilinear Hamiltonian by substituting these approximations into the spin-spin interaction energy. The magnon bilinear Hamiltonian runs through the whole thesis, playing the role of the starting point of all topics. We take the case of the ferromagnetic Heisenberg model as an example

$$H = -J \sum_{\langle i,j \rangle} \boldsymbol{S}_i \cdot \boldsymbol{S}_j \tag{1.30}$$

where $J > 0$ and $\langle i, j \rangle$ describes the nearest neighbors. Assuming the ground-state spins lie in the z-direction, the Hamiltonian is re-expressed as below

$$\begin{aligned} H &= -J \sum_{\langle i,j \rangle} S_i^z S_j^z + \frac{1}{2}(S_i^- S_j^+ + S_i^+ S_j^-) \\ &= JS(\sum_i Z a_i^\dagger a_i - \sum_{\langle i,j \rangle} a_i^\dagger a_j + a_i a_j^\dagger), \end{aligned} \tag{1.31}$$

where Z counts the neighboring sites of a given spin. The magnon operator bilinear form of the Hamiltonian enables us to discuss band structure by going to momentum space through the Fourier transformation

$$a_i = \frac{1}{\sqrt{N}} \sum_{\boldsymbol{k}} e^{i\boldsymbol{k}\cdot\boldsymbol{r}} a_{\boldsymbol{k}}, \qquad a_i^\dagger = \frac{1}{\sqrt{N}} \sum_{\boldsymbol{k}} e^{-i\boldsymbol{k}\cdot\boldsymbol{r}} a_{\boldsymbol{k}}^\dagger. \tag{1.32}$$

The Hamiltonian in momentum space reads

$$H = JS \sum_{\boldsymbol{k}} [Z - \sum_{\boldsymbol{\delta}} \cos(\boldsymbol{k} \cdot \boldsymbol{\delta})] a_{\boldsymbol{k}}^\dagger a_{\boldsymbol{k}} \tag{1.33}$$

where $\boldsymbol{\delta}$ represents the nearest neighbor shifting vector. Here, this simple example has only one band

$$E(\boldsymbol{k}) = JS[Z - \sum_{\boldsymbol{\delta}} \cos(\boldsymbol{k} \cdot \boldsymbol{\delta})]. \tag{1.34}$$

In more general cases, each unit cell contains more than one spin freedom. The Hamiltonian could be generally expressed in the form

$$H = \sum_{\boldsymbol{k}} \Psi_{\boldsymbol{k}}^{\dagger} H_{\boldsymbol{k}} \Psi_{\boldsymbol{k}} \tag{1.35}$$

where $\Psi_{\boldsymbol{k}} = (a_{1,\boldsymbol{k}}, a_{2,\boldsymbol{k}}, \cdots, a_{N,\boldsymbol{k}})^T$ with N being the number of spins per unit cell, and $H_{\boldsymbol{k}}$ is a $N \times N$ matrix. The high dimensionality of the Hamiltonian allows multiple magnon bands and thus makes the association with rich band structure topology possible. The most common topological invariant considered for magnon bands is the Chern number that can be defined for the Chern insulator or Weyl spectrum, as we will be discussing in the next section.

The magnons in antiferromagnets can be introduced by following the same logic, and similar derivations from the Heisenberg model can be carried out. However, the Hamiltonian will take a Bogoliubov-de Gennes (BdG) form that is usually used in superconductivity theory, because this form can capture the particle-nonconserved anomalous terms, $a_i b_j, a_i^{\dagger} b_j^{\dagger}$. In this thesis, we will extensively discuss the magnons in antiferromagnets. A complete procedure of Hamiltonian presentation, diagonalization, and relevant topology will be elaborated in Chapters 3 and 4.

1.3 Topological magnons

A key element of this thesis is the topology in the magnetic systems. As a warm-up, in this section, some basic topology in condensed matter physics and a brief review of the development in magnetic systems will be given by following Ref. [4, 56, 57].

1.3.1 Berry phase and Chern number

Consider a system described by a Hamiltonian $H[\boldsymbol{R}(t)]$ that evolves with time t through the parameter $\boldsymbol{R}(t) = \{R_1, R_2, \cdots, R_n\}$. At each moment, the system has an instantaneous eigenstate

$$H[\boldsymbol{R}(t)]|u_n(\boldsymbol{R}(t))\rangle = E_n(\boldsymbol{R}(t))|u_n(\boldsymbol{R}(t))\rangle. \tag{1.36}$$

However, the state at each moment cannot be fully determined by this equation due to the phase uncertainty. To understand this, we investigate the solution of the Schrödinger equation

$$\partial_t|\Phi(t)\rangle = H[\boldsymbol{R}(t)]|\Phi(t)\rangle. \tag{1.37}$$

In the adiabatic approximation, the system stays at one of the instantaneous eigenstates provided that the eigenvalues are separated from each other and the time evolution is very slow. In this case, the Schrödinger equation solution will take the form

$$|\Phi(t)\rangle = e^{i\gamma_n} e^{-\frac{i}{\hbar}\int_0^t dt' E_n(\boldsymbol{R}(t'))}|u_n(\boldsymbol{R}(t))\rangle \tag{1.38}$$

where the phase factor γ_n satisfies

$$\partial_t \gamma_n(t) = i\langle u_n(t)|\partial_t u_n(t)\rangle. \tag{1.39}$$

Alternatively, the extra phase γ_n can be expressed in the parameter space

$$\gamma_n = \int d\boldsymbol{R} \cdot \boldsymbol{A}_n(\boldsymbol{R}) \tag{1.40}$$

where $\boldsymbol{A}_n(\boldsymbol{R})$ is the so-called Berry connection and it is expressed as

$$\boldsymbol{A}_n(\boldsymbol{R}) = i\langle u_n(\boldsymbol{R})|\boldsymbol{\nabla} u_n(\boldsymbol{R})\rangle \tag{1.41}$$

which is gauge dependent. When the eigenstate acquires an extra phase factor

$$|u_n(\boldsymbol{R}(t))\rangle \to e^{i\chi_n(\boldsymbol{R}(t))}|u_n(\boldsymbol{R}(t))\rangle, \tag{1.42}$$

the Berry connection transforms as

$$\boldsymbol{A}_n(\boldsymbol{R}) \to \boldsymbol{A}_n(\boldsymbol{R}) - \boldsymbol{\nabla}_R\chi_n, \tag{1.43}$$

and the phase factor will correspondingly change by $\chi_n(\boldsymbol{R}(T)) - \chi_n(\boldsymbol{R}(0))$ if the system evolves from $t = 0$ to $t = T$. For a cyclic evolution of the system along a closed path in the parameter space with $\boldsymbol{R}(T) = \boldsymbol{R}(0)$, the variation of phase factor requires

$$\chi_n(\boldsymbol{R}(T)) - \chi_n(\boldsymbol{R}(0)) = 2\pi m, \qquad m \in \text{Integer}, \tag{1.44}$$

to make the phase choice of eigenstates to be single-valued. Therefore, the extra phase γ_n is gauge independent for a closed path and known as the Berry phase. For a closed path, the Berry phase can be re-expressed by Stokes' theorem

$$\gamma_n = \int_{\partial S} d\boldsymbol{R}\cdot\boldsymbol{A}_n(\boldsymbol{R}) = \int_S d\boldsymbol{S}\cdot\boldsymbol{\Omega}_n \tag{1.45}$$

where

$$\boldsymbol{\Omega}_n = \boldsymbol{\nabla}\times\boldsymbol{A}_n(\boldsymbol{R}) \tag{1.46}$$

is called Berry curvature. By utilizing the completeness identity

$$\mathbb{1} = \sum_n |u_n\rangle\langle u_n| \tag{1.47}$$

and the perturbation theory induced identity

$$\langle u_m|\boldsymbol{\nabla}|u_n\rangle = \frac{\langle u_m|\boldsymbol{\nabla} H(\boldsymbol{R})|u_n\rangle}{E_n - E_m}, \tag{1.48}$$

the Berry curvature can be expressed in terms of eigenstates

$$\boldsymbol{\Omega}_n = \mathrm{Im} \sum_{m \neq n} \frac{\langle u_n|\boldsymbol{\nabla} H(\boldsymbol{R})|u_m\rangle \times \langle u_m|\boldsymbol{\nabla} H(\boldsymbol{R})|u_n\rangle}{(E_n - E_m)^2}. \tag{1.49}$$

In condensed matter, the Hamiltonian can be presented in the momentum space $H = H(\boldsymbol{k})$ and the corresponding eigenenergies are called Bloch bands. The momentum variable falls into the Brillouin zone (BZ) which is naturally a closed manifold. For an isolated band, the Berry phase and Berry curvature are well defined. Especially, in a 2-D system, the Berry phase over the BZ is actually a Berry flux considering that the Berry curvature is a momentum-space "magnetic" field and the BZ is identical to a torus. When the flux is 2π multiplied by an integer, i.e.,

$$C_n = \frac{1}{2\pi} \int_{BZ} d\boldsymbol{S}_{\boldsymbol{k}} \cdot \boldsymbol{\Omega}_n(\boldsymbol{k}) \in \text{Integer}, \tag{1.50}$$

C_n, the integer, is the well-known Chern number for Block band n. In condensed matter physics, a nonzero total Chern number of occupied bands usually demonstrates nontrivial topology.

1.3.2 Haldane model and its realization in magnon systems

The Chern number introduced at the end of last section can bring us to a very important concept in condensed matter: topology. This section will review a famous topological insulator model, the Haldane model, and then discuss its realization in magnon systems. In developing this model, Haldane tried to mimic the quantum Hall effect without using a net magnetic flux [4]. He realized that the essential point is actually not the magnetic field but breaking time-reversal symmetry instead. As a result, he built a model on a honeycomb lattice without introducing a net magnetic flux. The way to achieve this is by introducing a next-nearest neighbor hopping with a path-dependent phase factor, and the overall flux around a plaquette corresponding to the phase factor is zero. The Hamiltonian of the model reads

$$H = t_1 \sum_{\langle ij \rangle} c_i^\dagger c_j + t_2 \sum_{\langle\langle ij \rangle\rangle} e^{-i\nu_{ij}\phi} c_i^\dagger c_j + M \sum_i \epsilon_i c_i^\dagger c_j \tag{1.51}$$

where t_1, t_2 are the strength of nearest and second nearest neighbor interaction, M is the on-site inversion symmetry breaking potential, $\epsilon_i = \pm 1$ depending on the type of atom on the site i, the sign of phase factor is determined by

$$\nu_{ij} = \text{sign}(\hat{\boldsymbol{d}}_1 \times \hat{\boldsymbol{d}}_2)_z = \pm 1 \tag{1.52}$$

with $\hat{\boldsymbol{d}}_{1,2}$ being the vector along the bonds bridging the second-nearest neighbor hopping. Fig. 1.3 shows the sign convention of the phase factor for different next-nearest hopping. In momentum space, the Hamiltonian is expressed as

$$h(\boldsymbol{k}) = \epsilon(\boldsymbol{k}) + d_i(\boldsymbol{k})\sigma_i \tag{1.53}$$

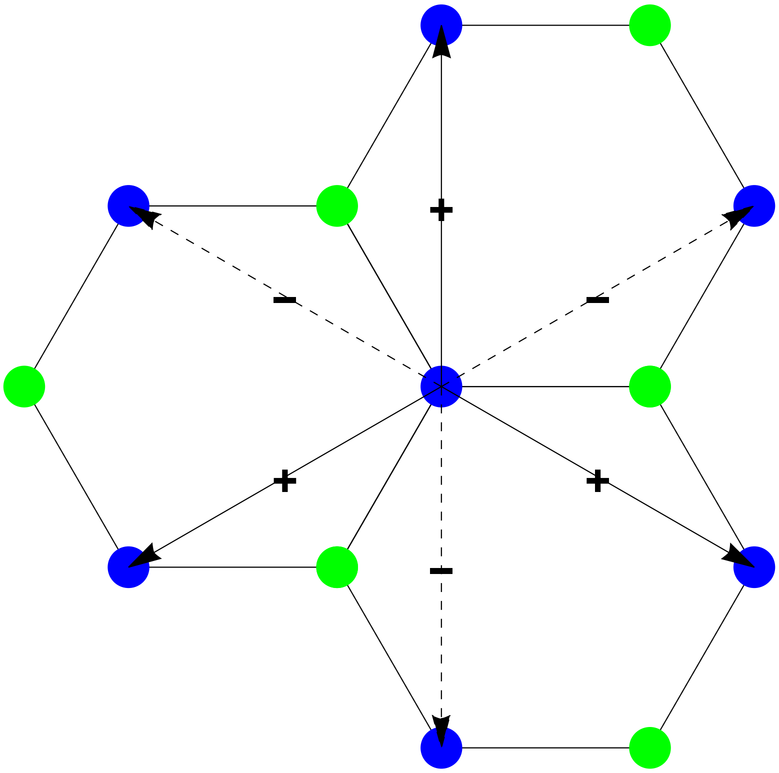

Figure 1.3: The phase arrangement in the honeycomb lattice for the Haldane model.

with σ_i ($i = 1, 2, 3$) being the Pauli matrix and

$$\begin{aligned}
\epsilon(\boldsymbol{k}) &= 2t_2 \cos\phi \sum_i \cos(\boldsymbol{k}\cdot\boldsymbol{b}_i),\\
d_1(\boldsymbol{k}) &= t_1 \sum_i \cos(\boldsymbol{k}\cdot\boldsymbol{a}_i),\\
d_2(\boldsymbol{k}) &= t_1 \sum_i \sin(\boldsymbol{k}\cdot\boldsymbol{a}_i),\\
d_3(\boldsymbol{k}) &= M - 2t_2 \sin\phi \sum_i \sin(\boldsymbol{k}\cdot\boldsymbol{b}_i).
\end{aligned} \tag{1.54}$$

Here, $\boldsymbol{a}_1 = (0, 1)$, $\boldsymbol{a}_2 = (-\frac{\sqrt{3}}{2}, -\frac{1}{2})$, $\boldsymbol{a}_3 = (\frac{\sqrt{3}}{2}, -\frac{1}{2})$, and $\boldsymbol{b}_1 = \boldsymbol{a}_2 - \boldsymbol{a}_3$, $\boldsymbol{b}_2 = \boldsymbol{a}_3 - \boldsymbol{a}_1$, $\boldsymbol{b}_3 = \boldsymbol{a}_1 - \boldsymbol{a}_2$.

Before exploring the topology, it is helpful to learn the symmetry of this model. Physically speaking, the imaginary hopping parameter implies the presence of a vector potential that breaks time-reversal symmetry. The staggered on-site potential breaks the inversion symmetry. To see this, we need to analyze the momentum space Hamiltonian. First, the time reversal operation changes the imaginary unit i to $-i$, which will also effectively flip the sign of the momentum variable, $\boldsymbol{k} \to -\boldsymbol{k}$. Overall, time-reversal symmetry requires $h(\boldsymbol{k}) = h^*(-\boldsymbol{k})$. It is obvious that the $d_3(\boldsymbol{k})$ term doesn't satisfy this except for $\phi = 0, \pi$. Second, the only possible inversion center is the center of the unit cell, with respect to which the A, B sublattices switch with each other. This switching is executed in the Hamiltonian matrix by σ_x. Furthermore, inversion also maps $\boldsymbol{k}$ to $-\boldsymbol{k}$. Therefore, the inversion symmetry imposes the constraint $h(\boldsymbol{k}) = \sigma_x h(-\boldsymbol{k})\sigma_x$ which is again broken by $d_3(\boldsymbol{k})$ due to the nonzero M. The goal of the model is to realize the (anomalous) quantum Hall effect which requires the absence of time-reversal symmetry, so the model is satisfying at least the symmetry aspect.

In a honeycomb lattice, the band gap closing and reopening occur around two Dirac points $\boldsymbol{K}$ and $\boldsymbol{K}'$. An easy way to understand the topology of the model is by observing the band gap behavior under tuning parameters. The Hamiltonian around two Dirac points reads

$$\begin{aligned} h_{\boldsymbol{K}} &= -3t_2\cos\phi + \frac{3}{2}t_1(k_y\sigma_x - k_x\sigma_y) + (M - 3\sqrt{3}t_2\sin\phi)\sigma_z, \\ h_{\boldsymbol{K}'} &= -3t_2\cos\phi - \frac{3}{2}t_1(k_y\sigma_x + k_x\sigma_y) + (M + 3\sqrt{3}t_2\sin\phi)\sigma_z. \end{aligned} \tag{1.55}$$

The energies of the two points are

$$E_{\boldsymbol{K}(\boldsymbol{K}')} = -3t_2\cos\phi \pm \sqrt{\frac{9}{4}t_1^2k^2 + \Delta^2_{\boldsymbol{K}(\boldsymbol{K}')}} \tag{1.56}$$

where the energy gaps are

$$\Delta_{\boldsymbol{K}(\boldsymbol{K}')} = M \mp 3\sqrt{3}t_2\sin\phi. \tag{1.57}$$

In an insulating system, the change of Chern number is always accompanied by gap closing and reopening, which is called a topological phase transition. Let us start from the limit $M \to \infty$, which describes a trivial atomic insulator in which all electrons are trapped at B site. For $\phi \in [0, \pi]$, the gap at $\boldsymbol{K}$ closes and reopens when the parameters go across the point $M = 3\sqrt{3}t_2 \sin\phi$, while the other gap stays open until $M = -3\sqrt{3}t_2 \sin\phi$. Therefore, in the region

$$-3\sqrt{3}t_2 \sin\phi < M < 3\sqrt{3}t_2 \sin\phi, \tag{1.58}$$

the system is nontrivial. When $M < -3\sqrt{3}t_2 \sin\phi$, two gaps remain open, and the system is topologically equivalent to the case $M \to -\infty$ in which the system is again a trivial insulator with all electrons trapped at site A. A similar analysis can be made for the case $\phi \in [\pi, 2\pi]$. Overall, the topologically nontrivial region is

$$M < |3\sqrt{3}t_2 \sin\phi|. \tag{1.59}$$

On the other hand, the topology of this model is marked by the Chern number of occupied bands, which is the lower band in the two-band model. In the present case with two Dirac cones, the Chern number can be shown to be the addition of the integral of Berry curvature around each Dirac point (labeled as $C_{\boldsymbol{K}(\boldsymbol{K}')}$), i.e.,

$$C = C_{\boldsymbol{K}} + C_{\boldsymbol{K}'}. \tag{1.60}$$

For a long wavelength Hamiltonian in the form of

$$h = \epsilon_0 + \sum_{i,j=x,y} k_i \mathcal{A}_{ij} \sigma_j + m\sigma_z, \tag{1.61}$$

the Chern number (integrated over whole momentum space) is

$$C = \frac{1}{2}\text{sign}(m)\text{sign}(\text{Det}\mathcal{A}). \tag{1.62}$$

Applying this conclusion to the model, the Chern number is

$$C = \frac{1}{2}[\text{sign}(M - 3\sqrt{3}t_2 \sin\phi) - \text{sign}(M + 3\sqrt{3}t_2 \sin\phi)] \tag{1.63}$$

from which the topological condition is doubly confirmed.

The Haldane model is a representative example of topological insulator. It is classified by a $\mathbb{Z}$-type (integer number) topological invariant, the Chern number. In recent years, much effort has been made to extend the band-structure topology from electronic systems to magnon systems. One successful attempt is a proposal of the magnonic Haldane model in a honeycomb ferromagnet [36, 37]. The spin-spin interaction Hamiltonian is

$$H = -J_1 \sum_{\langle i,j \rangle} \boldsymbol{S}_i \cdot \boldsymbol{S}_j + \sum_{\langle\langle i,j \rangle\rangle} -J_2 \boldsymbol{S}_i \cdot \boldsymbol{S}_j + \boldsymbol{D}_{ij} \cdot \boldsymbol{S}_i \times \boldsymbol{S}_j \tag{1.64}$$

where $\boldsymbol{D}_{ij} = \nu_{ij} D \hat{\boldsymbol{z}}$ with $\nu_{ij} = \text{sign}(\hat{\boldsymbol{d}}_i \times \hat{\boldsymbol{d}}_j)_z$. After performing Holstein-Primakoff transformation, the magnonic Hamiltonian reads

$$H = \epsilon_0 \sum_i a^\dagger a_i - \tilde{t}_1 \sum_{\langle i,j \rangle} a_i^\dagger a_j - \tilde{t}_2 \sum_{\langle\langle i,j \rangle\rangle} e^{i\nu_{ij}\phi} a_i^\dagger a_j \tag{1.65}$$

where $\epsilon_0 = (3J_1 + 6J_2)S$, $\tilde{t}_1 = J_1 S$, $\tilde{t}_2 = \sqrt{J_2^2 + D^2}S$, and $\phi = \arctan(D/J_2)$. Comparing with Eq. (1.51), the Haldane model can be mapped to the magnon model by

$$t_1 \to -\tilde{t}_1, \quad t_2 \to -\tilde{t}_2, \quad M \to 0, \tag{1.66}$$

and the constant term ϵ_0 is irrelevant to the topology. The Chern number for the lower band is acquired from Eq. (1.63)

$$C = \text{sign}(\sin\phi) = \text{sign}(D). \tag{1.67}$$

Apart from the magnon realization of the famous Haldane model, there has been extensive study of the edge-state transport of magnons in the so-called Chern insulator models, including the Haldane model [22,32–35,35,36,38,58,59,59–62,62–76]. There have also been suggestions to realize the Weyl spectrum of magnons [46–51]. However, compared to the electron system, the richness of magnon topology is limited due to the absence of a variety of orbital freedoms, which leads to the fact that many fascinating topology features, e.g., $\mathbb{Z}_2$ topological insulator, surface Dirac cone, are hardly found in magnon systems. In Chapter 2, we will attempt to generalize the discussion to a new topology for magnons.

1.4 Berry curvature in real space

Before the Berry curvature is introduced in momentum space as a key element of band-structure topology, it can be also defined in real space when the relevant parameters vary in time and space [77]. A representative example is electron motion in a temporally and spatially inhomogenous magnetic texture background. One can consider the system described by

$$i\hbar\partial_t|\psi\rangle = \left[\frac{\boldsymbol{p}^2}{2m} + J\boldsymbol{\sigma}\cdot\boldsymbol{m}(\boldsymbol{r},t)\right]|\psi\rangle \tag{1.68}$$

where $\psi = (\psi_\uparrow, \psi_\downarrow)$, $\boldsymbol{m}(\boldsymbol{r},t)$ is the local magnetization field, and J is the exchange coupling strength between electron spin and local magnetization. In the strong coupling regime, the spin direction of electrons adiabatically adjusts itself to the local magnetization direction, which means when an electron traverses a nonuniform spin texture it will pick up a Berry phase.

A transparent way to see this effect is by describing the electron motion in a local frame in which electrons can feel an emergent gauge field induced by the real-space Berry curvature of spin texture. The local frame switching is realized by a local transformation $\psi = U\varphi$ where $U = e^{-i(\theta/2)\boldsymbol{\sigma}\cdot\boldsymbol{n}}$ with $\boldsymbol{n} = \hat{\boldsymbol{z}} \times \boldsymbol{m}/|\hat{\boldsymbol{z}} \times \boldsymbol{m}|$, and thus Eq. (1.68) will be converted to

$$i\hbar\partial_t\varphi = \left[q^e V^e + \frac{(\boldsymbol{p} - q^e\boldsymbol{A}^e)^2}{2m} + J\sigma_z\right]. \tag{1.69}$$

Here, the matrix V^e and $\boldsymbol{A}^e$ are the scalar and vector part of the emergent gauge field with the following expressions

$$\begin{aligned} V^e &= -(i\hbar/q^e)U\partial_t U^\dagger, \\ \boldsymbol{A}^e &= -(i\hbar/q^e)U\nabla U^\dagger. \end{aligned} \tag{1.70}$$

The emergent charge q^e is artificially introduced to be in parallel with the standard form of coupling between charge and gauge field, and it actually drops out in the equation above. For a smooth magnetization texture, the emergent fields above can be regarded as a perturbation to the Hamiltonian $H = \frac{\boldsymbol{p}^2}{2m} + J\sigma_z$. In the adiabatic limit, the gauge fields act on each band separately, allowing us to introduce spin-dependent gauge potential

$$\begin{aligned} \mathcal{V}^e_\sigma &= \langle\psi_\sigma|V^e|\psi_\sigma\rangle = -(i\hbar/q^e)\langle\psi_\sigma|U\partial_t U^\dagger|\psi_\sigma\rangle, \\ \boldsymbol{\mathcal{A}}^e_\sigma &= \langle\psi_\sigma|\boldsymbol{A}^e|\psi_\sigma\rangle = -(i\hbar/q^e)\langle\psi_\sigma|U\nabla U^\dagger|\psi_\sigma\rangle. \end{aligned} \tag{1.71}$$

The gauge potentials have a similar form as the Berry connection defined in Eq. (1.41). It becomes clear that the emergent gauge field gives emergent electric and magnetic fields

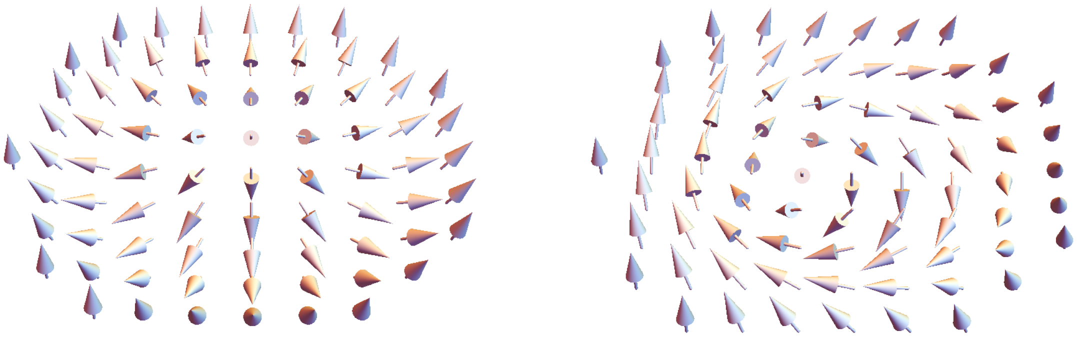

Figure 1.4: Two dimensional magnetic skyrmion texture: (a) Néel type (b) Bloch type.

as below

$$
\begin{aligned}
(\boldsymbol{E}^e_\sigma)_i &= (-\nabla \mathcal{V}^e_\sigma - \partial_t \boldsymbol{\mathcal{A}}^e_\sigma)_i = \mp \frac{\hbar}{2q^e} \boldsymbol{m} \cdot (\partial_i \boldsymbol{m} \times \partial_t \boldsymbol{m}), \\
(\boldsymbol{B}^e_\sigma)_i &= (\nabla \times \boldsymbol{\mathcal{A}}^e_\sigma)_i = \mp \frac{\hbar}{2q^e} \frac{\epsilon_{ijk}}{2} \boldsymbol{m} \cdot (\partial_j \boldsymbol{m} \times \partial_k \boldsymbol{m}).
\end{aligned} \tag{1.72}
$$

Note that the emergent magnetic field is a real space Berry curvature as it is the curl of a Berry connection. In addition, we can also regard the emergent electric field as a Berry curvature in the mixed space-time manifold.

As shown above, the emergent gauge field (real-space Berry curvature) relies on a spin texture background. In the recent decade, there has been a surge of interest in the skyrmion spin texture in chiral ferromagnetic or antiferromagnetic materials. Two typical magnetic skyrmion textures are shown in Fig. 1.4. The skyrmion in these magnetic materials is characterized by a topological charge

$$
Q = \frac{1}{4\pi} \int dxdy \boldsymbol{m} \cdot (\partial_x \boldsymbol{m} \times \partial_y \boldsymbol{m}) \tag{1.73}
$$

which takes a quantized value depending on the specific system. In a metallic ferromagnet with skyrmionic texture, the z-component emergent magnetic field can accumulate a quantized flux over an enlarged unit cell (due to magnetic field), which is proportional to the topological charge

$$\int d\boldsymbol{r}(\boldsymbol{B}^e_\sigma)_z = \mp 4\hbar Q. \tag{1.74}$$

This demonstrates that the magnetic skyrmion system is an ideal platform for the emergent gauge field. The topological Hall effect induced by the emergent magnetic field is usually used to detect the formation of skyrmions [78].

Moreover, the spin texture can also approximately induce an emergent gauge field for magnons in the long-wavelength regime, and it shares a similar expression as that for electrons. One can consider the free energy density of a ferromagnet

$$\mathcal{F} = \frac{\mathcal{J}}{2}(\partial_i \boldsymbol{m})^2 + \mathcal{D}(m_z \vec{\nabla} \cdot \boldsymbol{m} - \boldsymbol{m} \cdot \vec{\nabla} m_z) - \boldsymbol{B} \cdot \boldsymbol{m}. \tag{1.75}$$

Here, the three terms stand for exchange, DMI, and Zeeman coupling, respectively. We assume the parameter field is locally pointing along the direction $\boldsymbol{m}_0 = (\sin\theta\cos\phi, \sin\theta\sin\phi, \cos\theta) = R\hat{z}$, where $R = \exp(L_z\phi)\exp(L_y\theta)$ with $(L_i)_{jk} = -\epsilon_{ijk}$. To take the spin wave fluctuation around the local parameter direction, the spin field $\boldsymbol{m}$ can be parametrized by rotating a field $\boldsymbol{m}'$ that fluctuates around $\hat{z}$-axis, i.e., $\boldsymbol{m} = R\boldsymbol{m}'$, where $\boldsymbol{m}' = \hat{z}\sqrt{1-|\gamma|^2} + \hat{x}\gamma^x + \hat{y}\gamma^y$ with $|\gamma| = \sqrt{(\gamma^x)^2 + (\gamma^y)^2} \ll 1$ and $\gamma^{x(y)}$ being spin wave. Plugging this parametrized spin field into the free energy, to the leading-order spatial gradient of spin texture, the free energy is rewritten as

$$\mathcal{F} \quad = -\frac{\mathcal{J}}{2}\boldsymbol{m}' \cdot (\partial_i + \mathcal{A}^t_i - \frac{\mathcal{D}}{\mathcal{J}}\mathcal{A}^d_i)^2 \boldsymbol{m}' \tag{1.76}$$

where $\mathcal{A}^t_i = R^T\partial_i R$, $\mathcal{A}^d_i = \bar{R}^T L_i \bar{R}$ with $\bar{R} = \exp\{L_z\frac{\pi}{2}\}R$. Plugging the expression of $\boldsymbol{m}'$ with spin-wave field into free energy above, the magnon Hamiltonian is obtained

$$\mathcal{H} = \psi^* \frac{\mathcal{J}}{2}(-i\vec{\nabla} - \boldsymbol{a})^2 \psi, \tag{1.77}$$

where $a_i = -(\mathcal{A}_i^t - \frac{\mathcal{D}}{\mathcal{J}}\mathcal{A}_i^d)|_{12}$. Here, $\boldsymbol{a}$ is an emergent gauge field [79–81] with two components $\boldsymbol{a} = \boldsymbol{a}^t + \boldsymbol{a}^d$, where $a_i^t = \mathcal{A}_i^t|_{12} = \cos\theta\partial_i\phi$, $\boldsymbol{a}^d = \frac{\mathcal{D}}{\mathcal{J}}\boldsymbol{\mathcal{A}}^d|_{12} = -\frac{\mathcal{D}}{\mathcal{J}}\tilde{R}_z\boldsymbol{m}_0$ with $\boldsymbol{m}_0 = R\hat{z}$. These two parts result in emergent magnetic fields,

$$\begin{aligned} b_i^t &= (\vec{\nabla} \times \boldsymbol{a}^t)_i = -\frac{1}{2}\epsilon_{ijk}\boldsymbol{m}_0 \cdot (\partial_j\boldsymbol{m}_0 \times \partial_k\boldsymbol{m}_0), \\ \boldsymbol{b}^d &= \vec{\nabla} \times \boldsymbol{a}^d. \end{aligned} \tag{1.78}$$

We find the form of $\boldsymbol{b}^t$ resembles that for electrons and is also connected to the topological charge density. On the other hand, the kinetic term of magnons can be written as $\mathcal{L}_{kin} = \frac{\mathcal{S}}{2}\psi^*(i\partial_t - \varphi)\psi$ with $\varphi = \cos\theta\partial_t\phi$ being the scalar potential (see details in Chapter 5). Therefore, the Lagrangian is $\mathcal{L} = \mathcal{L}_{kin} - \mathcal{H}$, which leads to a Schrödinger equation

$$\mathcal{S}(i\partial_t - \varphi)\psi = \mathcal{J}(-i\vec{\nabla} - \boldsymbol{a})^2\psi. \tag{1.79}$$

Similar to the electronic system, the emergent gauge field also causes a Hall type response associated with magnons analogous to the topological Hall effect, e.g., the thermal Hall effect and the spin Nernst effect. We will discuss the relevant physics in more detail in Chapter 5.

1.5 Linear response theory

The main theory built in Chapters 3 and 4 is based on the linear response theory. This section introduces the basic quantum mechanical linear response theory by following Ref. [82] and gives relevant examples to lay the foundation for later discussions.

A simple statement of linear response theory is that for a given system, the response to a weak perturbation is proportional to the perturbation. To understand this we consider the following Hamiltonian

$$H(t) = H_0 + H'(t)\theta(t - t_0) \tag{1.80}$$

where H_0 describes the initial system, $H'(t)$ describes a perturbation starting from $t = t_0$. For a given observable A, its average value at a given time $t > 0$ is calculated as

$$\langle A(t)\rangle = \text{tr}[\rho(t)A] \tag{1.81}$$

with

$$\rho(t) = \frac{1}{Z}\sum_n |n(t)\rangle\langle n(t)|e^{-\beta E_n} \tag{1.82}$$

where $\beta = 1/(k_B T)$, Z is the partition function, E_n and $|n(t)\rangle$ are the eigenstate and eigenenergy of $H(t)$. From the Schrödinger equation, the eigenstate can be written in a form evolving from $t = t_0$

$$|n(t)\rangle = e^{-iH_0 t}\hat{U}(t, t_0)|n\rangle \tag{1.83}$$

where $|n\rangle = e^{iH_0 t_0}|n(t_0)\rangle$ and $\hat{U}(t, t_0) = e^{-i\int_{t_0}^{t} dt'\hat{H}'(t')}$. Here, $|n\rangle$ is the eigenstate of the time-independent Hamiltonian H_0. Inserting Eq. (1.83) into Eq. (1.81) and keeping the result to the first order of perturbation, the expectation value of the observable is

$$\langle A(t)\rangle = \langle A\rangle_0 - i\int_{t_0}^{t} dt'\langle[\hat{A}(t), \hat{H}'(t')]\rangle_0 \tag{1.84}$$

where $\langle\cdots\rangle_0$ means the expectation value with respect to the Hamiltonian H_0. Usually, we are interested in the variation of the observable after the perturbation is applied

$$\delta\langle A(t)\rangle = \langle A(t)\rangle - \langle A\rangle_0 = \int_{t_0}^{\infty} dt' C^R(t, t')e^{-\eta(t-t')} \tag{1.85}$$

with

$$C^R(t,t') = -i\theta(t-t')\langle[\hat{A}(t), \hat{H}'(t')]\rangle_0. \tag{1.86}$$

Here, the factor $e^{-\eta(t-t')}$ with $\eta = 0^+$, a infinitesimal positive value, is added to ensure that the response is substantially suppressed when $t \gg t'$.

When one switches the picture to the frequency domain, the Fourier transformation of the perturbation is

$$H'(t) = \int_{-\infty}^{\infty} \frac{d\omega}{2\pi} e^{-i\omega t} H'_\omega, \tag{1.87}$$

and the Fourier component of the response is given by

$$\langle \delta A_\omega \rangle = \int_{-\infty}^{\infty} e^{i(\omega+i\eta)t} C^R_{AH'_\omega}(t) \tag{1.88}$$

where

$$C^R_{AH'_\omega}(t) = -i\theta(t)\langle[\hat{A}(t), \hat{H}'(0)]\rangle_0. \tag{1.89}$$

The Kubo linear response formula is usually used to discuss the charge current response to an external electric field. The perturbation is

$$H' = \int d\boldsymbol{r} \boldsymbol{A}(\boldsymbol{r},t) \cdot \boldsymbol{J}(\boldsymbol{r}) \tag{1.90}$$

where the coupling between charge density and electric potential is removed through gauge transformation. Here, $\boldsymbol{J}(\boldsymbol{r})$ is the charge current that is composed of paramagnetic and diamagnetic terms: $\boldsymbol{J} = \boldsymbol{J}_{\text{para}} + \boldsymbol{J}_{\text{dia}}$, where

$$\begin{aligned}\boldsymbol{J}_{\text{para}}(\boldsymbol{r}) &= \frac{\hbar}{mV}\sum_{\boldsymbol{k},\boldsymbol{q}}(\boldsymbol{k}+\frac{1}{2}\boldsymbol{q})e^{i\boldsymbol{q}\cdot\boldsymbol{r}}a^{\dagger}_{\boldsymbol{k}}a_{\boldsymbol{k}+\boldsymbol{q}},\\ \boldsymbol{J}_{\text{dia}}(\boldsymbol{r}) &= \frac{-q}{mV}\boldsymbol{A}(\boldsymbol{r})\sum_{\boldsymbol{k},\boldsymbol{q}}e^{i\boldsymbol{q}\cdot\boldsymbol{r}}a^{\dagger}_{\boldsymbol{k}}a_{\boldsymbol{k}+\boldsymbol{q}}.\end{aligned} \tag{1.91}$$

In the frequency domain, $\boldsymbol{A}(\boldsymbol{r},\omega) = \frac{1}{i\omega}\boldsymbol{E}(\boldsymbol{r},\omega)$ with $\boldsymbol{E}$ being the electric field, and it is assumed that the response takes the form

$$\boldsymbol{J}(\boldsymbol{r},\omega) = \int d\boldsymbol{r}'\hat{\sigma}(\mathbf{r},\boldsymbol{r}',\omega)\cdot\boldsymbol{E}(\boldsymbol{r}',\omega). \tag{1.92}$$

Through the Kubo formula introduced before, the conductivity tensor can be calculated as

$$\sigma_{\mu\nu}(\mathbf{r},\boldsymbol{r}',\omega) = \frac{ie^2}{\omega}\Pi_{\mu\nu}(\mathbf{r},\boldsymbol{r}',\omega) + \frac{ie^2 n(\boldsymbol{r})}{\omega m}\delta(\boldsymbol{r}-\boldsymbol{r}')\delta_{\mu\nu} \tag{1.93}$$

where $n(\boldsymbol{r})$ is the local charge density, m is the electron mass, and

$$\Pi_{\mu\nu}(\boldsymbol{r},\boldsymbol{r}',t-t') = -i\theta(t-t')\langle[J_\mu(\boldsymbol{r},t),J_\nu(\boldsymbol{r}',t')]\rangle_0. \tag{1.94}$$

For a system with translational symmetry, the above equation can be converted to momentum space and all calculations can be performed in the eigenbasis representation. This will become clear in our discussion in Chapters 3 and 4.

In this thesis, we will mainly focus on the linear response induced by a temperature gradient, where the driving force will be temperature gradient $\boldsymbol{\nabla}T$. To deal with this statistical force, we need to introduce a coupling between the Hamiltonian and a pseudo-gravitational field. The response function will contain two parts: the Kubo-response part and orbital contributions. The Kubo part will be calculated with similar theory to that introduced here, while the orbital part requires some special techniques. All the details will be discussed in Chapters 3 and 4.

Chapter 2

Chiral topological insulator of magnons

2.1 Introduction

The discovery of topological insulators (TIs) [12, 13] is a remarkable achievement in condensed matter physics as it reveals fundamental connections to topology and is promising for applications in electronics and quantum computing. At the same time, the concept of topology has arisen in a variety of other fields under the encouragement of the success of topological insulators [83, 84]. Recently, there has been considerable interest in the topological physics of magnon systems [35, 36, 58–64]. Realizations of systems with a Weyl spectrum of magnons have been suggested [46–51]. Multiple theoretical works [22, 32–35, 38, 59, 62, 65–76] have discussed the edge or surface states of gapped magnon systems. Due to the absence of the Kramers degeneracy and the electronic orbital freedom for magnons, the investigation has been limited to the magnon analog of the Chern insulator. A magnon analog of the quantum spin Hall effect comprised of two copies of magnon Chern insulators has also been proposed [38, 72]. Nevertheless, the topologically protected helical surface states have not been discussed for magnon systems. According to the ten-fold way of classifying TIs [85, 86], the AIII class only requires the sublattice chiral symmetry for realization of a topological insulator with $\mathbb{Z}$ invariant in one and three dimensions [87–90]. Hosur *et al.* [87] discussed an electronic model of chiral topological insulator (cTI). Wang *et al.* suggested a realization of cTI in cold-atom systems [88].

In this chapter, we show that magnon chiral topological insulator (mcTI) can be realized in a Heisenberg model endowed with the Dzyaloshinskii-Moriya interaction (DMI) [91, 92]. We consider a layered honeycomb lattice structure [93, 94] in which the interactions are chosen such that the system possesses the chiral symmetry (see Fig. 2.1). The bulk is characterized by the $\mathbb{Z}$ topological invariant: winding number. In accordance with the bulk-boundary correspondence, our model supports a symmetry-protected magnon Dirac cone on its surface, provided the chiral symmetry is not broken on the surface. The helical surface states lack backscattering in the presence of the chiral symmetry. By breaking the chiral symmetry, a small gap can be introduced in the surface band, which leads to the magnon Hall response, e.g., under a temperature gradient. We observe that similar to electronic systems, the chiral symmetric perturbations can change the system to the nodal line and trivial phases. Furthermore, by adding terms breaking the chiral symmetry, we can bring our system into the three-dimensional magnon anomalous Hall (3D-mAH) and Weyl magnon phases.

2.2 Model

We consider a layered honeycomb magnetic structure with ferromagnetic ordering, as shown in Fig. 2.1. To realize mcTI, we construct a model with the magnon Dirac spectrum in the bulk. We then open a gap by adding a mass term corresponding to additional DMI, which can be done in various ways. The Hamiltonian is composed of the in-plane and interlayer exchange interactions, and the axial anisotropy terms,

$$H = H_{\text{in}} + H_{\text{inter}} + H_{\text{an}}, \tag{2.1}$$

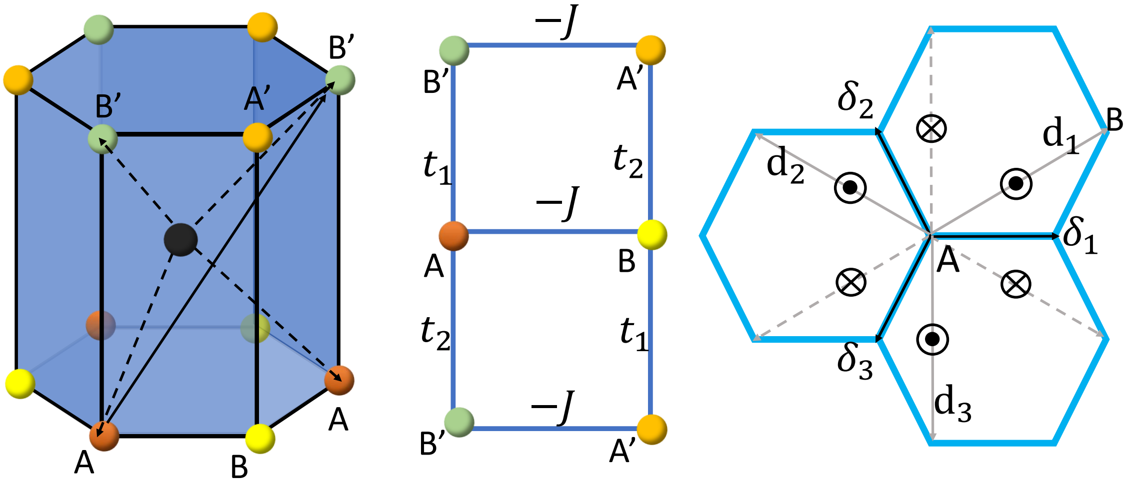

Figure 2.1: Left: The layered Honeycomb structure. The central non-magnetic atom generates DMI between interlayer third-nearest-neighbor atoms, e.g., A and B'. Middle: The in-plane and interlayer exchange energy. Right: The projection of interlayer DMI between A and B' on z direction.

where

$$\begin{aligned} H_{\text{in}} &= -J\sum_{z,i}\sum_{\mu=1}^{3}\mathbf{S}_{A,i}\cdot\mathbf{S}_{B,i+\boldsymbol{\delta}_\mu}+\mathbf{S}_{A',i}\cdot\mathbf{S}_{B',i-\boldsymbol{\delta}_\mu}, \\ H_{\text{inter}} &= -\sum_{i,z}(t_1\mathbf{S}_{A,z}\cdot\mathbf{S}_{B',z+1}+t_2\mathbf{S}_{A,z}\cdot\mathbf{S}_{B',z-1}) \\ &\quad +(t_1\leftrightarrow t_2, A\rightarrow B, B'\rightarrow A'), \\ H_{\text{an}} &= \sum_{i,z}\sum_{Q}K(S^z_{Q,(i,z)})^2. \end{aligned} \tag{2.2}$$

Here i corresponds to the in-plane index and z corresponds to the layer index; $\boldsymbol{\delta}_1 = (1,0,0)$, $\boldsymbol{\delta}_2 = (-\frac{1}{2},\frac{\sqrt{3}}{2},0)$, $\boldsymbol{\delta}_3 = (-\frac{1}{2},-\frac{\sqrt{3}}{2},0)$; J and K are nearest exchange and axial anisotropy energy with $K<0$. Q stands for different spin modes, i.e., $Q = A, B, A', B'$. In the Hamiltonian, we suppress unrelated coordinates for clarity. For in-plane interaction, we only consider nearest-neighbor exchange. For the interlayer interaction, we use a staggered pattern as shown in Fig. 2.1 (this limitation simplifies analysis but it is not necessary, as we show in Sec. 2.6). We perform Holstein-Primakoff transformation in the large S limit, $S^z_{Q,i} = (S - Q^\dagger_i Q_i)$ and $S^+_{Q,i} = \sqrt{2S}Q_i$, with $Q^\dagger_i$, Q_i being the magnon creation and annihilation operators for spin mode S_Q. The Hamiltonian in momentum space is written in the basis $\Psi_\mathbf{k} = (A_\mathbf{k}, B_\mathbf{k}, A'_\mathbf{k}, B'_\mathbf{k})$, where we label the layer and sublattice degrees of freedom by μ and τ Pauli matrices,

$$H = JS \sum_\mathbf{k} \Psi^\dagger_\mathbf{k} \mathcal{H}_\mathbf{k} \Psi_\mathbf{k}, \tag{2.3}$$

with

$$\begin{aligned} \mathcal{H}_\mathbf{k} &= \varepsilon_0 - \gamma_{1\mathbf{k}}\tau_x + \gamma_{2\mathbf{k}}\mu_z\tau_y + 2\lambda\cos(k_z)\mu_x\tau_x \\ &\quad -2\delta\sin(k_z)\mu_x\tau_y. \end{aligned} \tag{2.4}$$

Here $\varepsilon_0 = 3 - 2\lambda - 2\kappa$, $\gamma_\mathbf{k} = \sum_\mu e^{i\mathbf{k}\cdot\boldsymbol{\delta}_\mu} = \gamma_{1\mathbf{k}} + i\gamma_{2\mathbf{k}}$, with $\gamma_{1\mathbf{k}} = \cos(k_x) + 2\cos(\frac{k_x}{2})\cos(\frac{\sqrt{3}k_y}{2})$ and $\gamma_{2\mathbf{k}} = 2[\cos(\frac{k_x}{2}) - \cos(\frac{\sqrt{3}k_y}{2})]\sin(\frac{k_x}{2})$, $\lambda = -\frac{1}{2}(t_1 + t_2)/J$, $\delta = \frac{1}{2}(t_2 - t_1)/J$, and $\kappa = K/J$. Note that the Hamiltonian above has the chiral symmetry τ_z up to a constant term (below, we disregard this constant energy shift), i.e.,

$$\tau_z \mathcal{H}_\mathbf{k} \tau_z = -\mathcal{H}_\mathbf{k}. \tag{2.5}$$

First, we consider the case $\lambda = 0$, corresponding to the staggered interlayer exchange. In this pattern, the exchange term realizes the so-called π flux [87] for vertical plaquettes $\Pi_\square sign(t_{ij}) = -1$, e.g., $AB'A'BA$, where t_{ij} stands for the exchange strength between two spins. The eigenenergy,

$$E_\pm/JS = \pm\sqrt{|\gamma_\mathbf{k}|^2 + 4\delta^2\sin^2(k_z)}, \tag{2.6}$$

reveals two Dirac cones at $\mathbf{Q}_{R(L)} = (0, \pm\frac{4\pi}{3\sqrt{3}}, 0)$. Around the Dirac point $\mathbf{Q}_R$, the Hamiltonian reads

$$\mathcal{H}_{0,\mathbf{k}} = q_i \alpha_i, \tag{2.7}$$

where $q_x = \frac{3}{2}k_x$, $q_y = \frac{3}{2}k_y$, and $q_z = -2\delta k_z$; $\{\alpha_i\} = \{\mu_z\tau_y, \tau_x, \mu_x\tau_y\}$ satisfy the relation $\{\alpha_i, \alpha_j\} = 2\delta_{ij}$. For the other Dirac point, the Hamiltonian is easily obtained after the transformation $q_y \to -q_y$ in Eq. (2.7). Since the two Dirac cones give us equivalent physics, we use the form in Eq. (2.7) in the following discussion.

To realize the mcTI, the Hamiltonian should have a chiral symmetric mass term to open the gap in the bulk Dirac cone while preserving the surface Dirac cone. In a massive Dirac equation for the bulk, the mass term is described by the matrix β satisfying the anti-communication relation $\{\beta, \mathcal{H}_{0,\mathbf{k}}\} = 0$. The only possible term preserving the chiral symmetry is $\beta = \mu_y\tau_y$. To this end, we include the third-nearest-neighbor interlayer DMI in our model. The correct form of DMI can be produced by the central non-magnetic atom as it is shown in Figs. 2.1 and 2.2, where we assume an overlap of relevant orbitals and a sufficiently strong spin-orbit interaction. As an example, we calculate the interlayer DMI between $A1$ and $B'1$ spins in Fig. 2.2. Here, the displacements of the two spins to the central atom $C1$ are

$$\overrightarrow{C1A1} = \boldsymbol{\delta}_3 - \mathbf{c}, \qquad \overrightarrow{C1B'1} = \boldsymbol{\delta}_1 + \mathbf{c}, \tag{2.8}$$

where $2\mathbf{c}$ is the vertical interlayer vector, e.g., $\overrightarrow{A2B'1} = 2\mathbf{c}$. The DMI vector between $A1$ and $B'1$ can be presented as

$$\mathbf{D}_{A1\to B'1} = D(\overrightarrow{C1A1} \times \overrightarrow{C1B'1}) = D(\mathbf{e}_z + \mathbf{c} \times \boldsymbol{\delta}_2). \tag{2.9}$$

with D being the interaction strength. In Fig 2.2, we give all the DMI z-component pro-

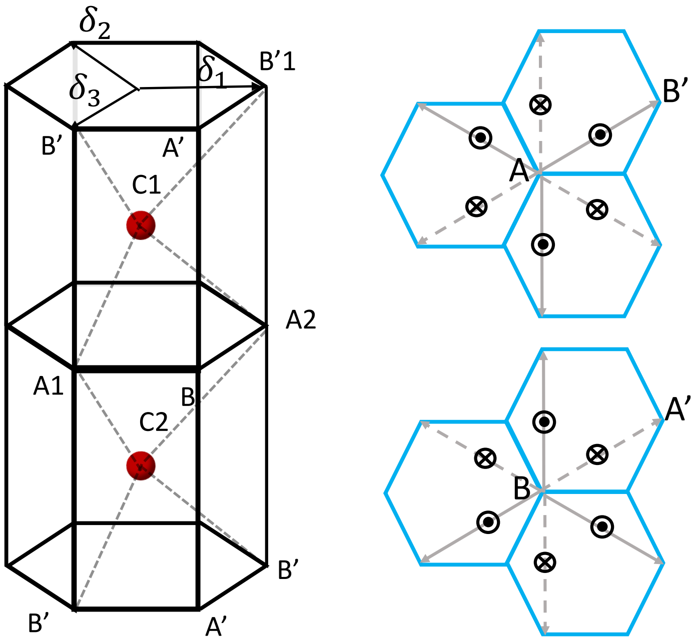

Figure 2.2: The interlayer DMI pattern.

jections; as shown, $B - A'$ and $A - B'$ have opposite sign along the same interaction path vector.

The DMI contributes to the Hamiltonian a term

$$\begin{aligned} H_{\mathrm{th}} &= \sum_{z,n=\pm 1} \sum_{i,\mathbf{d}_\lambda} \mathbf{D}_{AB'}(\mathbf{d}_\lambda) \cdot [\mathbf{S}_{A,(i,z)} \times \mathbf{S}_{B',(i+\mathbf{d}_\lambda,z+n)}] \\ &\quad + \{A \rightarrow B, B' \rightarrow A'\}, \end{aligned} \tag{2.10}$$

where i, z are the in-plane and layer coordinates with assumption of unit interlayer distance in the z direction, $\mathbf{d}_\lambda$ represents the in-plane second-nearest-neighbor between atoms with $\mathbf{d}_1 = (\frac{3}{2}, \frac{\sqrt{3}}{2}, 0)$, $\mathbf{d}_2 = (-\frac{3}{2}, \frac{\sqrt{3}}{2}, 0)$, and $\mathbf{d}_3 = (0, -\sqrt{3}, 0)$ (the other three are $-\mathbf{d}_1$,$-\mathbf{d}_2$,$-\mathbf{d}_3$). At the same time, we assume that the in-plane DMI between the second-nearest-neighbors is absent, as such a term would break the chiral symmetry. For the magnetization along the z axis, only the z component of DMI vectors is relevant, which is shown in Fig. 2.1. The z projections of DMI vectors have the same magnitude D^z and follow the staggered pattern shown in Fig. 2.1. In momentum space, the DMI term reads

$$\mathcal{H}_{\text{th}} = 4\delta_D \xi_{\mathbf{k}} \cos(k_z) \mu_y \tau_y, \tag{2.11}$$

where $\delta_D = D^z/J$ and $\xi_{\mathbf{k}} = \sum_{i=1}^{3} \sin(\mathbf{k} \cdot \mathbf{d}_i)$. Now, we have the full model given by Eqs. (2.4) and (2.11).

To confirm the existence of surface states, we diagonalize the Hamiltonian given by Eqs. (2.1) and (2.10) in a slab geometry. In our calculation, we consider two bulk regions with the opposite sign of DMI δ_D, which guarantees the sign change of the mass term across the interface. As expected, the model has Dirac states confined to the $x - y$ plane separating the two bulk regions as shown in Fig. 2.3, left. The model hosts two surface Dirac cones at the two-dimensional projection of $\mathbf{Q}_R$ and $\mathbf{Q}_L$ as long as all parameters are nonzero. We also considered a bulk terminated at a honeycomb plane with vacuum, which results in a single Dirac cone with a gap opening due to breaking of the chiral symmetry at the interface (see Fig. 2.3, right). The chiral symmetry breaking appears due to the exchange energy terms at the interface after application of the Holstein-Primakoff transformation.

Now, we see that the model based on layered honeycomb lattice is realized by considering various type of interlayer exchange or DM interactions. As a guidance, all possible chiral symmetry allowed terms in a honeycomb lattice can be listed to inspire other new models. For a ferromagnet on a layered honeycomb lattice with only intralayer exchange interactions considered, the long-wavelength magnon Hamiltonian around (2D) Dirac point is

$$H_{\boldsymbol{K}/\boldsymbol{K}'} = \frac{3JS}{2}(k_x \mu_z \tau_y \pm k_y \tau_x). \tag{2.12}$$

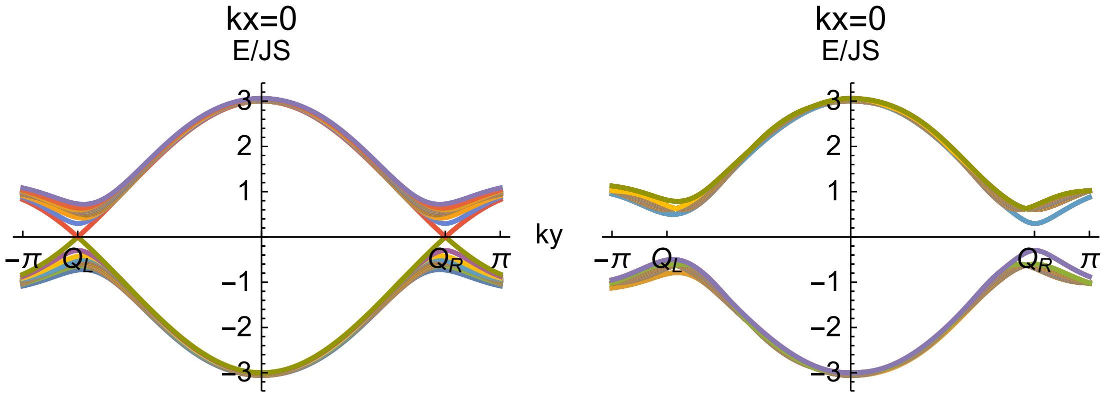

Figure 2.3: A plot corresponding to a slab geometry with the parameters, $\delta = 0.3$, $\delta_D = 0.15$. Left: The surface state with the Dirac cone at $\mathbf{Q}_L$ and $\mathbf{Q}_R$ where the surface states appear at the interface between the two bulk regions with the opposite sign of DMI δ_D. Right: The surface state cone splits when the bulk is interrupted at a honeycomb plane in contact with vacuum due to uncompensated exchange interactions leading to breaking of the chiral symmetry.

Possible matrices describing the chiral symmetry (satisfy Eq. (2.5)) include

$$\{\mu_0, \mu_z\} \otimes \tau_z, \qquad \{\mu_x, \mu_y\} \otimes \tau_y. \tag{2.13}$$

We can now write all possible chiral symmetric terms that anticommute with the chiral symmetry. All possibilities are listed in Table 2.1. A 3D chiral Hamiltonian will be obtained by adding possible terms generating these matrices to the layered Honeycomb system. For a system of localized spins, the corresponding hopping terms of magnons can be obtained from exchange interactions and DMI. To achieve our goal, one can first construct 3D Dirac magnons and then open a gap with a chiral symmetric perturbation. The minimal model only contains terms that anticommute with each other, but the chiral symmetric perturbations do not necessarily anticommute with the minimal model and can serve to drive the phase transition as discussed in Sec. 2.6. We note that the presence of the chiral symmetry does not guarantee the mcTI phase and one has to verify the nontrivial topology via winding number calculation.

The above-mentioned steps can be applied to an arbitrary lattice to obtain other models of mcTIs.

Table 2.1: Symmetry analysis

Chiral Symmetry	Possible Terms	
τ_z	$\{\mu_0, \mu_x, \mu_y, \mu_z\} \otimes \{\tau_x, \tau_y\}$	
$\mu_z\tau_z$	$\{\mu_x, \mu_y\} \otimes \{\tau_0, \tau_z\}$	$\{\mu_0, \mu_z\} \otimes \{\tau_x, \tau_y\}$
$\mu_x\tau_y$	$\{\mu_y, \mu_z\} \otimes \{\tau_0, \tau_y\}$	$\{\mu_0, \mu_x\} \otimes \{\tau_x, \tau_z\}$
$\mu_y\tau_y$	$\{\mu_x, \mu_z\} \otimes \{\tau_0, \tau_y\}$	$\{\mu_0, \mu_y\} \otimes \{\tau_x, \tau_z\}$

2.3 Topological invariant

The presence of chiral symmetry ensures that the Hamiltonian could be brought to an off-diagonal form by a unitary transformation. For our case, we need a transformation satisfying $U\tau_z U^\dagger = \mu_z$, under which,

$$\tilde{\mathcal{H}}_{\mathbf{k}} = U\mathcal{H}_{\mathbf{k}}U^\dagger = \begin{bmatrix} 0 & D_{\mathbf{k}} \\ D_{\mathbf{k}}^\dagger & 0 \end{bmatrix}, \tag{2.14}$$

with

$$D_{\mathbf{k}} = \begin{bmatrix} -\gamma_{\mathbf{k}} & \Delta_{\mathbf{k}} \\ -\Delta_{\mathbf{k}}^* & -\gamma_{-\mathbf{k}} \end{bmatrix}, \tag{2.15}$$

where $\Delta_{\mathbf{k}} = -4\delta_D\xi_{\mathbf{k}}\cos(k_z) + i2\delta\sin(k_z)$. This transformation matrix is identified as

$$U = \begin{bmatrix} 1 & 0 & 0 & 0 \\ 0 & 0 & 1 & 0 \\ 0 & 1 & 0 & 0 \\ 0 & 0 & 0 & 1 \end{bmatrix}. \tag{2.16}$$

Assuming that the eigenstates of $\tilde{\mathcal{H}}_{\mathbf{k}}$ have the form $\psi_a = (\chi_a, \eta_a)^T$, the eigenequation reads

$$\begin{bmatrix} 0 & D_{\mathbf{k}} \\ D_{\mathbf{k}}^\dagger & 0 \end{bmatrix} \begin{bmatrix} \chi_a \\ \eta_a \end{bmatrix} = \lambda_a \begin{bmatrix} \chi_a \\ \eta_a \end{bmatrix} \tag{2.17}$$

by applying $\tilde{\mathcal{H}}_{\mathbf{k}}$ on both sides of which again can produce

$$\begin{bmatrix} D_{\mathbf{k}} D_{\mathbf{k}}^\dagger & 0 \\ 0 & D_{\mathbf{k}}^\dagger D_{\mathbf{k}} \end{bmatrix} \begin{bmatrix} \chi_a \\ \eta_a \end{bmatrix} = \lambda_a^2 \begin{bmatrix} \chi_a \\ \eta_a \end{bmatrix}. \tag{2.18}$$

If one can find u_a that satisfies $D_{\mathbf{k}} D_{\mathbf{k}}^\dagger u_a = \lambda_a^2 u_a$ and $u_a u_a^\dagger = 1$ ($a = 1, 2$), the eigenstates are constructed as

$$\begin{bmatrix} \chi_a^\pm \\ \eta_a^\pm \end{bmatrix} = \frac{1}{\sqrt{2}} \begin{bmatrix} u_a \\ \pm v_a \end{bmatrix}, \tag{2.19}$$

with

$$v_a = \frac{1}{\lambda_a} D_{\mathbf{k}}^\dagger u_a. \tag{2.20}$$

Now, we can adiabatically deform $\tilde{\mathcal{H}}_{\mathbf{k}}$ into a flat-band Hamiltonian [85, 86]

$$Q_{\mathbf{k}} = 1 - 2 \sum_{a \in \text{B.G.}} |\psi_a\rangle\langle\psi_a| \tag{2.21}$$

where B.G. stands for the states below the gap. The matrix form reads

$$Q_{\mathbf{k}} = \begin{bmatrix} 0 & q_{\mathbf{k}} \\ q_{\mathbf{k}}^\dagger & 0 \end{bmatrix}, \tag{2.22}$$

where the off-diagonal term is $q_{\mathbf{k}} = \frac{1}{\lambda} D_{\mathbf{k}}$ with $\lambda = \sqrt{|\gamma_{\mathbf{k}}|^2 + |\Delta_{\mathbf{k}}|^2}$. The chiral topological state can be characterized by the three-dimensional winding number [85, 86]

$$\nu[q] = \int \frac{d^3k}{24\pi^2} \epsilon^{\mu\nu\rho} \mathrm{tr}[(q^\dagger \partial_\mu q)(q^\dagger \partial_\nu q)(q^\dagger \partial_\rho q)], \tag{2.23}$$

where $\mu, \nu = k_x, k_y, k_z$ and the integration goes over the whole Brillouin zone. Numerical results show that the winding number is quantized for nonzero δ_D and δ. When $\delta_D = 0$ or $\delta = 0$, the model falls into the Dirac phase with vanishing winding number. This result can be understood by considering the topologically equivalent Hamiltonian around $\mathbf{Q}_R$:

$$\mathcal{H}_{\mathbf{Q}_R + \mathbf{k}} \simeq q_y \tau_x + q_x \mu_z \tau_y + q_z \mu_x \tau_y + m \mu_y \tau_y, \tag{2.24}$$

where $q_x = \frac{3}{2} k_x$, $q_y = \frac{3}{2} k_y$, $q_z = -2\delta k_z$, $m = 2\sqrt{3}\delta_D$, and we dropped the momentum dependence of the mass term in topological sense. It's straightforward to get

$$\begin{aligned} D_{\mathbf{k}} &= q_y \sigma_0 - i q_z \sigma_x - i m \sigma_y - i q_x \sigma_z, \\ \lambda &= \sqrt{|\mathbf{q}|^2 + m^2}. \end{aligned} \tag{2.25}$$

It can be further shown that

$$\partial_{q_\mu} q = \frac{1}{\lambda}[\partial_{q_\mu} D_{\mathbf{k}} - \frac{1}{2\lambda^2}(\partial_{q_\mu}\lambda^2) D_{\mathbf{k}}] = \frac{1}{\lambda^3}(\lambda^2 \partial_{q_\mu} D_{\mathbf{k}} - q_\mu D_{\mathbf{k}}), \tag{2.26}$$

where the relation $\frac{1}{2}\partial_{q_\mu}\lambda^2 = q_\mu$ is used. Specifically,

$$\begin{aligned} \partial_{q_x} q &= \frac{1}{\lambda^3}[-q_x q_y \sigma_0 + i q_x q_z \sigma_x + i q_x m \sigma_y + i(q_x^2 - \lambda^2)\sigma_z], \\ \partial_{q_y} q &= \frac{1}{\lambda^3}[(\lambda^2 - q_y^2)\sigma_0 + i q_y q_z \sigma_x + i q_y m \sigma_y + i q_y q_x \sigma_z], \\ \partial_{q_z} q &= \frac{1}{\lambda^3}[-q_z q_y \sigma_0 + i(q_z^2 - \lambda^2)\sigma_x + i q_z m \sigma_y + i q_z q_x \sigma_z]. \end{aligned} \tag{2.27}$$

After some calculation, we obtain

$$\begin{aligned}
\nu_R[q] &= \int \frac{d^3k}{24\pi^2}\epsilon^{\mu\nu\rho}\text{tr}[(q^\dagger\partial_{k_\mu}q)(q^\dagger\partial_{k_\nu}q)(q^\dagger\partial_{k_\rho}q)] \\
&= -\text{sgn}(\delta)\int \frac{d^3q}{24\pi^2}\epsilon^{\mu\nu\rho}\text{tr}[(q^\dagger\partial_{q_\mu}q)(q^\dagger\partial_{q_\nu}q)(q^\dagger\partial_{q_\rho}q)] \\
&= \text{sgn}(\delta)\int \frac{d^3q}{24\pi^2}\frac{12m}{\lambda^4} \\
&= \text{sgn}(\delta)\frac{m}{2\pi^2}4\pi[-\frac{|\mathbf{q}|}{2(|\mathbf{q}|^2+m^2)}+\frac{1}{2m}\tan^{-1}(\frac{|\mathbf{q}|}{m})]_0^\infty \\
&= \text{sgn}(\delta)\frac{m}{2\pi^2}4\pi\frac{\pi}{4|m|} \\
&= \text{sgn}(\delta)\text{sgn}(m)/2 \\
&= \text{sgn}(\delta_D\delta)/2. \qquad (2.28)
\end{aligned}$$

For $\mathbf{Q}_L$ point, we replace $q_y \to -q_y$ and $m \to -m$ to get $\nu_L[q] = \text{sgn}(\delta_D\delta)/2$. The total winding number is the sum,

$$\nu[q] = \text{sgn}(\delta_D\delta), \qquad (2.29)$$

which is a quantized number for the nontrivial mcTI phase and zero for the trivial phase. In our model, there is only one Dirac cone on the surface projection point of $\mathbf{Q}_R$ or $\mathbf{Q}_L$. Specifically, when $\nu[q] = 1(-1)$, the Dirac cone appears on the projection of $\mathbf{Q}_R$ ($\mathbf{Q}_L$) point. In general, mcTI can have more than one Dirac cone at the boundary.

2.4 Surface state

We can get a physical insight into the formation of the surface Dirac cone by considering the interlayer Dirac cone pairing pattern [87]. For simplicity, we ignore the chiral symmetry-breaking terms appearing when we terminate a sample at one of the honeycomb planes in contact with vacuum. Such symmetry-breaking terms do not appear if the interface is formed between the two bulk regions with the opposite sign of DMI δ_D or if the interface is terminated in such a way that the chiral symmetry-breaking terms due to exchange energy do not appear. We consider the Hamiltonian that is Fourier transformed with respect to the in-plane momentum,

$$\begin{aligned} H_{j,j} &= -\gamma_{1\mathbf{k}_{\parallel}}\tau_x + \gamma_{2\mathbf{k}_{\parallel}}\mu_z\tau_y + (2\xi_{\mathbf{k}_{\parallel}}\delta_D - \delta)\mu_y\tau_y, \\ H_{j,j\pm1} &= \pm i(\delta + 2\delta_D\xi_{\mathbf{k}_{\parallel}})\mu_{\mp}\tau_y, \end{aligned} \tag{2.30}$$

where the index j labels the bilayer, $H_{j,j}$ describes intralayer terms, and $H_{j,j\pm1}$ describes the interlayer terms in the Hamiltonian written in the basis $(A_{\mathbf{k}_{\parallel},j}, B_{\mathbf{k}_{\parallel},j}, A'_{\mathbf{k}_{\parallel},j}, B'_{\mathbf{k}_{\parallel},j})$, with $\mathbf{k}_{\parallel}$ representing the in-plane momentum (see Fig. 2.4). The intralayer Hamiltonians describe two-dimensional Dirac cones (different from the bulk Dirac cones discussed before), which hybridize due to interlayer coupling. It is convenient to consider the Hamiltonian written in the subspace $(A_{R,j}, B_{R,j}, A'_{R,j}, B'_{R,j}, A_{L,j}, B_{L,j}, A'_{L,j}, B'_{L,j})$ where index $R(L)$ stands for the in-plane momentum $(0, \pm\frac{4\pi}{3\sqrt{3}})$, and Pauli matrix ν_z acts on R and L Dirac cones,

$$\begin{aligned} H_{j,j} &= -(\delta - \sqrt{3}\delta_D\nu_z)\mu_y\tau_y, \\ H_{j,j\pm1} &= \pm i(\delta + \sqrt{3}\delta_D\nu_z)\mu_{\mp}\tau_y. \end{aligned} \tag{2.31}$$

Here $\mu_{\pm} = \frac{1}{2}(\mu_x \pm i\mu_y)$. For $\delta = \sqrt{3}\delta_D$, we obtain that $H_{j,j} \propto \frac{1-\nu_z}{2}$ and $H_{j,j\pm1} \propto \frac{1+\nu_z}{2}$, which shows that R and L Dirac cones hybridize in a pattern shown in Fig. 2.4. In this special case, the surface states live on top and bottom surfaces without any penetration into the bulk. If $\delta = -\sqrt{3}\delta_D$, the R and L cones interchange in the hybridization pattern.

We can investigate the surface states further in the vicinity of $(0, \pm\frac{4\pi}{3\sqrt{3}})$ point using the $\mathbf{k}\cdot\mathbf{p}$ theory. After replacing k_z to its second order by $-i\partial_z$ in the Hamiltonian, the

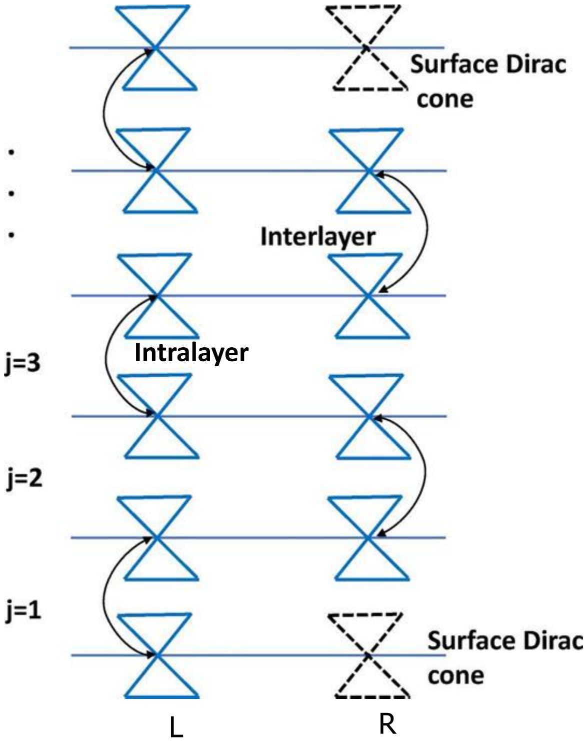

Figure 2.4: Pairing pattern for $\delta = \frac{\sqrt{3}}{2}\delta_D$. The R Dirac cone resides on the surface.

effective Hamiltonian becomes

$$\begin{aligned} H(z) &= -A(-i\partial_z)\mu_x\tau_y + M(1 - \frac{1}{2}(-i\partial_z)^2)\mu_y\tau_y \\ &= iA\partial_z\mu_x\tau_y + iM(1 + \frac{1}{2}\partial_z^2)(\mu_- - \mu_+)\tau_y, \end{aligned} \tag{2.32}$$

where $A = 2\delta$, $M = 4\delta_D\xi_{\mathbf{Q}_{R(L)}}(= \pm 2\sqrt{3}\delta_D)$. For the zero-energy surface state,

$$H(z)\psi(z) = 0, \tag{2.33}$$

which gives us the form of $\psi(z)$ as

$$\psi_{1(2)}(z) = \begin{bmatrix} \mathbf{\Phi}_{1(2)} \\ \mathbf{0} \end{bmatrix} e^{\lambda z}. \tag{2.34}$$

Here, $\mathbf{\Phi}_{1(2)}$ is the eigenstate of τ_z as demanded by the chiral symmetry, i.e., $(1,0)^T$ and $(0,1)^T$ with eigenvalues ± 1. Substituting Eq. (2.34) into Eq. (2.33) leads to

$$A\lambda + M(1 + \frac{1}{2}\lambda^2) = 0. \tag{2.35}$$

The solution is

$$\lambda^{\pm} = -\beta \pm \sqrt{\beta^2 - 2}, \tag{2.36}$$

where $\beta = A/M$, and this corresponds to a surface state only if $\beta > 0$, i.e., Re$(\lambda) < 0$. Assuming the boundary condition $\psi(0) = \psi(\infty) = 0$, we obtain two eigenstates:

$$\psi_1 = N \begin{pmatrix} 0 \\ 1 \\ 0 \\ 0 \end{pmatrix} (e^{\lambda^+ z} - e^{\lambda^- z}), \qquad \psi_2 = N \begin{pmatrix} 1 \\ 0 \\ 0 \\ 0 \end{pmatrix} (e^{\lambda^+ z} - e^{\lambda^- z}). \tag{2.37}$$

Here N is the normalization factor which fulfills

$$\int_0^{\infty} dz f(z)^* f(z) = 1, \tag{2.38}$$

for $f(z) = N(e^{\lambda^+ z} - e^{\lambda^- z}) = 2Ne^{-\beta z}\sinh(\sqrt{\beta^2 - 2}z)$. The normal factor is solved to be

$$N = \frac{\sqrt{\beta^2 - 2}}{\sqrt{2}|\beta|}, \tag{2.39}$$

so that

$$f(z) = \sqrt{2(1 - \frac{2}{\beta^2})}e^{-\beta z}\sinh(\sqrt{\beta^2 - 2}z) \qquad \text{with} \qquad \beta > 0. \tag{2.40}$$

As mentioned before, $\beta > 0$ has to be satisfied to ensure the existence of the surface state. For a given δ, $\beta_R = -\beta_L$ with $\beta_{R(L)}$ being the value of β at $\mathbf{Q}_{R(L)}$ point. It is clear that $\beta_R > 0$ when sgn$(\delta_D \delta) > 0$, and the surface Dirac cone exists at the projection of $\mathbf{Q}_R$

point; when $\mathrm{sgn}(\delta_D\delta) < 0$, $\beta_L > 0$, and the surface Dirac cone exists at the projection of $\mathbf{Q}_L$ point. This result is consistent with the earlier discussion.

Without loss of generality, we consider the surface state existing at the projection of $\mathbf{Q}_R$ point. In the vicinity of $\mathbf{Q}_R$ the Hamiltonian can be decomposed into two parts as below

$$\begin{aligned} H &= H_{xy} + H(z), \\ H_{xy} &= \frac{3}{2}k_y\tau_x + \frac{3}{2}k_x\mu_z\tau_y. \end{aligned} \tag{2.41}$$

It is easy to get

$$\begin{aligned} &\begin{pmatrix} \langle\psi_1| \\ \langle\psi_2| \end{pmatrix} H_{xy}(|\psi_1\rangle, |\psi_2\rangle) = \frac{3}{2}(k_y\tau_x - k_x\tau_y), \\ &\begin{pmatrix} \langle\psi_1| \\ \langle\psi_2| \end{pmatrix} H(z)(|\psi_1\rangle, |\psi_2\rangle) = 0. \end{aligned} \tag{2.42}$$

Therefore, the effective low-energy surface Hamiltonian reads,

$$H_{sur} = \frac{3}{2}(k_y\tau_x - k_x\tau_y) = v_F(\mathbf{k}\times\mathbf{e}_z)\cdot\boldsymbol{\tau}, \tag{2.43}$$

where $v_F = \frac{3}{2}$. This Hamiltonian exhibits magnon spin-momentum locking [95] in the spin space defined by sublattices A and B. The Rashba-like surface states in Eq. (2.43) are described by helical eigenvectors, i.e., the eigenstate of $\mathbf{k}$ and $-\mathbf{k}$ are orthogonal to each other, which prohibits backscattering between states with opposite momentum. The chiral symmetric perturbation can only shift the position of the Dirac cone as it adds additional terms of the form $M_1\tau_x + M_2\tau_y$ to Eq. (2.43). This is a manifestation of the fact that the surface modes are protected by chiral symmetry.

2.5 Surface state Hall response

Interesting physics can also arise when the chiral symmetry is weakly broken at the interface. We can break the surface Dirac cone by considering an interface with vacuum (see Fig. 2.3) or by contacting mcTI with another material that has a broken chiral symmetry. The gapped effective surface Hamiltonian reads, $\mathcal{H}_{\text{sur}} = v_F(\mathbf{k} \times \mathbf{e}_z) \cdot \boldsymbol{\tau} + m_s \tau_z$. The gap in the surface Dirac cone will result in a Hall response to a longitudinal driving force on the surface, similar to the surface Hall effect in 3D topological insulators with broken time-reversal symmetry [96], which can be detected by the spin Nernst response [97],

$$j_y^s = \alpha_{yx} \nabla_x T, \tag{2.44}$$

with response parameter

$$\alpha_{yx} = -\frac{k_B}{V} \sum_{\mathbf{k},n} \Omega_{yx}^n(\mathbf{k}) c_1(g(\varepsilon_n)) \tag{2.45}$$

where V is the surface area of the system, $\Omega_{yx}^n(\mathbf{k})$ is the momentum space Berry curvature, $c_1(x) = (1+x)\ln(1+x) - x\ln x$, and $g(\varepsilon) = 1/(e^{\beta\varepsilon} - 1)$ is the Bose-Einstein distribution function.

To get the Berry curvature around a Dirac cone, we write the gapped surface Hamiltonian above in a compact form

$$\mathcal{H}_{sur,\mathbf{k}} = \mathbf{d} \cdot \boldsymbol{\tau}, \tag{2.46}$$

with $\mathbf{d} = \{v_F k_y, -v_F k_x, m_s\}$. The energy and eigenstates are

$$E_{\mathbf{k},\pm}/JS = \pm d, \tag{2.47}$$

and

$$u_+ = \frac{1}{\sqrt{2d(d+d_3)}} \begin{bmatrix} d_3 + d \\ d_1 - id_2 \end{bmatrix}, \qquad u_- = \frac{1}{\sqrt{2d(d-d_3)}} \begin{bmatrix} d_3 - d \\ d_1 - id_2 \end{bmatrix}, \tag{2.48}$$

where $d = |d| = \sqrt{v_F^2|\mathbf{k}|^2 + m_s^2}$. As introduced in Chapter 1, the Berry connection for two bands is defined as $\boldsymbol{\mathcal{A}}_{\mathbf{d}}^{\pm} = -i\langle u_\pm|\boldsymbol{\nabla}_{\mathbf{d}}|u_\pm\rangle$, which helps to generate the corresponding Berry curvature field

$$\boldsymbol{\Omega}^{\pm}(\mathbf{d}) = \boldsymbol{\nabla}_{\mathbf{d}} \times \boldsymbol{\mathcal{A}}^{\pm}(\mathbf{d}) = \mp\frac{\mathbf{d}}{2d^3}. \tag{2.49}$$

By using the relation,

$$\Omega^{\alpha} = \frac{1}{2}\epsilon^{\alpha\mu\nu}\Omega_{\mu\nu}, \tag{2.50}$$

with $\Omega_{\mu\nu} = i(\partial_\mu\mathcal{A}_\nu - \partial_\nu\mathcal{A}_\mu)$, we can identify the concerned Berry curvature components as $\Omega^z = \Omega_{xy} = -\Omega_{yx}$. More explicitly,

$$\Omega_{yx}^{\pm}(\mathbf{k}) = v_F^2\Omega_{yx}^{\pm}(\mathbf{d}) = -v_F^2\Omega^{\pm,z}(\mathbf{d}) = \pm v_F^2\frac{m_s}{2d^3}. \tag{2.51}$$

Now we obtain the spin Nernst response coefficient by plugging the expression above into Eq. (2.45)

$$\alpha_{yx} = \frac{k_B m_s}{2}\int d\mathbf{k}\frac{v_F^2}{d^3}\{c_1[g(\varepsilon_0 - d)] - c_1[g(\varepsilon_0 + d)]\}, \tag{2.52}$$

where $\varepsilon_0 = 3 - 2\lambda - 2\kappa$ and we replaced $\frac{1}{V}\sum_{\mathbf{k}}$ by $\int d\mathbf{k}$. To identify the contribution from the Dirac cone, we introduce a small energy cutoff Λ around the Dirac cone, i.e., $\Lambda < \varepsilon_0$. So that we expand $c_1(\varepsilon_0 \pm d)$ to the first order of βd with $\beta = JS/(k_B T)$,

$$c_1[g(\varepsilon_0 - d)] - c_1[g(\varepsilon_0 + d)] = \frac{-\beta^2 d\varepsilon_0}{1 - \cosh(\beta\varepsilon_0)} + \mathcal{O}[(\beta d)^2]. \tag{2.53}$$

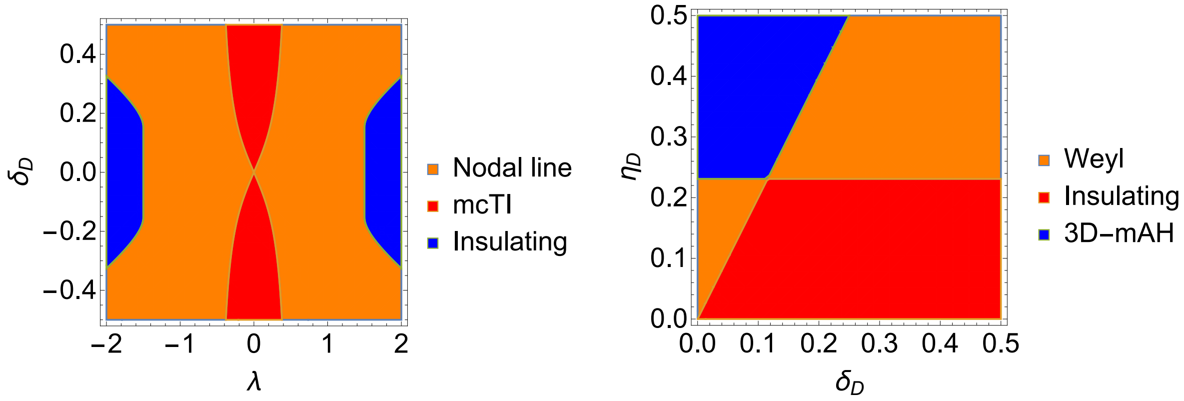

Figure 2.5: Left: Phase diagram in $\delta_D - \lambda$ parameter space with $\delta \neq 0$. The mcTI phase is continuously connected to the $\lambda = 0$ case considered in the previous sections. Right: Phase diagram in $\eta_D - \delta_D$ parameter space ($\lambda = 0$) with $\delta = 0.2$; The boundary lines between different phases are $\eta_D = 2\delta/\sqrt{3}$ and $\delta_D = \eta_D/2$.

Taking the transform $\int d\mathbf{k} = \int_0^\infty \int_0^{2\pi} |\mathbf{k}| d|\mathbf{k}| d\theta = \int_{m_s}^\infty \frac{1}{v_F^2} d(d) d \int_0^{2\pi} d\theta$, we have

$$\begin{aligned} \alpha_{yx} &= \frac{k_B m_s}{2} \int_0^{2\pi} d\theta \int_{|m_s|}^{\Lambda} d(d) \frac{1}{d^2} \{c_1[g(\varepsilon_0 - d)] - c_1[g(\varepsilon_0 + d)]\} \\ &\approx \frac{\pi k_B m_s \varepsilon_0 \beta^2}{\cosh(\beta\varepsilon_0) - 1} \ln(\Lambda/|m_s|). \end{aligned} \tag{2.54}$$

Unlike an electronic system, the response parameter is not quantized due to the Bose-Einstein statistics. In Eq. (2.54), only the contribution from the Dirac cone has been considered. We note that the Berry curvature from other parts of the Brillouin zone can also contribute to the spin Nernst response due to the Bose-Einstein statistics.

2.6 Topological phase transition

We now consider a more general model with a non-staggered pattern, i.e., $\lambda \neq 0$. We find that even for $\lambda \neq 0$ there is still some region in parameter space with mcTI phase. As we increase λ, we encounter a phase transition into a nodal line phase before we reach the trivial insulating phase (see Fig. 2.5). For the full Hamiltonian composed of Eqs. (2.4) and

(2.11), the energy is

$$\begin{aligned} E_{\mathbf{k}}^2/(JS)^2 &= [|2\lambda\cos k_z| \pm \sqrt{|\gamma_{\mathbf{k}}|^2+(4\delta_D)^2\xi_{\mathbf{k}}^2\cos^2 k_z}]^2 \\ &\quad +(2\delta)^2\sin^2 k_z. \end{aligned} \tag{2.55}$$

To get nodal line phase, it's required that $k_z = 0$ and $(2\lambda)^2 = |\gamma_{\mathbf{k}}|^2 + (4\delta_D)^2\xi_{\mathbf{k}}^2$. When $\min\{|\gamma_{\mathbf{k}}|^2 + (4\delta_D)^2\xi_{\mathbf{k}}^2\} \leqslant (2\lambda)^2 \leqslant \max\{|\gamma_{\mathbf{k}}|^2 + (4\delta_D)^2\xi_{\mathbf{k}}^2\}$, the system falls into the nodal line phase with the nodal lines lying on $k_z = 0$ plane. When $(2\lambda)^2 < \min\{|\gamma_{\mathbf{k}}|^2 + (4\delta_D)^2\xi_{\mathbf{k}}^2\}$, it's in mcTI phase that is continuously related to the $\lambda = 0$ case considered in the previous sections. Note that if $\delta = 0$, the gap is always closed at $(0, \pm\frac{4\pi}{3\sqrt{3}}, \pm\frac{\pi}{2})$, so that $\delta \neq 0$ has to be satisfied. The phase diagram is shown in Fig. 2.5. We find that there is a substantial region in parameter space with mcTI phase.

Besides the phase transition induced in the presence of the chiral symmetry, we find that the system can also be tuned to the Weyl and 3D-mAH phase by introducing the in-plane second-nearest-neighbor bulk DMI that breaks the chiral symmetry,

$$\delta H = \frac{1}{2}\sum_{Q}\sum_{z,i,\mathbf{d}_\lambda} \tilde{D}_Q^z(\mathbf{d}_\lambda)\mathbf{e}_z \cdot [\mathbf{S}_{Q,(i,z)} \times \mathbf{S}_{Q,(i+\mathbf{d}_\lambda,z)}], \tag{2.56}$$

where Q stands for different spin modes and $\tilde{D}_Q^z(\mathbf{d}_\lambda)$ is the in-plane DMI parameter. The presence of such DMI is consistent with the symmetry of the honeycomb lattice. In momentum space $\delta\mathcal{H}_{\mathbf{k}} = 2\eta_D\xi_{\mathbf{k}}\mu_z\tau_z$, where $\eta_D = |\tilde{D}_Q^z(\mathbf{d}_\lambda)|/J$. Now the system ($\lambda = 0$) has energy

$$\begin{aligned} E_{\mathbf{k}}^2/(JS)^2 &= |\gamma_{\mathbf{k}}|^2 + 4[|\eta_D\xi_{\mathbf{k}}| \pm \\ &\quad \sqrt{(2\delta_D\xi_{\mathbf{k}})^2\cos^2(k_z)+\delta^2\sin^2(k_z)}]^2. \end{aligned} \tag{2.57}$$

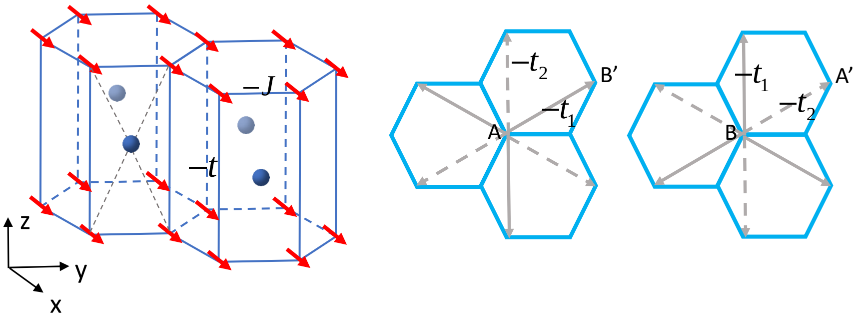

Figure 2.6: Left: Local spins are pointing in the x direction due to applied magnetic field. Nonmagnetic atoms in the face centers generate DMI along the x-axis for the vertical bonds. Middle and right: Top view depicts the third-nearest interlayer exchange interactions.

Conditions for the existence of Weyl point are $|\gamma_{\mathbf{k}}| = 0$ and $\eta_D^2\xi_{\mathbf{k}}^2 = (2\delta_D\xi_{\mathbf{k}})^2\cos^2(k_z) + \delta^2\sin^2(k_z)$, such that the Weyl nodes lie at $\mathbf{k}_\parallel = (0, \pm\frac{4\pi}{3\sqrt{3}})$ and $k_z = \frac{1}{2}\arccos(\frac{3\eta_D^2/2-3\delta_D^2-\delta^2}{3\delta_D^2-\delta^2})$. When $-1 < \frac{3\eta_D^2/2-3\delta_D^2-\delta^2}{3\delta_D^2-\delta^2} < 1$, there are four-momentum space Weyl nodes originating in the separation of two Dirac cones along k_z direction. Similar to Ref. [98], the system can be manipulated into the Weyl, 3D-mAH, and insulating phases by changing parameters. In parameter space, the insulating and the 3D-mAH phases are well separated by the Weyl phase as shown in Fig. 2.5, where we identify the 3D-mAH phase by the quantized Chern number ($C = 2$ in our model) for arbitrary given k_z, i.e., $C = \frac{1}{2\pi}\sum_{E_n<0}\int_{\text{B.Z.}} d\mathbf{k}_\parallel \Omega^{(n)}_{k_x,k_y}(k_z)$ with $\Omega^{(n)}_{k_x,k_y}(k_z)$ being the Berry curvature of bands bellow the gap and $B.Z.$ standing for the 2-D Brillouin zone.

2.7 Another model

Aside from the model we discussed so far, we show a different mcTI model based on the layered honeycomb ferromagnet system. We consider the same lattice structure and labels as in Fig. 2.1, but assume that all spins are aligned in the x direction, which can be realized by applying an external magnetic field. Instead of putting extra nonmagnetic atoms in the center of the unit cell, here we add atoms in the front and back face of each unit

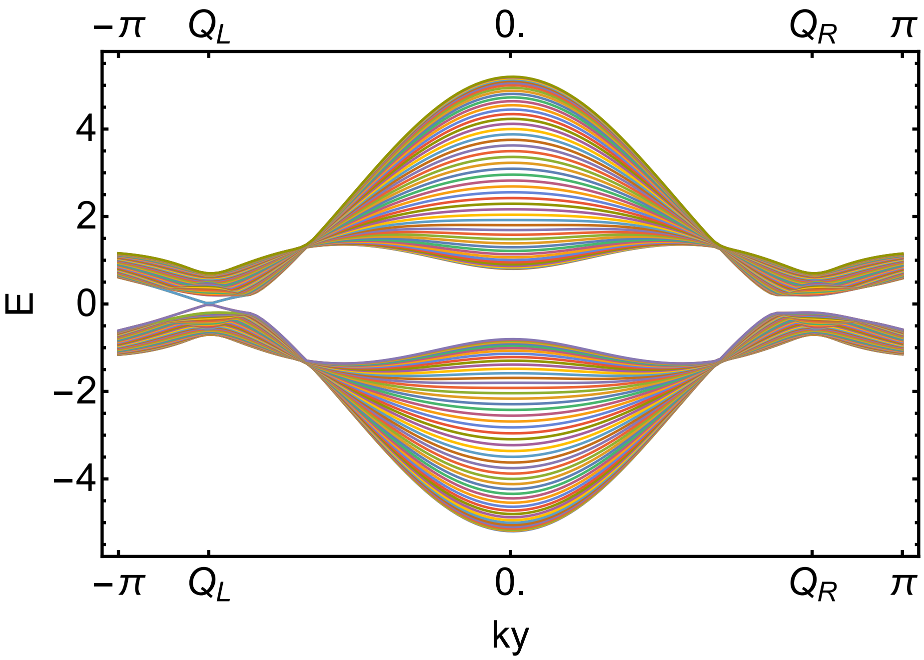

Figure 2.7: The spectrum of model 2 in a slab geometry shows the presence of surface states. The parameters are $r = 0.2$, $\eta = 0.1$, $\lambda = 0.2$, $\eta_0 = 0.15$. Here we neglected the boundary effects which shift the position of the surface cone. In principle, this effect can be weakened or even eliminated by an interface with another material.

cell to generate DMI along vertical interlayer bonds as shown in Fig. 2.6. We also need third-nearest-neighbor exchange interactions, with the exchange strength depending on the type of sublattices and their locations (see Fig. 2.6), to induce the Dirac cone mass term. The model Hamiltonian reads

$$H = H_{\text{in}} + H_{\text{inter}} + H_Z + H_D + H_3^{\text{ex}}, \tag{2.58}$$

where

$$\begin{aligned}
H_{\text{in}} &= -J\sum_{z,i}\sum_{\mu=1}^{3}\mathbf{S}_{A,i}\cdot\mathbf{S}_{B,i+\boldsymbol{\delta}_\mu}+\mathbf{S}_{A',i}\cdot\mathbf{S}_{B',i-\boldsymbol{\delta}_\mu},\\
H_{\text{inter}} &= -\sum_{i,z}(t\mathbf{S}_{A,z}\cdot\mathbf{S}_{B',z+1}+t\mathbf{S}_{A,z}\cdot\mathbf{S}_{B',z-1})+(A\to B,B'\to A'),\\
H_Z &= -\sum_{i,z}\sum_{Q}B_xS^x_{Q,(i,z)},\\
H_D &= \sum_{i,z}\sum_{\delta=\pm1}\mathbf{D}_{AB'}(\delta)\cdot(\mathbf{S}_{A,z}\times\mathbf{S}_{B,z+\delta})+\mathbf{D}_{BA'}(\delta)\cdot(\mathbf{S}_{B,z}\times\mathbf{S}_{A,z+\delta}),\\
H_3^{\text{ex}} &= -\sum_{i,z}\sum_{n=\pm1}\sum_{\mathbf{d}_\lambda}t_1\mathbf{S}_{A,(i,z)}\cdot\mathbf{S}_{B',(i+\mathbf{d}_\lambda,z+n)}+t_2\mathbf{S}_{A,(i,z)}\cdot\mathbf{S}_{B',(i-\mathbf{d}_\lambda,z+n)}+\\
&\quad\{t_1\leftrightarrow t_2,A\to B,B'\to A'\}.
\end{aligned} \tag{2.59}$$

Here, the first two terms coincide with the previous model, except that the interlayer nearest exchange interaction has uniform strength. The third term corresponds to the Zeeman interaction with the external magnetic field in the x direction. The term H_D represents vertical bond DMI contribution with $\mathbf{D}_{AB'}(\delta)=-\delta D\mathbf{e}_x$ and $\mathbf{D}_{BA'}(\delta)=\delta D\mathbf{e}_x$ $(\delta=\pm1)$. H_3^{ex} stands for the third-nearest-neighbor exchange interaction with the strength depending on the sublattice type and position, as shown in Fig. 2.6. After performing the Holstein-Primakoff transformation and the Fourier transformation, the Hamiltonian up to a constant term becomes

$$\mathcal{H}_{\mathbf{k}}=-\gamma_{1\mathbf{k}}\tau_x+\gamma_{2\mathbf{k}}\mu_z\tau_y-2r\sin(k_z)\mu_y\tau_y+4\eta\xi_{\mathbf{k}}\cos(k_z)\mu_x\tau_y+2\cos(k_z)(\lambda+2\eta_0\chi_{\mathbf{k}})\mu_x\tau_x, \tag{2.60}$$

where $r=D/J$, $\lambda=t/J$, $\eta_0=(t_1+t_2)/2J$, $\eta=(t_1-t_2)/2J$, and $\xi_{\mathbf{k}}=\sum_{i=1}^{3}\sin(\mathbf{k}\cdot\mathbf{d}_i)$, $\chi_{\mathbf{k}}=\sum_{i=1}^{3}\cos(\mathbf{k}\cdot\mathbf{d}_i)$ with $\mathbf{d}_1=(\frac{3}{2},\frac{\sqrt{3}}{2},0)$,$\mathbf{d}_1=(-\frac{3}{2},\frac{\sqrt{3}}{2},0)$,$\mathbf{d}_1=(0,-\sqrt{3},0)$. First, we consider the extreme case for which $\lambda=\eta_0=0$. The Hamiltonian has the same form as the mcTI model in the main text, i.e., we obtain an effective massive Dirac equation. If we turn on the parameters η_0 and λ, they will not immediately break the mcTI phase, similar

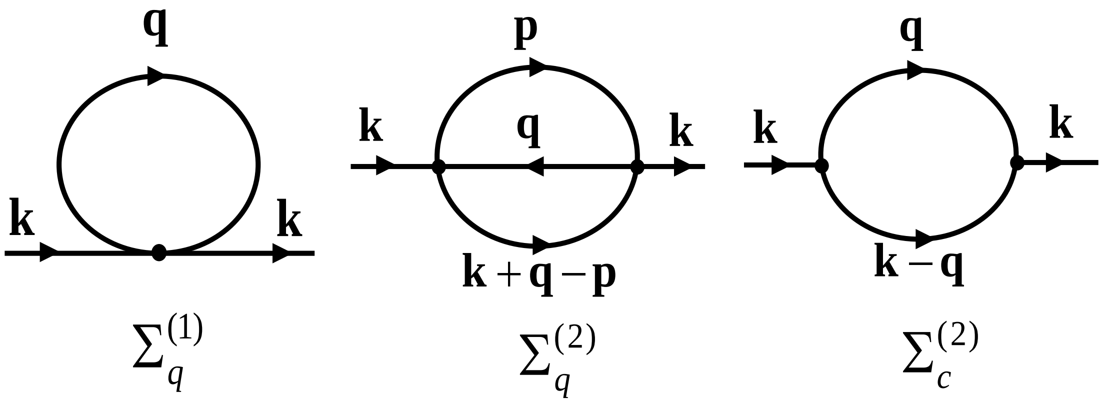

Figure 2.8: Left and middle: The self-energy diagrams corresponding to the first- and second-order corrections due to the quartic magnon-magnon interactions. Right: The self-energy diagram corresponding to the cubic magnon-magnon interactions.

to the case we discussed in Sec. 2.6. Specifically, the energy of Eq. (2.60) is

$$E_{\mathbf{k}}^2/(JS)^2 = [\sqrt{|\gamma_{\mathbf{k}}|^2 + 4r^2 \sin^2(k_z)} \pm 2|\cos(k_z)(\lambda + 2\eta_0\chi_{\mathbf{k}})|]^2 + 16\eta^2\xi_{\mathbf{k}}^2 \cos^2(k_z). \tag{2.61}$$

When $\eta = 0$, the spectrum is always gapless at two pairs of nodes lying at $\mathbf{k}_{\text{node}} = (0, \pm\frac{4\pi}{3\sqrt{3}}, \pm\arctan(\frac{\lambda+2\eta_0\chi_{\mathbf{Q}_{L/R}}}{|r|}))$. In addition, one needs to assume $\xi_{\mathbf{k}} = 0$ to close the gap, which leads to $k_y = 0$ or $\sqrt{3}k_x \pm k_y = 0$. For $\mathbf{k}_{\parallel}^*$ satisfying these conditions, the system is gapless at $k_z = \pm\arcsin\sqrt{\frac{4(\lambda+2\eta_0\chi_{\mathbf{k}_{\parallel}^*})^2-|\gamma_{\mathbf{k}_{\parallel}^*}|^2}{4(\lambda+2\eta_0\chi_{\mathbf{k}_{\parallel}^*})^2+4r^2}}$ when $4(\lambda+2\eta_0\chi_{\mathbf{k}_{\parallel}^*})^2 - |\gamma_{\mathbf{k}_{\parallel}^*}|^2 \geq 0$. When $\max\{4(\lambda + 2\eta_0\chi_{\mathbf{k}_{\parallel}^*})^2 - |\gamma_{\mathbf{k}_{\parallel}^*}|^2\} < 0$, the system is gapped and it is continuously connected with the magnon cTI model with $\eta_0 = \lambda = 0$ (see Fig. 2.7).

2.8 Discussion

In this section, we discuss the role of magnon-magnon interaction effects and give possible material candidates for realizations of topological phases of magnons. So far, our discussion has been limited to free magnon systems. It is known that magnon-magnon interactions do not play an important role for a ferromagnetic alignment of spins at low temperatures. In a general case, magnon-magnon interactions can induce band renormalizations and magnon decay [99]. It has also been shown that anharmonic terms due to DMI can lead to nonperturbative damping proportional to the strength of DMI in a kagome lattice for the spin alignment orthogonal to DMI vectors [100].

We have investigated the role of the above effects in our model by considering the higher-order terms of the Holstein-Primakoff transformation. Three diagrams in Fig. 2.8 contribute to the self-energy where the first two correspond to the quartic term in magnon-magnon interactions and the last one corresponds to the cubic anharmonic interaction. According to our analysis, the first two diagrams lead to the self-energy that is proportional to at least the second power of temperature. The effects induced by such diagrams are suppressed at low temperatures since all relevant terms behave in a continuous fashion without singularities. As for the third diagram, it is also suppressed by a factor $\propto D^2$ without singularities. The effect of such a diagram completely vanishes for the second model in Sec. 2.7. For the first model in the main text, we only observe a large contribution when magnetic moments are near orthogonal to DMI vectors. This situation can be avoided by tuning the strength of DMI in the model in the main text, in which case the anharmonic contributions do not lead to any singularities. Given nonsingular contributions from all three diagrams, we believe that magnon-magnon interactions cannot hinder topological phases in our models, at least at low temperatures and for typical DMI.

For realizations of the two models given in the main text and in Appendix B, we suggest to study stacked 2D honeycomb ferromagnets with additional nonmagnetic atoms. From the above discussion it seems that the model in Appendix B corresponding to D_{2h} point group is better suitable for realizations of the mcTI phase. Among material candidates, one could consider CrI_3 van der Waals crystals with honeycomb structure of magnetic atoms [101,102]. In addition, similar honeycomb magnetic lattices can be realized in transition metal trihalides TX_3 (X = F, Cl, Br, and I; T = transition metal) [103].

2.9 Summary

In this chapter, we constructed a chiral symmetry-protected topological insulator of magnons in light of the analogous works for electronic and cold-atom systems. In our model, the bulk gap opens due to the presence of DMI. We expect that there could be other magnonic models with mcTI phase and our analysis can facilitate finding other possible realizations. Following the tenfold classification of topological insulators, such models can be characterized by the 3D winding number. We found that the surface Dirac cone has Rashba-like form, so that the backscattering can be suppressed, which is similar to the surface of the electronic topological insulator. Systems with the broken chiral symmetry at the surface can also be of interest due to a small gap in the surface states and due to appearance of the magnonic Hall response. We showed that the spin Nernst response can be used as a signature of the chiral symmetry breaking at the surface. Finally, we constructed a phase diagram in parameter space, which shows that the system can be tuned between the mcTI, nodal line, 3D-mAH, and Weyl magnon phases. We hope that our work can pave the way for realizations of new topological phases of magnons.

Chapter 3

Intrinsic spin Nernst effect of magnons in a noncollinear antiferromagnet

3.1 Introduction

In this chapter, we turn the topic to the spin transport mediated by magnons. The possibility of coupling between various degrees of freedom has led to new visions for spintronics [15, 104], and resulted in new subfields such as spin caloritronics [105], in which spin carriers are manipulated by exciting heat flows. The study of spin currents is fundamental for the field of spintronics, and the spins carried by magnons possess certain advantages over electrons, e.g., low dissipation. At the same time, magnons exhibit rich and fascinating physics associated with the topology of magnonic bands, e.g., the thermal Hall effect has been observed in collinear ferromagent $Lu_2V_2O_7$ [29]. The spin Nernst effect [106,107], akin to the spin Hall effect [9], can also be realized in magnon systems [38–40, 72, 97, 108, 109].

Many spintronics concepts also apply to antiferromagnets [110]. In particular, collinear antiferromagnets can exhibit the spin Seebeck effect [111], spin pumping [112], spin-orbit torque [113], spin Nernst effect [38–40, 108, 109], etc. Noncollinear antiferromagnets (NAFMs) have attracted considerable attention in recent years, as such systems support nontrivial band structure topology. The anomalous Hall effect [114] and spin Hall effect [115, 116] have been realized in Mn_3X (X= Ge, Sn, Ga, Ir, Rh, or Pt) systems, where electrons act as charge or spin carriers. Furthermore, the thermal Hall effect, mediated by magnons, is also identified in NAFM insulators [40–44]. Nevertheless, the magnon-mediated spin transport in NAFMs [117–119] has not yet been well explored, especially in the context of the topology of magnon bands. As a new class of materials, NAFMs feature rich magnetic point group symmetries, chirality, and easily tunable properties (e.g., by magnetic field). As a result, studies of spin currents in NAFMs can bring new vitality to spintronics, especially in the context of spin caloritronics. In contrast to the unique spin polarization of a magnon current in the collinear system, the spin current in NAFMs can be arbitrarily polarized, which allows a better control of the spin current. NAFMs typically possess different ground states [120–122] depending on the ambient environment, e.g., external field, temperature, substrates, and one can envisage using the spin current as a probe of the ground state. Meanwhile, many NAFM materials can also hold exotic quantum effects [123]. Studies of spin currents in such systems can provide a new venue for probing these materials [124]. Motivated by these interesting possibilities, we initiate a discussion on the magnon-mediated spin current physics in noncollinear antiferromagnets therein and hope to stimulate subsequent research on, e.g., spin transport in topological magnon insulators [74], optical generation of magnon-mediated spin currents [125,126], and many others, as has been discussed above.

In this chapter, we formulate a linear response theory of magnon-mediated spin transport induced by temperature gradients in a noncollinear antiferromagnet, concentrating on the intrinsic contribution not reliant on magnon lifetime. The difficulty in considering a NAFM is similar to a typical spin Hall system in which spin is not conserved [127]. Magnons driven by temperature gradients require accounting for the effects associated with the orbital magnetization [38, 128]. We start by discussing the definition of spin current in particle-hole space by following Refs. [38, 127], where spin non-conservation is signaled by a source term. Next, we develop a linear response theory to temperature gradients for a general observable, i.e., the source term (torque) or spin current, and discuss the symmetry constraints. One of our main results is the expression for the intrinsic spin Nernst response in noncollinear antiferromagnetic insulators,

$$J_{\gamma\lambda} = \frac{2k_B}{V}\sum_{n=1}^{N}\sum_{\mathbf{k}}(\Omega^{js}_{n,\mathbf{k}})^{\gamma\lambda}_{\beta}c_1[g(\varepsilon_{n,\mathbf{k}})]\nabla_\beta T, \tag{3.1}$$

where $J_{\gamma\lambda}$ is the spin current with polarization γ, $(\Omega^{js}_{n,\mathbf{k}})^{\gamma\lambda}_{\beta}$ is the spin Berry curvature of magnons, and $c_1(x) = (1+x)\ln(1+x) - x\ln(x)$ is an auxiliary function stemming from the Bose-Einstein statistics of magnons. We apply our theory to the kagome antiferromagnet $\mathrm{KFe_3(OH)_6(SO_4)_2}$ (see Fig. 3.1) and show that the in-plane Dzyaloshinskii-Moriya interaction (DMI) leads to a measurable spin Nernst response. Our study opens a way for future studies of fascinating physics related to spin flows in noncollinear antiferromagnets, e.g., in the context of different magnetic orders and material realizations.

3.2 Hamiltonian and eigenstates

We consider a general Hamiltonian of the form:

$$H = \sum_{i,j}\left[J^{\alpha\beta}_{ij}S^\alpha_i S^\beta_j + \mathbf{D}_{ij}\cdot(\mathbf{S}_i\times\mathbf{S}_j)\right] + \sum_i H_i, \tag{3.2}$$

where i, j label different lattice sites and α, β stand for different spin vector components, i.e., x, y, z. Moreover, $J^{\alpha\beta}_{ij}$ is the symmetric exchange energy between α, β spin components on two sites i and j, while antisymmetric exchange is described by the DMI vector $\mathbf{D}_{ij}$ between spins on sites i and j. Effects of the on-site anisotropy and magnetic field may also be included in our analysis via the last term, $H_i = K_i(\mathbf{S}_i\cdot\hat{\mathbf{z}}_i)^2 + (\mathbf{S}_i\cdot\mathbf{B})$.

We proceed with the Holstein-Primakoff transformation [129] in the limit of large spin and map spin operators onto bosonic creation and annihilation operator, $a_i^\dagger$ and a_i:

$$\begin{aligned}\mathbf{S}_i \quad &= \sqrt{2S - a_i^\dagger a_i}\frac{a_i^\dagger + a_i}{2}\hat{\mathbf{x}}_i + i\sqrt{2S - a_i^\dagger a_i}\frac{a_i^\dagger - a_i}{2}\hat{\mathbf{y}}_i \\ &+(S - a_i^\dagger a_i)\hat{\mathbf{z}}_i. \end{aligned} \tag{3.3}$$

Here, the unit vectors $\hat{\mathbf{x}}_i$, $\hat{\mathbf{y}}_i$, and $\hat{\mathbf{z}}_i$ form a local coordinate frame at position i with $\hat{\mathbf{z}}_i$ pointing along the ground-state spin direction of site i determined by a particular magnetic ordering. Keeping the leading order terms of bosonic operators, we obtain the bilinear Hamiltonian written in magnon particle-hole space as

$$H = \frac{1}{2}\int d\mathbf{r}\Psi^\dagger(\mathbf{r})\hat{H}\Psi(\mathbf{r}), \tag{3.4}$$

where $\Psi(\mathbf{r}) = (a_1(\mathbf{r}), \dots, a_N(\mathbf{r}), a_1^\dagger(\mathbf{r}), \dots, a_N^\dagger(\mathbf{r}))^T$, $\hat{H}$ is the real-space single-particle Hamiltonian describing noninteracting magnons, and $\mathbf{r}$ describes the coordinate of a magnetic unit cell containing N atoms.

In momentum space, Hamiltonian (4.1) reads

$$H = \frac{1}{2}\sum_{\mathbf{k}}\Psi_{\mathbf{k}}^\dagger H_{\mathbf{k}}\Psi_{\mathbf{k}}, \tag{3.5}$$

where $\Psi_{\mathbf{k}} = (a_{1,\mathbf{k}}, \dots, a_{N,\mathbf{k}}, a_{1,-\mathbf{k}}^\dagger, \dots, a_{N,-\mathbf{k}}^\dagger)^T$. From the standard bosonic commutation relation $[a_{i,\mathbf{k}}, a_{j,\mathbf{k}}^\dagger] = \delta_{ij}$, it can be shown that

$$\left[\Psi_{i,\mathbf{k}}, \Psi_{j,\mathbf{k}}^\dagger\right] = (\sigma_3)_{ij}, \tag{3.6}$$

where here and henceforth σ_i ($i = 0, 1, 2, 3$) stands for the Pauli matrices acting in particle-hole space (with σ_0 being the identity matrix). Hamiltonian (4.2) can be diagonalized by a matrix $T_{\mathbf{k}}$, which introduces Bogoliubov quasiparticles: $\Gamma_{\mathbf{k}} = T_{\mathbf{k}}^{-1}\Psi_{\mathbf{k}}$ with

$\Gamma_{\mathbf{k}} = (\gamma_{1,\mathbf{k}}, \dots, \gamma_{N,\mathbf{k}}, \gamma^\dagger_{1,-\mathbf{k}}, \dots, \gamma^\dagger_{N,-\mathbf{k}})^T$. In terms of the eigenbasis, Eq. (4.2) reads

$$H = \frac{1}{2}\sum_{\mathbf{k}} \Gamma^\dagger_{\mathbf{k}} \mathcal{E}_{\mathbf{k}} \Gamma_{\mathbf{k}} = \sum_{\mathbf{k}} \sum_{n=1}^{N} \varepsilon_{n,\mathbf{k}} \left(\gamma^\dagger_{n,\mathbf{k}} \gamma_{n,\mathbf{k}} + \frac{1}{2} \right), \tag{3.7}$$

where $\mathcal{E}_{\mathbf{k}} = \mathrm{Diag}(\varepsilon_{1,\mathbf{k}}, \dots, \varepsilon_{N,\mathbf{k}}, \varepsilon_{1,-\mathbf{k}}, \dots, \varepsilon_{N,-\mathbf{k}})$ is the eigenenergy matrix containing the eigenvalues $\varepsilon_{n,\mathbf{k}}$. By plugging $\Psi_{\mathbf{k}} = T_{\mathbf{k}}\Gamma_{\mathbf{k}}$ into Eq. (3.6) and recalling that the normal mode quasiparticles are bosons as well, i.e., $[\Gamma_{i,\mathbf{k}}, \Gamma^\dagger_{j,\mathbf{k}}] = (\sigma_3)_{ij}$, we conclude that $T_{\mathbf{k}}$ is paraunitary:

$$T^\dagger_{\mathbf{k}} \sigma_3 T_{\mathbf{k}} = T_{\mathbf{k}} \sigma_3 T^\dagger_{\mathbf{k}} = \sigma_3. \tag{3.8}$$

To appreciate the differences to a unitary transformation, let us write the diagonalization in a more suggestive matrix form

$$T^\dagger_{\mathbf{k}} H_{\mathbf{k}} T_{\mathbf{k}} = T^\dagger_{\mathbf{k}} \sigma_3 (\sigma_3 H_{\mathbf{k}}) T_{\mathbf{k}} = \mathcal{E}_{\mathbf{k}}, \tag{3.9}$$

where $\sigma_3 H_{\mathbf{k}}$ can be regarded as a pseudo-Hermitian Hamiltonian. Although it violates hermiticity, it can still be diagonalized by different left and right eigenstates with corresponding real eigenvalues. $T^\dagger_{\mathbf{k}}\sigma_3$ and $T_{\mathbf{k}}$ are alignments of left and right eigenstates, respectively: the lth entry of the nth left (right) eigenstate reads $\langle u^L_{n,\mathbf{k}}|_l = (T^\dagger_{\mathbf{k}}\sigma_3)_{nl}$ ($|u^R_{n,\mathbf{k}}\rangle_l = (T_{\mathbf{k}})_{ln}$). Paraunitarity is then expressed as $\langle u^L_{m,\mathbf{k}}|u^R_{n,\mathbf{k}}\rangle = (\sigma_3)_{mn}$ and Eq. (4.3) is equivalent to $\langle u^L_{m,\mathbf{k}}|\sigma_3 H_{\mathbf{k}}|u^R_{n,\mathbf{k}}\rangle = (\mathcal{E}_{\mathbf{k}})_{nn}\delta_{mn}$. Thus, the pseudo-Hermitian Hamiltonian matrix in terms of its eigenbasis reads $\sigma_3 H_{\mathbf{k}} = \sum_n (\mathcal{E}_{\mathbf{k}})_{nn} |u^R_{n,\mathbf{k}}\rangle\langle u^L_{n,\mathbf{k}}|$, from which follows a pair of eigenequations [130]

$$\sigma_3 H_{\mathbf{k}} |u^R_{n,\mathbf{k}}\rangle = \bar{\varepsilon}_{n,\mathbf{k}} |u^R_{n,\mathbf{k}}\rangle, \tag{3.10}$$

$$\langle u^L_{n,\mathbf{k}}|\sigma_3 H_{\mathbf{k}} = \langle u^L_{n,\mathbf{k}}|\bar{\varepsilon}_{n,\mathbf{k}}, \tag{3.11}$$

where $\bar{\varepsilon}_{n,\mathbf{k}} = (\sigma_3 \mathcal{E}_{\mathbf{k}})_{nn}$. From here on, we will only refer to the right eigenstates as $|u^R_{n,\mathbf{k}}\rangle = |u_{n,\mathbf{k}}\rangle$, and their left partners can be always be obtained from $\langle u^L_{n,\mathbf{k}}| = \langle u_{n,\mathbf{k}}|\sigma_3$.

Finally, note that the magnon basis possesses particle-hole symmetry (PHS) $\Psi^\dagger_{\mathbf{k}} = (\sigma_1 \Psi_{-\mathbf{k}})^T$ so that the Hamiltonian obeys $\sigma_1 H_{\mathbf{k}} \sigma_1 = H^*_{-\mathbf{k}}$, which leads to $\bar{\varepsilon}_{n+N,\mathbf{k}} = -\bar{\varepsilon}_{n,-\mathbf{k}}$ and $|u_{n,\mathbf{k}}\rangle = e^{i\phi_n}\sigma_1 |u_{n+N,-\mathbf{k}}\rangle^*$, where ϕ_n is a redundant phase factor.

3.3 Time evolution of a local observable under a temperature gradient

In a system with a temperature gradient applied, the temperature gradient is a statistical force and doesn't directly enter the Hamiltonian. To perform linear response analysis, we introduce a perturbation corresponding to a pseudo-gravitational potential, $\chi(\mathbf{r})$, to account for the temperature gradient [38, 128, 131],

$$H' = \frac{1}{4}\int d\mathbf{r} \Psi^\dagger(\mathbf{r})(\chi \hat{H} + \hat{H}\chi)\Psi(\mathbf{r}). \tag{3.12}$$

With the perturbation, the total Hamiltonian is amended to $H = \frac{1}{2}\int d\mathbf{r} \tilde{\Psi}^\dagger(\mathbf{r})\hat{H}\tilde{\Psi}(\mathbf{r})$, where $\tilde{\Psi}(\mathbf{r}) = (1 + \mathbf{r}\cdot\boldsymbol{\nabla}\chi/2)\Psi(\mathbf{r})$. To linear order, the system will respond to a temperature gradient in the same way as to a perturbation with $\chi(\mathbf{r}) = -T(\mathbf{r})/T$.

We now introduce an arbitrary matrix $\hat{O}$ and a local observable $\mathcal{O}(\mathbf{r}) = \frac{1}{2}\Psi^\dagger(\mathbf{r})\hat{O}\Psi(\mathbf{r})$. In what follows, we will mostly consider $\hat{O} = \hat{S}^\alpha$, which corresponds to the magnon spin density operator given by $\hat{S}^\alpha = -\sigma_0 \otimes \mathrm{Diag}(\langle S^\alpha_1\rangle / S_1, \cdots, \langle S^\alpha_N\rangle / S_N)$, where $\alpha = x, y, z$, σ_0 describes the particle-hole space, and averages of spins within a unit cell have been taken. The time evolution of this operator can be obtained from the Heisenberg equation applied to the total Hamiltonian.

We first prepare a basic knowledge of the Hamiltonian operator and commutators in particle-hole space by following Ref. [38, 128]. The total Hamiltonian can be generally expressed as $H = \frac{1}{2}\int d\mathbf{r}\tilde{\Psi}^{\dagger}(\mathbf{r})\hat{H}\tilde{\Psi}(\mathbf{r})$ with $\hat{H} = \sum_{\boldsymbol{\delta}} H_{\boldsymbol{\delta}} e^{i\hat{\mathbf{p}}\cdot\boldsymbol{\delta}}$, in which $e^{i\hat{\mathbf{p}}\cdot\boldsymbol{\delta}}$ is the translation operator that satisfies $e^{i\hat{\mathbf{p}}\cdot\boldsymbol{\delta}}f(\mathbf{r}) = f(\mathbf{r}+\boldsymbol{\delta})$. Here $\boldsymbol{\delta}$ is the vector shift between unit cells, $\tilde{\Psi}(\mathbf{r}) = (1+\mathbf{r}\cdot\boldsymbol{\nabla}\chi/2)\Psi(\mathbf{r})$. Based on the basic commutators between bosons $[a_i(\mathbf{r}), a_j^{\dagger}(\mathbf{r}')] = \delta_{ij}\delta_{\mathbf{r},\mathbf{r}'}$, $[a_i(\mathbf{r}), a_j(\mathbf{r}')] = 0$, we can construct commutators in the particle-hole basis

$$\begin{aligned} &[\Psi_i(\mathbf{r}), \Psi_j^{\dagger}(\mathbf{r}')] = (\sigma_3)_{ij}\delta_{\mathbf{r},\mathbf{r}'}, \qquad [\Psi_i(\mathbf{r}), \Psi_j(\mathbf{r}')] = i(\sigma_2)_{ij}\delta_{\mathbf{r},\mathbf{r}'}, \\ &[\Psi_i^{\dagger}(\mathbf{r}), \Psi_j^{\dagger}(\mathbf{r}')] = -i(\sigma_2)_{ij}\delta_{\mathbf{r},\mathbf{r}'} \end{aligned} \tag{3.13}$$

where σ_i ($i = 1, 2, 3$) are Pauli matrices acting in particle-hole space. Now we use the above Hamiltonian and commutators to perform a local observable time evolution calculation in two steps. First, we work out the Heisenberg equation commutation as follow,

$$\begin{aligned} \frac{\partial \mathcal{O}(\mathbf{r})}{\partial t} = \quad & i[H, \mathcal{O}(\mathbf{r})] = i[\frac{1}{2}\sum_{\boldsymbol{\delta}}\int d\mathbf{r}'\tilde{\Psi}^{\dagger}(\mathbf{r}')H_{\boldsymbol{\delta}}\tilde{\Psi}(\mathbf{r}'+\boldsymbol{\delta}), \frac{1}{2}\Psi^{\dagger}(\mathbf{r})\hat{O}\Psi(\mathbf{r})] \\ & = \frac{i}{4}\sum_{\boldsymbol{\delta}}\int d\mathbf{r}'\xi(\mathbf{r}')(H_{\boldsymbol{\delta}})_{ij}\xi(\mathbf{r}'+\boldsymbol{\delta})O_{mn}[\Psi_i^{\dagger}(\mathbf{r}')\Psi_j(\mathbf{r}'+\boldsymbol{\delta}), \Psi_m^{\dagger}(\mathbf{r})\Psi_n(\mathbf{r})] \\ = \quad & -\frac{i}{2}\sum_{\boldsymbol{\delta}}[\tilde{\Psi}^{\dagger}(\mathbf{r})\hat{O}\sigma_3 H_{\boldsymbol{\delta}}\tilde{\Psi}(\mathbf{r}+\boldsymbol{\delta}) - \tilde{\Psi}^{\dagger}(\mathbf{r}-\boldsymbol{\delta})H_{\boldsymbol{\delta}}\sigma_3\hat{O}\tilde{\Psi}(\mathbf{r})]. \end{aligned} \tag{3.14}$$

Here we used the simplified notation $\xi(\mathbf{r}) = 1 + \mathbf{r}\cdot\boldsymbol{\nabla}\chi/2$. We also took advantage of particle-hole symmetry, i.e., $\Psi_n(\mathbf{r}) = (\sigma_1)_{nl}\Psi_l^{\dagger}(\mathbf{r})$ and $\sigma_1\hat{O}\sigma_1 = \hat{O}$, where the second relation results from the first one. Next, we reduce the above result to a continuous expression by properly sending the shift vector to an infinitely small value.

$$\begin{aligned}
\frac{\partial \mathcal{O}(\mathbf{r})}{\partial t} &= -\frac{i}{2}\sum_{\boldsymbol{\delta}}[\tilde{\Psi}^{\dagger}(\mathbf{r})\hat{O}\sigma_3 H_{\boldsymbol{\delta}}\tilde{\Psi}(\mathbf{r}+\boldsymbol{\delta}) - \tilde{\Psi}^{\dagger}(\mathbf{r}-\boldsymbol{\delta})H_{\boldsymbol{\delta}}\sigma_3\hat{O}\tilde{\Psi}(\mathbf{r})] \\
&= -\frac{1}{2}\sum_{\boldsymbol{\delta}}\frac{1}{\boldsymbol{\delta}}[\tilde{\Psi}^{\dagger}(\mathbf{r})\hat{O}\sigma_3(i\boldsymbol{\delta}H_{\boldsymbol{\delta}}e^{i\hat{\mathbf{p}}\cdot\boldsymbol{\delta}})\tilde{\Psi}(\mathbf{r}) - \tilde{\Psi}^{\dagger}(\mathbf{r}-\boldsymbol{\delta})(i\boldsymbol{\delta}H_{\boldsymbol{\delta}}e^{i\hat{\mathbf{p}}\cdot\boldsymbol{\delta}})\sigma_3\hat{O}\tilde{\Psi}(\mathbf{r}-\boldsymbol{\delta})] \\
&= -\frac{1}{2}\sum_{\boldsymbol{\delta}}\frac{1}{\boldsymbol{\delta}}[\tilde{\Psi}^{\dagger}(\mathbf{r})\frac{1}{2}(\hat{O}\sigma_3\hat{v}_{\boldsymbol{\delta}} + \hat{v}_{\boldsymbol{\delta}}\sigma_3\hat{O})\tilde{\Psi}(\mathbf{r}) + \tilde{\Psi}^{\dagger}(\mathbf{r})\frac{1}{2}(\hat{O}\sigma_3\hat{v}_{\boldsymbol{\delta}} - \hat{v}_{\boldsymbol{\delta}}\sigma_3\hat{O})\tilde{\Psi}(\mathbf{r})] \\
&\quad -\frac{1}{\boldsymbol{\delta}}[\tilde{\Psi}^{\dagger}(\mathbf{r}-\boldsymbol{\delta})\frac{1}{2}(\hat{O}\sigma_3\hat{v}_{\boldsymbol{\delta}} + \hat{v}_{\boldsymbol{\delta}}\sigma_3\hat{O})\tilde{\Psi}(\mathbf{r}-\boldsymbol{\delta}) - \tilde{\Psi}^{\dagger}(\mathbf{r}-\boldsymbol{\delta})\frac{1}{2}(\hat{O}\sigma_3\hat{v}_{\boldsymbol{\delta}} - \hat{v}_{\boldsymbol{\delta}}\sigma_3\hat{O})\tilde{\Psi}(\mathbf{r}-\boldsymbol{\delta})] \\
&= -\frac{1}{4}\sum_{\boldsymbol{\delta}}\frac{1}{\boldsymbol{\delta}}[\tilde{\Psi}^{\dagger}(\mathbf{r})(\hat{O}\sigma_3\hat{v}_{\boldsymbol{\delta}} + \hat{v}_{\boldsymbol{\delta}}\sigma_3\hat{O})\tilde{\Psi}(\mathbf{r}) - \tilde{\Psi}^{\dagger}(\mathbf{r}-\boldsymbol{\delta})(\hat{O}\sigma_3\hat{v}_{\boldsymbol{\delta}} + \hat{v}_{\boldsymbol{\delta}}\sigma_3\hat{O})\tilde{\Psi}(\mathbf{r}-\boldsymbol{\delta})] \\
&\quad -\frac{1}{4}\sum_{\boldsymbol{\delta}}\frac{1}{\boldsymbol{\delta}}[\tilde{\Psi}^{\dagger}(\mathbf{r})(\hat{O}\sigma_3\hat{v}_{\boldsymbol{\delta}} - \hat{v}_{\boldsymbol{\delta}}\sigma_3\hat{O})\tilde{\Psi}(\mathbf{r}) + \tilde{\Psi}^{\dagger}(\mathbf{r}-\boldsymbol{\delta})(\hat{O}\sigma_3\hat{v}_{\boldsymbol{\delta}} - \hat{v}_{\boldsymbol{\delta}}\sigma_3\hat{O})\tilde{\Psi}(\mathbf{r}-\boldsymbol{\delta})] \\
&= -\frac{1}{4}\boldsymbol{\nabla}\cdot[\tilde{\Psi}^{\dagger}(\mathbf{r})(\hat{O}\sigma_3\hat{\mathbf{v}} + \hat{\mathbf{v}}\sigma_3\hat{O})\tilde{\Psi}(\mathbf{r})] - \frac{i}{2}\tilde{\Psi}^{\dagger}(\mathbf{r})(\hat{O}\sigma_3\hat{H} - \hat{H}\sigma_3\hat{O})\tilde{\Psi}(\mathbf{r}). \qquad (3.15)
\end{aligned}$$

Here we used the notation $\hat{v}_{\boldsymbol{\delta}} = i\boldsymbol{\delta}H_{\boldsymbol{\delta}}e^{i\hat{\mathbf{p}}\cdot\boldsymbol{\delta}}$ and $\hat{\mathbf{v}} = i\sum_{\boldsymbol{\delta}}\boldsymbol{\delta}H_{\boldsymbol{\delta}}e^{i\hat{\mathbf{p}}\cdot\boldsymbol{\delta}} = i[\hat{H},\mathbf{r}]$. In the last line, we take the limit $\boldsymbol{\delta} \to 0$ to obtain the continuous expression. We can easily read out the current and source term from the final result [38]

$$\frac{\partial \mathcal{O}(\mathbf{r})}{\partial t} = i[H, \mathcal{O}(\mathbf{r})] = -\boldsymbol{\nabla}\cdot\mathbf{j}_O + S_O. \qquad (3.16)$$

Here $\mathbf{j}_O = \tilde{\Psi}^{\dagger}(\mathbf{r})\hat{\mathbf{j}}_O\tilde{\Psi}(\mathbf{r})$ and $S_O = \tilde{\Psi}^{\dagger}(\mathbf{r})\hat{S}_O\tilde{\Psi}(\mathbf{r})$ correspond to the local current and source densities, respectively, with

$$\begin{aligned}
\hat{\mathbf{j}}_O &= \frac{1}{4}(\hat{\mathbf{v}}\sigma_3\hat{O} + \hat{O}\sigma_3\hat{\mathbf{v}}) \\
\hat{S}_O &= -\frac{i}{2}(\hat{O}\sigma_3\hat{H} - \hat{H}\sigma_3\hat{O}) \qquad (3.17)
\end{aligned}$$

where $\hat{\mathbf{v}} = i[\hat{H},\mathbf{r}]$. To linear order in the temperature gradient, the above densities are explicitly decomposed as $\rho_\theta = \rho_\theta^{[0]} + \rho_\theta^{[1]}$, with

$$\begin{aligned}\rho_\theta^{[0]} &= \Psi^\dagger(\mathbf{r})\hat{\theta}\Psi(\mathbf{r}),\\ \rho_\theta^{[1]} &= \frac{1}{2}\Psi^\dagger(\mathbf{r})(\hat{\theta}r_\beta + r_\beta\hat{\theta})\Psi(\mathbf{r})\nabla_\beta\chi,\end{aligned} \tag{3.18}$$

where for θ one needs to substitute either $\mathbf{j}_O$ or S_O. We will use a four-vector convention in which $\theta_0 = S_O$ and $\boldsymbol{\theta} = \mathbf{j}_O$. The non-vanishing source term indicates the non-conservation of the observable, for instance, when $\mathcal{O}(\mathbf{r})$ corresponds to spin density, the source term represents torque density. We note in passing that the source term dipole $\mathbf{P}_O$ can be defined as $S_O = -\boldsymbol{\nabla}\cdot\mathbf{P}_O$ for vanishing total source $\frac{1}{V}\int d\mathbf{r}S_O = 0$, where V is the volume and $\mathbf{P}_O = \mathbf{r}S_O$. Thus, a conserved current can be defined as $\boldsymbol{\mathcal{J}}_O = \mathbf{j}_O + \mathbf{P}_O$ to restore the continuity equation [127]. The current term $\mathbf{j}_O$ coincides with the conventional definition in the literature of the spin Hall effect [9]. In general, based on Eq. (3.16) we can interpret $\mathbf{j}_O$ as a spin current and S_O as the torque. In our discussion below, we concentrate on the spin current term.

3.4 Linear response to a temperature gradient

We consider spatially averaged quantities $\Theta_\alpha = \Theta_\alpha^{[0]} + \Theta_\alpha^{[1]}$ with $\Theta_\alpha^{[0,1]} = \frac{1}{V}\int d\mathbf{r}\rho_{\theta_\alpha}^{[0,1]}(\mathbf{r})$. The thermal response to linear order in the temperature gradient reads

$$\Theta_\alpha = \langle\Theta_\alpha^{[0]}\rangle_{neq} + \langle\Theta_\alpha^{[1]}\rangle_{eq}, \tag{3.19}$$

where on the right hand side the first term is evaluated with respect to nonequilibrium states from the Kubo linear response calculation, while the second term corresponds to orbital magnetization in the system and is evaluated with respect to the equilibrium state.

In total, we can express the linear response as

$$\Theta_\alpha = (S^{\theta_\alpha}_\beta + M^{\theta_\alpha}_\beta)\nabla_\beta \chi, \tag{3.20}$$

where $S^{\theta_\alpha}_\beta$ and $M^{\theta_\alpha}_\beta$ correspond to the first and second terms in Eq. (3.19).

In the spirit of the Kubo response calculation [38, 97], the nonequilibrium part can be described by

$$\langle \Theta^{[0]}_\alpha \rangle_{\text{neq}} = \lim_{\omega \to 0} \frac{1}{i\omega}[\Pi_{\alpha\beta}(\omega) - \Pi_{\alpha\beta}(0)]\nabla_\beta \chi. \tag{3.21}$$

Here $\Pi_{\alpha\gamma}(i\omega_m) = -\int_0^\beta d\tau e^{i\omega_m \tau}\langle T_\tau \Theta^{[0]}_\alpha(\tau) J^q_\gamma(0)\rangle$, with $\beta = 1/(k_B T)$, where ω_m is the bosonic Matsubara frequency. $\mathbf{J}^q$ is the averaged heat current operator defined as $\mathbf{J}^q = \frac{1}{V}\int d\mathbf{r}\mathbf{j}^q(\mathbf{r})$, where the heat current density $\mathbf{j}^q = \frac{1}{4}\Psi^\dagger(\mathbf{r})(\hat{H}\sigma_3\hat{\mathbf{v}} + \hat{\mathbf{v}}\sigma_3\hat{H})\Psi(\mathbf{r})$. This heat current expression can be inferred from the energy conservation equation $\dot{\rho}_E + \boldsymbol{\nabla}\cdot\mathbf{j}^q = 0$, where ρ_E is the energy density of the system. After performing the linear response calculation, the intrinsic nonequilibrium coefficient reads

$$S^{\theta_\alpha}_\beta = \frac{1}{V}\sum_{n\mathbf{k}} -\left[(\Omega^\theta_{n,\mathbf{k}})^\alpha_\beta \bar{\varepsilon}_{n,\mathbf{k}} + (m^\theta_{n,\mathbf{k}})^\alpha_\beta\right] g(\bar{\varepsilon}_{n,\mathbf{k}}). \tag{3.22}$$

Here

$$(\Omega^\theta_{n,\mathbf{k}})^\alpha_\beta = \sum_{m(\neq n)} (\sigma_3)_{nn}(\sigma_3)_{mm} \frac{2\text{Im}[(\theta_{\alpha,\mathbf{k}})_{nm}(v_{\beta,\mathbf{k}})_{mn}]}{(\bar{\varepsilon}_{n,\mathbf{k}} - \bar{\varepsilon}_{m,\mathbf{k}})^2}, \tag{3.23}$$

$$(m^\theta_{n,\mathbf{k}})^\alpha_\beta = \sum_{m(\neq n)} (\sigma_3)_{nn}(\sigma_3)_{mm} \frac{-\text{Im}[(\theta_{\alpha,\mathbf{k}})_{nm}(v_{\beta,\mathbf{k}})_{mn}]}{\bar{\varepsilon}_{n,\mathbf{k}} - \bar{\varepsilon}_{m,\mathbf{k}}}, \tag{3.24}$$

where $(\dots)_{nm} = \langle u_{n,\mathbf{k}}|\dots|u_{m,\mathbf{k}}\rangle$ and $g(\bar{\varepsilon}_{n\mathbf{k}})$ is the Bose-Einstein distribution. Here $(\Omega^\theta_{n,\mathbf{k}})^\alpha_\beta$ is the generalized Berry curvature calculated for operator $\hat{\theta}_\alpha$.

The contribution corresponding to $\rho^{[1]}_{\theta_\alpha}$ is expressed as

$$M^{\theta_\alpha}_\beta = \frac{1}{2V}\langle \int d\mathbf{r}\Psi^\dagger(\mathbf{r})(\hat{\theta}_\alpha r_\beta + r_\beta \hat{\theta}_\alpha)\Psi(\mathbf{r})\rangle_{eq}. \tag{3.25}$$

To calculate this term, we can identify a thermodynamic expression for $M_\beta^{\theta_\alpha}$ by following Refs. [132–136]. We introduce a perturbation coupled with a four-component fictitious field $h_\alpha(\mathbf{r})$, i.e., $\hat{H}_1 = \hat{H}_0 - [\hat{\theta}_\alpha h_\alpha(\mathbf{r}) + h_\alpha(\mathbf{r})\hat{\theta}_\alpha]$. If the field varies very slowly on the scale of the lattice constant, we can identify a thermodynamic expression

$$M_\beta^{\theta_\alpha} = -\lim_{h_\alpha \to 0} \frac{1}{V} \frac{\partial \Omega}{\partial(\partial_{r_\beta} h_\alpha)} \tag{3.26}$$

where Ω is the thermodynamic grand potential of the system. The thermodynamic definition of grand potential reads

$$\Omega = E - TS - \mu N, \tag{3.27}$$

where S, μ, N are the entropy, chemical potential, particle number of the system, and E is the energy which reads

$$E = \langle H \rangle_{eq} = \frac{1}{2} \sum_{\mathbf{k},n=1}^{2N} (\sigma_3)_{nn} g(\bar{\varepsilon}_{n,\mathbf{k}}) \langle \psi_{n,\mathbf{k}} | \hat{H} | \psi_{n,\mathbf{k}} \rangle. \tag{3.28}$$

Here we use the relation $\langle \Gamma_{n,\mathbf{k}}^\dagger \Gamma_{m,\mathbf{k}} \rangle = (\sigma_3)_{nn} g(\bar{\varepsilon}_{n,\mathbf{k}})$ with $\Gamma_{m,\mathbf{k}} = \sum_l (T_\mathbf{k})_{ml} \Psi_{\mathbf{k},l}$. Below we will assume the chemical potential to be zero. If we regard the local fictitious field and its gradient as independent variables, the variation of the grand potential can be identified as

$$d\Omega = -SdT - \langle \Theta_\alpha^{[0]} \rangle dh_\alpha - M_\beta^{\theta_\alpha} d(\partial_{r_\beta} h_\alpha), \tag{3.29}$$

from which we can identify the Maxwell relation

$$\left(\frac{\partial M_\beta^{\theta_\alpha}}{\partial T} \right)_{h_\alpha, \partial_{r_\beta} h_\alpha} = \left[\frac{\partial S}{\partial(\partial_{r_\beta} h_\alpha)} \right]_{T, h_\alpha}. \tag{3.30}$$

To get rid of calculations involving entropy S, we first introduce an auxiliary quantity

$$\tilde{M}_{\beta}^{\theta_\alpha} = -\frac{1}{V}\frac{\partial K}{\partial(\partial_{r_\beta} h_\alpha)} \tag{3.31}$$

with $K = \Omega + TS = E\ (\mu = 0)$. By utilizing Eq. (3.30), we obtain

$$M_{\beta}^{\theta_\alpha} = \tilde{M}_{\beta}^{\theta_\alpha} + T\frac{\partial M_{\beta}^{\theta_\alpha}}{\partial T} \tag{3.32}$$

and hence the dipole moment contribution can be calculated as

$$\tilde{M}_{\beta}^{\theta_\alpha} = \frac{\partial(\beta M_{\beta}^{\theta_\alpha})}{\partial \beta}. \tag{3.33}$$

If we regard the fictitious field term as a perturbation, the variation of K to linear order reads

$$\begin{aligned}\delta K(\mathbf{r}) \quad &= \frac{1}{2}\sum_{n\mathbf{k}} \delta g(\bar{\varepsilon}_{n\mathbf{k}})(\sigma_3)_{nn}\langle\psi_{n\mathbf{k}}|\hat{H}|\psi_{n\mathbf{k}}\rangle - g(\bar{\varepsilon}_{n\mathbf{k}})(\sigma_3)_{nn}\langle\psi_{n\mathbf{k}}|[\hat{\theta}_\alpha h_\alpha(\mathbf{r}) + h_\alpha(\mathbf{r})\hat{\theta}_\alpha]|\psi_{n\mathbf{k}}\rangle \\ &+ g(\bar{\varepsilon}_{n\mathbf{k}})(\sigma_3)_{nn}(\langle\delta\psi_{n\mathbf{k}}|\hat{H}|\psi_{n\mathbf{k}}\rangle + \langle\psi_{n\mathbf{k}}|\hat{H}|\delta\psi_{n\mathbf{k}}\rangle),\end{aligned} \tag{3.34}$$

where $|\psi_{n\mathbf{k}}\rangle = \frac{e^{i\mathbf{k}\cdot\mathbf{r}}}{\sqrt{V}}|u_{n\mathbf{k}}\rangle$ is the Bloch wave function of the system. If we assume a special form of the fictitious field

$$h_\alpha(\mathbf{r}) = \frac{h_\alpha^0}{q}\sin(\mathbf{q}\cdot\mathbf{r}), \tag{3.35}$$

with $\mathbf{q} = q\hat{\mathbf{e}}_\beta$, where $\alpha, \beta = x, y, z$ in three dimensions or $\alpha, \beta = x, y$ in two dimensions, the auxiliary quantity can be identified by picking up the appropriate Fourier component

$$\tilde{M}_{\beta}^{\theta_\alpha} = \lim_{q\to 0}\frac{-2}{h_\alpha^0 V}\int d\mathbf{r}\delta K(\mathbf{r})\cos(\mathbf{q}\cdot\mathbf{r}). \tag{3.36}$$

As an example, we calculate $\tilde{M}_x^{\theta_y}$ by taking $\mathbf{q}_1 = q\hat{\mathbf{e}}_x$ and $h_\alpha(\mathbf{r}) = \frac{h}{q}\sin(\mathbf{q}_1\cdot\mathbf{r})\delta_{\alpha,y}$. Applying perturbation theory to linear order under the Bloch representation, we find

$$\langle \psi_{m,\mathbf{k}\pm\mathbf{q}_1}|\sigma_3|\delta\psi_{n\mathbf{k}}\rangle = \frac{ih}{2q}\frac{\langle u_{m,\mathbf{k}\pm\mathbf{q}_1}|(\theta_{y,\mathbf{k}}+\theta_{y,\mathbf{k}+\mathbf{q}_1})|u_{n,\mathbf{k}}\rangle}{\bar{\varepsilon}_{n\mathbf{k}}-\bar{\varepsilon}_{m,\mathbf{k}\pm\mathbf{q}_1}}, \tag{3.37}$$

and

$$|\delta\psi_{n\mathbf{k}}\rangle = \sum_m \frac{ih}{2q}(\sigma_3)_{mm}[e^{i(\mathbf{k}+\mathbf{q}_1)\cdot\mathbf{r}}|u_{m,\mathbf{k}+\mathbf{q}_1}\rangle\frac{\langle u_{m,\mathbf{k}+\mathbf{q}_1}|(\theta_{y,\mathbf{k}}+\theta_{y,\mathbf{k}+\mathbf{q}_1})|u_{n,\mathbf{k}}\rangle}{\bar{\varepsilon}_{n\mathbf{k}}-\bar{\varepsilon}_{m,\mathbf{k}+\mathbf{q}_1}} - (\mathbf{q}_1\to-\mathbf{q}_1)] \tag{3.38}$$

Here it is implied that we will use the operator under Bloch representation henceforth, i.e., $\hat{H}\to H_{\mathbf{k}} = e^{-i\mathbf{k}\cdot\mathbf{r}}\hat{H}e^{i\mathbf{k}\cdot\mathbf{r}}$, $\hat{\theta}_\alpha\to\theta_{\alpha,\mathbf{k}} = e^{-i\mathbf{k}\cdot\mathbf{r}}\hat{\theta}_\alpha e^{i\mathbf{k}\cdot\mathbf{r}}$. This step is guaranteed by the requirement that the operator $\hat{\theta}_\alpha$ is well defined in a periodic system. By using the results above we obtain

$$\begin{aligned}\tilde{M}_x^{\theta_y} \quad &= \lim_{q\to0}\frac{1}{2V}\sum_{\mathbf{k}}\sum_{mn}\frac{1}{i2q}g(\bar{\varepsilon}_{n\mathbf{k}})(\sigma_3)_{nn}(\sigma_3)_{mm}\bar{\varepsilon}_{n\mathbf{k}}\\ &\times[\frac{\langle u_{n\mathbf{k}}|\sigma_3|u_{m,\mathbf{k}+\mathbf{q}_1}\rangle\langle u_{m,\mathbf{k}+\mathbf{q}_1}|(\theta_{y,\mathbf{k}}+\theta_{y,\mathbf{k}+\mathbf{q}_1})|u_{n,\mathbf{k}}\rangle}{\bar{\varepsilon}_{n\mathbf{k}}-\bar{\varepsilon}_{m,\mathbf{k}+\mathbf{q}_1}} - (\mathbf{q}_1\to-\mathbf{q}_1)] + c.c.\\ &= \lim_{q\to0}\frac{1}{2V}\sum_{\mathbf{k}}\sum_{mn}\frac{1}{i2q}[g(\bar{\varepsilon}_{n\mathbf{k}})\bar{\varepsilon}_{n\mathbf{k}} - g(\bar{\varepsilon}_{m,\mathbf{k}+\mathbf{q}_1})\bar{\varepsilon}_{m,\mathbf{k}+\mathbf{q}_1}](\sigma_3)_{nn}(\sigma_3)_{mm}\\ &\times\frac{\langle u_{n\mathbf{k}}|\sigma_3|u_{m,\mathbf{k}+\mathbf{q}_1}\rangle\langle u_{m,\mathbf{k}+\mathbf{q}_1}|(\theta_{y,\mathbf{k}}+\theta_{y,\mathbf{k}+\mathbf{q}_1})|u_{n,\mathbf{k}}\rangle}{\bar{\varepsilon}_{n\mathbf{k}}-\bar{\varepsilon}_{m,\mathbf{k}+\mathbf{q}_1}} + c.c.\end{aligned} \tag{3.39}$$

Taking the limit, we get for $m\neq n$,

$$\begin{aligned}&(\tilde{M}_x^{\theta_y})_1\\ &= \frac{1}{V}\sum_{\mathbf{k}}\sum_{m\neq n}\frac{1}{2}[g(\bar{\varepsilon}_{m\mathbf{k}})\bar{\varepsilon}_{m\mathbf{k}} - g(\bar{\varepsilon}_{n,\mathbf{k}})\bar{\varepsilon}_{n,\mathbf{k}}](\sigma_3)_{nn}(\sigma_3)_{mm}\frac{i\langle u_{n,\mathbf{k}}|\sigma_3|\partial_{k_x}u_{m,\mathbf{k}}\rangle\langle u_{m,\mathbf{k}}|\theta_y|u_{n,\mathbf{k}}\rangle}{\bar{\varepsilon}_{n,\mathbf{k}}-\bar{\varepsilon}_{m,\mathbf{k}}} + c.c.\\ &= \frac{1}{V}\sum_{\mathbf{k}}\sum_{m\neq n}-\frac{1}{2}[g(\bar{\varepsilon}_{m\mathbf{k}})\bar{\varepsilon}_{m\mathbf{k}} - g(\bar{\varepsilon}_{n,\mathbf{k}})\bar{\varepsilon}_{n,\mathbf{k}}](\sigma_3)_{nn}(\sigma_3)_{mm}\frac{i\langle u_{n,\mathbf{k}}|v_x|u_{m,\mathbf{k}}\rangle\langle u_{m,\mathbf{k}}|\theta_y|u_{n,\mathbf{k}}\rangle}{(\bar{\varepsilon}_{n,\mathbf{k}}-\bar{\varepsilon}_{m,\mathbf{k}})^2} + c.c..\end{aligned} \tag{3.40}$$

For $m = n$, we have

$$\begin{aligned}
&(\tilde{M}_x^{\theta_y})_2 \\
&= \frac{1}{V}\sum_{\mathbf{k}}\sum_{n}\frac{1}{2i}[g(\bar{\varepsilon}_{n,\mathbf{k}}) + g'(\bar{\varepsilon}_{n,\mathbf{k}})\bar{\varepsilon}_{n,\mathbf{k}}][\langle u_{n,\mathbf{k}}|\sigma_3\partial_{k_x}u_{n,\mathbf{k}}\rangle\langle u_{n,\mathbf{k}}|\theta_y|u_{n,\mathbf{k}}\rangle \\
&+(\sigma_3)_{nn}\langle\partial_{k_x}u_{n,\mathbf{k}}|\theta_y|u_{n,\mathbf{k}}\rangle] + c.c. \\
&= \frac{1}{V}\sum_{\mathbf{k}}\sum_{n} -\frac{1}{2}[g(\bar{\varepsilon}_{n,\mathbf{k}}) + g'(\bar{\varepsilon}_{n,\mathbf{k}})\bar{\varepsilon}_{n,\mathbf{k}}](\sigma_3)_{nn}(\sigma_3)_{mm}\frac{i\langle u_{n,\mathbf{k}}|v_x|u_{m,\mathbf{k}}\rangle\langle u_{m,\mathbf{k}}|\theta_y|u_{n,\mathbf{k}}\rangle}{\bar{\varepsilon}_{n,\mathbf{k}} - \bar{\varepsilon}_{m,\mathbf{k}}} + c.c..
\end{aligned} \tag{3.41}$$

Above $v_x = \partial_{k_x}H$. In total, we have

$$\tilde{M}_x^{\theta_y} \quad = (\tilde{M}_x^{\theta_y})_1 + (\tilde{M}_x^{\theta_y})_2 = \frac{1}{V}\sum_{n\mathbf{k}} g(\bar{\varepsilon}_{n\mathbf{k}})\bar{\varepsilon}_{n\mathbf{k}}(\Omega^{\theta}_{n,\mathbf{k}})^y_x + [g(\bar{\varepsilon}_{n,\mathbf{k}}) + g'(\bar{\varepsilon}_{n,\mathbf{k}})\bar{\varepsilon}_{n,\mathbf{k}}](m^{\theta}_{n,\mathbf{k}})^y_x. \tag{3.42}$$

The calculation of all other components is fully analogous to what we have done. The general result will be

$$\tilde{M}_\beta^{\theta_\alpha} = \frac{1}{V}\sum_{n\mathbf{k}} g(\bar{\varepsilon}_{n\mathbf{k}})\bar{\varepsilon}_{n\mathbf{k}}(\Omega^{\theta}_{n,\mathbf{k}})^\alpha_\beta + [g(\bar{\varepsilon}_{n,\mathbf{k}}) + g'(\bar{\varepsilon}_{n,\mathbf{k}})\bar{\varepsilon}_{n,\mathbf{k}}](m^{\theta}_{n,\mathbf{k}})^\alpha_\beta, \tag{3.43}$$

Note that here the Berry curvature in the above equation is summed over both particle and hole space. Finally, by using Eq. (3.33) we obtain

$$M_\beta^{\theta_\alpha} = \frac{1}{\beta}\int_0^\beta d\bar{\beta}\tilde{M}_\beta^{\theta_\alpha} = \frac{1}{V}\sum_{n\mathbf{k}}[(\Omega^{\theta}_{n,\mathbf{k}})^\alpha_\beta\int_0^{\bar{\varepsilon}_{n\mathbf{k}}} d\eta g(\eta) + (m^{\theta}_{n,\mathbf{k}})^\alpha_\beta g(\bar{\varepsilon}_{n,\mathbf{k}})]. \tag{3.44}$$

Here we used the relation $\frac{1}{\beta}\int_0^\beta d\bar{\beta} g(\bar{\varepsilon}_{n,\mathbf{k}})\bar{\varepsilon}_{n,\mathbf{k}} = \int_0^{\bar{\varepsilon}_{n\mathbf{k}}} d\eta g(\eta)$ with $g(\eta) = \frac{1}{e^{\beta\eta}-1}$ and $\frac{d}{d\bar{\beta}}[\bar{\beta} g(\bar{\varepsilon}_{n,\mathbf{k}})] = g(\bar{\varepsilon}_{n,\mathbf{k}}) + g'(\bar{\varepsilon}_{n,\mathbf{k}})\bar{\varepsilon}_{n,\mathbf{k}}$.

Now we can combine the nonequilibrium contribution in Eq. (3.22) and Eq. (3.44) together to obtain the total response coefficient

$$\begin{aligned} S^{\theta_\alpha}_\beta + M^{\theta_\alpha}_\beta \quad &= \frac{1}{V}\sum_{n\mathbf{k}}(\Omega^\theta_{n,\mathbf{k}})^\alpha_\beta[-\bar{\varepsilon}_{n\mathbf{k}}g(\bar{\varepsilon}_{n\mathbf{k}}) + \int_0^{\bar{\varepsilon}_{n\mathbf{k}}} d\eta g(\eta)] \\ &= -\frac{1}{V}\sum_{n\mathbf{k}}(\Omega^\theta_{n,\mathbf{k}})^\alpha_\beta \int_0^{\bar{\varepsilon}_{n\mathbf{k}}} d\eta\eta\frac{dg(\eta)}{d\eta} \\ &= -\frac{1}{V}\sum_{n\mathbf{k}}(\Omega^\theta_{n,\mathbf{k}})^\alpha_\beta \tilde{c}_1(\bar{\varepsilon}_{n\mathbf{k}}), \end{aligned} \tag{3.45}$$

where $\tilde{c}_1(x) = \int_0^x d\eta\eta\frac{dg(\eta)}{d\eta}$ with $g(\eta) = \frac{1}{e^{\beta\eta}-1}$.

Before proceeding toward the final result, we provide two useful properties of Berry curvature defined in (3.23).

(1) Summation rule:

$$\begin{aligned} \sum_{n=1}^{2N}(\Omega^\theta_{n,\mathbf{k}})^\alpha_\beta \quad &= \sum_{m\neq n}(\sigma_3)_{nn}(\sigma_3)_{mm}\mathrm{Im}[\frac{\langle u_{n,\mathbf{k}}|\theta_\alpha|u_{m,\mathbf{k}}\rangle\langle u_{m,\mathbf{k}}|v_\beta|u_{n,\mathbf{k}}\rangle}{(\bar{\varepsilon}_{n,\mathbf{k}}-\bar{\varepsilon}_{m,\mathbf{k}})^2} \\ &+ \frac{\langle u_{m,\mathbf{k}}|\theta_\alpha|u_{n,\mathbf{k}}\rangle\langle u_{n,\mathbf{k}}|v_\beta|u_{m,\mathbf{k}}\rangle}{(\bar{\varepsilon}_{n,\mathbf{k}}-\bar{\varepsilon}_{m,\mathbf{k}})^2}] = 0. \end{aligned} \tag{3.46}$$

In the middle step, we utilized the property that the band indices m, n can be interchanged.

(2) Mapping between particle and hole space. We note that the velocity operator $v_\mathbf{k}$ satisfies

$$\sigma_1 v_\mathbf{k}\sigma_1 = \sigma_1\frac{\partial H_\mathbf{k}}{\partial \mathbf{k}}\sigma_1 = -v^*_{-\mathbf{k}}. \tag{3.47}$$

At the same time, the particle-hole symmetry of the Hamiltonian enforces the relation

$$\sigma_1\theta_{\alpha,\mathbf{k}}\sigma_1 = \theta^*_{\alpha,-\mathbf{k}}, \tag{3.48}$$

which is clearly satisfied when we consider the current and source term response for a given operator $\hat{O}$. Using the particle-hole symmetry property of the eigenstates and eigenvalues, we are able to show

$$
\begin{aligned}
&(\Omega^{\theta}_{n,\mathbf{k}})^{\alpha}_{\beta} \\
&= \sum_{m(\neq n)} (\sigma_3)_{nn}(\sigma_3)_{mm} \frac{2\mathrm{Im}(\langle u_{n,\mathbf{k}}|\theta_{\alpha,\mathbf{k}}|u_{m,\mathbf{k}}\rangle\langle u_{m,\mathbf{k}}|v_{\beta,\mathbf{k}}|u_{n,\mathbf{k}}\rangle)}{(\bar{\varepsilon}_{n,\mathbf{k}}-\bar{\varepsilon}_{m,\mathbf{k}})^2} \\
&= \sum_{m+N(\neq n+N)} (\sigma_3)_{n+N,n+N}(\sigma_3)_{m+N,m+N} \\
&\times \frac{2\mathrm{Im}(\langle u^*_{n+N,-\mathbf{k}}|\sigma_1\theta_{\alpha,\mathbf{k}}\sigma_1|u^*_{m+N,-\mathbf{k}}\rangle\langle u^*_{m+N,-\mathbf{k}}|\sigma_1 v_{\beta,\mathbf{k}}\sigma_1|u^*_{n+N,-\mathbf{k}}\rangle)}{(\bar{\varepsilon}_{n+N,-\mathbf{k}}-\bar{\varepsilon}_{m+N,-\mathbf{k}})^2} \\
&= \sum_{m(\neq n+N)} (\sigma_3)_{n+N,n+N}(\sigma_3)_{mm} \frac{2\mathrm{Im}[(\langle u_{n+N,-\mathbf{k}}|\theta_{\alpha,-\mathbf{k}}|u_{m,-\mathbf{k}}\rangle)^*(\langle u_{m,-\mathbf{k}}|-v_{\beta,-\mathbf{k}}|u_{n+N,-\mathbf{k}}\rangle)^*]}{(\bar{\varepsilon}_{n+N,-\mathbf{k}}-\bar{\varepsilon}_{m,-\mathbf{k}})^2} \\
&= (\Omega^{\theta}_{n+N,-\mathbf{k}})^{\alpha}_{\beta}. \qquad (3.49)
\end{aligned}
$$

Now, from the relation $-g(-\eta) = 1 + g(\eta)$, we have $\tilde{c}(x) = \tilde{c}(-x)$. By using the two properties of the general Berry curvature Eq. (3.46) and (3.49), the total response function can be further reduced as below

$$
\begin{aligned}
S^{\theta_\alpha}_{\beta} + M^{\theta_\alpha}_{\beta} &= -\frac{1}{V}\sum_{n=1}^{N}\sum_{\mathbf{k}}[(\Omega^{\theta}_{n,\mathbf{k}})^{\alpha}_{\beta}\tilde{c}_1(\varepsilon_{n\mathbf{k}}) + (\Omega^{\theta}_{n+N,\mathbf{k}})^{\alpha}_{\beta}\tilde{c}_1(-\varepsilon_{n,-\mathbf{k}})] \\
&= -\frac{1}{V}\sum_{n=1}^{N}\sum_{\mathbf{k}}[(\Omega^{\theta}_{n,\mathbf{k}})^{\alpha}_{\beta} + (\Omega^{\theta}_{n+N,-\mathbf{k}})^{\alpha}_{\beta}]\tilde{c}_1(\varepsilon_{n,\mathbf{k}}) \\
&= -\frac{1}{V}\sum_{n=1}^{N}\sum_{\mathbf{k}}[(\Omega^{\theta}_{n,\mathbf{k}})^{\alpha}_{\beta} + (\Omega^{\theta}_{n+N,-\mathbf{k}})^{\alpha}_{\beta}][\tilde{c}_1(\varepsilon_{n,\mathbf{k}}) - \int_0^{\infty} d\eta\,\eta\frac{dg(\eta)}{d\eta}] \\
&= -\frac{k_B T}{V}\sum_{n=1}^{N}\sum_{\mathbf{k}}[(\Omega^{\theta}_{n,\mathbf{k}})^{\alpha}_{\beta} + (\Omega^{\theta}_{n+N,-\mathbf{k}})^{\alpha}_{\beta}]c_1[g(\varepsilon_{n,\mathbf{k}})] \\
&= -\frac{2k_B T}{V}\sum_{n=1}^{N}\sum_{\mathbf{k}}(\Omega^{\theta}_{n,\mathbf{k}})^{\alpha}_{\beta}c_1[g(\varepsilon_{n,\mathbf{k}})]. \qquad (3.50)
\end{aligned}
$$

Here we used the relation $-\int_{\varepsilon_n}^{\infty}\eta\frac{dg(\eta)}{d\eta}d\eta = \frac{1}{\beta}c_1[g(\varepsilon_n)]$. By substituting the coefficient above in to Eq. (3.20), we obtain the thermal response formula which constitutes the main

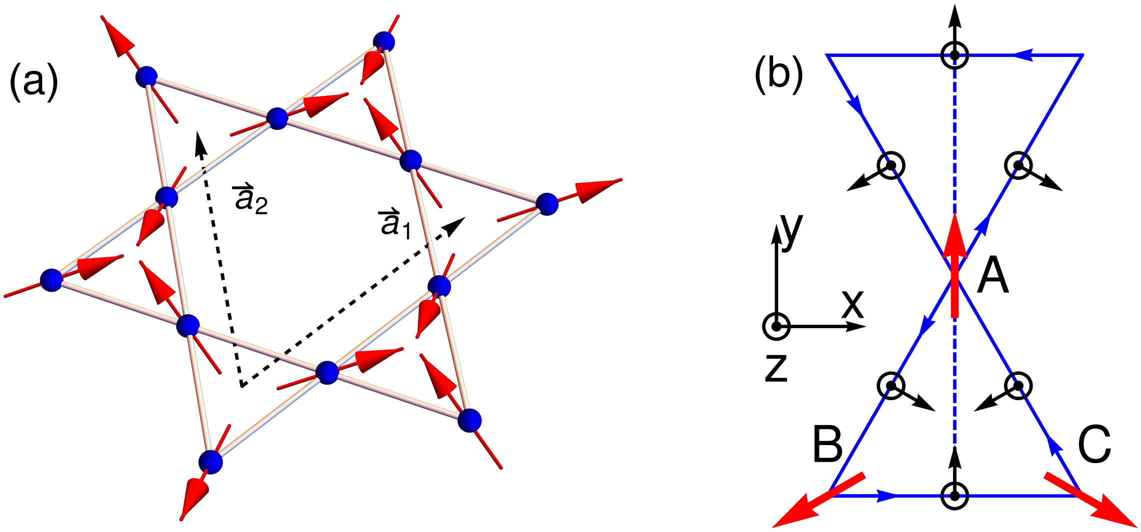

Figure 3.1: (a) Kagome antiferromagnet lattice with small out-of-plane spin canting. (b) Spin order in-plane projection and DMI vectors for kagome antiferromagnet, where the dashed line shows the mirror plane $\mathcal{M}_x$.

result of this paper:

$$\Theta_\alpha = \frac{2k_B}{V}\sum_{n=1}^{N}\sum_{\mathbf{k}}(\Omega^{\theta}_{n,\mathbf{k}})^{\alpha}_{\beta}c_1[g(\varepsilon_{n,\mathbf{k}})]\nabla_\beta T. \tag{3.51}$$

Note that we express our result using particle bands ($n \leq N$) by utilizing PHS.

It is useful to identify the symmetry constraints leading to a vanishing source term response. In general, for the averaged torque density this can happen for only some of the torque components. However, for an inversion symmetric system, i.e., $H_{\mathbf{k}} = H_{-\mathbf{k}}$, the Berry curvature of the torque term satisfies $(\Omega^{S_O}_{n,\mathbf{k}})_\beta = -(\Omega^{S_O}_{n,-\mathbf{k}})_\beta$. Together with the relation $\varepsilon_{n,\mathbf{k}} = \varepsilon_{n,-\mathbf{k}}$, this results in the vanishing of all torque components in Eq. (3.51).

3.5 Spin Nernst effect in kagome antiferromagnet

We use the result in Eq. (3.51) to calculate the spin Nernst response tensor in a noncollinear kagome antiferromagnet in Eq. (3.1) where the spin Berry curvature is calculated with respect to operator $\hat{j}_{\gamma,\lambda} = \frac{1}{4}(\hat{v}_\lambda\sigma_3\hat{S}^\gamma + \hat{S}^\gamma\sigma_3\hat{v}_\lambda)$ corresponding to the spin current. We can immediately identify that the spin Berry curvature in Eq. (3.1) is even under the time reversal transformation. As a result, the spin Nernst conductivity is also even under the time reversal transformation, and this result will be used in the symmetry analysis below. Furthermore, in a kagome antiferromagnet, due to the presence of inversion symmetry, the averaged torque density (source term) vanishes. We consider the Hamiltonian

$$H = \sum_{\langle ij \rangle} J_1 \mathbf{S}_i \cdot \mathbf{S}_j + \mathbf{D}_{ij} \cdot (\mathbf{S}_i \times \mathbf{S}_j) + \sum_{\langle\langle ij \rangle\rangle} J_2 \mathbf{S}_i \cdot \mathbf{S}_j, \tag{3.52}$$

where the first and third terms represent nearest and second-nearest neighbor Heisenberg exchange, and the second term represents nearest neighbor Dzyaloshinskii-Moriya interaction (DMI) with both in-plane and out-of-plane DMI vectors, as shown in Fig. 3.1. The DMI vector can be expressed as $\mathbf{D}_{ij} = D_p \hat{n}_{ij} + D_z \hat{z}$, where D_p and D_z correspond to the in-plane and out-of-plane DMI strength, and $\hat{n}_{ij}$ is an in-plane unit vector corresponding to the direction of the in-plane DMI. The in-plane DMI can only arise when $\mathcal{M}_z$ symmetry is broken [114], i.e., time-reversal followed by mirror symmetry with respect to the kagome plane is not a symmetry in such a case. This introduces a small out-of-plane canting angle η to spin order with magnitude $\eta = \frac{1}{2}\tan^{-1}(\frac{-2D_p}{\sqrt{3}(J_1+J_2)-D_z})$ [40]. Here we consider the $\mathbf{q} = 0$ phase with spin order as shown in Fig. 3.1. The magnetic moments orient according to $\langle \mathbf{S}_i \rangle = S(\cos\eta\cos\phi_i, \cos\eta\sin\phi_i, \sin\eta)$, where ϕ_i is the angle formed by the in-plane projection of moment with the x axis. Specifically, $\phi_A = \pi/2$, $\phi_B = 7\pi/6$, and $\phi_C = -\pi/6$. For the spin Nernst response, we identify $\hat{O}$ discussed above as the spin operator in the magnon basis $\Psi(\mathbf{r}) = [b_A(\mathbf{r}), b_B(\mathbf{r}), b_C(\mathbf{r}), b_A^\dagger(\mathbf{r}), b_B^\dagger(\mathbf{r}), b_C^\dagger(\mathbf{r})]^T$, i.e., $\hat{S}^\alpha = -\sigma_0 \otimes \text{Diag}(\langle S_A^\alpha \rangle, \langle S_B^\alpha \rangle, \langle S_C^\alpha \rangle)/S$.

The spin conductivity tensor of a spin-polarized current in a noncollinear antiferromagnet [116,137] is restricted to a certain form by the magnetic space group of the system. Suppose the Hamiltonian respects a symmetry g with matrix representation $U(g)$ for unitary operation and $U(g)\mathcal{K}$ for anti-unitary operation (containing time-reversal) with $\mathcal{K}$

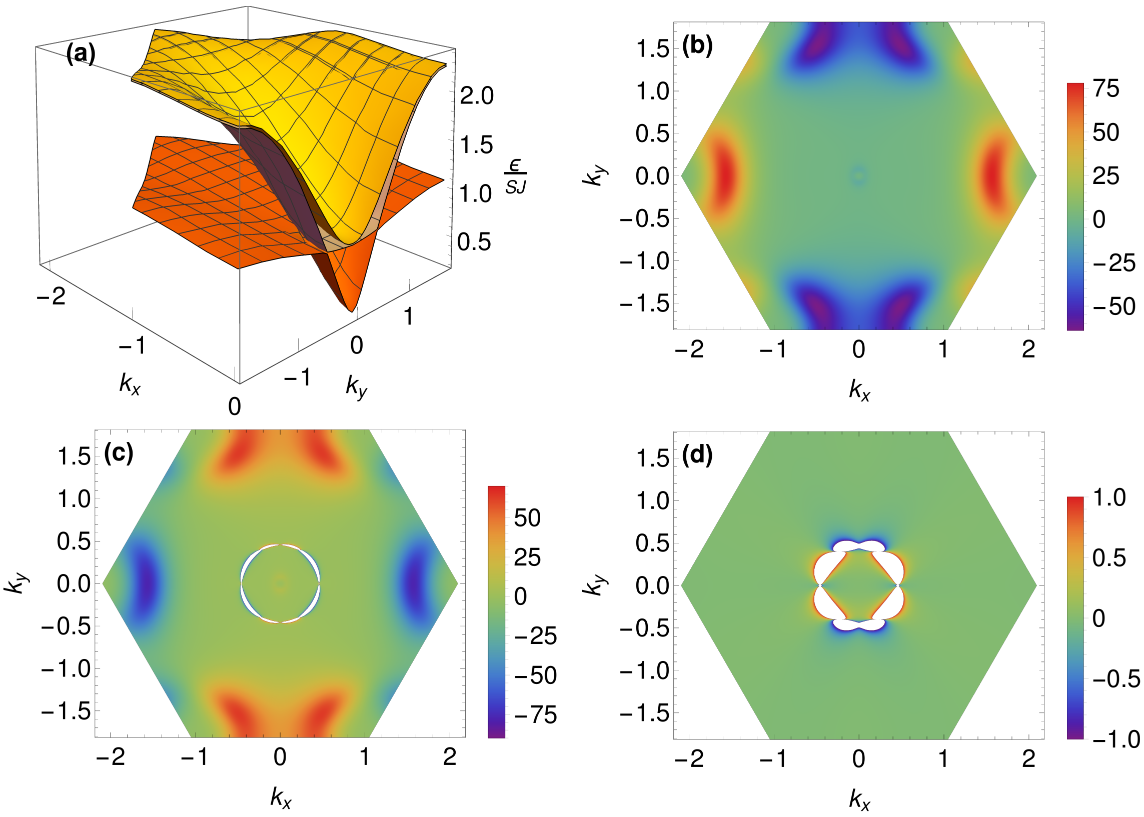

Figure 3.2: Plots for kagome antiferromagnet $KFe_3(OH)_6(SO_4)_2$. (a) Energy bands. (b-d) The spin Berry curvature for α^y_{yx} for top, middle, and lowest band. Detailed plots of the spin Berry curvature in the vicinity of the white regions, corresponding to the values outside of the range of the scale bar, can be found in Fig. 3.3.

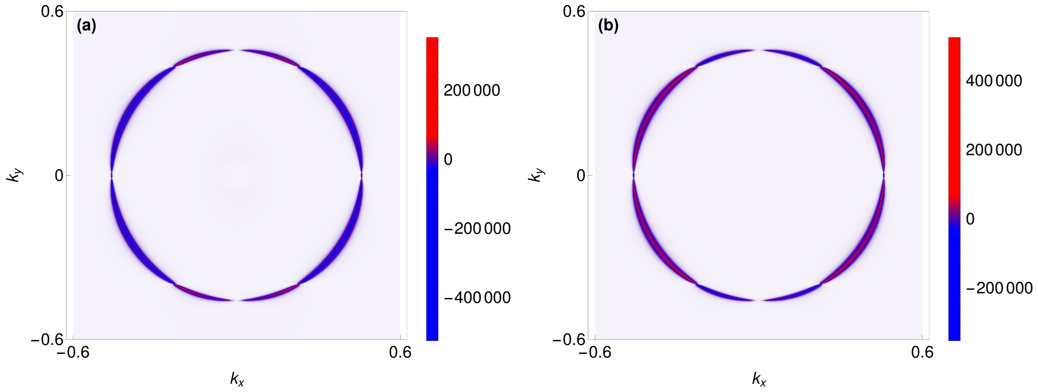

Figure 3.3: Spin Berry curvature plots for kagome antiferromagnet $KFe_3(OH)_6(SO_4)_2$. (a) Middle energy band. (b) Lowest energy band.

being the complex conjugate operator. Here $U(g)$ corresponds to the point group operation on spin mode orbitals, which is a unitary matrix that satisfies $U(g)^\dagger = U(g)^T$. On the other hand, the point group symmetries don't mix particle and hole symmetry, such that $[\sigma_3, U(g)] = 0$. For the unitary case, we assume

$$U(g)H_{\mathbf{k}}U^\dagger(g) = H_{M(g)\mathbf{k}}, \tag{3.53}$$

where $M(g)$ is the matrix acting on momentum variables. This can lead to relations below

$$|\psi_{n,M(g)\mathbf{k}}\rangle = U(g)|\psi_{n,\mathbf{k}}\rangle, \qquad \varepsilon_{M(g)\mathbf{k}} = \varepsilon_{\mathbf{k}}. \tag{3.54}$$

As a consequence, by inserting the symmetry operation in the matrix elements of an observable, we find

$$\langle\psi_{n,\mathbf{k}}|\hat{A}|\psi_{m,\mathbf{k}}\rangle = \langle\psi_{n,M(g)\mathbf{k}}|U(g)\hat{A}U(g)^\dagger|\psi_{m,M(g)\mathbf{k}}\rangle. \tag{3.55}$$

Similarly, for the anti-unitary case, assume the symmetry contraint on Hamiltonian reads

$$U(g)H^*_{\mathbf{k}}U^\dagger(g) = H_{M(g)\mathbf{k}}, \tag{3.56}$$

such that

$$|\psi_{n,M(g)\mathbf{k}}\rangle = U(g)\mathcal{K}|\psi_{n,\mathbf{k}}\rangle, \qquad \varepsilon_{M(g)\mathbf{k}} = \varepsilon_{\mathbf{k}}. \tag{3.57}$$

These relations will lead to

$$\langle\psi_{n,\mathbf{k}}|\hat{A}|\psi_{m,\mathbf{k}}\rangle = \langle\psi_{n,M(g)\mathbf{k}}|U(g)\hat{A}U(g)^\dagger|\psi_{m,M(g)\mathbf{k}}\rangle^*. \tag{3.58}$$

If the operator $\hat{A}$ satisfies

$$U(g)\hat{A}_iU(g)^\dagger = \sum_j R(g)_{ij}\hat{A}_j, \tag{3.59}$$

it can be combined with the operator element symmetry relation to produce a transformation relation for the spin Nernst response coefficient

$$\alpha^{\gamma}_{\lambda\beta} = \pm R^s(g)_{\gamma i}R^v(g)_{\lambda j}R^v(g)_{\beta k}\alpha^{i}_{jk}, \tag{3.60}$$

where the plus and minus sign correspond to unitary and anti-unitary symmetry, and $R^{s/v}(g)$ stands for the transformation matrix for the spin and velocity operator, respectively. Moreover, suppose the involved non-magnetic point group symmetry $U(g)$ corresponds to a spatial operation with matrix form R in Cartesian coordinates. If $\hat{g}$ is a unitary operation,

$$R^s(g) = \text{det}(R)R, \qquad R^v(g) = R. \tag{3.61}$$

If $\hat{g}$ is an anti-unitary operation,

$$R^s(g) = -\text{det}(R)R, \qquad R^v(g) = -R. \tag{3.62}$$

Plugging Eq. (3.61), (3.62) into Eq. (3.60), we find

$$\alpha^{\gamma}_{\lambda\beta} = \text{det}(R)R_{\gamma\gamma'}R_{\lambda\lambda'}R_{\beta\beta'}\alpha^{\gamma'}_{\lambda'\beta'} \tag{3.63}$$

In the kagome AF, we focus on two symmetries of the system: the mirror reflection with respect to the $y-z$ plane plus time-reversal $\hat{g}_1 = \mathcal{M}_{yz}\mathcal{T}$, and the threefold rotation about the z axis $\hat{g}_2 = \mathcal{C}_{3z}$. It is straightforward to obtain the matrix representation in

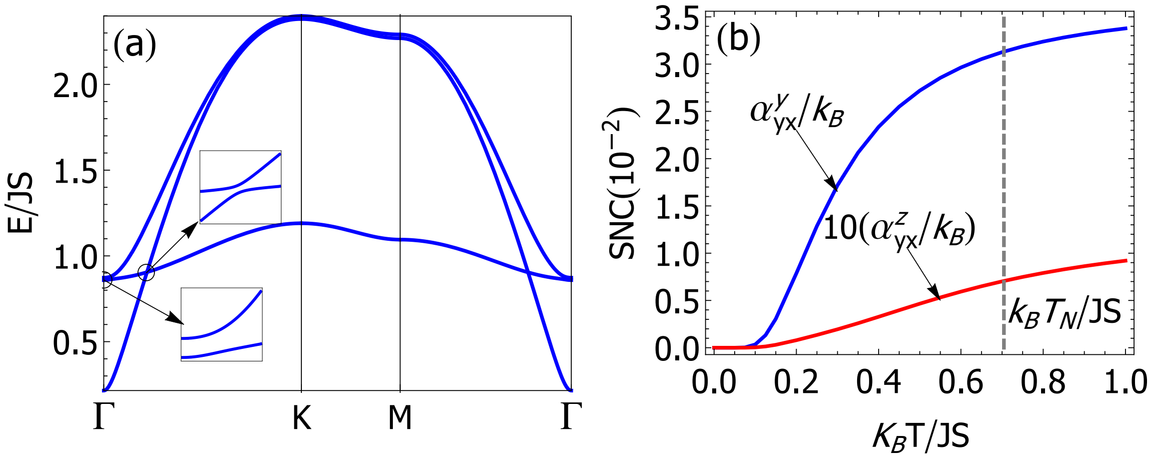

Figure 3.4: Plots for kagome antiferromagnet KFe$_3$(OH)$_6$(SO$_4$)$_2$. (a) Band structure. (b) Spin Nernst conductivity (SNC) α^y_{yx} and α^z_{yx}, where α^z_{yx} is scaled for visibility. Relevant parameters are $J_1 = 3.18\text{meV}$, $J_2 = 0.11\text{meV}$, $|D_p|/J_1 = 0.062$, $D_z/J_1 = -0.062$.

Cartesian coordinates of these two symmetry operations

$$R(g_1) = \begin{pmatrix} -1 & 0 & 0 \\ 0 & 1 & 0 \\ 0 & 0 & 1 \end{pmatrix}, \qquad R(g_2) = \begin{pmatrix} -\frac{1}{2} & -\frac{\sqrt{3}}{2} & 0 \\ \frac{\sqrt{3}}{2} & -\frac{1}{2} & 0 \\ 0 & 0 & 1 \end{pmatrix}. \tag{3.64}$$

By applying these symmetries to Eq. (3.63), the spin Nernst response tensor (only considering in-plane driven response) can be fixed to

$$[\hat{\alpha}^x, \hat{\alpha}^y, \hat{\alpha}^z] = \left[\begin{pmatrix} -\alpha_1 & 0 \\ 0 & \alpha_1 \end{pmatrix}, \begin{pmatrix} 0 & \alpha_1 \\ \alpha_1 & 0 \end{pmatrix}, \begin{pmatrix} 0 & -\alpha_2 \\ \alpha_2 & 0 \end{pmatrix} \right]. \tag{3.65}$$

Here, the $\mathcal{M}_x\mathcal{T}$ symmetry can be replaced by $\mathcal{C}_{2x}\mathcal{T}$, twofold rotation about the x axis and time-reversal, which will lead us to the same result. We note that our results are consistent with the spin Hall response tensors in Mn$_3$X (X= Rh, Ir or Pt) [115].

We apply our theory to a single layer of potassium iron jarosite, KFe$_3$(OH)$_6$(SO$_4$)$_2$, for which the material parameters are $J_1 = 3.18\text{meV}$, $J_2 = 0.11\text{meV}$, $|D_p|/J_1 = 0.062$, $D_z/J_1 = -0.062$ [40, 138]. We note, however, that the magnon dispersion in this material can also be explained by $J_2 = 0$, in which case the flat band is broadened by fluctuations [139]. The numerically obtained form of the spin Nernst conductivities agrees with Eq. (3.65). In Fig. 3.2, we plot the magnon bands and the spin Berry curvature for the y polarization of the spin. The spin Berry curvature is peaked at avoided crossings as shown in Fig. 3.3, which give the largest contribution to the spin Nernst effect. The integral of the ordinary Berry curvature gives the Chern numbers $-3, 1$, and 2, from the bottom to the top bands in Fig. 3.2. In Fig. 3.4, we show the spin Nernst response coefficients as a function of temperature for the y and z spin polarizations. The spin Nernst response sharply increases at temperatures sufficient to excite magnons in the Brillouin zone where the spin Berry curvature is large. The z direction polarized spin current is two orders of magnitude smaller than the current with in-plane spin polarization, which is due to the fact that the canting angle is fairly small, $\eta = 1.9^\circ$ [40]. By applying magnetic field, the canting angle and the spin Nernst response with the z polarization direction can be substantially increased. The predicted spin currents should be easily detectable in three dimensional structures as a temperature gradient of 20 K/mm should result in a spin current of the order of 10^{-11} J/m^2 according to Fig. 3.4, where $\alpha^{3D} = \alpha/c$, with c being the interlayer distance. Finally, we note that the spin Nernst effect reported in Ref. [117] differs from the intrinsic effect reported here as the former has the symmetry of the extrinsic effect.

3.6 Summary

In this chapter, we have developed a theory of magnon-mediated intrinsic spin currents in insulating noncollinear antiferromagnets and applied this theory to potassium iron jarosite $KFe_3(OH)_6(SO_4)_2$. Our results are applicable to two- and three-dimensional systems, promising to reveal fascinating physics in other layered quasi-2D antiferromagnets, e.g., silver iron jarosite $AgFe_3(OH)_6(SO4)_2$ [140], chromium jarosite $KCr_3(OH)_6(SO4)_2$ [141], vesignieite $BaCu_3V_2O_8(OH)_2$ [142], and 3D pyrochlore antiferromagnets $LiGaGr_4O_8$ and

$\mathrm{LiInGr_4O_8}$ [143, 144]. Besides exploring material candidates, one can also study the effect of magnetic order on the spin Nernst effect, e.g., in kagome antiferromagnets other possible spin chiralities exist [44, 122]. Recently proposed antiferromagnetic skyrmions with noncollinear magnetic order [145] can also be explored using our theory.

Chapter 4

Magnonic analogue of Edelstein effect in antiferromagnetic insulators

4.1 Introduction

Generation of nonequilibrium spin imbalance is increasingly important for current spintronics research [15], especially in the context of nonequilibrium torques [113]. In metallic and semiconductor materials, spin-orbit coupling (SOC) facilitates the interplay between the orbital and spin degrees of freedom, which allows feasible electric manipulation of spins, e.g., for technological applications. One consequence of such coupling is the inverse spin-galvanic effect [146–148] which attracted considerable interest in recent years [149–155, 155–160]. The nonequilibrium spin polarization contains an extrinsic part dependent on the transport relaxation time and an intrinsic part independent of the relaxation time [113], and it can lead to spin-orbit torques. Both field-like and damping-like spin-orbit torques can arise due to the nonequilibrium spin polarization at interfaces between magnetic and nonmagnetic materials [161–167].

In ferromagnetic and antiferromagnetic insulators, magnons – the quantum quasiparticles carrying energy and spin – can mediate various transport phenomena. The

Dzyaloshinskii-Moriya interaction (DMI) [168, 169] in such systems can lead to magnon spin-momentum locking [170], magnon-mediated magnetization torques [97, 171, 172], and magnonic thermal Hall [28–31, 40–44, 81, 128, 173] and spin Nernst effects [22, 38, 39, 72, 97, 108, 109, 117, 174–176]. Ref. [174] has speculated about the possibility of magnon-mediated spin polarization in insulating antiferromagnets lacking inversion symmetry.

In this chapter, we will use the theory developed in the last chapter to study the magnonic analogue of the Edelstein effect by considering antiferromagnetic insulators [177]. The spin nonconservation in such systems can be caused by noncollinear spin order or anisotropic exchange. The final result for the magnonic spin polarization is separated into the extrinsic and intrinsic contributions [177]. We apply our theory to several models and discuss relevant material candidates. In 1D, an antiferromagnetic spin chain with anisotropic nearest neighbor exchange and Rashba-like DMI serves as a toy model exhibiting both intrinsic and extrinsic contributions to the magnonic analogue of the Edelstein effect. In 2D and 3D, we concentrate on realistic noncollinear antiferromagnets on the kagome and breathing pyrochlore lattices. From the magnetic point group, we establish the response tensor shapes which agree with our numerical results.

4.2 Review of magnon Hamiltonian and linear response theory

We first briefly review the theory of magnonic systems introduced in the last chapter. To capture magnonic excitation at low temperature, we can perform Holstein-Primakoff transformation at the large-S limit, which leads us to a general Hamiltonian

$$H = \frac{1}{2}\int d\mathbf{r}\Psi^\dagger(\mathbf{r})\mathcal{H}\Psi(\mathbf{r}), \tag{4.1}$$

where $\Psi(\mathbf{r}) = (a_1(\mathbf{r}), \ldots, a_N(\mathbf{r}), a_1^\dagger(\mathbf{r}), \ldots, a_N^\dagger(\mathbf{r}))^T$, $\mathcal{H}$ is the real-space single-particle Hamiltonian describing noninteracting magnons, and $\mathbf{r}$ describes the coordinate of a magnetic unit cell containing N atoms. In momentum space, Hamiltonian (4.1) reads

$$H = \frac{1}{2}\sum_{\mathbf{k}} \Psi_{\mathbf{k}}^\dagger \mathcal{H}_{\mathbf{k}} \Psi_{\mathbf{k}}, \tag{4.2}$$

where $\Psi_{\mathbf{k}} = (a_{1,\mathbf{k}}, \ldots, a_{N,\mathbf{k}}, a_{1,-\mathbf{k}}^\dagger, \ldots, a_{N,-\mathbf{k}}^\dagger)^T$. Here, $\mathcal{H}_{\mathbf{k}}$ can be diagonalized by a paraunitary matrix $T_{\mathbf{k}}$

$$T_{\mathbf{k}}^\dagger \mathcal{H}_{\mathbf{k}} T_{\mathbf{k}} = \mathcal{E}_{\mathbf{k}}, \tag{4.3}$$

where $T_{\mathbf{k}}$ satisfies paraunitary relation

$$T_{\mathbf{k}}^\dagger \sigma_3 T_{\mathbf{k}} = T_{\mathbf{k}} \sigma_3 T_{\mathbf{k}}^\dagger = \sigma_3. \tag{4.4}$$

The diagonalization can be re-expressed in terms of the eigenequation of pseudoHamiltonian $\sigma_3\mathcal{H}_{\mathbf{k}}$ [130]

$$\sigma_3\mathcal{H}_{\mathbf{k}}|u_{n,\mathbf{k}}^R\rangle = \bar{\varepsilon}_{n,\mathbf{k}}|u_{n,\mathbf{k}}^R\rangle, \tag{4.5}$$

$$\langle u_{n,\mathbf{k}}^L|\sigma_3\mathcal{H}_{\mathbf{k}} = \langle u_{n,\mathbf{k}}^L|\bar{\varepsilon}_{n,\mathbf{k}}, \tag{4.6}$$

where $\bar{\varepsilon}_{n,\mathbf{k}} = (\sigma_3\mathcal{E}_{\mathbf{k}})_{nn}$, $\langle u_{n,\mathbf{k}}^L|_l = (T_{\mathbf{k}}^\dagger\sigma_3)_{nl}$ ($|u_{n,\mathbf{k}}^R\rangle_l = (T_{\mathbf{k}})_{ln}$), and the paraunitarity is then expressed as $\langle u_{m,\mathbf{k}}^L|u_{n,\mathbf{k}}^R\rangle = (\sigma_3)_{mn}$. From here on, we will only refer to the right eigenstates as $|u_{n,\mathbf{k}}^R\rangle = |u_{n,\mathbf{k}}\rangle$, and their left partners can be always be obtained from $\langle u_{n,\mathbf{k}}^L| = \langle u_{n,\mathbf{k}}|\sigma_3$. Finally, note that the magnon basis possesses particle-hole symmetry (PHS) $\Psi_{\mathbf{k}}^\dagger = (\sigma_1\Psi_{-\mathbf{k}})^T$ so that the Hamiltonian obeys $\sigma_1 H_{\mathbf{k}}\sigma_1 = H_{-\mathbf{k}}^*$, which leads to $\bar{\varepsilon}_{n+N,\mathbf{k}} = -\bar{\varepsilon}_{n,-\mathbf{k}}$ and $|u_{n,\mathbf{k}}\rangle = e^{i\phi_n}\sigma_1|u_{n+N,-\mathbf{k}}\rangle^*$, where ϕ_n is a redundant phase factor.

Since we are interested in a nonequilibrium spin density response to an external force, we must denote the spin density operator in terms of the aforementioned magnonic variables. We introduce the $\mu = x, y, z$ component of the magnonic spin density operator as

$$\Sigma_\mu = \frac{1}{V}\sum_{\mathbf{k}} \Psi_{\mathbf{k}}^\dagger \hat{\Sigma}_\mu \Psi_{\mathbf{k}}, \tag{4.7}$$

where

$$\hat{\Sigma}_\mu = -\frac{1}{2}\text{Diag}\left(z_1^\mu, \ldots, z_N^\mu, z_1^\mu, \ldots, z_N^\mu\right), \tag{4.8}$$

and the unit vectors z_i^μ corresponding to directions of magnetic moments have been introduced in Eq. (3.3). We note that PHS implies $\langle u_{n,\mathbf{k}}|\hat{\Sigma}_\mu|u_{n,\mathbf{k}}\rangle = \langle u_{n+N,-\mathbf{k}}|\hat{\Sigma}_\mu|u_{n+N,-\mathbf{k}}\rangle$.

The linear response of the nonequilibrium spin density with respect to a temperature gradient $\nabla_\nu T$ can be expressed as,

$$\langle \Sigma_\mu \rangle = \chi_{\mu\nu}\nabla_\nu T = \left(\chi_{\mu\nu}^{\text{ex}} + \chi_{\mu\nu}^{\text{in}}\right)\nabla_\nu T, \tag{4.9}$$

where we separated the response tensor $\chi_{\mu\nu}$ into extrinsic, $\chi_{\mu\nu}^{\text{ex}}$, and intrinsic, $\chi_{\mu\nu}^{\text{in}}$, parts. According to the Kubo formula calculation in Appendix A and the method we developed in the last chapter, the response coefficient reads

$$\chi_{\mu\nu}^{\text{ex}} = \frac{1}{VT}\sum_{\mathbf{k},n=1}^{N} \frac{1}{\Gamma_n}(\Sigma_{\mu,\mathbf{k}})_{nn} v_{n\mathbf{k},\nu}\varepsilon_{n,\mathbf{k}}\left[-\frac{\partial n_{\text{B}}(\varepsilon_{n,\mathbf{k}})}{\partial \varepsilon}\right]. \tag{4.10}$$

$$\chi_{\mu\nu}^{\text{in}} = \frac{2k_B}{V}\sum_{n=1}^{N}\sum_{\mathbf{k}}(\Omega_{n,\mathbf{k}}^{\Sigma})_{\mu\nu} c_1[n_{\text{B}}(\varepsilon_{n,\mathbf{k}})], \tag{4.11}$$

with

$$(\Omega^{\Sigma}_{n,\mathbf{k}})_{\mu\nu} = \sum_{m(\neq n)} \frac{2\mathrm{Im}[(\sigma_3 \Sigma_{\mu,\mathbf{k}})_{nm}(\sigma_3 \tilde{v}_{\nu,\mathbf{k}})_{mn}]}{(\bar{\varepsilon}_{n,\mathbf{k}} - \bar{\varepsilon}_{m,\mathbf{k}})^2}. \tag{4.12}$$

Here, we used the notation $c_1(x) = (1+x)\ln(1+x) - x\ln(x)$. The extrinsic part can also be obtained from the Boltzmann transport theory with the relaxation time $\tau_n = 1/(2\Gamma_n)$. In following the approach introduced in the last chapter to calculate the intrinsic response coefficient, we explicitly introduce a perturbation corresponding to an external magnetic field $\mathbf{B}(\mathbf{r})$ into Hamiltonian H [132–134]:

$$\hat{\mathcal{H}}_B = -[\mathbf{B}(\mathbf{r}) \cdot \hat{\mathbf{\Sigma}} + \hat{\mathbf{\Sigma}} \cdot \mathbf{B}(\mathbf{r})], \tag{4.13}$$

where $\mathbf{B}(\mathbf{r})$ varies slowly in space, i.e., on a length scale much larger than the lattice constant. Apart from this, the intrinsic response fully agrees with Eq. (3.51) in the last chapter by replacing the operator $\hat{\theta}$ by $\hat{\mathbf{\Sigma}}$.

Equations (4.10) and (4.11) are the main formulas that will be used in this chapter. In Sec. 4.4, we use these formulas to make numerical predictions of the nonequilibrium spin density for several relevant models, including material candidates.

Before proceeding to subsequent discussions, some useful remarks about the response theory developed above are due. The validity of the magnon representation is well established at low temperatures. Higher-order magnon-magnon interaction corrections to the theory start with $\mathcal{O}(1/S)$ terms. These corrections include both effects from thermally activated processes and spontaneous decay [99, 121]. The former are frozen in the low-temperature regime. The latter contribute to spectrum broadening and renormalization, both of which are further suppressed by the weak magnon-magnon coupling factor and the restriction of energy and momentum conservation. The magnon-phonon scattering effects lead to the phenomenological broadening factor Γ_n in our theory [178]. Higher order corrections, such as vertex corrections, could in principle be important in some cases but their consideration goes beyond the scope of this thesis. In a special case, when the magnon-phonon coupling is strong enough, it may become necessary to explore the magnon-phonon hybrid system [179, 180], where our theory still applies by treating quasi-particles as a mixture of magnon and phonon.

4.3 Symmetry constraints

In this section, we discuss constraints on the magnon response tensor, $\chi_{\mu\nu}$, posed by the symmetries. To generate the nonequilibrium spin density with magnons one needs a system in which spin is not conserved locally or globally, at least for one direction of the spin polarization. This is often the case in non-collinear antiferromagnets or in systems with Dzyaloshinskii-Moriya interactions. For example, for inversion symmetric systems spin density is *globally* conserved [174]. To see this, note that inversion symmetry implies $\mathcal{H}_{\mathbf{k}} = \mathcal{H}_{-\mathbf{k}}$, which leads to $T_{\mathbf{k}} = T_{-\mathbf{k}}$, $\mathcal{E}_{\mathbf{k}} = \mathcal{E}_{-\mathbf{k}}$ and $\mathbf{v}_{n,\mathbf{k}} = -\mathbf{v}_{n,-\mathbf{k}}$. Substituting these relations into Eq. (4.10) results in $\chi^{\text{ex}}_{\mu\nu} = -\chi^{\text{ex}}_{\mu\nu} = 0$. Furthermore, inversion symmetry also enforces the relation $(\Omega^{\Sigma}_{n,\mathbf{k}})_{\mu\nu} = -(\Omega^{\Sigma}_{n,-\mathbf{k}})_{\mu\nu}$, which results in $\chi^{\text{in}}_{\mu\nu} = -\chi^{\text{in}}_{\mu\nu} = 0$, that is, in a vanishing intrinsic response. Below, in Sec. 4.4, we show several examples of collinear and non-collinear systems in which spin can be generated.

In general, the response tensor will be constrained by the symmetry operations of a specific material under consideration. The constraining relations can be readily found within the framework of linear response theory [137, 181]. Assuming that a system respects a symmetry operation represented by g, we find for an arbitrary operator $\hat{A}$ that $\langle g(\psi_{n\mathbf{k}})|\hat{A}|g(\psi_{m\mathbf{k}})\rangle = \langle \psi_{ng(\mathbf{k})}|g^{-1}\hat{A}g|\psi_{mg(\mathbf{k})}\rangle$ when the operation is unitary, and $\langle g(\psi_{n\mathbf{k}})|\hat{A}|g(\psi_{m\mathbf{k}})\rangle = \langle \psi_{ng(\mathbf{k})}|g^{-1}\hat{A}g|\psi_{mg(\mathbf{k})}\rangle^*$ when the operation is antiunitary. Operators transform as $g^{-1}\hat{v}_i g = \sum_j R^v_{ij}\hat{v}_j$ and $g^{-1}\hat{\Sigma}_i g = \sum_j R^s_{ij}\hat{\Sigma}_j$, where $R^{v/s}$ is the corresponding matrix representation of g with respect to the Cartesian components $\hat{v}_j$ or $\hat{\Sigma}_j$. We find $R^v = \pm R$ and $R^s = \pm\det(R)R$ where $\pm$ refers to unitary $(+)$ or antiunitary

$(-)$ symmetries, respectively. Under the above premises, the following symmetry requirements on elements of the response tensor arise:

$$\begin{aligned} \chi^{\mathrm{ex}}_{\mu\nu} &= \det(R) R_{\mu i} R_{\nu j} \chi^{\mathrm{ex}}_{ij} \\ \chi^{\mathrm{in}}_{\mu\nu} &= \pm \det(R) R_{\mu i} R_{\nu j} \chi^{\mathrm{in}}_{ij}, \end{aligned} \tag{4.14}$$

where $\pm$ corresponds to unitary and antiunitary symmetry operations, respectively. Later on, we show that these two relations result in different shapes of the response tensors, which is useful for distinguishing extrinsic and intrinsic contributions. Notice that tensors $\chi^{\mathrm{ex}}_{\mu\nu}$ and $\chi^{\mathrm{in}}_{\mu\nu}$ transform differently under antiunitary operations, which is a consequence of a complex factor in the expression for $(\Omega^{\Sigma}_{n,\mathbf{k}})_{\mu\nu}$ corresponding to taking the imaginary part in Eq. (4.12). Given the transformation properties of velocity and spin, one finds that $\chi^{\mathrm{ex}}_{\mu\nu}$ is even and $\chi^{\mathrm{in}}_{\mu\nu}$ is odd under the time-reversal transformation. Consequently, a reversal of the magnetic ordering causes $\chi^{\mathrm{in}}_{\mu\nu}$ to flip sign while $\chi^{\mathrm{ex}}_{\mu\nu}$ is invariant under such transformation:

$$\chi^{\mathrm{in}}_{\mu\nu}[\{\mathbf{S}_i\}] = -\chi^{\mathrm{in}}_{\mu\nu}[\{-\mathbf{S}_i\}], \tag{4.15a}$$

$$\chi^{\mathrm{ex}}_{\mu\nu}[\{\mathbf{S}_i\}] = \chi^{\mathrm{ex}}_{\mu\nu}[\{-\mathbf{S}_i\}]. \tag{4.15b}$$

Thus, it is possible to disentangle extrinsic from intrinsic contributions by measuring the nonequilibrium spin density for two antiferromagnetically ordered states related by the time reversal transformation. Such an approach has been used in studies of the spin Hall effect [182].

A short note on the similarity to the electronic Edelstein effect is in order. In principle, the latter also consists of a time-reversal even extrinsic and time-reversal odd intrinsic contribution [183–185]. However, since the Edelstein effect is, for historical reasons, mainly studied in nonmagnetic materials, the extrinsic contribution has been analyzed in more detail. On the other hand, since the very notion of a magnon is tied to magnetism, both contributions are, in general, expected to be of equal importance.

4.4 Models

In this section, we apply our theory to specific models. To obtain some intuition, we first focus on a toy model of a collinear antiferromagnetic spin chain with anisotropic exchange and inversion asymmetry resulting in Rashba-type DMI. We then focus on more realistic noncollinear kagome and breathing pyrochlore antiferromagnets, for which we use material parameters established in the literature. To satisfy the requirement of inversion asymmetry, we assume that the kagome antiferromagnet can have interfacial inversion asymmetry, e.g., due to thin film geometry in contact with another material. The breathing pyrochlore antiferromagnet has bulk inversion asymmetry. The details of the Holstein-Primakoff transformations and explicit expressions of the magnon Hamiltonians are discussed in Appendix B.

4.4.1 Antiferromagnetic spin chain

As a simple model, we first consider the antiferromagnetic spin chain shown in Fig. 4.1(a). Similar to Eq. (3.2), the Hamiltonian

$$\begin{aligned} H = \quad & \sum_i \sum_{\nu=\pm 1} [J(\gamma S^x_{1,i} S^x_{2,i+\nu} + S^y_{1,i} S^y_{2,i+\nu} + \lambda S^z_{1,i} S^z_{2,i+\nu}) \\ & + D^\nu_{12} \mathbf{e}_z \cdot (\mathbf{S}_{1,i} \times \mathbf{S}_{2,i+\nu})], \end{aligned} \tag{4.16}$$

contains the anisotropic symmetric exchange interaction, which is given in terms of an energy J and dimensionless factors γ and λ, and the antisymmetric exchange interaction described by DMI vectors along the z direction. We choose $\gamma \leq 1$ and $\lambda \geq 1$, such that the collinear state with Néel vector along the z direction is the classical magnetic ground state. For $\gamma \neq 1$, the anisotropy causes the magnons to experience the effect of "squeezing"

[186]. Note that λ has to be larger than a critical value to prevent the spins from canting due to DMI. The DMI strength is set to $D_{12}^{+} = D_1$ and $D_{12}^{-} = D_2$, where $\nu = \pm$ refers to the direction of the bond [$+$ for going from the left to the right in Fig. 4.1(a)].

It is convenient to reparameterize the DMI as $D_0 = (D_1 + D_2)/2J$ and $\delta_D = (D_1 - D_2)/2J$. The staggered contribution to DMI is necessary for the model to exhibit both intrinsic as well as extrinsic effects. To see this, observe that only in the absence of the inversion symmetry can we have $D_0 \neq 0$. However, when $\delta_D = 0$, the system still holds a $\mathcal{T} * \mathcal{M}_x$ symmetry, where $\mathcal{T}$ is time reversal and $\mathcal{M}_x$ is the mirror symmetry with respect to the $y - z$ plane passing through the atoms. Applying the corresponding Cartesian representation matrix $R = \mathrm{Diag}\{-1, 1, 1\}$ of $\mathcal{T} * \mathcal{M}_x$ to Eq. (4.14), the intrinsic part χ_{zx}^{in} is rendered zero. Therefore, we set $\delta_D \neq 0$ to ensure the appearance of intrinsic contributions.

In Fig. 4.1(b), we show the magnon band structure. The degeneracy of spin-up and -down modes is lifted by the DMI and $\gamma \neq 1$. On top of that, since $\gamma \neq 1$, spin is not conserved and we observe the magnon spin-momentum locking [170] as shown in Fig. 4.1(c), which is in agreement with Ref. [186]. This is in contrast to the usual case of uniaxial collinear AFMs that features two eigenmodes with opposite spin quanta $\pm\hbar$. Figs. 4.1(d) and (e) show the extrinsic and intrinsic response coefficient, respectively. For the calculation of the extrinsic response, we regarded the broadening as a constant, $\Gamma_n = \hbar/2\tau$, where τ is the magnon lifetime [187]. In Figs. 4.1(d) and (e), the extrinsic spin accumulation dominates.

To obtain an intuitive understanding of the extrinsic contributions, we recall the usual electronic Edelstein effect scenario in a Rashba system. Upon shifting the spin-momentum locked Fermi circles in reciprocal space due to application of an electric field, electronic states with a particular spin polarization are more occupied than those with opposite spin polarization (e.g., see Fig. 13 of Ref. [188]). Consequently, this redistribution leads to a nonzero macroscopic spin density in nonequilibrium. A similar explanation can

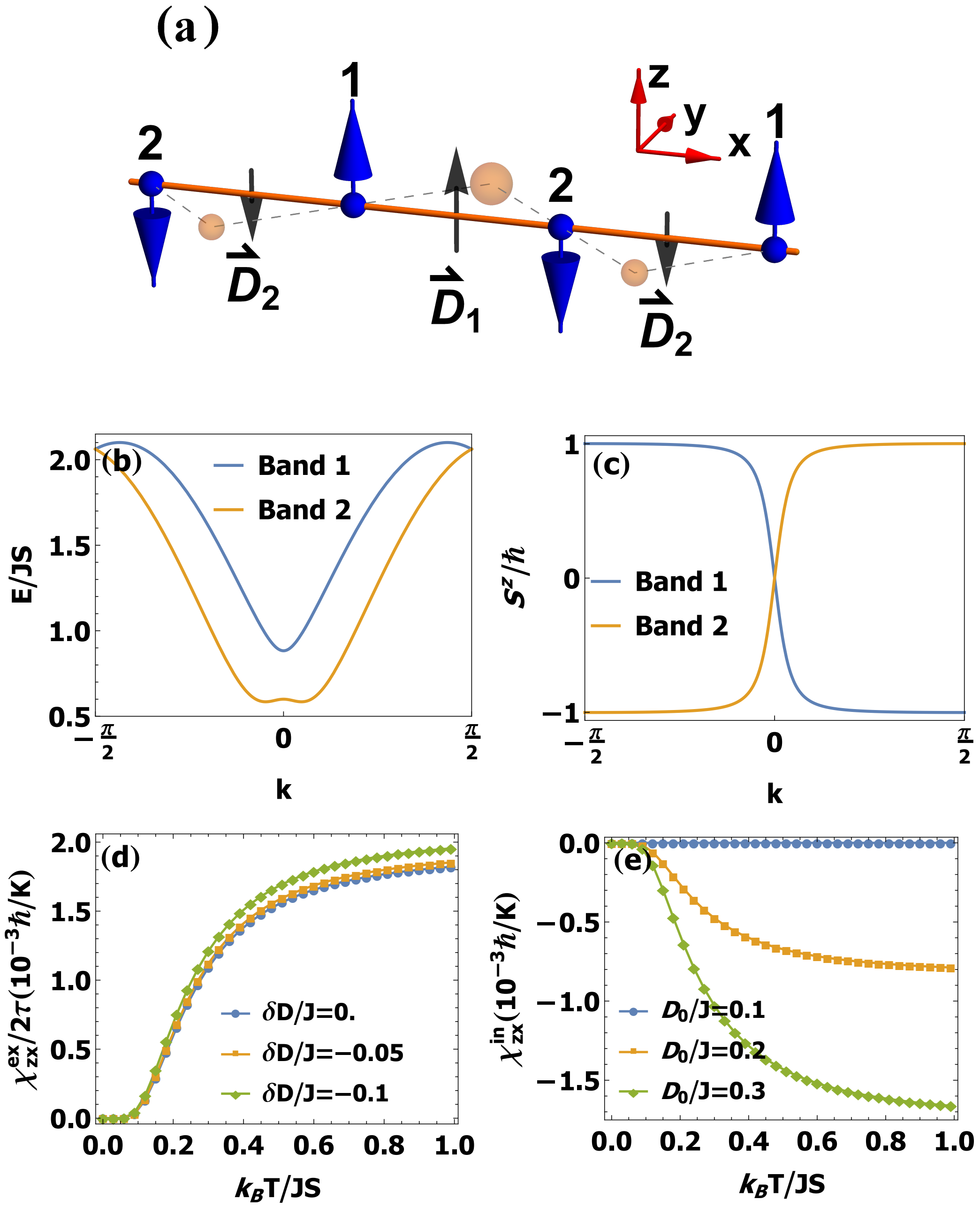

Figure 4.1: (a) Spin order and DMI vectors in the antiferromagnet spin chain model. (b) and (c) Magnon dispersion and magnon spin expectation value in the 1D Brillouin zone. We used $D_0/J = 0.2$, $\delta D/J = -0.1$. (d) and (e) Extrinsic and intrinsic response coefficients. In (d), $\tau = JS/(2\Gamma_n)$ is the dimensionless magnon lifetime ($\hbar$ is set to one). Parameters read $\lambda = 1.05$, $\gamma = 0.95$, $J = 2$meV, $S = 3/2$, and $D_0/J = 0.2$.

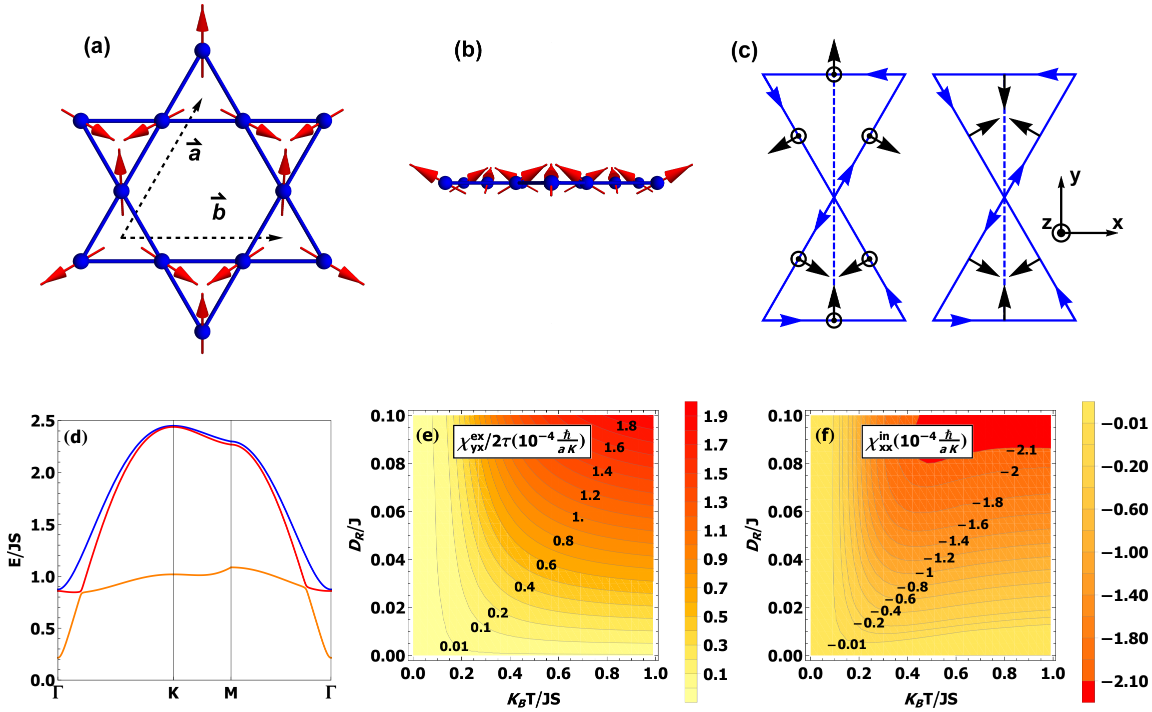

Figure 4.2: Noncollinear antiferromagnetic PVC order on the kagome lattice. (a) and (b) Ground state spin configuration from above and front view. Lattice vectors are denoted by $\vec{a}$ and $\vec{b}$. (c) Left: intrinsic DMI vectors; right: Rashba DMI vectors. Arrows along the bonds indicate ordering of sites in DMI terms. (d) Magnon dispersion with $D_R/J = 0.06$. (e), (f) Extrinsic and intrinsic response tensor elements χ^{ex}_{yx} and χ^{in}_{xx}, respectively. τ is the dimensionless magnon lifetime and a denotes the lattice constant. We used the material parameters of $\text{KFe}_3(\text{OH})_6(\text{SO}_4)_2$: $J_1 = 3.18\text{meV}$, $J_2 = 0.11\text{meV}$, $|D_p|/J_1 = 0.062$, $D_z/J_1 = -0.062$ and $S = 5/2$.

by given for the magnonic case. First, we consider the band 2 [cf. Fig. 4.1(b)]. According to Fig. 4.1(c), magnons in band 2 have a positive (negative) spin for negative (positive) momentum k, which corresponds to magnon spin-momentum locking discussed in Ref. [170]. Upon application of the temperature gradient (or the pseudo-gravitational potential) we redistribute magnons from k to $-k$ (or *vice versa*, depending on the direction of the gradient), causing an excess of magnons with positive spin. Although there is some cancellation between the lower and upper band, the different thermal occupation ensures that there is a nonzero resulting net spin density in nonequilibrium. There is no such simple picture for the intrinsic contributions, which arise due to interband mixing [113].

4.4.2 Kagome antiferromagnet

In several real materials, spin nonconservation naturally emerges due to noncollinear antiferromagnetism. For example, noncollinear antiferromagnets (NAFMs) exist in layered quasi-two-dimensional kagome and triangular magnetic structures, and in three-dimensional pyrochlore magnetic structures. We first take the kagome antiferromagnet in the so-called $\mathbf{q} = 0$ phase with positive vector chirality (PVC) [120–122], which is depicted in Fig. 4.2(a), as an example.

The spin Hamiltonian under consideration is

$$H = \sum_{\langle ij \rangle} J_1 \mathbf{S}_i \cdot \mathbf{S}_j + \mathbf{D}_{ij} \cdot (\mathbf{S}_i \times \mathbf{S}_j) + \sum_{\langle\langle ij \rangle\rangle} J_2 \mathbf{S}_i \cdot \mathbf{S}_j, \tag{4.17}$$

where the three terms describe the nearest-neighbor exchange with $J_1 > 0$, DMI, and the second-nearest neighbor exchange with $J_2 > 0$. The DMI vector $\mathbf{D}_{ij}$ is composed of intrinsic DMI and extrinsic Rashba-DMI, i.e., $\mathbf{D}_{ij} = \mathbf{D}_{\text{in}} + \mathbf{D}_R$. The intrinsic DMI $\mathbf{D}_{\text{in}} = \mathbf{D}_p + D_{z,ij}\hat{z}$ has out-of-plane contributions $D_{z,ij}$ as well as in-plane contributions $\mathbf{D}_p = D_p \hat{n}_{ij}$ along $\hat{n}_{ij}$. The DMI vectors are arranged as shown in the left part of Fig. 4.2(c). Accounting for the antiferromagnetic exchange interactions and only for the intrinsic DMI, the classical ground state is the 120°-ordered antiferromagnetic state [cf. Fig. 4.2(a)] with a small out-of-plane canting, with an angle given by $\eta = \frac{1}{2}\tan^{-1}(\frac{-2D_p}{\sqrt{3(J_1+J_2)}-D_z})$ [cf. Fig. 4.2(b)]. Thus, there is a weak ferromagnetic moment in the z direction and the texture is not fully compensated. Here, we are concentrating on nonequilibrium spin densities in the x and y direction, along which the texture is compensated.

Although nonzero $\mathbf{D}_p$ breaks the mirror symmetry of the kagome lattice, the system is still inversion symmetric. Thus, we need the Rashba-like DMI described by $\mathbf{D}_R$ that we envision to arise in an inversion-symmetry breaking environment, as caused, e.g., by putting a single kagome layer on a substrate. The vector $\mathbf{D}_R$ lies in the kagome plane and has direc-

Table 4.1: The shape of spin polarization response tensors enforced by magnetic point group symmetry for selected noncollinear antiferromagnets.

Structure	Extrinsic	Intrinsic
Kagome(PVC,SVC)	$\begin{pmatrix} 0 & -\chi_{yx}^{\mathrm{ex}} \\ \chi_{yx}^{\mathrm{ex}} & 0 \end{pmatrix}$	$\begin{pmatrix} \chi_{xx}^{\mathrm{in}} & 0 \\ 0 & \chi_{xx}^{\mathrm{in}} \end{pmatrix}$
Kagome(NVC)	$\begin{pmatrix} 0 & \chi_{xy}^{\mathrm{ex}} \\ \chi_{yx}^{\mathrm{ex}} & 0 \end{pmatrix}$	$\begin{pmatrix} \chi_{xx}^{\mathrm{in}} & 0 \\ 0 & \chi_{yy}^{\mathrm{in}} \end{pmatrix}$
Triangle	$\begin{pmatrix} 0 & -\chi_{yx}^{\mathrm{ex}} \\ \chi_{yx}^{\mathrm{ex}} & 0 \end{pmatrix}$	$\begin{pmatrix} \chi_{xx}^{\mathrm{in}} & 0 \\ 0 & \chi_{xx}^{\mathrm{in}} \end{pmatrix}$
Pyrochlore (AIAO)	$\begin{pmatrix} 0 & 0 & 0 \\ 0 & 0 & 0 \\ 0 & 0 & 0 \end{pmatrix}$	$\begin{pmatrix} \chi_{xx}^{\mathrm{in}} & 0 & 0 \\ 0 & \chi_{xx}^{\mathrm{in}} & 0 \\ 0 & 0 & \chi_{xx}^{in} \end{pmatrix}$

tions similar to $\mathbf{D}_p$, but with the crucial difference that its directions are always pointing in the same direction relative to the bond [compare the left and right part of Fig. 4.2(c)]. We also note that a large Rashba-DMI can twist the system into a spiral state. We confirmed numerically that this does not happen for $|\mathbf{D}_R|/J < 0.06$ using computational package SpinW [189].

The kagome NAFM described above exhibits two symmetries: (i) the mirror reflection with respect to the $y-z$ plane plus time-reversal, $g_1 = \mathcal{M}_x\mathcal{T}$, and (ii) the threefold rotation about the z axis, $g_2 = \mathcal{C}_{3z}$. According to Eq. (4.14), these two symmetries fix the extrinsic and intrinsic response tensors to the forms in Table 4.1 (Kagome PVC), where only the in-plane spin polarizations are allowed.

Based on what we have discussed so far, we propose potassium iron jarosite $\mathrm{KFe_3(OH)_6(SO_4)_2}$ as a candidate material. Concentrating on a single kagome layer of this material and assuming that the mirror symmetry is broken due to a proper environment, the magnon dispersion is given in Fig. 4.2(d). We used parameters $J_1 = 3.18\mathrm{meV}$, $J_2 = 0.11\mathrm{meV}$, $|D_p|/J_1 = 0.062$, $D_z/J_1 = -0.062$ and $S = 5/2$ [40, 138]. The spin density response is captured by virtue of Eqs. (4.10) and (4.11). The results for the extrinsic, χ_{yx}^{ex}, and intrinsic, χ_{xx}^{in}, contributions are shown in Figs. 4.2 (e) and (f), respectively. The effect becomes stronger as we increase Rashba-DMI. The contributions χ^{ex}_{xx} and χ^{in}_{yx} are zero, in agreement with tensor shapes in Table 4.1.

Approximating the magnon band broadening $\Gamma_n \sim \hbar/2\tau$ as a constant, with a magnon lifetime $\tau \sim 10^{-10}\,\text{s}$, and using a lattice constant $a = 10^{-9}\,\text{m}$, a Rashba-DMI $D_R = 0.06J$, a temperature gradient $\partial_x T = 10\,\text{K/mm}$ [190], and a temperature $T = 0.5JS$ [which corresponds to a temperature $\approx 46\,\text{K}$ for $\text{KFe}_3(\text{OH})_6(\text{SO}_4)_2$] we obtain the extrinsic part of the temperature-gradient-induced spin density $\langle S^y \rangle_{\text{ex}} \simeq 5 \times 10^6\,\hbar/\text{cm}^2$; and the intrinsic part $\langle S^x \rangle_{\text{in}} \simeq 2 \times 10^5\,\hbar/\text{cm}^2$. With larger temperature gradients, the extrinsic contribution can be made comparable to spin densities generated by the electronic Edelstein effect [157], which are of the order of $10^8 \sim 10^{10}\,\hbar/\text{cm}^2$.

4.4.3 Breathing pyrochlore antiferromagnets

The 3D pyrochlore lattices, which consist of corner-sharing tetrahedra, are well-known for exhibiting noncollinear spin structures. Here, to break bulk inversion symmetry, we concentrate on the so-called "breathing" pyrochlore antiferromagnets that possess different exchange interaction in up-pointing (u) and down-pointing (d) tetrahedra [see Fig. 4.3(a)]. The minimal Heisenberg model is [21]

$$H = J \sum_{\langle i,j \rangle \in u} \mathbf{S}_i \cdot \mathbf{S}_j + J' \sum_{\langle i,j \rangle \in d} \mathbf{S}_i \cdot \mathbf{S}_j + D \sum_i (\mathbf{S}_i \cdot \hat{\mathbf{z}}_i)^2 \tag{4.18}$$

The first two terms describe the antiferromagnetic exchange interactions in up-pointing and down-pointing tetrahedra, respectively. The last term comprises easy-axis anisotropy ($D < 0$), with $\hat{\mathbf{z}}_i$ being a unit vector pointing either towards or away from the tetrahedron's center of gravity. This model can be energetically optimized to different spin configurations depending on the values of J'/J, and D/J [21, 191], but here we only concentrate on the all-in–all-out (AIAO) order depicted in Fig. 4.3(b), in which all spins of a single

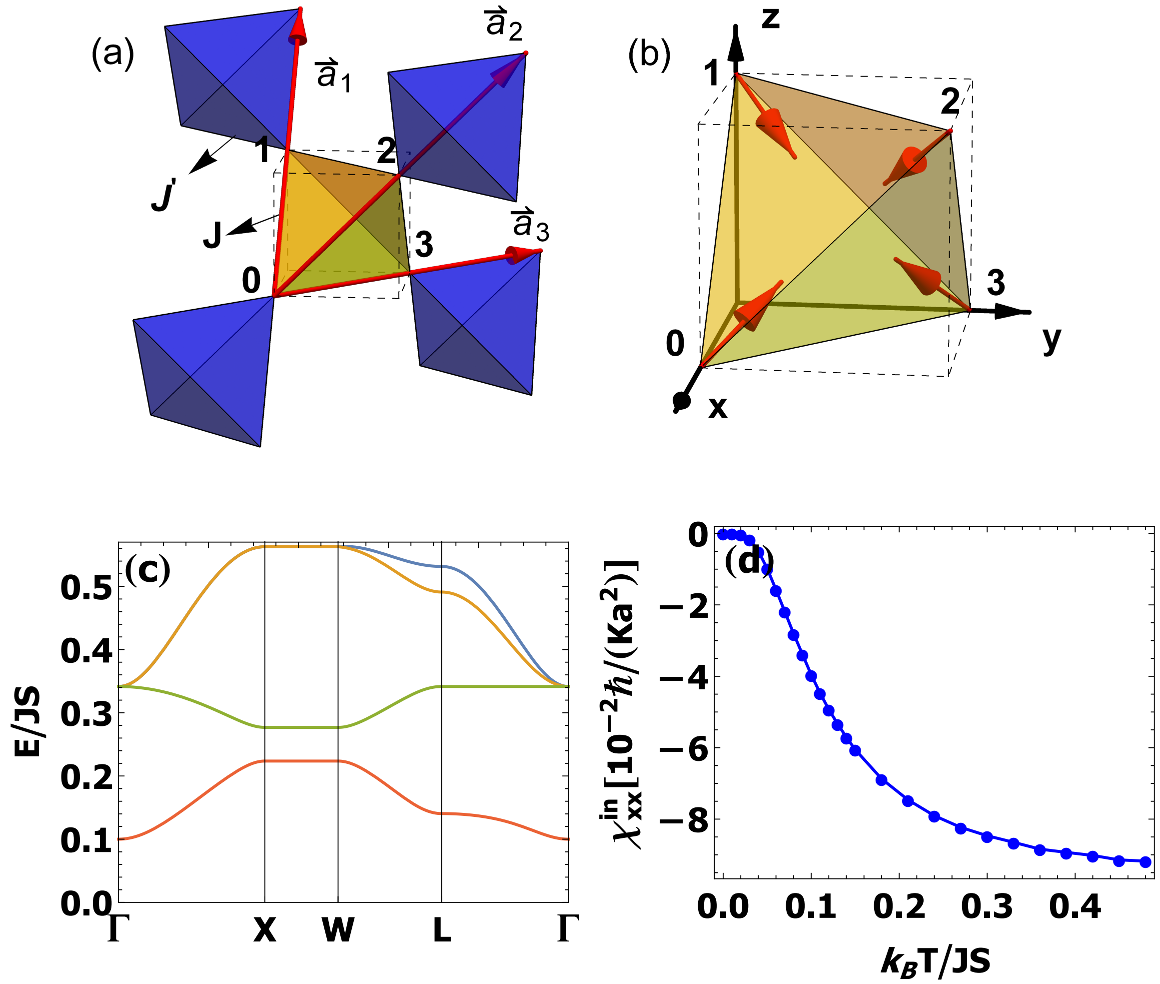

Figure 4.3: (a) Breathing pyrochlore lattice with indicated lattice vectors $\vec{a}_i$ ($i = 1, 2, 3$) and nearest-neighbor exchange in up-pointing (blue, J') and down-pointing (yellow, J) tetrahedra. (b) Spin order in the all-in-all-out configuration. (c) Magnon band structure. (d) The intrinsic response χ^{in}_{xx}, with a denoting the lattice constant. Parameters read $J \approx 50K$ (4.3 meV), $J'/J = 0.6$, $D/J = -0.2$, $S = 3/2$ to mimic the material LiGaCr$_4$O$_8$.

tetrahedron are either pointing inward [yellow tetrahedron in Fig. 4.3(b)] or outward (blue tetrahedra).

The AIAO order respects the magnetic point group $\bar{T}_d = \text{Span}\{C_3, C_2, \mathcal{T} * \sigma_d, \mathcal{T} * S_4\}$ [51, 63]. Here, we give the representative generators of these symmetries: C_3 is the three-fold rotation with respect to $[1, 1, 1]$ axis; C_2 is two-fold rotation about $[1, 0, 0]$ axis; $\mathcal{T} * \sigma_d$ is time-reversal followed by the reflection about $(\bar{1}, 1, 0)$ plane; and $\mathcal{T} * S_4$ is time-reversal followed by the combination of the four-fold rotation about $[1, 0, 0]$ and the reflection about $(1, 0, 0)$. We find that this symmetry constraint eliminates any extrinsic response and enforces the intrinsic response tensor to be proportional to a unit matrix, see Table 4.1. In Fig. 4.3 (c), we plot the dispersion of the four magnon bands for the AIAO phase with $J \approx 50K$ (4.3 meV) and $J'/J = 0.6$, which is the breathing ratio of LiGaCr$_4$O$_8$ [192]. We used $D/J = -0.2$ to stabilize the AIAO order. In Fig. 4.3 (d), we show the intrinsic response $\chi^{\text{in}}_{xx} = \chi^{\text{in}}_{yy} = \chi^{\text{in}}_{zz}$, which are the only nonzero tensor elements, in agreement with the symmetry analysis. If we assume $\partial_x T = 10\,\mathrm{K/mm}$, $T = 0.12JS$, and $a \sim 10^{-9}\,\mathrm{m}$, the intrinsic spin accumulation is estimated to be $\langle S^x \rangle_{\text{in}} \simeq 5 \times 10^{14}\,\hbar/\mathrm{cm}^3$. We can compare this result with the electronic Edelstein effect by converting its 2D spin density to a bulk density: $\langle S \rangle^{\text{2D}}_{\text{electron}}/a \sim 10^{15} - 10^{17}\,\hbar/\mathrm{cm}^3$. Thus, the intrinsic contribution in breathing pyrochlores is comparable with the electronic Edelstein effect. We believe that this result is detectable in experiment either by transport measurements similar to those used for detection of the inverse spin Hall effect, by magneto-optical Kerr microscopy, or by magnetic sensing based on the nitrogen-vacancy (NV) centers [193].

4.5 Computer experiments

To better understand the nonequilibrium spin density brought about by the magnonic counterpart to the Edelstein effect, we use atomistic spin dynamics simulations. We describe spin dynamics using the stochastic Landau-Lifshitz-Gilbert (sLLG) equation

$$\dot{\mathbf{S}}_i = -\frac{\gamma}{\mu\,(1+\alpha^2)} \left[\mathbf{S}_i \times \mathbf{B}_i + \alpha \mathbf{S}_i \times (\mathbf{S}_i \times \mathbf{B}_i)\right], \tag{4.19}$$

comprising the damped precession of $\mathbf{S}_i$ about its local field $\mathbf{B}_i = \mathbf{b}_i - \partial H/\partial \mathbf{S}_i$. The stochastic field $\mathbf{b}_i(t) = \sqrt{2\alpha k_{\text{B}} T \mu/(\gamma \Delta t)}\,\mathbf{G}(t)$ simulates thermal noise [194, 195]. $\mathbf{G}(t)$ is a three-dimensional Gaussian random number distribution with zero mean. α, γ, and $\mu = 2\mu_{\text{B}}\sqrt{S(S+1)}$ are the dimensionless Gilbert damping, the gyromagnetic ratio, and the modulus of the magnetic moment at each lattice site, respectively. The numerical integration of Eq. (4.19) is done by the Heun method [195] with time steps $\Delta t \leq 1\,\mathrm{fs}$.

We consider the antiferromagnetic spin chain introduced in Sec. 4.4.1 and study this model in a nonequilibrium situation. As was shown in Sec. 4.4.1, the extrinsic contribution to the nonequilibrium spin density dominates over the intrinsic contribution for the spin chain model. Thus, we focus on the extrinsic contributions and set $D_1 = D_2 = D$ such that $\delta_D = 0$, rendering intrinsic contributions zero by symmetry.

We simulate a spin chain of $N = 480$ spins with spin Hamiltonian as in Eq. (4.16). First, to characterize the chain in terms of magnon variables, i.e., in terms of (i) the magnon dispersion and (ii) the magnon spin, we calculate the dynamical structure factor

$$\mathcal{F}(k,\omega) = \frac{1}{\sqrt{2\pi}N} \sum_{i,j} \mathrm{e}^{\mathrm{i}k(x_i - x_j)} \int_{-\infty}^{\infty} \mathrm{e}^{\mathrm{i}\omega t} \left\langle S_i^+(t) S_j^-(0) \right\rangle \mathrm{d}t, \tag{4.20}$$

i.e., the time and space Fourier transform of the spin-spin time-correlation function. x_i denotes the x coordinate of the ith spin and $S_i^\pm = S_i^x \pm \mathrm{i} S_i^y$.

The numerically determined magnon spectra for the spin chain are shown in Fig. 4.4(a), (c), (e), and (g); they agree with those obtained analytically in the previous section [shown as black lines in Fig. 4.4(b), (d), (f), and (h)]. In Fig. 4.4(a), we depict the dispersion of the isotropic antiferromagnetic spin chain ($\lambda = 1$, $D = 0$, $\gamma = 1$) with the two degenerate linear Goldstone modes. This degeneracy is lifted in the presence of spin-nonconserving anisotropies $\lambda > 1$ and $\gamma < 1$ [cf. Fig. 4.4(c)]. In Fig. 4.4(e), we show the Rashba-like spin-split dispersion in the presence of nonzero DMI and $\lambda > 1$, and in Fig. 4.4(g) the dispersion in the presence of both anisotropies as well as DMI, for which the band degeneracy at $k = 0$ is lifted [as compared to (e)].

The magnon spin is extracted by computing the Stokes parameters $I(k,\omega) = |\mathcal{S}^x|^2 + |\mathcal{S}^y|^2$ and $V(k,\omega) = -2\mathrm{Im}(\mathcal{S}^x \mathcal{S}^{y,*})$ [196], where $\boldsymbol{\mathcal{S}} = \boldsymbol{\mathcal{S}}(k,\omega)$ is the space and time Fourier transform of the spin configuration $\{\mathbf{S}_i(t)\}$. The quantity $\sigma(k,\omega) =$

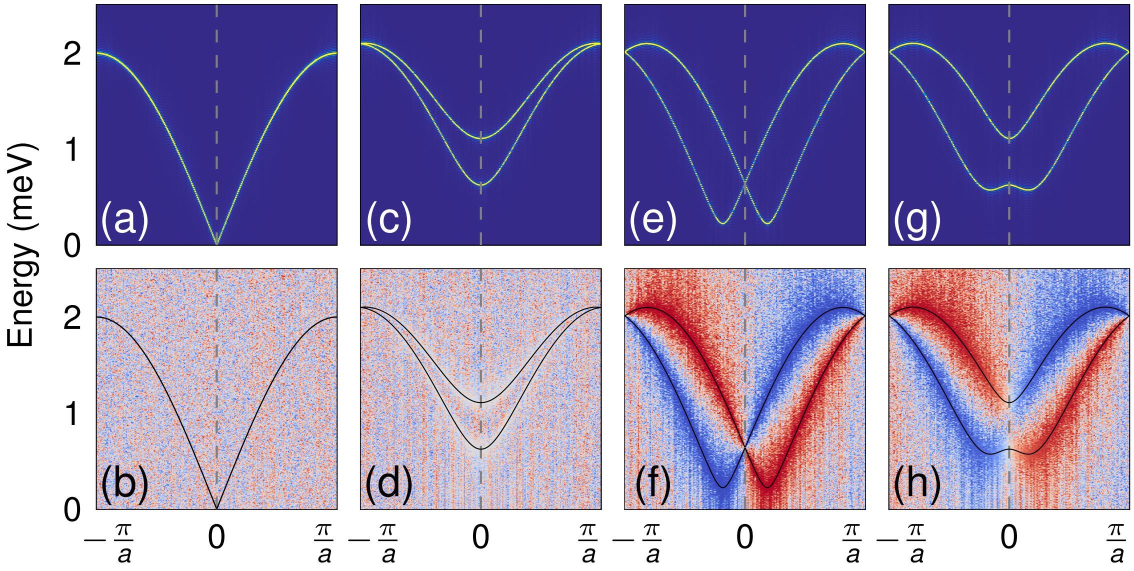

Figure 4.4: Magnon spectra of the antiferromagnetic spin chain as obtained from numerical simulations for selected parameters; top row: dynamical structure factor; bottom row: the spin of magnons or Stokes parameter ratio $\sigma(k,\omega)$ (red: negative; gray: zero; blue: positive). Black solid lines show the analytically obtained magnon dispersion (within linear spin-wave theory). Parameters read $J = 1\,\mathrm{meV}$, and (a,b) $\lambda = 1$, $D = 0$, $\gamma = 1$, (c,d) $\lambda = 1.05$, $D = 0$, $\gamma = 0.9$, (e,f) $\lambda = 1.05$, $D = 0.3\,\mathrm{meV}$, $\gamma = 1$, and (g,h) $\lambda = 1.05$, $D = 0.3\,\mathrm{meV}$, $\gamma = 0.9$. A small simulation temperature $T = 0.01\,\mathrm{K}$ and Gilbert damping $\alpha = 0.001$ were chosen to reduce lifetime broadening.

$V(k,\omega)/I(k,\omega)$ measures the ratio of circular to total polarization intensity; its sign reveals the sign of the magnon spin. There is no feature of $\sigma(k,\omega)$ in Fig. 4.4(b), in agreement with the previous section. In contrast, $\sigma(k,\omega)$ becomes zero (gray color) in Fig. 4.4(d), indicating that the magnon spin is suppressed due to ellipticity or “squeezing”, which is in agreement with Ref. [186]. Without squeezing but with nonzero DMI we identify spin-up and spin-down magnons by the antisymmetric blue-red features in Fig. 4.4(f). In the presence of squeezing and DMI this asymmetric feature survives [panel (h)] and shows that the spin expectation value continuously goes through zero upon crossing $k = 0$, an observation which is in agreement with Fig. 4.1(c).

In the previous section, we obtained a nonzero magnonic spin polarization for the case in Fig. 4.4(g) and (h) [which are respectively reminiscent of Fig. 4.1(b) and (c)], but zero effect for the other cases. We will now put this prediction to the test.

To do so, direct nonequilibrium simulations with an imprinted temperature gradient were performed. The spin chain was separated into three parts of equal length (160 spins each). The terminating parts have temperature $T \pm \Delta T/2$, while the temperature in the central part linearly interpolates between the two ends. Following this temperature profile, a heat bath with temperature T_i is assigned to each spin i. After establishing a steady state in this nonequilibrium situation, the spin density $\langle \mathbf{S} \rangle = \frac{1}{160} \sum_{i=161}^{320} \langle \mathbf{S}_i \rangle$ of the central chain segment is measured and normalized to the number of spins in this segment.

There is an additional technicality of the simulation: Since two neighboring spins in the central chain segment experience slightly different temperatures ($T_i \neq T_{i+1}$), their net moment does not compensate exactly. Repeating this argument for all spins of the central segment, we conclude that there is a tiny net magnetization simply due to the temperature dependence of the sublattice magnetizations. The sign of this artificial magnetization is determined by the direction of the first spin at the cold end of the central segment. This artificial effect would superimpose with the magnon analogue of the Edelstein effect. Thus, to avoid the non-Edelstein contribution, we simulate two uncoupled spin chains with opposite spin direction in parallel (The two chains are time-reversal partners). The non-Edelstein contributions are exactly opposite, because the sublattice magnetization is reversed, and sum to zero. In contrast, the extrinsic Edelstein contributions are time-reversal even as shown in Eq. (4.15b) and do *not* cancel out.

Our simulation results are presented in Fig. 4.5. The z spin accumulation $\langle S^z \rangle$ is zero in equilibrium [$\Delta T = 0$ in Fig. 4.5(a)], as expected for an antiferromagnet in zero magnetic field. It stays zero in nonequilibrium ($\Delta T \neq 0$), if either DMI or squeezing (or both) are absent [compare brown, blue, and purple marks in Fig. 4.5(a)]. However, it becomes nonzero if DMI and squeezing are present (red marks), in full agreement with theory.

The other Cartesian components of the spin density, i.e, $\langle S^x \rangle$ and $\langle S^y \rangle$ are zero even in nonequilibrium [blue and green marks in Fig. 4.5(b)]. This is not surprising, because no magnon state has a nonzero x or y spin. Thus, a nonequilibrium state cannot give rise to

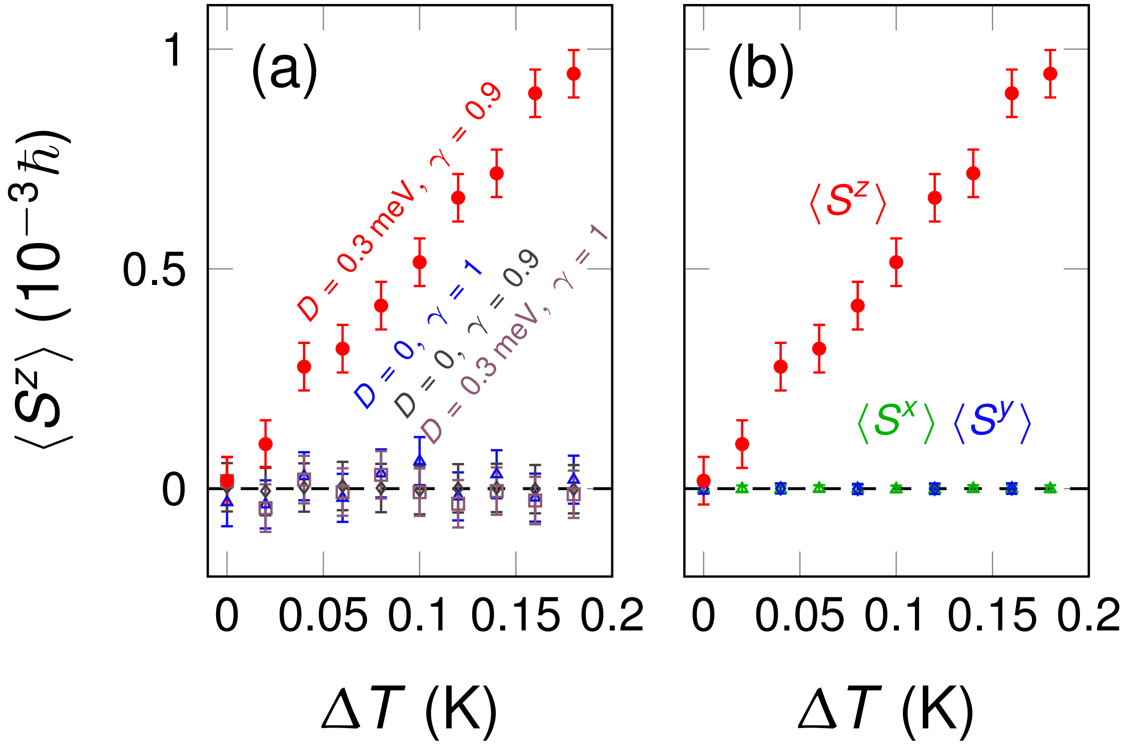

Figure 4.5: Results from direct nonequilibrium spin dynamics simulations of the thermally induced magnonic analogue of the Edelstein effect in an anisotropic antiferromagnetic spin chain; parameters read $J = 1\,\mathrm{meV}$, $\lambda = 1.02$, and $\alpha = 10^{-4}$. (a) Nonequilibrium spin density $\langle S^z \rangle$ in dependence on temperature difference ΔT for selected parameter combinations. (b) $\langle S^i \rangle$ ($i = x, y, z$) in dependence on ΔT. An average temperature of $T = 0.2\,\mathrm{K}$ was used for all simulations.

spin density of those components. In contrast, $\langle S^z \rangle$ increases approximately linearly with the external force ΔT.

We note in passing other results that are not explicitly shown. We found that (i) reversing D reverses $\langle S^z \rangle$ due to the reversion of the magnon spin, (ii) increasing λ increases the magnon gap, leading to a decreasing $\langle S^z \rangle$, and (iii) increasing the Gilbert damping α diminishes the $\langle S^z \rangle$, because the magnon transport lifetime decreases.

Overall, we find excellent qualitative agreement with theory (Sec. 4.4.1). However, we mention that we cannot compare numbers, because the classical white noise used to model the temperature bath results in a Rayleigh-Jeans distribution rather than in the true Bose-Einstein distribution. Thus, the simulation suffers from the classical equipartition and

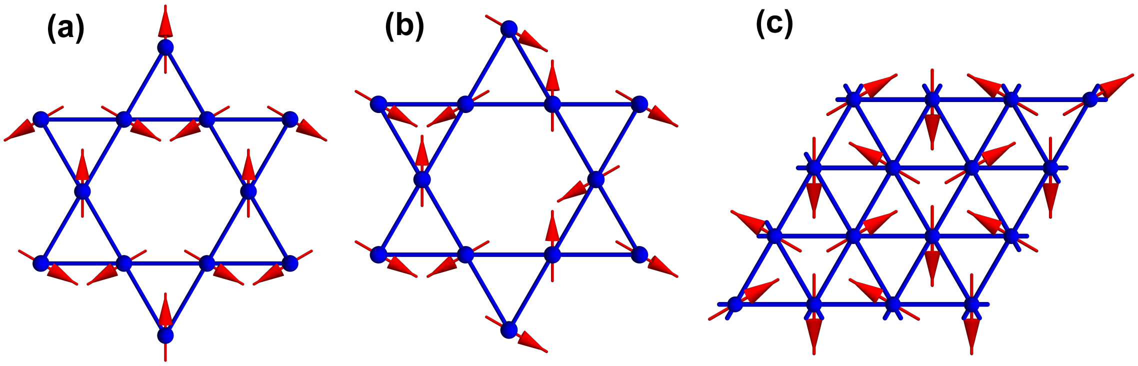

Figure 4.6: (a), (b) Noncollinear spin textures on the kagome lattice, with (a) negative vector chirality (NVC) and (b) staggered vector chirality (SVC). (c) Noncollinear antiferromagnetic ground state on the 2D triangular lattice.

does not account for the quantum freezing of degrees of freedom as temperature goes to zero.

4.6 Summary

We have shown that a temperature gradient can induce a nonequilibrium spin density due to magnonic transport in antiferromagnetic insulators with inversion asymmetry and spin non-conservation. Our linear response theory revealed both intrinsic and extrinsic contributions that behave differently under time reversal. Consequently, these two contributions correspond to different elements of the response tensor, which can facilitate their experimental disentanglement, e.g., in the presence of magnetic domains. Our proposal can be realized in (quasi-)2D and 3D noncollinear antiferromagnets, for which we find sizable effects in realistic material candidates. Our predictions can be tested by transport measurements similar to those used for detection of the inverse spin Hall effect, by magneto-optical Kerr microscopy, or by magnetic sensing based on the nitrogen-vacancy (NV) centers. Given the omnipresence of inversion-symmetry-breaking interfaces (or surfaces) in experimental setups, observation of the magnonic analogue of the Edelstein effect can stimulate further developments in the field of spintronics. In particular, with the important role played by the electronic Edelstein effect in modern spintronics in mind, we hope to have stimulated experimental research on the magnonic analogue of the Edelstein effect.

The abundance of antiferromagnetic materials holds great promise for the identification of well-suited experimental candidates. In kagome NAFMs, the coplanar magnetic order can exhibit three types of vector chiralities: positive, negative, and staggered, which are respectively abbreviated by PVC, NVC, and SVC [122, 197] and depicted in Figs. 4.2(a), 4.6(a), and 4.6(b). Their distinct magnetic symmetries cause distinct magnonic spin polarization responses, which are tabulated in Table 4.1. Besides kagome magnets, quasi-2D triangular antiferromagnets [cf. Fig. 4.6(c)] with the 120° spin order [198, 199] could be suitable candidates. Such systems as $\mathrm{RbFe(MoO_4)_2}$ [200] and $\mathrm{Ba_3NiNb_2O_9}$ [201] share symmetries with the PVC kagome NAFMs, resulting in identical response tensor shapes [cf. Table 4.1]. Similar to kagome NAFMs, the 3D breathing pyrochlores can exhibit magnetic orders different from the AIAO order [21, 191], which changes their magnetic symmetries and, thus, the expected response tensor shapes. Experimentally, the breathing pyrochlore materials $\mathrm{Ba_3Yb_2Zn_5O_{11}}$ [202, 203], $\mathrm{LiInCr_4O_8}$ [144] have been studied, all of which may be considered for a proof-of-principle study of our predictions.

Chapter 5

Magnon Landau levels and topological spin responses in antiferromagnets

5.1 Introduction

Emergent electromagnetism [204, 205] is at the core of a multitude of fascinating physical phenomena ranging from the topological Hall effect [78, 206–211] in skyrmion crystals [212–215] to the formation of topological magnons [20,24,32,33,38,72,216–218]. Many applications related to information storage and processing can emerge from such useful features of magnetic systems as topological protection and low-dissipation spin transport [219–222]. The need for minimizing losses due to Joule heating has shifted the focus of recent research to insulating materials lacking itinerant electrons but still capable of carrying spin currents [110].

Recently, antiferromagnets (AFM) became the focus of active research as they possess unique features associated with lack of stray fields and ultrafast dynamics in THz range [223]. Many spintronics concepts readily extend to AFM materials, as is the case with spin-orbit torques [113] demonstrated experimentally in CuMnAs [224, 225]. Skyrmions in AFM can be potentially stabilized by staggered fields [226, 227] induced by field-like spin-orbit torques in CuMnAs and Mn_2Au or by coupling to boundary magnetization in Cr_2O_3. AFMs are expected to exhibit interesting physics associated with vanishing topological and skyrmion Hall effects [228–232].

The topological spin Hall effect has been predicted for conducting systems [226, 233, 234]. In insulating materials, the topological spin Hall effect mediated by magnons has been studied for isolated skyrmions [176]. The topological spin Nernst effect in skyrmion crystals has not been studied in insulators. The nature of topological response in skyrmion crystals can be associated with the appearance of Landau levels of magnons [81, 235]. Interestingly, in AFM the Landau levels are described by the relativistic Klein-Gordon equation, which is reflected in the shape of steps describing the accumulation of the spin Chern number. This also suggests a realization of an unconventional magnonic topological insulator which in contrast to previous proposals [72] maps to the Klein-Gordon equation in the presence of magnetic field.

In this chapter, we study the magnonic topological spin Nernst response in AFM skyrmion crystals and square crystals of vortices and antivortices, which, as we show, can both be stabilized by staggered magnetic field and anisotropy. The topological spin responses can be qualitatively understood by considering Landau levels induced by a uniform magnetic flux in a generic model of an AFM magnonic topological insulator. We construct a model of an AFM magnonic topological insulator that in the long wavelength limit maps to the Klein-Gordon equation in the presence of uniform magnetic field. In contrast to previous proposals [72], our model does not rely on the Aharonov-Casher effect with prefactor $1/c^2$ but originates in the Dzyaloshinskii-Moriya interactions (DMI).

5.2 AFM skyrmions and stability phase diagram

We begin by considering the free energy density of a quasi-two-dimensional AFM written in a long wavelength limit:

$$\mathcal{F}[\boldsymbol{n}] = \frac{\mathcal{J}}{2}\left(\partial_i \boldsymbol{n}\right)^2 + \mathcal{K}(\boldsymbol{n}\cdot\hat{u})^2 - \mathcal{H}_s(\boldsymbol{n}\cdot\hat{u}) + \boldsymbol{\mathcal{D}}_j(\partial_j \boldsymbol{n}\times\boldsymbol{n}), \tag{5.1}$$

where we sum over repeated index $i = x, y$, $\boldsymbol{n}$ is a unit vector along the Néel order, $\mathcal{J}$ is the exchange constant, $\mathcal{K}$ is the effective uniaxial anisotropy along the direction $\hat{u}$ (typically $\hat{u} = \hat{z}$), $\mathcal{H}_s$ is the staggered magnetic field along the direction $\hat{u}$ arising due to the spin-orbit torque or the effect of boundary magnetization [226, 227], and $\mathcal{D}_{ij} = (\boldsymbol{\mathcal{D}}_j)_i$ is the DMI described by a general tensor. When DMI is induced by an axially symmetric interface with a heavy metal, which is the focus of this paper, there are only two non-zero tensor coefficients $\mathcal{D}_{12} = -\mathcal{D}_{21} = \mathcal{D}$ [236]. The free energy density in Eq. (5.1) and resulting phase diagram can also describe other spin textures obtained from Néel skyrmions by global transformation in spin space (e.g., antiskyrmions or Bloch skyrmions) [237]. This can be seen by applying a global transformation to the spin texture followed by similar transformations on $\hat{u}$ and $\mathcal{D}_{ij}$ [237]. The zero temperature phase diagram in Fig. 5.1 has been calculated using the method of Ref. [237] relying on energy minimization [238] and rescaling of the unit cell. In addition to the AFM-SkX phase identified in Ref. [227], we also identify an AFM-SC vortex-antivortex lattice [237, 239–243] stabilized by the in-plane anisotropy. Such textures can also contain antiferromagnetic antimerons with fractional topological charge as shown in Fig. 5.1. In the following, we study the effect of fictitious magnetic fields due to quantized topological charge per unit cell in SkX and SC phases.

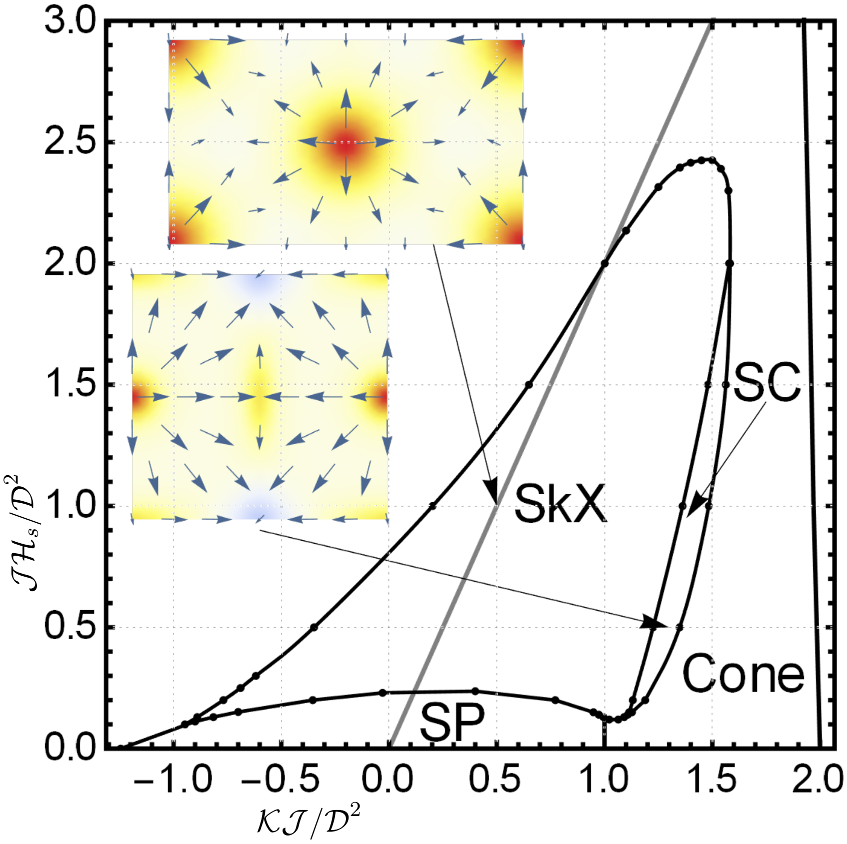

Figure 5.1: Zero temperature phase diagram of AFM with DMI. The axes correspond to the dimensionless staggered magnetic field and dimensionless effective anisotropy. The gray line separates the aligned and the tilted regions of the FM phase. This phase is taken over by the hexagonal skyrmion lattice (SkX), spiral (SP), cone phase, and the square crystal of vortices and antivortices (SC). The upper inset shows a hexagonal lattice unit cell with a skyrmion in the center. The lower inset shows a square crystal unit cell with AFM antimeron in the center. Red and yellow correspond to positive topological charge density and blue corresponds to the negative topological charge density.

5.3 AFM magnons and fictitious gauge fields

To describe magnonic excitations on top of a Néel texture, we turn to the picture with unit sublattice spin fields $\boldsymbol{m}_A$ and $\boldsymbol{m}_B$. To this end, we consider the free energy density,

$$\mathcal{F}[\boldsymbol{m},\boldsymbol{n}] = \mathcal{F}[\boldsymbol{n}] + \frac{\mathcal{A}}{2}\boldsymbol{m}^2 \tag{5.2}$$

with $\mathcal{A}$ being the transverse spin susceptibility. We consider a system with smoothly varying spin textures and limit the discussion to the leading order of its spatial derivative. As the size of DMI induced textures scales as $\mathcal{J}/\mathcal{D}$, we systematically perform analysis up to the first order in $\mathcal{D}/\mathcal{J}$ and discard anisotropy and staggered magnetic field terms (for the SkX phase, $\mathcal{H}_s\mathcal{J}/\mathcal{D}^2 \sim \mathcal{K}\mathcal{J}/\mathcal{D}^2 \sim 1$), according to Fig. 5.1 [227, 235]. With these preconditions, the free energy is explicitly written as

$$\mathcal{F} = \frac{\mathcal{A}}{2}\boldsymbol{m}^2 + \frac{\mathcal{J}}{2}(\partial_i \boldsymbol{n})^2 + \mathcal{D}(n_z \vec{\nabla} \cdot \boldsymbol{n} - \boldsymbol{n} \cdot \vec{\nabla} n_z), \tag{5.3}$$

which can be rewritten as

$$\mathcal{F} = \frac{\mathcal{A}}{2}\boldsymbol{m}^2 + \boldsymbol{n}(-\frac{\mathcal{J}}{2}\partial_i^2 + \hat{\mathcal{D}})\boldsymbol{n} \tag{5.4}$$

where $\hat{\mathcal{D}} = \mathcal{D}\tilde{R}_z^T L_i \tilde{R}_z \partial_i$ with $\tilde{R}_z = \exp\{L_z \frac{\pi}{2}\}$, $(L_i)_{jk} = -\epsilon_{ijk}$. Now we replace the field $\boldsymbol{m}, \boldsymbol{n}$ with sublattice spin field $\boldsymbol{m}_A, \boldsymbol{m}_B$ by plugging $\boldsymbol{m} = (\boldsymbol{m}_A + \boldsymbol{m}_B)/2$ and $\boldsymbol{n} = (\boldsymbol{m}_A - \boldsymbol{m}_B)/2$ into the free energy above. As a result, it is converted to a form in terms of sublattice-spin fields, up to some irrelevant constants,

$$\begin{aligned}\mathcal{F} \quad &= \frac{\mathcal{A}}{4}\boldsymbol{m}_A \cdot \boldsymbol{m}_B + \frac{1}{4}\sum_{a=A,B} \boldsymbol{m}_a(-\frac{\mathcal{J}}{2}\partial_i^2 + \hat{\mathcal{D}})\boldsymbol{m}_a - \frac{1}{4}\boldsymbol{m}_A(-\frac{\mathcal{J}}{2}\partial_i^2 + \hat{\mathcal{D}})\boldsymbol{m}_B \\ &-\frac{1}{4}\boldsymbol{m}_B(-\frac{\mathcal{J}}{2}\partial_i^2 + \hat{\mathcal{D}})\boldsymbol{m}_A.\end{aligned} \tag{5.5}$$

Furthermore, we assume that in the ground state $\boldsymbol{m}_0 = 0$ and $\boldsymbol{n}_0 = (\sin\theta\cos\phi, \sin\theta\sin\phi, \cos\theta)$ where θ, ϕ are spherical angles. This assumption ensures decoupling of the two chirality subspaces. We will see that lifting this assumption does not substantially modify our conclusions according to the numerical results. The local spin field can be conveniently parametrized by a rotational matrix $R = \exp(L_z\phi)\exp(L_y\theta)$ with $(L_i)_{jk} = -\epsilon_{ijk}$ ($i = x, y, z$ or $1, 2, 3$) being the generators of rotational matrices.

Specifically, $\boldsymbol{m}_{A(B)} = R\boldsymbol{m}'_{A(B)}$, with

$$\begin{aligned}\boldsymbol{m}'_A &= \hat{z}\sqrt{1-|\gamma_A|^2} + \hat{x}\gamma_A^x + \hat{y}\gamma_A^y,\\ \boldsymbol{m}'_B &= -\hat{z}\sqrt{1-|\gamma_B|^2} + \hat{x}\gamma_B^x - \hat{y}\gamma_B^y,\end{aligned} \tag{5.6}$$

where $\gamma^{x,y}_{A(B)}$ stands for the spin wave, and $|\gamma_{A(B)}|^2 = (\gamma^x_{A(B)})^2 + (\gamma^y_{A(B)})^2$. Note that

$$\partial_i(R\boldsymbol{m}'_a) = R(\partial_i + R^{-1}\partial_i R)\boldsymbol{m}'_a, \qquad \partial_i^2(R\boldsymbol{m}'_a) = R(\partial_i + R^{-1}\partial_i R)^2\boldsymbol{m}'_a, \tag{5.7}$$

where we used $\partial_\mu R^{-1}\partial_\mu R + R^{-1}\partial_\mu R R^{-1}\partial_\mu R = 0$ in the second equation above. Also,

$$\boldsymbol{m}_a\hat{\mathcal{D}}\boldsymbol{m}_b = \mathcal{D}\boldsymbol{m}'_a(\bar{R}^T L_i\partial_i\bar{R} + \bar{R}^T L_i\bar{R}\partial_i)\boldsymbol{m}'_b = \mathcal{D}\boldsymbol{m}'_a(\mathcal{A}^d_i\mathcal{A}^t_i + \mathcal{A}^d_i\partial_i)\boldsymbol{m}'_b \tag{5.8}$$

where $\mathcal{A}^d_i = \bar{R}^T L_i\bar{R}$ with $\bar{R} = \tilde{R}_z R$, and $\mathcal{A}^t_i = \bar{R}^T\partial_i\bar{R} = R^T\partial_i R$. Therefore, we have

$$\begin{aligned}\boldsymbol{m}_a(-\frac{\mathcal{J}}{2}\partial_i^2 + \hat{\mathcal{D}})\boldsymbol{m}_b \quad &= \boldsymbol{m}'_a[-\frac{\mathcal{J}}{2}(\partial_i + \mathcal{A}^t_i)^2 + \mathcal{D}(\mathcal{A}^d_i\mathcal{A}^t_i + \mathcal{A}^d_i\partial_i)]\boldsymbol{m}'_b\\ &= -\frac{\mathcal{J}}{2}\boldsymbol{m}'_a(\partial_i + \mathcal{A}^t_i - \frac{\mathcal{D}}{\mathcal{J}}\mathcal{A}^d_i)^2\boldsymbol{m}'_b + \mathcal{O}(\partial_i^2).\end{aligned} \tag{5.9}$$

Utilizing the relation above the free energy can be rewritten as

$$\begin{aligned}\mathcal{F} = \quad &\frac{\mathcal{A}}{4}\boldsymbol{m}'_A\cdot\boldsymbol{m}'_B - \frac{\mathcal{J}}{8}\sum_{a=A,B}\boldsymbol{m}'_a\cdot(\partial_i + \mathcal{A}_i)^2\boldsymbol{m}'_a + \frac{\mathcal{J}}{8}\boldsymbol{m}'_A\cdot(\partial_i + \mathcal{A}_i)^2\boldsymbol{m}'_B\\ &+\frac{\mathcal{J}}{8}\boldsymbol{m}'_B\cdot(\partial_i + \mathcal{A}_i)^2\boldsymbol{m}'_A\end{aligned} \tag{5.10}$$

where $\mathcal{A}_i = \mathcal{A}^t_i - \frac{\mathcal{D}}{\mathcal{J}}\mathcal{A}^d_i$. In the discussion, the second and higher orders of the spin-texture spatial derivative will not be treated systematically. By substituting Eq. (5.6) into Eq. (5.10), the magnon energy density reads

$$\begin{aligned}\mathcal{H}_{mag} \quad &= \frac{\mathcal{A}}{4}[-1+\frac{1}{2}(\psi_A^*\psi_A+\psi_B^*\psi_B)+\frac{1}{2}(\psi_A^*\psi_B^*+\psi_A\psi_B)]+\frac{\mathcal{J}}{16}[\psi_A(\vec{\nabla}+i\boldsymbol{a})^2\psi_B \\ &+\psi_A^*(\vec{\nabla}-i\boldsymbol{a})^2\psi_B^*]+\frac{\mathcal{J}}{16}[\psi_B(\vec{\nabla}-i\boldsymbol{a})^2\psi_A+\psi_B^*(\vec{\nabla}+i\boldsymbol{a})^2\psi_A^*]-\frac{\mathcal{J}}{16}[\psi_A^*(\vec{\nabla}-i\boldsymbol{a})^2\psi_A \\ &+\psi_A(\vec{\nabla}+i\boldsymbol{a})^2\psi_A^*]-\frac{\mathcal{J}}{16}[\psi_B^*(\vec{\nabla}+i\boldsymbol{a})^2\psi_B+\psi_B(\vec{\nabla}-i\boldsymbol{a})^2\psi_B^*] \qquad (5.11)\end{aligned}$$

where $\psi_a=\gamma_a^x+i\gamma_a^y$, and $a_i=-(\mathcal{A}_i^t-\frac{\mathcal{D}}{\mathcal{J}}\mathcal{A}_i^d)_{12}$. Here $\boldsymbol{a}$ is an emergent gauge field [79–81] with two components $\boldsymbol{a}=\boldsymbol{a}^t+\boldsymbol{a}^d$ with $a_i^t=\mathcal{A}_i^t|_{12}=\cos\theta\partial_i\phi$, $\boldsymbol{a}^d=\frac{\mathcal{D}}{\mathcal{J}}\boldsymbol{\mathcal{A}}^d|_{12}=-\frac{\mathcal{D}}{\mathcal{J}}\tilde{R}_z\boldsymbol{n}_0$ where $\boldsymbol{n}_0=R\hat{z}$. These two parts result in emergent magnetic fields,

$$\begin{aligned}&b_i^t=(\vec{\nabla}\times\boldsymbol{a}^t)_i=-\frac{1}{2}\epsilon_{ijk}\boldsymbol{n}_0\cdot(\partial_j\boldsymbol{n}_0\times\partial_k\boldsymbol{n}_0), \\ &\boldsymbol{b}^d=\vec{\nabla}\times\boldsymbol{a}^d. \qquad (5.12)\end{aligned}$$

The kinetic term of spin waves is considered by dividing the spin field into slow and fast modes $\boldsymbol{m}_a=\boldsymbol{m}_a^{(0)}+\delta\boldsymbol{m}_a$ where the fast modes $\delta\boldsymbol{m}_a$ represents the spin wave. Re-expressing these modes in a local frame, $\boldsymbol{m}_a^{(0)}=\hat{e}_a^z$, and $\delta\boldsymbol{m}_a\simeq\gamma_a^x\hat{e}_a^x+\gamma_a^y\hat{e}_a^y-\frac{1}{2}\hat{e}_a^z|\gamma_a|^2$, where $(\hat{e}_A^x,\hat{e}_A^y,\hat{e}_A^z)=R(\hat{x},\hat{y},\hat{z})$ and $(\hat{e}_B^x,\hat{e}_B^y,\hat{e}_B^z)=R(\hat{x},-\hat{y},-\hat{z})$. The variation of spin Berry phase due to the second order of fast modes is [53, 244]

$$\begin{aligned}\delta\mathcal{S}_B^{(2)} \quad &= \sum_{a=A,B}\mathcal{S}\int dt\delta^2(\boldsymbol{A}_a\cdot\dot{\boldsymbol{m}}_a)=\sum_a\frac{\mathcal{S}}{2}\int dt\boldsymbol{m}_a\cdot(\delta\dot{\boldsymbol{m}}_a\times\delta\boldsymbol{m}_a) \\ &=\sum_a\int dt\frac{\mathcal{S}}{2}\delta\dot{\boldsymbol{m}}_a\cdot(-\gamma_a^x\hat{e}_a^y+\gamma_a^y\hat{e}_a^x) \\ &=\sum_a\int dt\frac{\mathcal{S}}{2}(\dot{\gamma}_a^x\hat{e}_a^x+\dot{\gamma}_a^y\hat{e}_a^y+\gamma_a^x\dot{\hat{e}}_a^x+\gamma_a^y\dot{\hat{e}}_a^y)\cdot(-\gamma_a^x\hat{e}_a^y+\gamma_a^y\hat{e}_a^x) \\ &=\sum_a\int dt\frac{\mathcal{S}}{2}[\gamma_a^y\dot{\gamma}_a^x-\dot{\gamma}_a^y\gamma_a^x+(\dot{\hat{e}}_a^y\cdot\hat{e}_a^x)\gamma_a^y\gamma_a^y-(\dot{\hat{e}}_a^x\cdot\hat{e}_a^y)\gamma_a^x\gamma_a^x] \\ &=\sum_a\int dt\frac{\mathcal{S}}{4}[\psi_a^*(i\partial_t-\nu_a\varphi)\psi_a+\psi_a(-i\partial_t-\nu_a\varphi)\psi_a^*], \qquad (5.13)\end{aligned}$$

where $\boldsymbol{A}_a$ satisfies $\vec{\nabla}_{\boldsymbol{m}_a}\times\boldsymbol{A}_a=\boldsymbol{m}_a$, $\varphi=-R^T\partial_tR|_{12}=\cos\theta\partial_t\phi$, and $\nu_{A(B)}=+(-)$.

Here we used

$$\begin{aligned}\dot{\hat{e}}_a^x\cdot\hat{e}_a^y &= \nu_a(\partial_t R\hat{x})\cdot R\hat{y}=\nu_a\hat{x}^T\partial_t R^T R\hat{y}=\nu_a\partial_t R^T R|_{12}=-\nu_a R^T\partial_t R|_{12},\\ \dot{\hat{e}}_a^y\cdot\hat{e}_a^x &= \nu_a(\partial_t R\hat{y})\cdot R\hat{x}=\nu_a\hat{y}^T\partial_t R^T R\hat{x}=\nu_a\partial_t R^T R|_{21}=-\nu_a R^T\partial_t R|_{21}=\nu_a R^T\partial_t R|_{12}.\end{aligned} \tag{5.14}$$

Note $\delta\mathcal{S}_B^{(2)}$ contains both the kinetic energy of magnons and the coupling between magnons and an emergent scalar gauge field φ. Later, this coupling term will be attributed to a part of the full Hamiltonian.

Combining the kinetic term and the magnon Hamiltonian together , the magnon Lagrangian of the system under basis $\psi=(\psi_A,\psi_B^*,\psi_A^*,\psi_B)^T$ reads

$$\mathcal{L}=i\frac{\mathcal{S}}{4}\psi^\dagger\sigma_3\otimes\tau_3\dot{\psi}-\frac{1}{2}\psi^\dagger\hat{\mathcal{H}}\psi, \tag{5.15}$$

where $\hat{\mathcal{H}}=\hat{\mathcal{H}}_+\oplus\hat{\mathcal{H}}_-$ with

$$\hat{\mathcal{H}}_\chi=[\frac{\mathcal{A}}{8}-\frac{\mathcal{J}}{8}(\vec{\nabla}-i\chi\boldsymbol{a})^2]\mathbb{1}+[\frac{\mathcal{A}}{8}+\frac{\mathcal{J}}{8}(\vec{\nabla}-i\chi\boldsymbol{a})^2]\tau_1+\frac{\mathcal{S}}{2}\varphi\tau_3. \tag{5.16}$$

From the Lagrangian, it is straightforward to give a Schrödinger-like equation for the magnon field in subspace $\eta_\pm$

$$i\chi\frac{\mathcal{S}}{2}\tau_3\partial_t\eta_\chi=\hat{\mathcal{H}}_\chi\eta_\chi. \tag{5.17}$$

Through some linear combination, this equation is shown to be equivalent to a Klein-Gordon equation

$$[(i\partial_t-\chi\varphi)^2-c^2(-i\vec{\nabla}-\chi\boldsymbol{a})^2]\eta_\chi^{(-)}=0, \tag{5.18}$$

where $\eta_\chi^{(-)}=\eta_{\chi,1}-\eta_{\chi,2}$ and $c=\sqrt{\mathcal{J}\mathcal{A}}/\mathcal{S}$.

In fact, the mapping to the Klein-Gordon equation can be also understood by considering the field theory of Néel field. The Lagrangian density of $\boldsymbol{m}, \boldsymbol{n}$ reads

$$\mathcal{L}[\boldsymbol{m}, \boldsymbol{n}] = \mathcal{S}\boldsymbol{m} \cdot (\boldsymbol{n} \times \partial_t \boldsymbol{n}) - \frac{\mathcal{A}}{2}\boldsymbol{m}^2 + \boldsymbol{n}(\frac{\mathcal{J}}{2}\partial_i^2 + \hat{\mathcal{D}})\boldsymbol{n} \tag{5.19}$$

where the $\boldsymbol{m}$ field can be eliminated by integrating it out to produce

$$\mathcal{L}[\boldsymbol{n}] = \frac{\mathcal{S}^2}{2\mathcal{A}}(\partial_t \boldsymbol{n})^2 + \boldsymbol{n}(\frac{\mathcal{J}}{2}\partial_i^2 + \hat{\mathcal{D}})\boldsymbol{n}. \tag{5.20}$$

By substituting a rotational-matrix parametrized Néel field $\boldsymbol{n} = R\boldsymbol{n}'$, where $\boldsymbol{n}' = \hat{z}\sqrt{1 - \delta\boldsymbol{n}'^2} + \delta n'_x \hat{x} + \delta n'_y \hat{y}$ with $\delta n'_x, \delta n'_y$ describing the fluctuation of the Neel field, and R is defined as $R\hat{z} = (\sin\theta\cos\phi, \sin\theta\sin\phi, \cos\theta)$, we obtain a Lagrangian for the Néel field fluctuation

$$\mathcal{L}[\delta n'_+, \delta n'_-] = \frac{\mathcal{S}^2}{2\mathcal{A}}\delta n'_-[(i\partial_t - \varphi)^2 - c^2(-i\vec{\nabla} - \boldsymbol{a})^2]\delta n'_+. \tag{5.21}$$

Here, $\delta n'_\pm = \delta n'_x \pm i\delta n'_y$. The Lagrangian gives us the Klein-Gordon equation for the Néel field fluctuation

$$[(i\partial_t \mp \varphi)^2 - c^2(-i\vec{\nabla} \mp \boldsymbol{a})^2]\delta n'_\pm = 0 \tag{5.22}$$

This result implies that $\delta n'_\pm \propto \eta_\pm^{(-)}$, which agrees with the definition of the Néel field.

5.4 Magnon Landau levels

To understand physics associated with the emergence of Landau levels, we approximate the emergent magnetic field by its spatial average, which is justified for smooth enough textures. In particular, we consider $\boldsymbol{b} = -B\hat{z}$, with $B = |\langle\vec{\nabla} \times \boldsymbol{a}\rangle| = 4\pi\langle\rho_{top}\rangle > 0$, where $\rho_{top} = \boldsymbol{n}_0 \cdot (\partial_x \boldsymbol{n}_0 \times \partial_y \boldsymbol{n}_0)$ and the DMI induced contribution vanishes. As shown in the last section, the Hamiltonian is block diagonalized and the corresponding eigenproblem could be solved in each block. We assume the spin texture is static, i.e.,$\varphi = 0$. With the emergent gauge field replaced by its average value $\boldsymbol{a}_0$ and choosing the Landau gauge $\boldsymbol{a}_0 = (yB, 0, 0)$ ($B > 0$), it's easy to find

$$(-i\vec{\nabla} - \chi\boldsymbol{a}_0)^2 \xi^{\chi}_{n,k_x} = \lambda_n \xi^{\chi}_{n,k_x}, \tag{5.23}$$

where

$$\xi^{\chi}_{n,k_x} = \frac{N_n}{\sqrt{L}} e^{-ik_x x} e^{-\frac{1}{2}B(y+\chi\frac{k_x}{B})^2} H_n[\sqrt{B}(y + \chi\frac{k_x}{B})], \qquad \text{and} \quad \lambda_n = B(2n+1). \tag{5.24}$$

Here, $N_n = \frac{1}{L\sqrt{2^n n!}}(\frac{B}{\pi})^{1/4}$. Suppose the eigenstate of the system takes the form of $\xi^{\chi}_{n,k_x}\Phi_{\chi,n}$ with $\Phi_{\chi,n}$ being a spinor. The eigenequation of the system is reduced to

$$\chi\mathcal{S}\tau_3\varepsilon_{\chi}\Phi_{\chi,n} = [(\frac{\mathcal{A}}{4} + \frac{\mathcal{J}}{4}\lambda_n)\mathbb{1} + (\frac{\mathcal{A}}{4} - \frac{\mathcal{J}}{4}\lambda_n)\tau_1]\Phi_{\chi,n}. \tag{5.25}$$

Solving this equation shows that the eigenvalues are independent of χ

$$\varepsilon^{+,-}_n \quad = \pm\frac{1}{2\mathcal{S}}\sqrt{\mathcal{J}\mathcal{A}\lambda_n} = \pm\frac{1}{2\mathcal{S}}\sqrt{\mathcal{A}\mathcal{J}B(2n+1)}. \tag{5.26}$$

This agrees with the Landau levels of the Klein-Gordon equation [245]. The corresponding eigenstates are

$$\Phi^{+}_{\chi,n} = (\tau_1)^{\frac{1-\chi}{2}} \begin{pmatrix} \cosh\frac{\vartheta_n}{2} \\ -\sinh\frac{\vartheta_n}{2} \end{pmatrix}, \quad \Phi^{-}_{\chi,n} = \tau_1\Phi^{+}_{\chi,n}, \tag{5.27}$$

with $\cosh\vartheta_n = (\mathcal{A} + \mathcal{J}\lambda_n)/(2\sqrt{\mathcal{J}\mathcal{A}\lambda_n})$, and $\sinh\vartheta_n = (\mathcal{A} - \mathcal{J}\lambda_n)/(2\sqrt{\mathcal{J}\mathcal{A}\lambda_n})$. Here, the eigenstates are degenerate with respect to the index k_x. The number of degenerate states is determined by the total number of the magnetic flux quanta, where each unit cell with topological charge $|Q| = 1$ contributes two flux quanta. The magnon Landau levels result in various Hall-like responses. However, the two species of magnons with opposite chirality feel opposite magnetic flux in Eq. (5.3) as they are time-reversal partners of each other, which always results in vanishing thermal Hall response (see next section). On the other hand, spin and chirality current responses are nonzero.

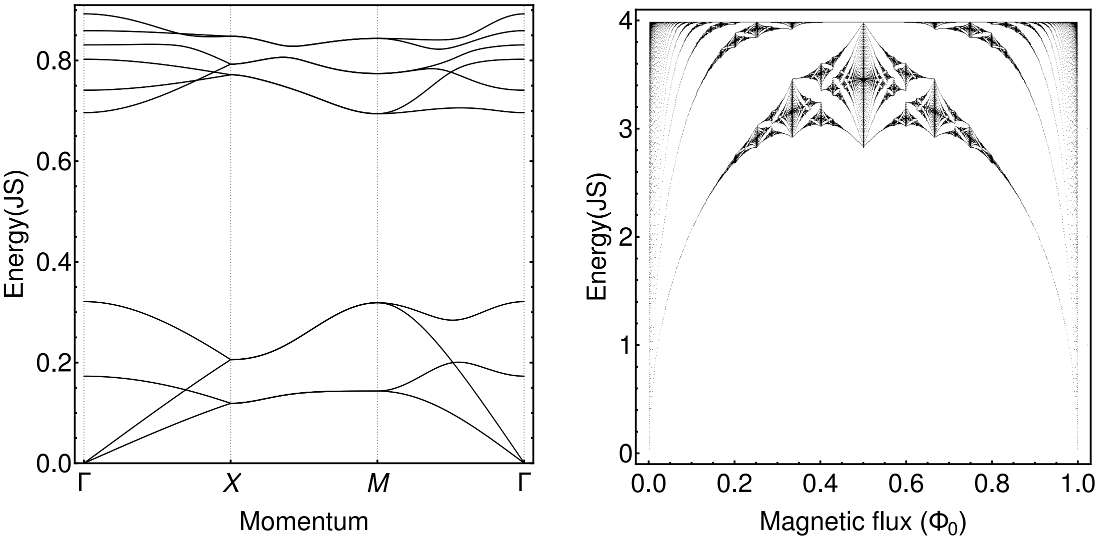

Figure 5.2: Left: Lowest magnon bands of skyrmion crystal in a square lattice AFM along the Brillouin zone loop $\Gamma - X - M - \Gamma$. A splitting of chiral modes can be clearly identified. Right: The Hofstadter butterfly of AFM with uniform magnetic flux $\Phi = \frac{p}{q}\Phi_0$ per unit cell for $q = 1000$, Φ_0 is the flux quantum.

For a nonuniform fictitious field of a skyrmion lattice with basis vectors $\vec{a}_1$ and $\vec{a}_2$, the Landau-level wave functions can be linearly combined to a new periodic basis for each energy level, $\tilde{\varphi}^{\chi}_{nm\boldsymbol{k}}$, which satisfies $T_{\vec{a}_{1(2)}}\tilde{\varphi}^{\chi}_{nm\boldsymbol{k}} = e^{i\boldsymbol{k}\cdot\vec{a}_{1(2)}}\tilde{\varphi}^{\chi}_{nm\boldsymbol{k}}$ with magnetic translational operator $T_{\vec{a}_{1,2}}$ satisfying $T_{\vec{a}_1}T_{\vec{a}_2} = e^{i\chi Q 4\pi}T_{\vec{a}_2}T_{\vec{a}_1}$. The phase factor indicates that each skyrmion unit cell contains topological charge Q which leads to splitting into $2|Q|$ subbands described by quantum number m. In this new basis, one can include perturbations to the Hamiltonian due to nonuniform fictitious flux and higher order terms disregarded earlier [235] (see Appendix C for more details). This treatment leads to splitting of Landau levels and to coupling of magnons with opposite chiralities, as confirmed by calculating the magnon spectrum of a skyrmion crystal in a square lattice AFM in Fig. 5.2. To understand the above effects, in the following we construct and solve various lattice models corresponding to Eq. (5.3).

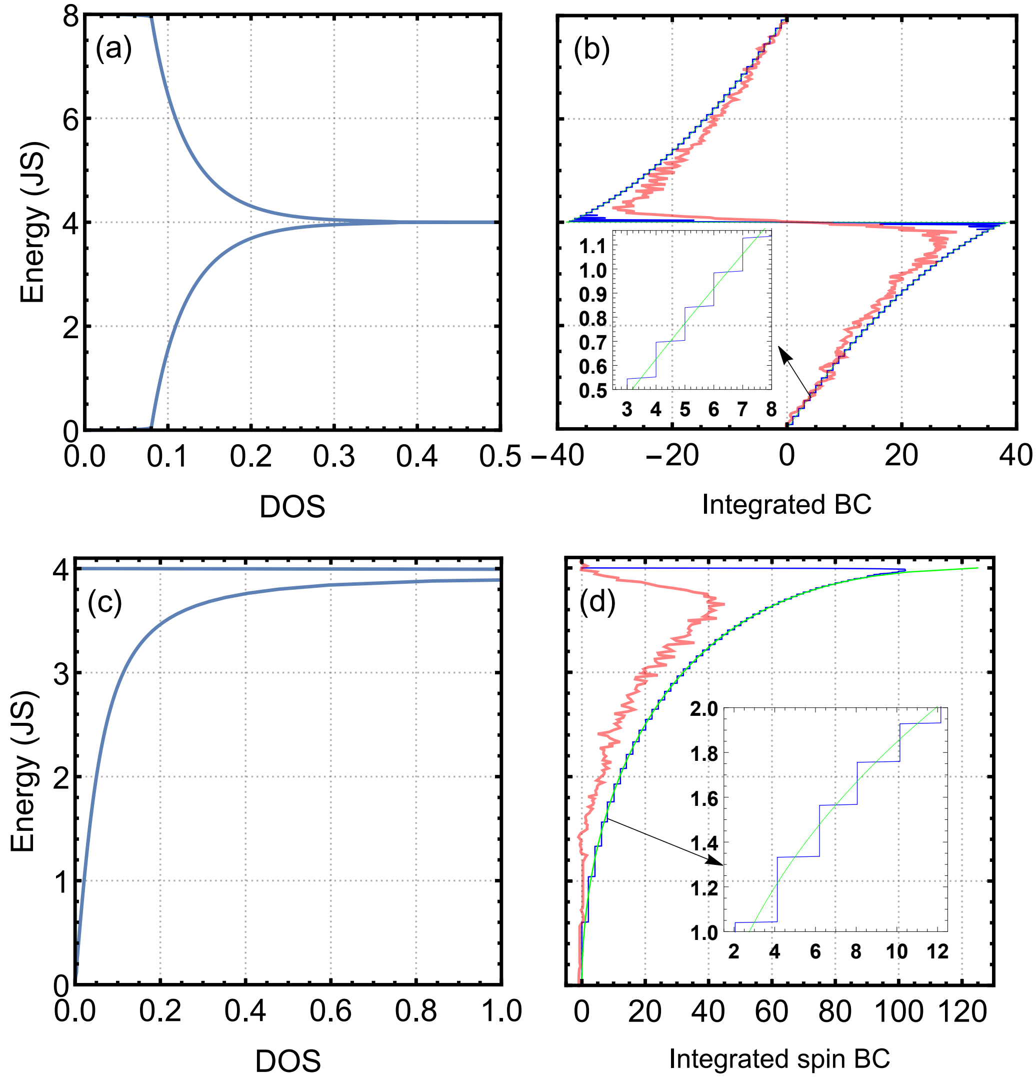

Figure 5.3: The total (integrated) Berry and spin Berry curvatures for magnonic systems exhibiting spin and topological spin responses of magnons. (a) and (c) The density of states (DOS) of magnons in a square lattice FM or AFM in the absence of gauge fields. (b) The total Berry curvature due to gauge fields induced by skyrmion crystal (red curve) or DMI (blue curve). The semiclassical appoximation is shown by the green curve. (d) The total spin Berry curvature due to gauge fields induced by DMI (blue curve) and the total sublattice Berry curvature due to gauge fields induced by skyrmion crystal (red curve). The semiclassical appoximation is shown by the green curve.

5.5 Vanishing thermal Hall response

In this section, we discuss the thermal Hall effect in the AFM skyrmions in the approximated Landau-level picture in a single skyrmion and from symmetry analysis for a skyrmion crystal. Both of these methods confirm the vanishing of the thermal Hall response.

5.5.1 Thermal Hall calculation based on Landau-level picture

We first consider the thermal Hall response in a single AFM skyrmion based on the approximated Landau-level picture. Assuming a temperature gradient is applied along the x-direction, in which the translational symmetry is conserved, the thermal conductivity is [128]

$$\kappa_{yx} = -\frac{k_B^2 T}{L_x}\sum_{\chi}\sum_{n_+=0_+}^{N_+}\sum_{k_x}\Omega^{\chi}_{n_+}\{c_2[g(\varepsilon_n)] - \frac{\pi^2}{3}\} \tag{5.28}$$

where

$$\begin{aligned}
\Omega^{\chi}_{n_+} &= \sum_{s=\pm1}\sum_{(m_s\neq n_+)m_s=0_s}^{N_s}(\bar{\sigma}_3)_{n_+n_+}(\bar{\sigma}_3)_{m_sm_s}\frac{2\mathrm{Im}[(v^{\chi}_y)_{n_+m_s}(v^{\chi}_x)_{m_sn_+}]}{(\bar{\varepsilon}_{n_+}-\bar{\varepsilon}_{m_s})^2}\\
&= \sum_{s=\pm1}\sum_{(m_s\neq n_+)m_s=0_s}^{N_s} s\frac{2\mathrm{Im}[(v^{\chi}_y)_{n_+m_s}(v^{\chi}_x)_{m_sn_+}]}{(\varepsilon_n - s\varepsilon_m)^2},
\end{aligned} \tag{5.29}$$

with

$$\begin{aligned}
\hat{v}^{\chi}_i &= i[\hat{\mathcal{H}}_{\chi}, r_i] = -i\frac{\mathcal{J}}{8}[(\partial_j - i\chi a_j)^2(\mathbb{1}-\tau_1), r_i]\\
&= -i\frac{\mathcal{J}}{8}(\mathbb{1}-\tau_1)\{(\partial_j - i\chi a_j)[(\partial_j - i\chi a_j), r_i] + [(\partial_j - i\chi a_j), r_i](\partial_j - i\chi a_j)\}\\
&= \frac{\mathcal{J}}{4}(\mathbb{1}-\tau_1)(-i\partial_i - \chi a_i) = \frac{\mathcal{J}}{4}(\mathbb{1}-\tau_1)\mathcal{D}^{\chi}_i.
\end{aligned} \tag{5.30}$$

Here, $\bar{\sigma}_3 = \sigma_3 \otimes \mathbb{1}_N$ with N being the number of Landau Levels, $(\bar{\sigma}_3)_{m_s m_s} = s$, and $\bar{\varepsilon}_{m_s} = s\varepsilon_m$ (here, ε_m means the positive energy ε_m^+). Note $s = \pm 1$ respectively label the particle and hole space. In the one-dimensional case, $\Omega^\chi_{n_+}$ doesn't represent the Berry curvature, but it is regarded as an interband function, as that normally appears in a linear response theory. Notice

$$\begin{aligned}(v_x^\chi)_{m_s n_+} &= \frac{\mathcal{J}}{4}\langle \xi_m^\chi| \otimes \langle \Phi^s_{\chi,m}|(\mathbb{1}-\tau_1)\mathcal{D}_x^\chi|\Phi^+_{\chi,n}\rangle \otimes |\xi_n^\chi\rangle = \frac{\mathcal{J}}{4}\langle \Phi^s_{\chi,m}|(\mathbb{1}-\tau_1)|\Phi^+_{\chi,n}\rangle\langle \xi_m^\chi|\mathcal{D}_x^\chi|\xi_n^\chi\rangle \\ &= -\chi\tilde{v}G^{s,+}_{m,n}(\sqrt{n}\delta_{m,n-1} + \sqrt{n+1}\delta_{m,n+1}),\end{aligned}$$

where $\tilde{v} = \frac{\mathcal{J}}{4}\sqrt{\frac{B}{2}}$, $G^{s,s'}_{m,n} = \langle \Phi^s_{\chi,m}|(\mathbb{1}-\tau_1)|\Phi^{s'}_{\chi,n}\rangle$, which is independent of χ as a result of the property $|\Phi^s_{-\chi,n}\rangle = \tau_1|\Phi^s_{\chi,n}\rangle$. In a similar way,

$$(v_y^\chi)_{n_+ m_s} = -i\tilde{v}G^{+s}_{nm}(\sqrt{n}\delta_{m,n-1} - \sqrt{n+1}\delta_{m,n+1}). \tag{5.31}$$

Above, we used the relation

$$\mathcal{D}_x^\chi \xi_n^\chi = -\chi\sqrt{\frac{B}{2}}(\sqrt{n}\xi^\chi_{n-1} + \sqrt{n+1}\xi^\chi_{n+1}), \qquad \mathcal{D}_y^\chi \xi_n^\chi = -i\sqrt{\frac{B}{2}}(\sqrt{n}\xi^\chi_{n-1} - \sqrt{n+1}\xi^\chi_{n+1}), \tag{5.32}$$

which can be easily verified by using the property of Hermite functions. Substituting Eq (5.31), (5.31) into (5.29) results in

$$\Omega^\chi_{n_+} = \chi\sum_{s=\pm 1}\sum_{(m_s\neq n_+)m_s=0_s}^{N_s} s\frac{2\tilde{v}^2|G^{+s}_{nm}|^2[n\delta_{m,n-1} - (n+1)\delta_{m,n+1}]}{(\varepsilon_n - s\varepsilon_m)^2}. \tag{5.33}$$

This expression tells us that the response kernels of two species of magnons take opposite sign. Given that the bands of two chiralities are degenerate, the total thermal Hall vanishes. This result illustrates that the magnons with opposite chirality propagate in opposite transverse directions as they feel opposite emergent magnetic flux. The vanishing of the thermal Hall response for a lattice model will be also confirmed below by a symmetry analysis.

5.5.2 From symmetry point of view

Strictly speaking, the two-chiralities-magnon picture fails in an AFM-SkX, and thus the thermal response cancellation between two chiralities doesn't exist. Alternatively, to understand the thermal Hall therein we can study it in a symmetry point of view. We will first build up a framework for symmetry analysis in a magnon tight-binding model and then confirm the vanishing of the thermal Hall effect in the antiferromagntic SkX.

Suppose the SkX respects a unitary symmetry g or an antiunitary symmetry (containing time reversal) f. We first analyze the symmetry restriction on the Hamiltonian. For simplicity, we focus on a Hamiltonian element

$$h_{i,j} = \boldsymbol{S}_i^T(\vec{r}_i)\Gamma_{ij}\boldsymbol{S}_j(\vec{r}_j) = \boldsymbol{S}_i'^T(\vec{r}_i)\Lambda_{ij}\boldsymbol{S}_j'(\vec{r}_j) \tag{5.34}$$

where $\boldsymbol{S}_i, \boldsymbol{S}_i'$ are connected by a local rotational matrix $\boldsymbol{S}_i = R_i\boldsymbol{S}_i'$ with $\boldsymbol{S}_i' \simeq (S - a_i^\dagger a_i)\hat{z} + \sqrt{\frac{S}{2}}(a_i^\dagger + a_i)\hat{x} + i\sqrt{\frac{S}{2}}(a_i^\dagger - a_i)\hat{y}$, $a_i(a_i^\dagger)$ being the annihilation (creation) operator, and $\Lambda_{ij} = R_i^T\Gamma_{ij}R_j$. Rewriting the element in magnon basis

$$h_{ij} = \Psi_i^\dagger\hat{h}_{ij}\Psi_j - \frac{1}{2}(\Lambda_{ij})_{33}(\Psi_i^\dagger\Psi_i + \Psi_j^\dagger\Psi_j), \tag{5.35}$$

where $\Psi_i = (a_i, a_i^\dagger)^T$, $\hat{h}_{ij} = P^\dagger\Lambda_{ij}^\perp P$ with $\Lambda_{ij}^\perp$ being the upper-left 2×2 block of Λ_{ij}, $P = \sqrt{\frac{S}{2}}\begin{pmatrix} 1 & 1 \\ -i & i \end{pmatrix}$ and $(S_i'^x, S_i'^y) = \Psi_i^\dagger P^\dagger$. The symmetry operation simultaneously happens in atom, spin (spin components), and spatial space. For a global symmetry, all these operations can be implemented as $[\theta_i(\vec{r}_i), \phi_i(\vec{r}_i)] \to [\pm\theta_{i'}(\vec{r}_{i'}) + \Delta\theta, \phi_{i'}(\vec{r}_{i'}) + \Delta\phi]$, which is usually realized by performing a unitary transformation on the Hamiltonian matrix (this will become clear when we go to specific examples). Meanwhile, if a symmetry contains time reversal, P will be transformed to its complex conjugate P^*. Specifically,

$$\begin{aligned} g &: \hat{h}_{ij}[\theta_{i(j)}, \phi_{i(j)}] \rightarrow \hat{h}_{i'j'}[\pm\theta_{i'(j')} + \Delta\theta, \phi_{i'(j')} + \Delta\phi], \\ f &: \hat{h}_{ij}[\theta_{i(j)}, \phi_{i(j)}] \rightarrow \hat{h}^*_{i'j'}[\pm\theta_{i'(j')} + \Delta\theta, \phi_{i'(j')} + \Delta\phi]. \end{aligned} \tag{5.36}$$

Similar operations happen to $(\Lambda_{ij})_{33}$ as well. From now on, we will mainly concentrate on the transformation of $\hat{h}_{ij}$, as natural generalization to $(\Lambda_{ij})_{33}$ is easily realized. The magnon basis simply transforms as $\Psi_i(\vec{r}_i) \rightarrow \Psi_{i'}(\vec{r}'_i) = \Psi_{i'}(M^{-1}\vec{r}_i)$, where M is an operation on spatial variables, $\vec{r}_i = M\vec{r}'_i$.

Now, we show how to implement the global variation of θ, ϕ angles for a real symmetry operation. We discuss two types of operations: (i) unitary operation, (ii) time reversal operation. Note their results could be superimposed to an antiunitary operation. To be specific, we consider the exchange and DMI between two spins, i.e., $h_{ij} = J\boldsymbol{S}_i \cdot \boldsymbol{S}_j + \boldsymbol{D}_{ij} \cdot (\boldsymbol{S}_i \times \boldsymbol{S}_j)$, which corresponds to $(\Gamma_{ij})_{\alpha\beta} = J\delta_{\alpha\beta} + D^\gamma \epsilon_{\gamma\alpha\beta}$. Through direct calculation, it can be shown

$$h_{ij} = A_0(a_i^\dagger a_i + a_j^\dagger a_j) + A_1 a_i a_j + A_2 a_i^\dagger a_j + h.c. \tag{5.37}$$

with

$$\begin{aligned} A_0 = \quad & JS(\cos\theta_i \cos\theta_j + \cos\theta_{ij} \sin\theta_i \sin\theta_j) + D_\perp S \sin\theta_{ij} \sin(\phi_i - \phi_d), \\ A_{1,2} = \quad & \frac{JS}{2}[\cos\phi_{ij}(\pm 1 + \cos\theta_i \cos\theta_j) + i(\cos\theta_i \pm \cos\theta_j)\sin\phi_{ij} + \sin\theta_i \sin\theta_j] \\ & + \frac{S}{2}[iD_z(\cos\theta_i \pm \cos\theta_j) + iD_\perp \cos(\phi_i - \phi_d)(\sin\theta_i \pm \sin\theta_j) \\ & + D_\perp \sin\theta_{ij} \sin(\phi_i - \phi_d)]. \end{aligned} \tag{5.38}$$

Here, $\phi_{ij} = \phi_i - \phi_j$, $\theta_{ij} = \theta_i - \theta_j$, and we expressed the DMI vector as $\boldsymbol{D}_{ij} =$

$D_z\hat{z} + D_\perp \cos\phi_d \hat{x} + D_\perp \sin\phi_d \hat{y}$. For case (i), as we mainly focus on 2-D lattices, all relevant symmetry transformations usually keep the angle θ unchanged, i.e., $\Delta\theta = 0$. Under a global transformation, $\phi_{i,j}$ and ϕ_d simultaneously change by an angle $\Delta\phi$, which has no effect on the expression above. For case (ii), $\theta_i \to \pi - \theta_i$, $\phi_i \to \phi_i + \pi$, which changes the Hamiltonian elements to their complex conjugates. Therefore, the symmetry operations are effectively implemented as

$$g : \hat{h}_{ij}[\theta_{i(j)}, \phi_{i(j)}] \to \hat{h}_{i'j'}[\theta_{i'(j')}, \phi_{i'(j')}] \qquad f : \hat{h}_{ij}[\theta_{i(j)}, \phi_{i(j)}] \to \hat{h}^*_{i'j'}[\theta_{i'(j')}, \phi_{i'(j')}] \tag{5.39}$$

The same analysis works equivalently for the anisotropy term and the staggered Zeeman interaction. The transformation above still holds with these terms added to the system.

Now, we turn to the discussion of the transformation under the full magnon basis, $\Psi = (a_1, \cdots, a_N; a_1^\dagger, \cdots, a_N^\dagger)$. The symmetry operation only exchanges the order of magnon species and its spatial argument, which can be realized by a unitary matrix U, $\Psi(\vec{R}) \to U\Psi(M^{-1}\vec{R})$, where U doesn't mix the particle and hole space, i.e., $[U, \sigma_3] = 0$ with σ_3 acting in the particle-hole space. In the momentum space

$$g : \Psi_{\boldsymbol{k}} \to U_g \Psi_{M_g \boldsymbol{k}}, \qquad f : \Psi_{\boldsymbol{k}} \to U_f \Psi_{-M_f \boldsymbol{k}}. \tag{5.40}$$

Combining the operation on the Hamiltonian matrix and magnon basis, the symmetries of the system enforce the momentum space Hamiltonian matrix to satisfy

$$g : U_g H_{\boldsymbol{k}} U_g^{-1} = H_{M_g^{-1}\boldsymbol{k}}, \qquad f : U_f H^*_{\boldsymbol{k}} U_f^{-1} = H_{-M_f^{-1}\boldsymbol{k}}. \tag{5.41}$$

As a result, the eigenenergy and eigenstate satisfy

$$g : \varepsilon_{\boldsymbol{k}} = \varepsilon_{M_g \boldsymbol{k}}, \quad |\psi_{n,\boldsymbol{k}}\rangle = U_g |\psi_{n,M_g \boldsymbol{k}}\rangle, \qquad f : \varepsilon_{\boldsymbol{k}} = \varepsilon_{-M_f \boldsymbol{k}}, \quad |\psi_{n,\boldsymbol{k}}\rangle = U_f |\psi_{n,-M_f \boldsymbol{k}}\rangle^* \tag{5.42}$$

Equipped with these results, we consider two symmetries of the SkX : $\Theta * S_{\frac{1}{2}}$ with Θ and $S_{\frac{1}{2}}$ being the time reversal and half-unit-cell shift, and C_2, a two-fold rotation with respect to the out-of-plane direction. The former is an antiunitary symmetry with $M_{\Theta * S_{\frac{1}{2}}} = 1$, and the latter is a unitary symmetry with $M_{C_2} = -1$. Therefore, the eigensolution of the system fulfills the conditions

$$\varepsilon_{\boldsymbol{k}} = \varepsilon_{-\boldsymbol{k}}, \qquad |\psi_{n,\boldsymbol{k}}\rangle = U_{C_2}|\psi_{n,-\boldsymbol{k}}\rangle = U_{\Theta * S_{1/2}}|\psi_{n,-\boldsymbol{k}}\rangle^*. \tag{5.43}$$

The Berry curvature satisfies

$$\Omega^z_{n,\boldsymbol{k}} = 2\mathrm{Im}\langle\partial_{k_y}\psi_{n,\boldsymbol{k}}|\sigma_3\partial_{k_x}\psi_{n,\boldsymbol{k}}\rangle = 2\mathrm{Im}\langle\partial_{k_y}\psi_{n,-\boldsymbol{k}}|U^\dagger_{C_2}\sigma_3 U_{C_2}\partial_{k_x}\psi_{n,-\boldsymbol{k}}\rangle = \Omega^z_{n,-\boldsymbol{k}}, \tag{5.44}$$

where we used $[U_{C_2}, \sigma_3] = 0$ and $U^\dagger_{C_2} = U^{-1}_{C_2}$. In a simiar way, the $\Theta * S_{1/2}$ suggests

$$\Omega^z_{n,\boldsymbol{k}} = -\Omega^z_{n,-\boldsymbol{k}}. \tag{5.45}$$

Eq. (5.44) and (5.45) together enforce the Berry curvature to vanish everywhere in momentum space, $\Omega^z_{n,\boldsymbol{k}} = 0$. As a result, the thermal Hall response vanishes as long as the system has an effective time reversal symmetry.

5.6 Spin Nernst effect in AFM topological insulator

In this section we build a squre-lattice AFM magnon model whose low-energy spectrum can be exactly mapped to the Klein-Gordon Landau levels. Then we calculate the spin Nernst response and make a comparison with the same response in an AFM-SkX.

A square lattice Hamiltonian of collinear FM (AFM) reads

$$H = \sum_{\langle ij\rangle} J\boldsymbol{S}_i\cdot\boldsymbol{S}_j + \boldsymbol{D}_{ij}(\boldsymbol{S}_i\times\boldsymbol{S}_j) - \sum_i H_i S^y_i - K(S^y_i)^2. \tag{5.46}$$

As the order parameter direction controls the DMI effect on magnons, the order parameter is oriented along the y-axis to realize the Landau gauge. Above, the exchange parameter is $J < 0$ ($J > 0$) for FM (AFM), H_i is (staggered) magnetic field, K is the magnetic anisotropy, and $\boldsymbol{D}_{ij} = D(\boldsymbol{r})\hat{z} \times \boldsymbol{\delta}_{ij}$ describes DMI with Rashba symmetry for a bond $\boldsymbol{\delta}_{ij}$. In FM case, the exchange interaction and DMI between two neighboring spins is

$$J\boldsymbol{S}_i \cdot \boldsymbol{S}_j + \boldsymbol{D}_{ij} \cdot (\boldsymbol{S}_i \times \boldsymbol{S}_j) = \boldsymbol{S}_i^T \Gamma_{ij} \boldsymbol{S}_j \tag{5.47}$$

where

$$\Gamma_{ij} = \begin{bmatrix} J & 0 & -D_{ij,y} \\ 0 & J & D_{ij,x} \\ D_{ij,y} & -D_{ij,x} & J \end{bmatrix}. \tag{5.48}$$

Reparametrizing the interaction by $\boldsymbol{S}'$ leads to

$$\begin{aligned} \boldsymbol{S}_i'^T R^T \Gamma_{ij} R \boldsymbol{S}_j' &= J S_i^z S_j^z + \frac{1}{2}(J - i\boldsymbol{D}_{ij} \cdot \boldsymbol{n}_0) S_i^- S_j^+ + \frac{1}{2}(J + i\boldsymbol{D}_{ij} \cdot \boldsymbol{n}_0) S_i^+ S_j^- \\ &= J S_i^z S_j^z + \frac{\tilde{J}_{ij}}{2}(e^{-i\phi_{ij}} S_i^- S_j^+ + e^{i\phi_{ij}} S_i^+ S_j^-) \end{aligned} \tag{5.49}$$

where $\boldsymbol{n}_0$ is the direction of order parameter, $\tilde{J}_{ij} = \sqrt{J^2 + (\boldsymbol{D}_{ij} \cdot \boldsymbol{n}_0)^2}$, and $\phi_{ij} = \tan^{-1}[(\boldsymbol{D}_{ij} \cdot \boldsymbol{n}_0)/J]$. In AFM case, we need to replace $S_j^\pm \to S_j^\mp$, and $S_j^z \to -S_j^z$ for one of sublattices.

When $D/J \ll 1$, $\phi_{ij} \approx (\boldsymbol{D}_{ij} \cdot \boldsymbol{n}_0)/J$, and

$$e^{-i\phi_{ij}} S_i^-(\vec{r}) S_j^+(\vec{r} + \boldsymbol{\delta}_{ij}) = S_i^-(\vec{r}) e^{i\boldsymbol{\delta}_{ij} \cdot [\hat{\boldsymbol{p}} - (\boldsymbol{n}_0 \times \hat{z}) D(\vec{r})/J]} S_j^+(\vec{r}) \tag{5.50}$$

with $\hat{\boldsymbol{p}}$ being the translational operator. Therefore, a fictitious gauge field for magnons can be recoganized as $\boldsymbol{A}_m(\vec{r}) = (\boldsymbol{n}_0 \times \hat{z}) D(\vec{r})/J$, and the corresponding fictitious magnetic field is $\boldsymbol{B}_m = -\hat{z}(\boldsymbol{n}_0 \cdot \vec{\nabla}) D(\boldsymbol{r})/J$. For a uniform magnetic field $\boldsymbol{B}_m = -B\hat{z}$, to replicate the Landau gauge, it requires $n_{0,x} = 0$ and $n_{0,y}D(\vec{r})/J = By$. For the special case with spins aligned along the y-direction, i.e., $\boldsymbol{n}_0 = \hat{y}$, the strength of the nonuniform DMI satisfies $D(\vec{r})/J = By$.

Using the Holstein-Primakoff transformation in the limit of large S, i.e. $S_j^+ \approx \sqrt{2S}a_i$, $S_j^- \approx \sqrt{2S}a_i^\dagger$, $S_i^z \approx S - a_i^\dagger a_i$, we recover discrete realization of noninteracting magnons subjected to uniform magnetic field described by a vector potential $\boldsymbol{a}_0 = (yB, 0, 0)$. In the long wavelength limit FM magnons are described by the Schrödinger equation while AFM magnons are described by the Klein-Gordon equation. In what follows, we concentrate on AFM, using FM system only for comparison. The role of the chiral index χ in Eq. (5.3) is played by the spin index s_z, as the spin along the quantization axis is conserved. After the Fourier transform, the Hamiltonian for $s_z = 1$ becomes

$$H_+ = \frac{1}{2}JS\sum_{\boldsymbol{k}} \Psi_+^\dagger(\boldsymbol{k})\hat{H}_+(\boldsymbol{k})\Psi_+(\boldsymbol{k}), \tag{5.51}$$

where $\Psi_+ = (a_1(\boldsymbol{k}), b_1^\dagger(-\boldsymbol{k}) \dots b_{2N}^\dagger(-\boldsymbol{k}), a_{2N}(\boldsymbol{k}))^T$ is the bosonic field, and the unit cell contains N by 2 array of atoms from each sublattice of the square-lattice AFM. The Hamiltonian has a block structure

$$\hat{H}_+(\boldsymbol{k}) = \begin{pmatrix} \hat{a} & \hat{b} \\ \hat{b} & \hat{a} \end{pmatrix}, \tag{5.52}$$

where for $2N \times 2N$ matrices $\hat{a}$ and $\hat{b}$ the nonzero elements are given by $a_{i,j} = 4$, $b_{i,j} = \cos(k_x + j\phi_0)$ for $i = j$, and $a_{i,j} = a_{j,i}^* = e^{-ik_y}$ for $i - j = 1$ modulo $2N$. Here the phase factor $\phi_0 = 2\pi p/q$ describes the strength of magnetic field, i.e., $2p$ is the number of flux quanta for enlarged unit cell and $q = 2N$. For $s_z = -1$, $\hat{H}_-(\boldsymbol{k}) = \hat{H}_+^T(-\boldsymbol{k})$ and $\Psi_-(\boldsymbol{k}) = (a_1^\dagger(-\boldsymbol{k}), b_1(\boldsymbol{k}) \cdots b_{2N}(\boldsymbol{k}), a_{2N}^\dagger(-\boldsymbol{k}))^T$. The total Hamiltonian matrix can be diagonalized by a paraunitary matrix $T_{\boldsymbol{k}}$, i.e., $T_{\boldsymbol{k}}^\dagger \hat{H} T_{\boldsymbol{k}} = \hat{\mathcal{E}}_{\boldsymbol{k}}$, where $\hat{\mathcal{E}}_{\boldsymbol{k}}$ is a diagonal matrix describing eigenvalues [246]. By varying the strength of DMI, we can control the magnetic flux per unit cell which allows us to observe the Hofstadter butterfly in full analogy with electronic systems (see Fig. 5.2). Similar to electronic systems, the exact energy bands can be found from expansion of p/q into continuous fractions or from the Diophantine equation [3,247]. As can be seen from Fig. 5.2, the form of the Hofstadter butterfly differs from the case of nonrelativistic electrons.

The spin responses of magnons can be described with the help of the spin Berry curvature [38, 248],

$$\boldsymbol{\Omega}_n^\alpha = i\sum_{m\neq n}(\tilde{\sigma}_3)_{nn}(\tilde{\sigma}_3)_{mm}\frac{\frac{1}{2}\{\hat{\boldsymbol{v}},\hat{\Sigma}^\alpha\}_{nm}\times\hat{\boldsymbol{v}}_{mn}}{(\bar{\varepsilon}_{n,\boldsymbol{k}}-\bar{\varepsilon}_{m,\boldsymbol{k}})^2}, \tag{5.53}$$

where we define the anticommutator $\{\hat{\boldsymbol{v}},\hat{\Sigma}^\alpha\} = \hat{\boldsymbol{v}}\tilde{\sigma}_3\hat{\Sigma}^\alpha + \hat{\Sigma}^\alpha\tilde{\sigma}_3\hat{\boldsymbol{v}}$, $\bar{\varepsilon}_{m,\boldsymbol{k}} = (\tilde{\sigma}_3\hat{\mathcal{E}}_{\boldsymbol{k}})_{mm}$, and the Pauli matrix in the particle-hole space, i.e., $(\tilde{\sigma}_3)_{mm} = 1$ for particle-like states and $(\tilde{\sigma}_3)_{mm} = -1$ for hole-like states. The magnon spin density operator along the α-axis is given by $\Sigma^\alpha(\boldsymbol{r}) = \frac{1}{2}\Psi^\dagger(\boldsymbol{r})\hat{\Sigma}^\alpha\Psi(\boldsymbol{r})$ where $\hat{\Sigma}^\alpha = -\sigma_0\otimes\text{Diag}(m_1^\alpha,\cdots,m_M^\alpha)$ with the Pauli matrix σ_0 describing the particle-hole space and $\boldsymbol{m}_i$ being the direction of magnetic moment at position i in a unit cell of M atoms [248]. We consider the spin Nernst response [97],

$$\alpha_{xy}^s = \frac{k_B}{V}\sum_{\boldsymbol{k},n=1}^{N} c_1(g(\varepsilon_{n,\boldsymbol{k}}))\Omega_n^{(z)}(\boldsymbol{k}) \tag{5.54}$$

where $g(\varepsilon) = (e^{\varepsilon/T}-1)^{-1}$ is the Bose-Einstein distribution and $c_1(x) = (1+x)\ln(1+x) - x\ln(x)$. Due to degeneracy, we apply Eq. (5.53) to each subspace $s_z = \pm 1$ separately. The total spin Chern number is a sum of spin Chern numbers for each subspace, i.e., $C_n^s = (1/2\pi)\int_{BZ}\Omega_n^{(z)}d^2k$ where $\Omega_n^{(z)} = \Omega_n^{(z)+} + \Omega_n^{(z)-}$. To establish a connection to QHE, we study the total spin Berry curvature of states below a certain energy, $C^s(\varepsilon) = (1/2\pi)\int_{BZ}\sum_{\varepsilon_{n,k}<\varepsilon}\Omega_n^{(z)}d^2k$.

As a comparison, we first study the Berry curvature accumulation as a function of energy. For a ferromagnetic square lattice with fictitious magnetic flux $\Phi_m = Ba^2/2\pi = p/q$ (a is the lattice constant, and p, q are integers that don't share any common factor) in each unit cell, if we choose a Landau gauge $\boldsymbol{A}_m = (By, 0, 0)$, the effective magnetic unit cell becomes a rectangle with size $(1 \times q)a^2$, one unit cell in the x-direction and q unit cells in the y-direction. After performing the Holstein-Primakoff transformation, the magnon Hamiltonian reads $H = JS\sum_{\boldsymbol{k}} \Psi_{\boldsymbol{k}}^\dagger H_{\boldsymbol{k}} \Psi_{\boldsymbol{k}}$ with $\Psi_{\boldsymbol{k}} = (a_{1,\boldsymbol{k}}, a_{2,\boldsymbol{k}}, \cdots, a_{q,\boldsymbol{k}})^T$ and

$$H_{\boldsymbol{k}} = \begin{bmatrix} h_1 & -e^{ik_ya} & 0 & \cdots & 0 & -e^{-ik_ya} \\ -e^{-ik_ya} & h_2 & -e^{ik_ya} & \cdots & 0 & 0 \\ 0 & -e^{-ik_ya} & h_3 & \cdots & 0 & 0 \\ \vdots & \vdots & \vdots & \ddots & \vdots & \vdots \\ 0 & 0 & 0 & \cdots & h_{q-1} & -e^{ik_ya} \\ -e^{ik_ya} & 0 & 0 & \cdots & -e^{-ik_ya} & h_q \end{bmatrix} \tag{5.55}$$

where $h_j = 4 - 2\cos(k_x a - 2\pi jp/q)$. It's easy to envision that the basis vectors for the lattice of magnetic unit cells still point in the x, y directions but with the y-direction basis vector elongated to q times longer. Based on the Hamiltonian above, the results for the total Berry curvature and the magnon density of states (DOS) are shown in Figs. 5.3(a) and (b) where we choose $p = 1$ and $q = 77$ to replicate the flux produced by two skyrmions in an SkX unit cell of 14×22 atoms (see Fig. 5.1). We observe a behavior associated with the van Hove singularity [249] of the magnon band structure. This causes a sign change in the total Berry curvature at the transition between particle- and hole-like states [250, 251].

For AFM magnons, we choose $p = 2$ and $q = 270$ for the magnon topological insulator model to replicate AFM SkX on a lattice of 18×30 atoms (which will be discussed later). The total spin Berry curvature shown in Fig. 5.3(d) exhibits steps of 2 and uneven energy height even in the long wavelength limit. We observe sharp change in the spin Berry curvature at the DOS singularity in Fig. 5.3(c).

For both FM and AFM magnons, away from the DOS singularity the formation of magnon Landau levels can be described by the Onsager quantization scheme [252, 253]. We confirm this by comparing the semiclassical curve corresponding to the area enclosed by DOS with the Berry curvature curves in Fig. 5.3. The spin Nernst response is shown in Fig. 5.4.

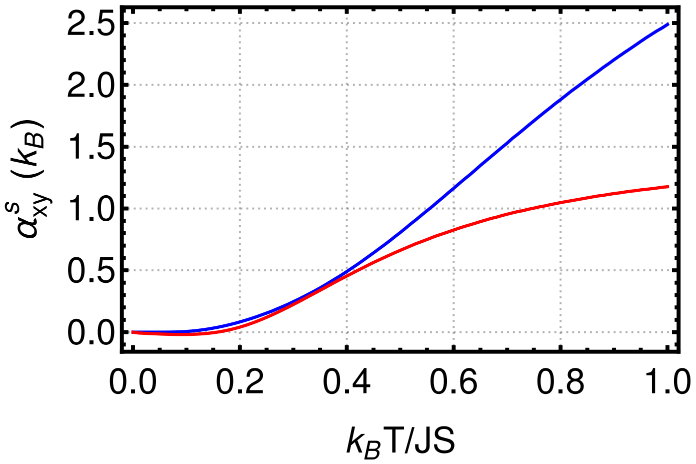

Figure 5.4: Spin Nernst conductivity as a function of temperature. The red curve describes the topological spin Nernst response for square lattice AFM with a unit cell of 18×30 atoms containing two skyrmions. The blue curve describes the spin Nernst response in AFM magnonic topological insulator with DMI induced fictitious flux $\Phi = \frac{p}{q}\Phi_0$ for $p = 2$ and $q = 270$.

5.7 Topological spin Nernst effect in AFM

To describe magnon excitations on top of textures in Fig. 5.1, we use the Holstein-Primakoff transformation in a local frame [145]. The resulting Hamiltonian describes non-interacting magnons and can be diagonalized using the paraunitary matrices $T_{\boldsymbol{k}}$. The spectrum for the lowest bands of a lattice contaning 18×30 atoms is shown in Fig. 5.2. We observe that the Landau levels become dispersive and that AFM chiral modes split. The total sublattice Berry curvature is shown in Fig. 5.3(d) where we use sublattice index instead of spin index in Eq. (5.53). The sublattice index in Eq. (5.3) and spin index in Eq. (5.51) can be mapped onto each other in the absence of coupling between chiral modes. We observe only qualitative agreement with Landau levels in AFM calculated earlier for $p = 2$ and $q = 270$

due to coupling of chiral modes in AFM SkX as a consequence of higher order corrections. In Fig. 5.3(b), we observe better agreement between Berry curvatures calculated for FM SkX (lattice of 14×22 atoms) and for Landau levels in FM with DMI induced uniform flux ($p = 1$ and $q = 77$). The sign change of the Berry curvatures in Figs. 5.3(b) and (d) can lead to the sign change of the topological thermal Hall and spin Nernst responses as a function of temperature. Using the spin Berry curvature, we calculate the topological spin Nernst response in Fig. 5.4 and confirm the sign change. As expected, the spin Nernst response in AFM SkX is suppressed compared to similar response in AFM topological insulator (see Fig. 5.4).

5.8 Summary

We have shown that AFM-SkX should exhibit a large topological spin Nernst response. The spin response is associated with the formation of dispersive Landau levels. AFM magnon Landau levels exhibit relativistic physics which in the long wavelength limit can be described by the Klein-Gordon equation. Similar physics also arises in the AFM square vortex-antivortex phase. To further uncover this behavior, we have constructed a model of AFM topological insulator where the fictitious flux is induced by inhomogeneous DMI and leads to the formation of an unconventional Hofstadter butterfly. Our predictions can be tested in magnetoelectrics where the staggered field can be induced by the boundary magnetization [254]. The spin Nernst response can be potentially observed in ferrimagnets, e.g., similar to TmIG [255].

Chapter 6

Conclusion and outlook

As a key element of the magnetic insulator, magnons contribute rich physics ranging from band structure topology to various kinds of transport phenomena. The research on magnon physics is always inspired by the prosperous development of electronic systems, partially because they both are (quasi-)particles and possess intrinsic spin freedom, while the differences between the two systems also provide appealing reasons to study one or the other. Electrons have both spin and orbital freedoms, which makes for diverse topology. Many types of quantum response can only be found for electrons, not bosons (magnons), because of the Fermi-Dirac distribution. The coupling between electrons and electromagnetic field gives a handle on the transport by taking advantage of diverse band structures in a solid. On the other hand, magnon transport has no Joule heating due to decoupling with gauge field (except the Zeeman coupling). Due to the long coherent distance, spin waves can mediate long-distance information transport. The goal of this thesis is investigating the possible underlying nature or applicability of magnon physics, especially by following various successful examples in electronic systems.

In Chapter 2, we introduced our work on a 3D magnon topological insulator model protected by sublattice chiral symmetry. The work is stimulated by a surge of interest on generalizing the diversity of topological insulators from the fermion system to bosons, including magnons, photons, and phonons. In magnon systems, the main focus was on the realization of Weyl and Dirac spectrum and chiral edge states in a Chern insulator. However, the absence of Kramer pairs and orbital freedoms hinders the realization of the more fascinating $\mathbb{Z}_2$ topological insulator that holds a helical edge state in 2D and a Dirac cone surface state in 3D. Our work fills in the gap by constructing a 3D magnon topological insulator model with a surface Dirac cone. An essential point for such a model is that it is protected by a feasible sublattice symmetry for magnons instead of time-reversal symmetry. Therefore, this kind of model belongs to a $\mathbb{Z}$ classification (AIII class) in the tenfold way classification of topological insulators. We show that the magnon chiral topological insulator (mcTI) can be realized in a Heisenberg model endowed with the Dzyaloshinskii-Moriya interaction (DMI) in a layered honeycomb lattice structure. All interactions are chosen such that the system possesses the chiral symmetry: the Hamiltonian anticommutes with a chiral operator. The bulk is characterized by a topological invariant: winding number, which is also equal to the number of surface Dirac cones as a result of the bulk-boundary correspondence, provided the chiral symmetry is not broken on the surface. At the same time, the helical surface states lack backscattering in the presence of the chiral symmetry. By breaking the chiral symmetry, a small gap can be introduced in the surface band, which leads to the magnon Hall response, e.g., under a temperature gradient. This is analogous to the quantum Hall effect on the surface of a topological insulator. Finally, we show that the model exhibits a rich phase diagram in parameter space, which covers mcTI, nodal line, three-dimensional magnon anomalous Hall, and Weyl magnon phases.

This work can be regarded as a springboard for exploring possible 3D topological magnon phases. Though the model includes seemingly unrealistic interlayer couplings and DMI, it could be possibly realized in the van der Waals magnets with careful fabrication. More importantly, the idea of creating a bosonic topological insulator protected by chiral symmetry is inspiring because it could be transplanted to other bosonic systems, e.g., acoustic or photonic systems. At the same time, searching for other different and realistic structures with chiral symmetry in magnetic materials is also a continuing direction for exploration.

In Chapter 3, we studied the magnon-mediated intrinsic transverse spin current induced by a longitudinal temperature gradient (spin Nernst effect) in a noncollinear antiferromagnet (NAFM) insulator. Compared to collinear systems, the spin current in noncollinear antiferromagnets can be polarized along any direction, which adds to the control of spin current in an insulator. The main difficulty of discussing spin current in NAFMs is magnon spin nonconservation due to noncollinear ground-state background. We overcome this difficulty by drawing an analogy with the scenario of spin Hall effect where spin-orbit coupling usually breaks spin conservation. The spin current can be defined if an accompanying spin-torque term is clearly identified. As for the response theory to a temperature gradient, we used a pseudogravitational field to incorporate the gradient field in a linear response frame. In addition to the typical Kubo-formula contribution, we also identify a dipole contribution which originates from a correction to the spin current operator due to the pseudogravitational field. This dipole contribution can be calculated by a thermodynamic approach which is generally useful in treating the equilibrium average of an observable containing spatial variables. In principle, the formula we obtained can be generalized to other bosonic systems for calculating other temperature-gradient-induced response. Finally, we applied our theory to a kagome NAFM $\mathrm{KFe_3(OH)_6(SO_4)_2}$ and found a sizable response. It is worth noticing that the response coefficient is always restricted by the magnetic point group symmetry of a given material.

With this theory of spin Nernst effect in NAFMs, we expect further studies could be focused on searching for materials and potential applications of this effect. In general, any systems with noncollinear spin order can be used to generate magnon-mediated transverse spin current. In three dimensions, more magnetic materials with noncollinearity are available, which allows more control of spin polarization. In Chapter 5, we also applied this theory to discuss spin transport in an antiferromagnet skyrmion crystal. In regard to application, the spin Nernst response could be used to detect the ground-state information of quantum magnet materials, as the response signal is very sensitive to spin order configurations. Moreover, designing a spin source (injector) based on NAFMs also seems promising in the study of spintronics.

In Chapter 4, we moved our attention to the spin polarization in fully compensated antiferromagnets. The motivation comes from the famous Edelstein effect due to which a uniform spin accumulation can be generated by applying an electric field in an electron gas with Rashba spin-orbit coupling. The key features of the system are zero equilibrium spin density and the spin-orbit coupling that breaks inversion symmetry and the spin conservation. We generalize this effect to magnons in noncollinear antiferromagnets (NAFMs), where equilibrium magnon spin density also vanishes and spin conservation is naturally lost due to the noncollinearity of spin arrangement. Moreover, through basic symmetry argument, it is found that the inversion asymmetry is also required as otherwise, the related response function will vanish. In NAFMs, we could either pay attention to noncentrosymmetric materials (e.g., breathing pyrochlore) or supply the materials with a Rashba-like DMI (e.g., a kagome layer on a substrate). In an electron gas, the nonequilibrium state is driven by an electric field, while for the charge neutral magnons the driving force is a temperature gradient. The developed response theory is reminiscent of the theory in Chapter 3. We divided the magnon spin polarization response function into intrinsic and extrinsic parts, which are respectively independent and dependent on the magnon lifetime. It is also found that these two parts behave differently under time reversal and are restricted in different ways by the magnetic point group symmetry of materials. We proposed three models for the effect, including spin chain, kagome NAFM, and pyrochlore NAFM, and further performed computer experiments on the spin chain model to verify our findings. According to our estimation, the accumulated spin density is detectable in experiment.

Given the importance of the Edelstein effect in spintronics, its magnonic analog, in principle, should also bring new vitality to spintronics research. Further studies on this effect could be in the following directions. First, the experimental confirmation will be an important step. This effect can be tested by transport measurements similar to those used for detection of the inverse spin Hall effect, by magneto-optical Kerr microscopy, or by magnetic sensing based on the nitrogen-vacancy centers. Second, on account of the diversity of antiferromagnetic materials, finding a suitable material that can optimize the effect deserves some effort. Finally, considering its potential application is also an interesting question. Like the spin Nernst effect discussed in Chapter 3, the effect could also be used to make spin sources, or detect the ground state of quantum magnets as implied by the connection between response coefficients and the underlying spin structure.

In Chapter 5, we continued the exploration of magnon-mediated spin transport, the spin Nernst effect, in a bipartite antiferromagnet (AFM) system, instead of NAFM. The focus in this chapter is magnon transport in a spin texture, which is essentially treated by using the formula developed in Chapters 3 and 4. However, the understanding of the underlying mechanism is enhanced by considering spin-texture-induced fictitious magnetic field in a long-wavelength limit. We first generated a new phase diagram that identifies the AFM skyrmion crystal and vortex-antivortex square lattice phases. These two phases are ideal platforms for the spin-texture induced spin Nernst effect, which is alternatively recognized as a topological Nernst effect duo to its association with the topological spin texture. Due to the aforementioned fictitious magnetic field, the magnon spectrum approximately forms unevenly spaced Landau levels, which originate from the fact that the long-wavelength description of magnons in such systems can be roughly mapped to the Klein-Gordon equation of a charged particle in a magnetic field. In this sense, the transverse spin transport is due to the magnon Landau-level structure. Nevertheless, by numerical calculation, we find this picture is far from accurate, though it is conceptually transparent. To further appreciate the interesting Landau levels of a Klein-Gordon equation, we develop a new magnon AFM topological insulator (TI) model, which could exactly map to the equation in the long-wavelength limit and thus forms exact uneven magnon Landau levels. Interestingly, we numerically investigated the quantum Hall signature of this model, the accumulated spin Chern number in energy regime, and found that a clear step formed. Moreover, a similar quantity in AFM skyrmion crystal shows qualitative agreement with the magnon TI model, which confirms the validity of the Landau-level picture on a qualitative level in the skyrmion case.

Aside from the understanding of the intrinsic mechanism mentioned above, the work brings out two surprising results: (1) the spin response magnitude in both AFM skyrmion crystal and AFM magnon TI are unexpectedly large, which makes the response promising for experimental observation and application in spintronics, e.g., as a spin current source; (2) the magnon AFM topological insulator model shows a new Hofstadter butterfly as the signature of the uneven Landal levels, which can serve as a smoking gun for experimentalists to confirm the new physics.

Overall, this thesis investigated the rich magnon physics in various systems. A systematic framework of theoretically treating the magnon-mediated spin transport in magnetic insulators and its connection with band topology were extensively discussed. Though many of the results obtained are still waiting for experimental observation, the useful theoretical tools and interesting predictions provided by this thesis already demonstrate the appealing aspects of magnon physics. Furthermore, more exciting physics in magnetic systems could be boosted by this thesis. For instance, all the topics here focus on low temperature, where the magnon picture is valid. If one goes to higher temperatures, representations other than magnons, e.g., Schwinger bosons, need to be considered. The results here will fail to capture the physics, but they can still provide some insight for possible extensions.

References

[1] K. v. Klitzing, G. Dorda, and M. Pepper. New Method for High-Accuracy Determination of the Fine-Structure Constant Based on Quantized Hall Resistance. *Phys. Rev. Lett.*, 45:494–497, Aug 1980.

[2] R. B. Laughlin. Quantized Hall conductivity in two dimensions. *Phys. Rev. B*, 23:5632–5633, May 1981.

[3] D. J. Thouless, M. Kohmoto, M. P. Nightingale, and M. den Nijs. Quantized Hall Conductance in a Two-Dimensional Periodic Potential. *Phys. Rev. Lett.*, 49:405–408, Aug 1982.

[4] F. D. M. Haldane. Model for a Quantum Hall Effect without Landau Levels: Condensed-Matter Realization of the "Parity Anomaly". *Phys. Rev. Lett.*, 61:2015–2018, Oct 1988.

[5] Naoto Nagaosa, Jairo Sinova, Shigeki Onoda, A. H. MacDonald, and N. P. Ong. Anomalous Hall effect. *Rev. Mod. Phys.*, 82:1539–1592, May 2010.

[6] Cui-Zu Chang, Jinsong Zhang, Xiao Feng, Jie Shen, Zuocheng Zhang, Minghua Guo, Kang Li, Yunbo Ou, Pang Wei, Li-Li Wang, Zhong-Qing Ji, Yang Feng, Shuaihua Ji, Xi Chen, Jinfeng Jia, Xi Dai, Zhong Fang, Shou-Cheng Zhang, Ke He, Yayu Wang, Li Lu, Xu-Cun Ma, and Qi-Kun Xue. Experimental Observation of the Quantum Anomalous Hall Effect in a Magnetic Topological Insulator. *Science*, 340(6129):167–170, 2013.

[7] C. L. Kane and E. J. Mele. Quantum Spin Hall Effect in Graphene. *Phys. Rev. Lett.*, 95:226801, Nov 2005.

[8] B. Andrei Bernevig, Taylor L. Hughes, and Shou-Cheng Zhang. Quantum Spin Hall Effect and Topological Phase Transition in HgTe Quantum Wells. *Science*, 314(5806):1757–1761, 2006.

[9] Jairo Sinova, Sergio O. Valenzuela, J. Wunderlich, C. H. Back, and T. Jungwirth. Spin Hall effects. *Rev. Mod. Phys.*, 87:1213–1260, Oct 2015.

[10] Y. Zhang, N. P. Ong, Z. A. Xu, K. Krishana, R. Gagnon, and L. Taillefer. Determining the Wiedemann-Franz Ratio from the Thermal Hall Conductivity: Application to Cu and $\mathrm{YBa_2Cu_3}O_{6.95}$. *Phys. Rev. Lett.*, 84:2219–2222, Mar 2000.

[11] C. Strohm, G. L. J. A. Rikken, and P. Wyder. Phenomenological Evidence for the Phonon Hall Effect. *Phys. Rev. Lett.*, 95:155901, Oct 2005.

[12] M. Z. Hasan and C. L. Kane. Colloquium: Topological insulators. *Rev. Mod. Phys.*, 82:3045–3067, Nov 2010.

[13] Xiao-Liang Qi and Shou-Cheng Zhang. Topological insulators and superconductors. *Rev. Mod. Phys.*, 83:1057–1110, Oct 2011.

[14] N. P. Armitage, E. J. Mele, and Ashvin Vishwanath. Weyl and Dirac semimetals in three-dimensional solids. *Rev. Mod. Phys.*, 90:015001, Jan 2018.

[15] Igor Žutić, Jaroslav Fabian, and S. Das Sarma. Spintronics: Fundamentals and applications. *Rev. Mod. Phys.*, 76:323–410, Apr 2004.

[16] Wenchao Tian, Wenbo Yu, Jing Shi, and Yongkun Wang. The Property, Preparation and Application of Topological Insulators: A Review. *Materials*, 10(7), 2017.

[17] Joel E. Moore. The birth of topological insulators. *Nature*, 464(7286):194–198, Mar 2010.

[18] Se Kwon Kim, Héctor Ochoa, Ricardo Zarzuela, and Yaroslav Tserkovnyak. Realization of the Haldane-Kane-Mele Model in a System of Localized Spins. *Phys. Rev. Lett.*, 117:227201, Nov 2016.

[19] S A Owerre. Magnonic analogs of topological Dirac semimetals. *J. Phys. Commun.*, 1(2):025007, sep 2017.

[20] Alexander Mook, Jürgen Henk, and Ingrid Mertig. Edge states in topological magnon insulators. *Phys. Rev. B*, 90:024412, Jul 2014.

[21] Fei-Ye Li, Yao-Dong Li, Yong Baek Kim, Leon Balents, Yue Yu, and Gang Chen. Weyl magnons in breathing pyrochlore antiferromagnets. *Nat.Commun.*, 7:12691, Sep 2016.

[22] Vladimir A. Zyuzin and Alexey A. Kovalev. Spin Hall and Nernst effects of Weyl magnons. *Phys. Rev. B*, 97:174407, May 2018.

[23] Ying Su, X. S. Wang, and X. R. Wang. Magnonic Weyl semimetal and chiral anomaly in pyrochlore ferromagnets. *Phys. Rev. B*, 95:224403, Jun 2017.

[24] Bo Li and Alexey A. Kovalev. Chiral topological insulator of magnons. *Phys. Rev. B*, 97:174413, May 2018.

[25] Cheng He, Xu Ni, Hao Ge, Xiao-Chen Sun, Yan-Bin Chen, Ming-Hui Lu, Xiao-Ping Liu, and Yan-Feng Chen. Acoustic topological insulator and robust one-way sound transport. *Nat. Phys.*, 12:1124, Aug 2016.

[26] Zhaoju Yang, Fei Gao, Xihang Shi, Xiao Lin, Zhen Gao, Yidong Chong, and Baile Zhang. Topological Acoustics. *Phys. Rev. Lett.*, 114:114301, Mar 2015.

[27] Tomoki Ozawa, Hannah M. Price, Alberto Amo, Nathan Goldman, Mohammad Hafezi, Ling Lu, Mikael C. Rechtsman, David Schuster, Jonathan Simon, Oded Zil-

berberg, and Iacopo Carusotto. Topological photonics. *Rev. Mod. Phys.*, 91:015006, Mar 2019.

[28] Hosho Katsura, Naoto Nagaosa, and Patrick A. Lee. Theory of the Thermal Hall Effect in Quantum Magnets. *Phys. Rev. Lett.*, 104:066403, Feb 2010.

[29] Y. Onose, T. Ideue, H. Katsura, Y. Shiomi, N. Nagaosa, and Y. Tokura. Observation of the Magnon Hall Effect. *Science*, 329(5989):297–299, 2010.

[30] Ryo Matsumoto and Shuichi Murakami. Theoretical Prediction of a Rotating Magnon Wave Packet in Ferromagnets. *Phys. Rev. Lett.*, 106:197202, May 2011.

[31] Ryo Matsumoto and Shuichi Murakami. Rotational motion of magnons and the thermal Hall effect. *Phys. Rev. B*, 84:184406, Nov 2011.

[32] Lifa Zhang, Jie Ren, Jian-Sheng Wang, and Baowen Li. Topological magnon insulator in insulating ferromagnet. *Phys. Rev. B*, 87:144101, Apr 2013.

[33] Ryuichi Shindou, Ryo Matsumoto, Shuichi Murakami, and Jun-ichiro Ohe. Topological chiral magnonic edge mode in a magnonic crystal. *Phys. Rev. B*, 87:174427, May 2013.

[34] Ryuichi Shindou, Jun-ichiro Ohe, Ryo Matsumoto, Shuichi Murakami, and Eiji Saitoh. Chiral spin-wave edge modes in dipolar magnetic thin films. *Phys. Rev. B*, 87:174402, May 2013.

[35] Alexander Mook, Jürgen Henk, and Ingrid Mertig. Magnon Hall effect and topology in kagome lattices: A theoretical investigation. *Phys. Rev. B*, 89:134409, Apr 2014.

[36] S. K. Kim, H. Ochoa, R. Zarzuela, and Y. Tserkovnyak. Realization of the Haldane-Kane-Mele Model in a System of Localized Spins. *Phys. Rev. Lett.*, 117(22):227201, November 2016.

[37] S A Owerre. A first theoretical realization of honeycomb topological magnon insulator, journal = J. Phys. Condens. Matter. 28(38):386001, jul 2016.

[38] Vladimir A. Zyuzin and Alexey A. Kovalev. Magnon Spin Nernst Effect in Antiferromagnets. *Phys. Rev. Lett.*, 117:217203, Nov 2016.

[39] Ran Cheng, Satoshi Okamoto, and Di Xiao. Spin Nernst Effect of Magnons in Collinear Antiferromagnets. *Phys. Rev. Lett.*, 117:217202, Nov 2016.

[40] Pontus Laurell and Gregory A. Fiete. Magnon thermal Hall effect in kagome antiferromagnets with Dzyaloshinskii-Moriya interactions. *Phys. Rev. B*, 98:094419, Sep 2018.

[41] Yalei Lu, Xing Guo, Vladimir Koval, and Chenglong Jia. Topological thermal Hall effect driven by spin-chirality fluctuations in frustrated antiferromagnets. *Phys. Rev. B*, 99:054409, Feb 2019.

[42] S. A. Owerre. Topological thermal Hall effect in frustrated kagome antiferromagnets. *Phys. Rev. B*, 95:014422, Jan 2017.

[43] Hayato Doki, Masatoshi Akazawa, Hyun-Yong Lee, Jung Hoon Han, Kaori Sugii, Masaaki Shimozawa, Naoki Kawashima, Migaku Oda, Hiroyuki Yoshida, and Minoru Yamashita. Spin Thermal Hall Conductivity of a Kagome Antiferromagnet. *Phys. Rev. Lett.*, 121:097203, Aug 2018.

[44] Alexander Mook, Jürgen Henk, and Ingrid Mertig. Thermal Hall effect in noncollinear coplanar insulating antiferromagnets. *Phys. Rev. B*, 99:014427, Jan 2019.

[45] Kangkang Li, Chenyuan Li, Jiangping Hu, Yuan Li, and Chen Fang. Dirac and Nodal Line Magnons in Three-Dimensional Antiferromagnets. *Phys. Rev. Lett.*, 119:247202, Dec 2017.

[46] F.-Y. Li, Y.-D. Li, Y. B. Kim, L. Balents, Y. Yu, and G. Chen. Weyl magnons in breathing pyrochlore antiferromagnets. *Nat. Commun.*, 7:12691, September 2016.

[47] A. Mook, J. Henk, and I. Mertig. Tunable Magnon Weyl Points in Ferromagnetic Pyrochlores. *Phys. Rev. Lett.*, 117(15):157204, October 2016.

[48] Y. Su, X. S. Wang, and X. R. Wang. Magnonic Weyl semimetal and chiral anomaly in pyrochlore ferromagnets. *Phys. Rev. B*, 95(22):224403, June 2017.

[49] Ying Su and X. R. Wang. Chiral anomaly of Weyl magnons in stacked honeycomb ferromagnets. *Phys. Rev. B*, 96:104437, Sep 2017.

[50] S. A. Owerre. Weyl magnons in noncoplanar stacked kagome antiferromagnets. *Phys. Rev. B*, 97:094412, Mar 2018.

[51] Shao-Kai Jian and Wenxing Nie. Weyl magnons in pyrochlore antiferromagnets with an all-in-all-out order. *Phys. Rev. B*, 97:115162, Mar 2018.

[52] Jonathan Cookmeyer and Joel E. Moore. Spin-wave analysis of the low-temperature thermal Hall effect in the candidate Kitaev spin liquid $\alpha - RuCl_3$. *Phys. Rev. B*, 98:060412, Aug 2018.

[53] A. Auerbach. *Interacting Electrons and Quantum Magnetism*. Graduate Texts in Contemporary Physics. Springer New York, 1998.

[54] Carsten Timm. Theory of Magnetism (lecture note). 2015.

[55] Alexei Kitaev. Anyons in an exactly solved model and beyond. *Annals of Physics*, 321(1):2 – 111, 2006. January Special Issue.

[56] Shun-Qing Shen. Topological insulators. Dirac equation in condensed matters, Jul 2012.

[57] Bogdan Andrei Bernevig and Taylor L. Hughes. *Topological insulators and topological superconductors*. Princeton University Press, United States, March 2013.

[58] H. Katsura, N. Nagaosa, and P. A. Lee. Theory of the Thermal Hall Effect in Quantum Magnets. *Phys. Rev. Lett.*, 104(6):066403, February 2010.

[59] Alexander Mook, Jürgen Henk, and Ingrid Mertig. Edge states in topological magnon insulators. *Phys. Rev. B*, 90:024412, Jul 2014.

[60] A. Mook, J. Henk, and I. Mertig. Topologically nontrivial magnons at an interface of two kagome ferromagnets. *Phys. Rev. B*, 91(22):224411, June 2015.

[61] H. Lee, J. H. Han, and P. A. Lee. Thermal Hall effect of spins in a paramagnet. *Phys. Rev. B*, 91(12):125413, March 2015.

[62] S. A. Owerre. Topological honeycomb magnon Hall effect: A calculation of thermal Hall conductivity of magnetic spin excitations. *J. Appl. Phys.*, 120(4):043903, July 2016.

[63] Kyusung Hwang, Nandini Trivedi, and Mohit Randeria. Topological magnons with nodal-line and triple-point degeneracies: Implications for thermal Hall effect in pyrochlore iridates. page arXiv:1712.08170, Dec 2017.

[64] P. A. McClarty, X.-Y. Dong, M. Gohlke, J. G. Rau, F. Pollmann, R. Moessner, and K. Penc. Topological Magnons in Kitaev Magnets at High Fields. *arXiv*, February 2018.

[65] Hosho Katsura, Naoto Nagaosa, and Alexander V. Balatsky. Spin Current and Magnetoelectric Effect in Noncollinear Magnets. *Phys. Rev. Lett.*, 95:057205, Jul 2005.

[66] R. Chisnell, J. S. Helton, D. E. Freedman, D. K. Singh, R. I. Bewley, D. G. Nocera, and Y. S. Lee. Topological Magnon Bands in a Kagome Lattice Ferromagnet. *Phys. Rev. Lett.*, 115:147201, Sep 2015.

[67] S A Owerre. A first theoretical realization of honeycomb topological magnon insulator. *J. Phys.: Condens. Matter*, 28(38):386001, 2016.

[68] R. Chisnell, J. S. Helton, D. E. Freedman, D. K. Singh, F. Demmel, C. Stock, D. G. Nocera, and Y. S. Lee. Magnetic transitions in the topological magnon insulator Cu(1,3-bdc). *Phys. Rev. B*, 93:214403, Jun 2016.

[69] Pontus Laurell and Gregory A. Fiete. Topological Magnon Bands and Unconventional Superconductivity in Pyrochlore Iridate Thin Films. *Phys. Rev. Lett.*, 118:177201, Apr 2017.

[70] X. S. Wang, Ying Su, and X. R. Wang. Topologically protected unidirectional edge spin waves and beam splitter. *Phys. Rev. B*, 95:014435, Jan 2017.

[71] X. S. Wang, H. W. Zhang, and X. R. Wang. Reconfigurable topological spin wave beamsplitters and interferometers. *arXiv*, June 2017.

[72] Kouki Nakata, Se Kwon Kim, Jelena Klinovaja, and Daniel Loss. Magnonic topological insulators in antiferromagnets. *Phys. Rev. B*, 96:224414, Dec 2017.

[73] A Roldán-Molina, A S Nunez, and J Fernández-Rossier. Topological spin waves in the atomic-scale magnetic skyrmion crystal. *New Journal of Physics*, 18(4):045015, 2016.

[74] Andreas Rückriegel, Arne Brataas, and Rembert A. Duine. Bulk and edge spin transport in topological magnon insulators. *Phys. Rev. B*, 97:081106, Feb 2018.

[75] P. A. Pantaleón and Y. Xian. Edge on-site potential effects in a honeycomb topological magnon insulator. *arXiv*, January 2018.

[76] Ki Hoon Lee, Suk Bum Chung, Kisoo Park, and Je-Geun Park. Magnonic quantum spin Hall state in the zigzag and stripe phases of the antiferromagnetic honeycomb lattice. *Phys. Rev. B*, 97:180401, May 2018.

[77] Karin Everschor-Sitte and Matthias Sitte. Real-space Berry phases: Skyrmion soccer (invited). *Journal of Applied Physics*, 115(17):172602, 2014.

[78] A. Neubauer, C. Pfleiderer, B. Binz, A. Rosch, R. Ritz, P. G. Niklowitz, and P. Böni. Topological Hall Effect in the A Phase of MnSi. *Phys. Rev. Lett.*, 102:186602, May 2009.

[79] Alexey A. Kovalev and Yaroslav Tserkovnyak. Thermomagnonic spin transfer and Peltier effects in insulating magnets. *EPL (Europhysics Letters)*, 97(6):67002, March 2012.

[80] Matthew W. Daniels, Ran Cheng, Weichao Yu, Jiang Xiao, and Di Xiao. Nonabelian magnonics in antiferromagnets. *Phys. Rev. B*, 98:134450, Oct 2018.

[81] Se Kwon Kim, Kouki Nakata, Daniel Loss, and Yaroslav Tserkovnyak. Tunable Magnonic Thermal Hall Effect in Skyrmion Crystal Phases of Ferrimagnets. *Phys. Rev. Lett.*, 122:057204, Feb 2019.

[82] Henrik Bruus and Karsten Flensberg. *Many-body quantum theory in condensed matter physics - an introduction*. Oxford University Press, United States, 2004.

[83] A. B. Khanikaev, S. Hossein Mousavi, W.-K. Tse, M. Kargarian, A. H. MacDonald, and G. Shvets. Photonic topological insulators. *Nat. Mater.*, 12:233–239, March 2013.

[84] R. Süsstrunk and S. D. Huber. Classification of topological phonons in linear mechanical metamaterials. *PNAS*, 113:E4767–E4775, August 2016.

[85] Andreas P. Schnyder, Shinsei Ryu, Akira Furusaki, and Andreas W. W. Ludwig. Classification of topological insulators and superconductors in three spatial dimensions. *Phys. Rev. B*, 78:195125, Nov 2008.

[86] Shinsei Ryu, Andreas P Schnyder, Akira Furusaki, and Andreas W W Ludwig. Topological insulators and superconductors: tenfold way and dimensional hierarchy. *New J. Phys.*, 12(6):065010, 2010.

[87] Pavan Hosur, Shinsei Ryu, and Ashvin Vishwanath. Chiral topological insulators, superconductors, and other competing orders in three dimensions. *Phys. Rev. B*, 81:045120, Jan 2010.

[88] S.-T. Wang, D.-L. Deng, and L.-M. Duan. Probe of Three-Dimensional Chiral Topological Insulators in an Optical Lattice. *Phys. Rev. Lett.*, 113:033002, Jul 2014.

[89] Kazuki Hasebe. Chiral topological insulator on Nambu 3-algebraic geometry. *Nucl. Phys. B*, 886(Supplement C):681 – 690, 2014.

[90] Linhu Li, Chuanhao Yin, Shu Chen, and Miguel A. N. Araújo. Chiral topological insulating phases from three-dimensional nodal loop semimetals. *Phys. Rev. B*, 95:121107, Mar 2017.

[91] I. Dzyaloshinsky. A thermodynamic theory of "weak" ferromagnetism of antiferromagnetics. *J. Phys. Chem. Solids*, 4:241–255, 1958.

[92] T. Moriya. Anisotropic Superexchange Interaction and Weak Ferromagnetism. *Phys. Rev.*, 120:91–98, October 1960.

[93] J. Fransson, A. M. Black-Schaffer, and A. V. Balatsky. Magnon Dirac materials. *Phys. Rev. B*, 94:075401, Aug 2016.

[94] Sergey S. Pershoguba, Saikat Banerjee, J. C. Lashley, Jihwey Park, Hans Ågren, Gabriel Aeppli, and Alexander V. Balatsky. Dirac Magnons in Honeycomb Ferromagnets. *Phys. Rev. X*, 8:011010, Jan 2018.

[95] N. Okuma. Magnon Spin-Momentum Locking: Various Spin Vortices and Dirac magnons in Noncollinear Antiferromagnets. *Phys. Rev. Lett.*, 119(10):107205, September 2017.

[96] Rui-Lin Chu, Junren Shi, and Shun-Qing Shen. Surface edge state and half-quantized Hall conductance in topological insulators. *Phys. Rev. B*, 84:085312, Aug 2011.

[97] Alexey A. Kovalev and Vladimir Zyuzin. Spin torque and Nernst effects in Dzyaloshinskii-Moriya ferromagnets. *Phys. Rev. B*, 93:161106, Apr 2016.

[98] A. A. Burkov and Leon Balents. Weyl Semimetal in a Topological Insulator Multilayer. *Phys. Rev. Lett.*, 107:127205, Sep 2011.

[99] M. E. Zhitomirsky and A. L. Chernyshev. Colloquium: Spontaneous magnon decays. *Rev. Mod. Phys.*, 85:219–242, Jan 2013.

[100] A. L. Chernyshev and P. A. Maksimov. Damped Topological Magnons in the Kagome-Lattice Ferromagnets. *Phys. Rev. Lett.*, 117:187203, Oct 2016.

[101] C. Gong, L. Li, Z. Li, H. Ji, A. Stern, Y. Xia, T. Cao, W. Bao, C. Wang, Y. Wang, Z. Q. Qiu, R. J. Cava, S. G. Louie, J. Xia, and X. Zhang. Discovery of intrinsic ferromagnetism in two-dimensional van der Waals crystals. *Nature*, 546:265–269, June 2017.

[102] B. Huang, G. Clark, E. Navarro-Moratalla, D. R. Klein, R. Cheng, K. L. Seyler, D. Zhong, E. Schmidgall, M. A. McGuire, D. H. Cobden, W. Yao, D. Xiao, P. Jarillo-Herrero, and X. Xu. Layer-dependent ferromagnetism in a van der Waals crystal down to the monolayer limit. *Nature*, 546:270–273, June 2017.

[103] Ludovicus Josephus de Jongh. *Magnetic properties of layered transition metal compounds*, volume 9. Springer Science & Business Media, Netherlands, 2012.

[104] Igor Žutić, Alex Matos-Abiague, Benedikt Scharf, Hanan Dery, and Kirill Belashchenko. Proximitized materials. *Mater. Today*, 22:85 – 107, 2019.

[105] Gerrit E. W. Bauer, Eiji Saitoh, and Bart J. van Wees. Spin caloritronics. *Nat. Mater.*, 11:391, Apr 2012.

[106] S. Meyer, Y.-T. Chen, S. Wimmer, M. Althammer, T. Wimmer, R. Schlitz, S. Geprägs, H. Huebl, D. Ködderitzsch, H. Ebert, G. E. W. Bauer, R. Gross, and S. T. B. Goennenwein. Observation of the spin Nernst effect. *Nat. Mater.*, 16:977, Sep 2017.

[107] A. Bose, S. Bhuktare, H. Singh, S. Dutta, V. G. Achanta, and A. A. Tulapurkar. Direct detection of spin nernst effect in platinum. *Appl. Phys. Lett.*, 112(16):162401, 2018.

[108] Y. Shiomi, R. Takashima, and E. Saitoh. Experimental evidence consistent with a magnon Nernst effect in the antiferromagnetic insulator $\mathrm{MnPS_3}$. *Phys. Rev. B*, 96:134425, Oct 2017.

[109] Yinhan Zhang, Satoshi Okamoto, and Di Xiao. Spin-Nernst effect in the paramagnetic regime of an antiferromagnetic insulator. *Phys. Rev. B*, 98:035424, Jul 2018.

[110] V. Baltz, A. Manchon, M. Tsoi, T. Moriyama, T. Ono, and Y. Tserkovnyak. Antiferromagnetic spintronics. *Rev. Mod. Phys.*, 90:015005, Feb 2018.

[111] Stephen M. Wu, Wei Zhang, Amit KC, Pavel Borisov, John E. Pearson, J. Samuel Jiang, David Lederman, Axel Hoffmann, and Anand Bhattacharya. Antiferromagnetic Spin Seebeck Effect. *Phys. Rev. Lett.*, 116:097204, Mar 2016.

[112] Ran Cheng, Jiang Xiao, Qian Niu, and Arne Brataas. Spin Pumping and Spin-Transfer Torques in Antiferromagnets. *Phys. Rev. Lett.*, 113:057601, Jul 2014.

[113] A. Manchon, J. Železný, I. M. Miron, T. Jungwirth, J. Sinova, A. Thiaville, K. Garello, and P. Gambardella. Current-induced spin-orbit torques in ferromagnetic and antiferromagnetic systems. *Rev. Mod. Phys.*, 91:035004, Sep 2019.

[114] Hua Chen, Qian Niu, and A. H. MacDonald. Anomalous Hall Effect Arising from Noncollinear Antiferromagnetism. *Phys. Rev. Lett.*, 112:017205, Jan 2014.

[115] Yang Zhang, Yan Sun, Hao Yang, Jakub Železný, Stuart P. P. Parkin, Claudia Felser, and Binghai Yan. Strong anisotropic anomalous Hall effect and spin Hall effect in

the chiral antiferromagnetic compounds Mn_3X ($X = \mathrm{Ge}$, Sn, Ga, Ir, Rh, and Pt). *Phys. Rev. B*, 95:075128, Feb 2017.

[116] Jakub Železný, Yang Zhang, Claudia Felser, and Binghai Yan. Spin-Polarized Current in Noncollinear Antiferromagnets. *Phys. Rev. Lett.*, 119:187204, Nov 2017.

[117] Alexander Mook, Robin R. Neumann, Jürgen Henk, and Ingrid Mertig. Spin Seebeck and spin Nernst effects of magnons in noncollinear antiferromagnetic insulators. *Phys. Rev. B*, 100:100401, Sep 2019.

[118] Benedetta Flebus, Yaroslav Tserkovnyak, and Gregory A. Fiete. Interfacial spin Seebeck effect in noncollinear magnetic systems. *Phys. Rev. B*, 99:224410, Jun 2019.

[119] Bowen Ma, Benedetta Flebus, and Gregory A. Fiete. Longitudinal Spin Seebeck effect in Pyrochlore Iridates with Bulk and Interfacial Dzyaloshinskii-Moriya interaction. Sep 2019.

[120] A. L. Chernyshev and M. E. Zhitomirsky. Quantum Selection of Order in an XXZ Antiferromagnet on a Kagome Lattice. *Phys. Rev. Lett.*, 113:237202, Dec 2014.

[121] A. L. Chernyshev and M. E. Zhitomirsky. Order and excitations in large$-S$ kagome-lattice antiferromagnets. *Phys. Rev. B*, 92:144415, Oct 2015.

[122] Ryutaro Okuma, Takeshi Yajima, Daisuke Nishio-Hamane, Tsuyoshi Okubo, and Zenji Hiroi. Weak ferromagnetic order breaking the threefold rotational symmetry of the underlying kagome lattice in $\mathrm{CdCu_3(OH)_6(NO_3)_2 \cdot H_2O}$. *Phys. Rev. B*, 95:094427, Mar 2017.

[123] C. Lacroix, P. Mendels, and F. Mila. *Introduction to Frustrated Magnetism: Materials, Experiments, Theory*. Springer Series in Solid-State Sciences. Springer Berlin Heidelberg, 2011.

[124] Wei Han, Sadamichi Maekawa, and Xin-Cheng Xie. Spin current as a probe of quantum materials. *Nature Materials*, August 2019.

[125] Masahiro Sato, Shintaro Takayoshi, and Takashi Oka. Laser-Driven Multiferroics and Ultrafast Spin Current Generation. *Phys. Rev. Lett.*, 117:147202, Sep 2016.

[126] Hiroaki Ishizuka and Masahiro Sato. Rectification of Spin Current in Inversion-Asymmetric Magnets with Linearly Polarized Electromagnetic Waves. *Phys. Rev. Lett.*, 122:197702, May 2019.

[127] Junren Shi, Ping Zhang, Di Xiao, and Qian Niu. Proper Definition of Spin Current in Spin-Orbit Coupled Systems. *Phys. Rev. Lett.*, 96:076604, Feb 2006.

[128] Ryo Matsumoto, Ryuichi Shindou, and Shuichi Murakami. Thermal Hall effect of magnons in magnets with dipolar interaction. *Phys. Rev. B*, 89:054420, Feb 2014.

[129] T. Holstein and H. Primakoff. Field Dependence of the Intrinsic Domain Magnetization of a Ferromagnet. *Phys. Rev.*, 58:1098–1113, Dec 1940.

[130] Christina Psaroudaki, Silas Hoffman, Jelena Klinovaja, and Daniel Loss. Quantum Dynamics of Skyrmions in Chiral Magnets. *Phys. Rev. X*, 7:041045, Nov 2017.

[131] J. M. Luttinger. Theory of Thermal Transport Coefficients. *Phys. Rev.*, 135:A1505–A1514, Sep 1964.

[132] Liang Dong, Cong Xiao, Bangguo Xiong, and Qian Niu. Berry-phase effects in dipole density and Mott relation. Dec 2018.

[133] Junren Shi, G. Vignale, Di Xiao, and Qian Niu. Quantum Theory of Orbital Magnetization and Its Generalization to Interacting Systems. *Phys. Rev. Lett.*, 99:197202, Nov 2007.

[134] Atsuo Shitade, Akito Daido, and Youichi Yanase. Theory of spin magnetic quadrupole moment and temperature-gradient-induced magnetization. *Phys. Rev. B*, 99:024404, Jan 2019.

[135] Yang Gao and Di Xiao. Orbital magnetic quadrupole moment and nonlinear anomalous thermoelectric transport. *Phys. Rev. B*, 98:060402, Aug 2018.

[136] Yang Gao, David Vanderbilt, and Di Xiao. Microscopic theory of spin toroidization in periodic crystals. *Phys. Rev. B*, 97:134423, Apr 2018.

[137] M. Seemann, D. Ködderitzsch, S. Wimmer, and H. Ebert. Symmetry-imposed shape of linear response tensors. *Phys. Rev. B*, 92:155138, Oct 2015.

[138] K. Matan, D. Grohol, D. G. Nocera, T. Yildirim, A. B. Harris, S. H. Lee, S. E. Nagler, and Y. S. Lee. Spin Waves in the Frustrated Kagomé Lattice Antiferromagnet $\mathrm{KFe_3(OH)_6(SO_4)_2}$. *Phys. Rev. Lett.*, 96:247201, Jun 2006.

[139] A. L. Chernyshev. Strong quantum effects in an almost classical antiferromagnet on a kagome lattice. *Phys. Rev. B*, 92:094409, Sep 2015.

[140] K. Matan, B. M. Bartlett, J. S. Helton, V. Sikolenko, S. Mat'aš, K. Prokeš, Y. Chen, J. W. Lynn, D. Grohol, T. J. Sato, M. Tokunaga, D. G. Nocera, and Y. S. Lee. Dzyaloshinskii-Moriya interaction and spin reorientation transition in the frustrated kagome lattice antiferromagnet. *Phys. Rev. B*, 83:214406, Jun 2011.

[141] T. Inami, T. Morimoto, M. Nishiyama, S. Maegawa, Y. Oka, and H. Okumura. Magnetic ordering in the kagomé lattice antiferromagnet $\mathrm{KCr_3(OD)_6(SO_4)_2}$. *Phys. Rev. B*, 64:054421, Jul 2001.

[142] A. Zorko, F. Bert, A. Ozarowski, J. van Tol, D. Boldrin, A. S. Wills, and P. Mendels. Dzyaloshinsky-Moriya interaction in vesignieite: A route to freezing in a quantum kagome antiferromagnet. *Phys. Rev. B*, 88:144419, Oct 2013.

[143] K. Kimura, S. Nakatsuji, and T. Kimura. Experimental realization of a quantum breathing pyrochlore antiferromagnet. *Phys. Rev. B*, 90:060414, Aug 2014.

[144] Yu Tanaka, Makoto Yoshida, Masashi Takigawa, Yoshihiko Okamoto, and Zenji Hiroi. Novel Phase Transitions in the Breathing Pyrochlore Lattice: $^7\mathrm{Li}-\mathrm{NMR}$ on $\mathrm{LiInCr_4O_8}$ and $\mathrm{LiGaCr_4O_8}$. *Phys. Rev. Lett.*, 113:227204, Nov 2014.

[145] Sebastián A. Díaz, Jelena Klinovaja, and Daniel Loss. Topological Magnons and Edge States in Antiferromagnetic Skyrmion Crystals. *Phys. Rev. Lett.*, 122:187203, May 2019.

[146] AG Aronov and Yu B Lyanda-Geller. Nuclear electric resonance and orientation of carrier spins by an electric field. *JETP Lett.*, 50:431, 1989.

[147] V.M. Edelstein. Spin polarization of conduction electrons induced by electric current in two-dimensional asymmetric electron systems. *Solid State Commun.*, 73(3):233 – 235, 1990.

[148] S. D. Ganichev, M. Trushin, and J. Schliemann. In E. Y. Tsymbal and I. Žutić, editors, *Handbook of spin transport and magnetism*, page 487. CRC, Boca Raton, FL, 2011.

[149] Maxim Trushin and John Schliemann. Anisotropic current-induced spin accumulation in the two-dimensional electron gas with spin-orbit coupling. *Phys. Rev. B*, 75:155323, Apr 2007.

[150] A. Yu. Silov, P. A. Blajnov, J. H. Wolter, R. Hey, K. H. Ploog, and N. S. Averkiev. Current-induced spin polarization at a single heterojunction. *Appl. Phys. Lett.*, 85(24):5929–5931, 2004.

[151] C. L. Yang, H. T. He, Lu Ding, L. J. Cui, Y. P. Zeng, J. N. Wang, and W. K. Ge. Spectral Dependence of Spin Photocurrent and Current-Induced Spin Polarization in an $\mathrm{InGaAs/InAlAs}$ Two-Dimensional Electron Gas. *Phys. Rev. Lett.*, 96:186605, May 2006.

[152] N. P. Stern, S. Ghosh, G. Xiang, M. Zhu, N. Samarth, and D. D. Awschalom. Current-Induced Polarization and the Spin Hall Effect at Room Temperature. *Phys. Rev. Lett.*, 97:126603, Sep 2006.

[153] Pietro Gambardella and Ioan Mihai Miron. Current-induced spin–orbit torques. *Philos. Trans. R. Soc. London A*, 369(1948):3175–3197, 2011.

[154] Jun-ichiro Inoue, Gerrit E. W. Bauer, and Laurens W. Molenkamp. Diffuse transport and spin accumulation in a Rashba two-dimensional electron gas. *Phys. Rev. B*, 67:033104, Jan 2003.

[155] Ka Shen, G. Vignale, and R. Raimondi. Microscopic Theory of the Inverse Edelstein Effect. *Phys. Rev. Lett.*, 112:096601, Mar 2014.

[156] J. Borge, C. Gorini, G. Vignale, and R. Raimondi. Spin Hall and Edelstein effects in metallic films: From two to three dimensions. *Phys. Rev. B*, 89:245443, Jun 2014.

[157] Annika Johansson, Jürgen Henk, and Ingrid Mertig. Theoretical aspects of the Edelstein effect for anisotropic two-dimensional electron gas and topological insulators. *Phys. Rev. B*, 93:195440, May 2016.

[158] Cosimo Gorini, Amin Maleki Sheikhabadi, Ka Shen, Ilya V. Tokatly, Giovanni Vignale, and Roberto Raimondi. Theory of current-induced spin polarization in an electron gas. *Phys. Rev. B*, 95:205424, May 2017.

[159] S. D. Ganichev, E. L. Ivchenko, V. V. Bel'kov, S. A. Tarasenko, M. Sollinger, D. Weiss, W. Wegscheider, and W. Prettl. Spin-galvanic effect. *Nature*, 417(6885):153–156, 2002.

[160] Ion Garate and M. Franz. Inverse Spin-Galvanic Effect in the Interface between a Topological Insulator and a Ferromagnet. *Phys. Rev. Lett.*, 104:146802, Apr 2010.

[161] A. Chernyshov, M. Overby, X. Liu, J. K. Furdyna, Y. Lyanda-Geller, and L. P. Rokhinson. Evidence for reversible control of magnetization in a ferromagnetic material by means of spin-orbit magnetic field. *Nat. Phys.*, 5:656–659, September 2009.

[162] I. M. Miron, G. Gaudin, S. Auffret, B. Rodmacq, A. Schuhl, S. Pizzini, J. Vogel, and P. Gambardella. Current-driven spin torque induced by the Rashba effect in a ferromagnetic metal layer. *Nat. Mater.*, 9:230–234, March 2010.

[163] I. M. Miron, K. Garello, G. Gaudin, P.-J. Zermatten, M. V. Costache, S. Auffret, S. Bandiera, B. Rodmacq, A. Schuhl, and P. Gambardella. Perpendicular switching of a single ferromagnetic layer induced by in-plane current injection. *Nature*, 476:189–193, August 2011.

[164] D. A. Pesin and A. H. MacDonald. Quantum kinetic theory of current-induced torques in Rashba ferromagnets. *Phys. Rev. B*, 86:014416, Jul 2012.

[165] A. Qaiumzadeh, R. Â. A. Duine, and M. Titov. Spin-orbit torques in two-dimensional Rashba ferromagnets. *Phys. Rev. B*, 92(1):014402, July 2015.

[166] I. A. Ado, O. A. Tretiakov, and M. Titov. Microscopic theory of spin-orbit torques in two dimensions. *Phys. Rev. B*, 95(9):094401, March 2017.

[167] K. D. Belashchenko, Alexey A. Kovalev, and M. van Schilfgaarde. First-principles calculation of spin-orbit torque in a Co/Pt bilayer. *Phys. Rev. Materials*, 3:011401, Jan 2019.

[168] I. Dzyaloshinsky. A thermodynamic theory of "weak" ferromagnetism of antiferromagnetics. *J. Phys. Chem. Solids*, 4(4):241, 1958.

[169] T. Moriya. Anisotropic Superexchange Interaction and Weak Ferromagnetism. 120:91, 1960.

[170] Nobuyuki Okuma. Magnon Spin-Momentum Locking: Various Spin Vortices and Dirac magnons in Noncollinear Antiferromagnets. *Phys. Rev. Lett.*, 119:107205, Sep 2017.

[171] Aurélien Manchon, Papa Birame Ndiaye, Jung-Hwan Moon, Hyun-Woo Lee, and Kyung-Jin Lee. Magnon-mediated Dzyaloshinskii-Moriya torque in homogeneous ferromagnets. *Phys. Rev. B*, 90:224403, Dec 2014.

[172] Alexey A. Kovalev, Vladimir A. Zyuzin, and Bo Li. Pumping of magnons in a Dzyaloshinskii-Moriya ferromagnet. *Phys. Rev. B*, 95:165106, Apr 2017.

[173] Alexander Mook, Jürgen Henk, and Ingrid Mertig. Spin dynamics simulations of topological magnon insulators: From transverse current correlation functions to the family of magnon Hall effects. *Phys. Rev. B*, 94:174444, Nov 2016.

[174] Bo Li, Shane Sandhoefner, and Alexey A. Kovalev. Intrinsic spin Nernst effect of magnons in a noncollinear antiferromagnet. page arXiv:1907.10567, Jul 2019.

[175] Alexander Mook, Börge Göbel, Jürgen Henk, and Ingrid Mertig. Taking an electron-magnon duality shortcut from electron to magnon transport. *Phys. Rev. B*, 97:140401, Apr 2018.

[176] Matthew W. Daniels, Weichao Yu, Ran Cheng, Jiang Xiao, and Di Xiao. Topological spin Hall effects and tunable skyrmion Hall effects in uniaxial antiferromagnetic insulators. *Phys. Rev. B*, 99:224433, Jun 2019.

[177] B. Li, A. Mook, and A. Kovalev. Magnon-mediated analog to the Edelstein effect in an antiferromagnet. In *APS Meeting Abstracts*, page R22.014, 2018.

[178] Simon Streib, Nicolas Vidal-Silva, Ka Shen, and Gerrit E. W. Bauer. Magnon-phonon interactions in magnetic insulators. *Phys. Rev. B*, 99:184442, May 2019.

[179] Takashi Kikkawa, Ka Shen, Benedetta Flebus, Rembert A. Duine, Ken-ichi Uchida, Zhiyong Qiu, Gerrit E. W. Bauer, and Eiji Saitoh. Magnon Polarons in the Spin Seebeck Effect. *Phys. Rev. Lett.*, 117:207203, Nov 2016.

[180] Sungjoon Park and Bohm-Jung Yang. Topological magnetoelastic excitations in noncollinear antiferromagnets. *Phys. Rev. B*, 99:174435, May 2019.

[181] J. Železný, H. Gao, Aurélien Manchon, Frank Freimuth, Yuriy Mokrousov, J. Zemen, J. Mašek, Jairo Sinova, and T. Jungwirth. Spin-orbit torques in locally and globally noncentrosymmetric crystals: Antiferromagnets and ferromagnets. *Phys. Rev. B*, 95:014403, Jan 2017.

[182] Motoi Kimata, Hua Chen, Kouta Kondou, Satoshi Sugimoto, Prasanta K. Muduli, Muhammad Ikhlas, Yasutomo Omori, Takahiro Tomita, Allan H. MacDonald, Satoru Nakatsuji, and Yoshichika Otani. Magnetic and magnetic?inverse spin Hall effects in a non-collinear antiferromagnet. *Nature*, 565(7741):627–630, 2019.

[183] J. Železný, H. Gao, K. Výborný, J. Zemen, J. Mašek, Aurélien Manchon, J. Wunderlich, Jairo Sinova, and T. Jungwirth. Relativistic Néel-Order Fields Induced by Electrical Current in Antiferromagnets. *Phys. Rev. Lett.*, 113:157201, Oct 2014.

[184] J. Železný, H. Gao, Aurélien Manchon, Frank Freimuth, Yuriy Mokrousov, J. Zemen, J. Mašek, Jairo Sinova, and T. Jungwirth. Spin-orbit torques in locally and globally noncentrosymmetric crystals: Antiferromagnets and ferromagnets. *Phys. Rev. B*, 95:014403, Jan 2017.

[185] Leandro Salemi, Marco Berritta, Ashis K. Nandy, and Peter M. Oppeneer. Orbitally dominated Rashba-Edelstein effect in noncentrosymmetric antiferromagnets. *Nat. Commun.*, 10(1):5381, 2019.

[186] Akashdeep Kamra, Utkarsh Agrawal, and Wolfgang Belzig. Noninteger-spin magnonic excitations in untextured magnets. *Phys. Rev. B*, 96:020411, Jul 2017.

[187] Ulrike Ritzmann. *Modeling spincaloric transport: Magnon accumulation and propagation*. PhD thesis, University of Konstanz, Konstanz, 2015.

[188] Frances Hellman, Axel Hoffmann, Yaroslav Tserkovnyak, Geoffrey S. D. Beach, Eric E. Fullerton, Chris Leighton, Allan H. MacDonald, Daniel C. Ralph, Dario A. Arena, Hermann A. Dürr, Peter Fischer, Julie Grollier, Joseph P. Heremans, Tomas Jungwirth, Alexey V. Kimel, Bert Koopmans, Ilya N. Krivorotov, Steven J. May, Amanda K. Petford-Long, James M. Rondinelli, Nitin Samarth, Ivan K. Schuller, Andrei N. Slavin, Mark D. Stiles, Oleg Tchernyshyov, André Thiaville, and Barry L. Zink. Interface-induced phenomena in magnetism. *Rev. Mod. Phys.*, 89:025006, Jun 2017.

[189] S Toth and B Lake. Linear spin wave theory for single-Q incommensurate magnetic structures. *J. Phys. Condens. Matter*, 27(16):166002, mar 2015.

[190] Se Kwon Kim and Yaroslav Tserkovnyak. Landau-Lifshitz theory of thermomagnonic torque. *Phys. Rev. B*, 92:020410, Jul 2015.

[191] Fei-Ye Li and Gang Chen. Competing phases and topological excitations of spin-1 pyrochlore antiferromagnets. *Phys. Rev. B*, 98:045109, Jul 2018.

[192] Yoshihiko Okamoto, Gøran J. Nilsen, J. Paul Attfield, and Zenji Hiroi. Breathing Pyrochlore Lattice Realized in A-Site Ordered Spinel Oxides $\mathrm{LiGaCr_4O_8}$ and $\mathrm{LiInCr_4O_8}$. *Phys. Rev. Lett.*, 110:097203, Feb 2013.

[193] Francesco Casola, Toeno van der Sar, and Amir Yacoby. Probing condensed matter physics with magnetometry based on nitrogen-vacancy centres in diamond. *Nat. Rev. Mater.*, 3(1):17088, 2018.

[194] W. F. Brown. Thermal Fluctuations of a Single-Domain Particle. *Phys. Rev.*, 130:1677–1686, Jun 1963.

[195] R. F. L. Evans, W. J. Fan, P. Chureemart, T. A. Ostler, M. O. A. Ellis, and R. W. Chantrell. Atomistic spin model simulations of magnetic nanomaterials. *J. Phys. Condens. Matter*, 26(10):103202, 2014.

[196] Joseph Barker and Gerrit E. W. Bauer. Thermal Spin Dynamics of Yttrium Iron Garnet. *Phys. Rev. Lett.*, 117:217201, Nov 2016.

[197] D.S. Inosov. Quantum magnetism in minerals. *Adv. Phys.*, 67(3):149–252, 2018.

[198] A. L. Chernyshev and M. E. Zhitomirsky. Spin waves in a triangular lattice antiferromagnet: Decays, spectrum renormalization, and singularities. *Phys. Rev. B*, 79:144416, Apr 2009.

[199] M V Gvozdikova, P-E Melchy, and M E Zhitomirsky. Magnetic phase diagrams of classical triangular and kagome antiferromagnets. *J. Phys. Condens. Matter*, 23(16):164209, apr 2011.

[200] L. E. Svistov, A. I. Smirnov, L. A. Prozorova, O. A. Petrenko, L. N. Demianets, and A. Ya. Shapiro. Quasi-two-dimensional antiferromagnet on a triangular lattice $\mathrm{RbFe(MoO_4)_2}$. *Phys. Rev. B*, 67:094434, Mar 2003.

[201] J. Hwang, E. S. Choi, F. Ye, C. R. Dela Cruz, Y. Xin, H. D. Zhou, and P. Schlottmann. Successive Magnetic Phase Transitions and Multiferroicity in the Spin-One Triangular-Lattice Antiferromagnet $\mathrm{Ba_3NiNb_2}\mathbf{O}_9$. *Phys. Rev. Lett.*, 109:257205, Dec 2012.

[202] J. G. Rau, L. S. Wu, A. F. May, L. Poudel, B. Winn, V. O. Garlea, A. Huq, P. Whitfield, A. E. Taylor, M. D. Lumsden, M. J. P. Gingras, and A. D. Christianson. Anisotropic Exchange within Decoupled Tetrahedra in the Quantum Breathing Pyrochlore $\mathrm{Ba_3Yb_2Zn_5O_{11}}$. *Phys. Rev. Lett.*, 116:257204, Jun 2016.

[203] T. Haku, K. Kimura, Y. Matsumoto, M. Soda, M. Sera, D. Yu, R. A. Mole, T. Takeuchi, S. Nakatsuji, Y. Kono, T. Sakakibara, L.-J. Chang, and T. Masuda. Low-energy excitations and ground-state selection in the quantum breathing pyrochlore antiferromagnet $\mathrm{Ba_3Yb_2Zn_5O_{11}}$. *Phys. Rev. B*, 93:220407, Jun 2016.

[204] G E Volovik. Linear momentum in ferromagnets. *J. Phys. C*, 20(7):L83–L87, mar 1987.

[205] Gen Tatara, Hiroshi Kohno, and Junya Shibata. Microscopic approach to current-driven domain wall dynamics. *J., Phys. Rep.*, 468(6):213–301, November 2008.

[206] P. Bruno, V. K. Dugaev, and M. Taillefumier. Topological Hall Effect and Berry Phase in Magnetic Nanostructures. *Phys. Rev. Lett.*, 93:096806, Aug 2004.

[207] Minhyea Lee, W. Kang, Y. Onose, Y. Tokura, and N. P. Ong. Unusual Hall Effect Anomaly in MnSi under Pressure. *Phys. Rev. Lett.*, 102:186601, May 2009.

[208] N. Kanazawa, Y. Onose, T. Arima, D. Okuyama, K. Ohoyama, S. Wakimoto, K. Kakurai, S. Ishiwata, and Y. Tokura. Large Topological Hall Effect in a Short-Period Helimagnet MnGe. *Phys. Rev. Lett.*, 106:156603, Apr 2011.

[209] T. Schulz, R. Ritz, A. Bauer, M. Halder, M. Wagner, C. Franz, C. Pfleiderer, K. Everschor, M. Garst, and A. Rosch. Emergent electrodynamics of skyrmions in a chiral magnet. *Nature Phys.*, 8(4):301–304, February 2012.

[210] Papa Birame Ndiaye, Collins Ashu Akosa, and Aurélien Manchon. Topological Hall and spin Hall effects in disordered skyrmionic textures. *Phys. Rev. B*, 95:064426, Feb 2017.

[211] Börge Göbel, Alexander Mook, Jürgen Henk, and Ingrid Mertig. Signatures of lattice geometry in quantum and topological Hall effect. *New J. Phys.*, 19(6):063042, June 2017.

[212] A. Bogdanov and A. Hubert. Thermodynamically stable magnetic vortex states in magnetic crystals. *J. Magn. Magn. Mater.*, 138:255–269, December 1994.

[213] U. K. Rößler, A. N. Bogdanov, and C. Pfleiderer. Spontaneous skyrmion ground states in magnetic metals. *Nature*, 442:797–801, August 2006.

[214] S. Mühlbauer, B. Binz, F. Jonietz, C. Pfleiderer, A. Rosch, A. Neubauer, R. Georgii, and P. Böni. Skyrmion Lattice in a Chiral Magnet. *Science*, 323:915, February 2009.

[215] X. Z. Yu, Y. Onose, N. Kanazawa, J. H. Park, J. H. Han, Y. Matsui, N. Nagaosa, and Y. Tokura. Real-space observation of a two-dimensional skyrmion crystal. *Nature*, 465:901–904, June 2010.

[216] S A Owerre. A first theoretical realization of honeycomb topological magnon insulator. *J. Phys.: Condens. Matter*, 28(38):386001, July 2016.

[217] Ranjani Seshadri and Diptiman Sen. Topological magnons in a kagome-lattice spin system with XXZ and Dzyaloshinskii-Moriya interactions. *Phys. Rev. B*, 97:134411, Apr 2018.

[218] P. A. McClarty, X.-Y. Dong, M. Gohlke, J. G. Rau, F. Pollmann, R. Moessner, and K. Penc. Topological magnons in Kitaev magnets at high fields. *Phys. Rev. B*, 98:060404, Aug 2018.

[219] Albert Fert, Nicolas Reyren, and Vincent Cros. Magnetic skyrmions: advances in physics and potential applications. *Nat. Rev. Mater.*, 2(7), June 2017.

[220] Yan Zhou and Motohiko Ezawa. A reversible conversion between a skyrmion and a domain-wall pair in a junction geometry. *Nat. Commun.*, 5(1), August 2014.

[221] A. V. Chumak, V. I. Vasyuchka, A. A. Serga, and B. Hillebrands. Magnon spintronics. *Nature Phys.*, 11(6):453–461, June 2015.

[222] Börge Göbel, Alexander F. Schäffer, Jamal Berakdar, Ingrid Mertig, and Stuart S. P. Parkin. Electrical writing, deleting, reading, and moving of magnetic skyrmioniums in a racetrack device. *Sci. Rep.*, 9(1), August 2019.

[223] Kamil Olejník, Tom Seifert, Zdeněk Kašpar, Vít Novák, Peter Wadley, Richard P. Campion, Manuel Baumgartner, Pietro Gambardella, Petr Němec, Joerg Wunderlich, Jairo Sinova, Petr Kužel, Melanie Müller, Tobias Kampfrath, and Tomas Jungwirth. Terahertz electrical writing speed in an antiferromagnetic memory. *Sci. Adv.*, 4(3):eaar3566, March 2018.

[224] J. Železný, H. Gao, K. Výborný, J. Zemen, J. Mašek, Aurélien Manchon, J. Wunderlich, Jairo Sinova, and T. Jungwirth. Relativistic Néel-Order Fields Induced by Electrical Current in Antiferromagnets. *Phys. Rev. Lett.*, 113:157201, Oct 2014.

[225] P. Wadley, B. Howells, J. elezny, C. Andrews, V. Hills, R. P. Campion, V. Novak, K. Olejnik, F. Maccherozzi, S. S. Dhesi, S. Y. Martin, T. Wagner, J. Wunderlich, F. Freimuth, Y. Mokrousov, J. Kune, J. S. Chauhan, M. J. Grzybowski, A. W. Rushforth, K. W. Edmonds, B. L. Gallagher, and T. Jungwirth. Electrical switching of an antiferromagnet. *Science*, 351(6273):587–590, January 2016.

[226] Börge Göbel, Alexander Mook, Jürgen Henk, and Ingrid Mertig. Antiferromagnetic skyrmion crystals: Generation, topological Hall, and topological spin Hall effect. *Phys. Rev. B*, 96:060406, Aug 2017.

[227] Ricardo Zarzuela, Se Kwon Kim, and Yaroslav Tserkovnyak. Stabilization of the skyrmion crystal phase and transport in thin-film antiferromagnets. *Phys. Rev. B*, 100:100408, Sep 2019.

[228] Se Kwon Kim, Oleg Tchernyshyov, and Yaroslav Tserkovnyak. Thermophoresis of an antiferromagnetic soliton. *Phys. Rev. B*, 92:020402, Jul 2015.

[229] Joseph Barker and Oleg A. Tretiakov. Static and Dynamical Properties of Antiferromagnetic Skyrmions in the Presence of Applied Current and Temperature. *Phys. Rev. Lett.*, 116:147203, Apr 2016.

[230] H Velkov, O Gomonay, M Beens, G Schwiete, A Brataas, J Sinova, and R A Duine. Phenomenology of current-induced skyrmion motion in antiferromagnets. *New J. Phys.*, 18(7):075016, jul 2016.

[231] Chendong Jin, Chengkun Song, Jianbo Wang, and Qingfang Liu. Dynamics of antiferromagnetic skyrmion driven by the spin Hall effect. *Appl. Phys. Lett.*, 109(18):182404, October 2016.

[232] Xichao Zhang, Yan Zhou, and Motohiko Ezawa. Antiferromagnetic Skyrmion: Stability, Creation and Manipulation. *Sci. Rep.*, 6(1):24795, April 2016.

[233] C. A. Akosa, O. A. Tretiakov, G. Tatara, and A. Manchon. Theory of the Topological Spin Hall Effect in Antiferromagnetic Skyrmions: Impact on Current-Induced Motion. *Phys. Rev. Lett.*, 121:097204, Aug 2018.

[234] Patrick M. Buhl, Frank Freimuth, Stefan Blügel, and Yuriy Mokrousov. Topological spin Hall effect in antiferromagnetic skyrmions. *Phys. Status Solidi RRL*, 11(4):1700007, 2017.

[235] Kevin A. van Hoogdalem, Yaroslav Tserkovnyak, and Daniel Loss. Magnetic texture-induced thermal Hall effects. *Phys. Rev. B*, 87:024402, Jan 2013.

[236] Alexey A. Kovalev and Shane Sandhoefner. Skyrmions and Antiskyrmions in Quasi-Two-Dimensional Magnets. *Frontiers in Physics*, 6:00098, September 2018.

[237] U. Güngördü, R. Nepal, O. A. Tretiakov, K. Belashchenko, and A. A. Kovalev. Stability of skyrmion lattices and symmetries of quasi-two-dimensional chiral magnets. *Phys. Rev. B.*, 93:064428, 2016.

[238] Arne Vansteenkiste, Jonathan Leliaert, Mykola Dvornik, Mathias Helsen, Felipe Garcia-Sanchez, and Bartel Van Waeyenberge. The design and verification of MuMax3. *AIP Advances*, 4(10):107133, October 2014.

[239] Su Do Yi, Shigeki Onoda, Naoto Nagaosa, and Jung Hoon Han. Skyrmions and anomalous Hall effect in a Dzyaloshinskii-Moriya spiral magnet. *Phys. Rev. B*, 80:054416, Aug 2009.

[240] Shi-Zeng Lin, Avadh Saxena, and Cristian D. Batista. Skyrmion fractionalization and merons in chiral magnets with easy-plane anisotropy. *Phys. Rev. B*, 91:224407, Jun 2015.

[241] Ryo Ozawa, Satoru Hayami, Kipton Barros, Gia-Wei Chern, Yukitoshi Motome, and Cristian D. Batista. Vortex Crystals with Chiral Stripes in Itinerant Magnets. *Journal of the Physical Society of Japan*, 85(10):103703, October 2016.

[242] Mark Vousden, Maximilian Albert, Marijan Beg, Marc-Antonio Bisotti, Rebecca Carey, Dmitri Chernyshenko, David Cortés-Ortuño, Weiwei Wang, Ondrej Hovorka, Christopher H. Marrows, and Hans Fangohr. Skyrmions in thin films with easy-plane magnetocrystalline anisotropy. *Appl. Phys. Lett.*, 108(13):132406, March 2016.

[243] X. Z. Yu, W. Koshibae, Y. Tokunaga, K. Shibata, Y. Taguchi, N. Nagaosa, and Y. Tokura. Transformation between meron and skyrmion topological spin textures in a chiral magnet. *Nature*, 564(7734):95–98, December 2018.

[244] Assa Auerbach, Federico Berruto, and Luca Capriotti. Quantum Magnetism Approaches to Strongly Correlated Electrons. *Field Theories for Low-Dimensional Condensed Matter Systems Springer Series in Solid-State Sciences*, pages 143–170, 2000.

[245] Lui Lam. Motion in Electric and Magnetic Fields. I. Klein-Gordon Particles. *Journal of Mathematical Physics*, 12(2):299–303, February 1971.

[246] J.H.P. Colpa. Diagonalization of the quadratic boson hamiltonian. *Physica (Amsterdam)*, 93A(3-4):327–353, September 1978.

[247] Douglas R. Hofstadter. Energy levels and wave functions of Bloch electrons in rational and irrational magnetic fields. *Phys. Rev. B*, 14:2239–2249, Sep 1976.

[248] Bo Li, Shane Sandhoefner, and Alexey A. Kovalev. Intrinsic spin Nernst effect of magnons in a noncollinear antiferromagnet. *Phys. Rev. Research*, 2:013079, Jan 2020.

[249] Börge Göbel, Alexander Mook, Jürgen Henk, and Ingrid Mertig. Unconventional topological Hall effect in skyrmion crystals caused by the topology of the lattice. *Phys. Rev. B*, 95:094413, Mar 2017.

[250] Yasuhiro Hatsugai, Takahiro Fukui, and Hideo Aoki. Topological analysis of the quantum Hall effect in graphene: Dirac-Fermi transition across van Hove singularities and edge versus bulk quantum numbers. *Phys. Rev. B*, 74:205414, Nov 2006.

[251] D. N. Sheng, L. Sheng, and Z. Y. Weng. Quantum Hall effect in graphene: Disorder effect and phase diagram. *Phys. Rev. B*, 73:233406, Jun 2006.

[252] I. M. Lifshits, M. Ya. Azbel', and M. I. Kaganov. *Sov. Phys. JETP*, 4:41, 1957.

[253] Masao Arai and Yasuhiro Hatsugai. Quantum Hall effects of graphene with multi-orbitals: Topological numbers, Boltzmann conductance, and semiclassical quantization. *Phys. Rev. B*, 79:075429, Feb 2009.

[254] Xi He, Yi Wang, Ning Wu, Anthony N. Caruso, Elio Vescovo, Kirill D. Belashchenko, Peter A. Dowben, and Christian Binek. Robust isothermal electric control of exchange bias at room temperature. *Nat. Mater.*, 9(7):579–585, June 2010.

[255] Qiming Shao, Yawen Liu, Guoqiang Yu, Se Kwon Kim, Xiaoyu Che, Chi Tang, Qing Lin He, Yaroslav Tserkovnyak, Jing Shi, and Kang L. Wang. Topological Hall

effect at above room temperature in heterostructures composed of a magnetic insulator and a heavy metal. *Nat. Electron.*, 2(5):182–186, May 2019.

[256] M. C. Chang and Q. Niu. Electron band structure in a two-dimensional periodic magnetic field. *Phys. Rev. B*, 50:10843–10850, Oct 1994.

Appendix A

Linear response for antiferromagnets

A.0.1 General theory

For the μ component of a spatially averaged observable $A_\mu = \frac{1}{V}\int d\mathbf{r}\Psi^\dagger(\mathbf{r})\hat{A}_\mu\Psi(\mathbf{r})$, the non-equilibrium response to a temperature gradient is

$$\langle A_\mu\rangle_{\text{ne}} = \lim_{\omega\to 0}\frac{1}{i\omega}[\Pi_{\mu\nu}(\omega) - \Pi_{\mu\nu}(0)]\nabla_\nu\phi, \tag{A.1}$$

where the correlator in frequency space is defined as

$$\Pi_{\mu\nu}(i\omega_m) = -\int_0^\beta d\tau e^{i\omega_m\tau}\langle T_\tau A_\mu(\tau)J^q_\nu(0)\rangle. \tag{A.2}$$

In momentum space, $A_\mu = \frac{1}{V}\sum_{\mathbf{k}}\Psi^\dagger_{\mathbf{k}}A_{\mu,\mathbf{k}}\Psi_{\mathbf{k}}$ and $J^q_\nu = \sum_{\mathbf{k}}\Psi^\dagger_{\mathbf{k}}J^q_{\nu,\mathbf{k}}\Psi_{\mathbf{k}}$, with $J^q_{\nu,\mathbf{k}} = \frac{1}{4}(\mathcal{H}_{\mathbf{k}}\sigma_3\mathbf{v}_{\nu,\mathbf{k}} + \mathbf{v}_{\nu,\mathbf{k}}\sigma_3\mathcal{H}_{\mathbf{k}})$. Here, J^q_ν comes from $\frac{\partial H'}{\partial t} = \frac{i}{\hbar}[H, H'] = J^q_\nu\nabla_\nu\phi$, see the supplementary of Refs. [38, 97]. Plugging in above expressions, the correlation tensor can be presented as

$$\begin{aligned}\Pi_{\mu\nu}(i\omega_m) &= -\frac{1}{V}\sum_{\mathbf{k},\mathbf{k}'}\int_0^\beta d\tau e^{i\omega_m\tau}\langle\Psi^\dagger_{\mathbf{k}}(\tau)A_{\mu,\mathbf{k}}\Psi_{\mathbf{k}}(\tau)\Psi^\dagger_{\mathbf{k}'}J^q_{\nu,\mathbf{k}'}\Psi_{\mathbf{k}'}\rangle \\ &= -\frac{1}{V}\sum_{\mathbf{k},\mathbf{k}'}\int_0^\beta d\tau e^{i\omega_m\tau}(A_{\mu,\mathbf{k}})_{\alpha\gamma}(J^q_{\nu,\mathbf{k}\prime})_{\rho\sigma}\langle T_\tau\Psi^\dagger_{\mathbf{k},\alpha}(\tau)\Psi_{\mathbf{k},\gamma}(\tau)\Psi^\dagger_{\mathbf{k}',\rho}(0)\Psi_{\mathbf{k}',\sigma}(0)\rangle.\end{aligned} \tag{A.3}$$

According to Wick's theorem,

$$\begin{aligned}&\langle T_\tau\Psi^\dagger_{\mathbf{k},\alpha}(\tau)\Psi_{\mathbf{k},\gamma}(\tau)\Psi^\dagger_{\mathbf{k}',\rho}(0)\Psi_{\mathbf{k}',\sigma}(0)\rangle_{\text{connected}} \\ =\ &\langle T_\tau\Psi_{\mathbf{k}',\sigma}(0)\Psi^\dagger_{\mathbf{k},\alpha}(\tau)\rangle\langle T_\tau\Psi_{\mathbf{k},\gamma}(\tau)\Psi^\dagger_{\mathbf{k}\prime,\rho}(0)\rangle + \langle T_\tau\Psi^\dagger_{\mathbf{k},\alpha}(\tau)\Psi^\dagger_{\mathbf{k}\prime,\rho}(0)\rangle\langle T_\tau\Psi_{\mathbf{k}',\gamma}(\tau)\Psi_{\mathbf{k},\sigma}(0)\rangle.\end{aligned} \tag{A.4}$$

Here, the second anomalous term can be shown to be equivalent to the first term. First, we note that the basis $\Psi_{\mathbf{k}}$ obeys the particle-hole symmetry, $\Psi_{\mathbf{k}} = (\Psi^\dagger_{-\mathbf{k}}\sigma_1)^T$, which leads to the relation

$$A_\mu = \frac{1}{V}\sum_{\mathbf{k},\alpha\beta}\Psi^\dagger_{\mathbf{k},\alpha}(A_{\mu,\mathbf{k}})_{\alpha\beta}\Psi_{\mathbf{k},\beta} = \frac{1}{V}\sum_{\mathbf{k},\lambda\gamma}\Psi^\dagger_{-\mathbf{k},\lambda}(\sigma_1 A^T_{\mu,\mathbf{k}}\sigma_1)_{\lambda\gamma}\Psi_{-\mathbf{k},\gamma}. \tag{A.5}$$

Hence, we gain the relation: $\sigma_1 A^T_{\mathbf{k},\mu}\sigma_1 = A_{\mu,-\mathbf{k}}$, which will be used repeatedly in the later proof. Second, the systematic linear response analysis needs a plain expression of the particle-hole space Green function, whose definition is $\mathcal{G}(\mathbf{k},\tau;\mathbf{k}',0)_{i,j} \equiv \mathcal{G}(\mathbf{k},\mathbf{k}';\tau)_{i,j} \equiv -\langle T_\tau\Psi_{\mathbf{k},i}(\tau)\Psi^\dagger_{\mathbf{k}',j}(0)\rangle$. We derive the Green function expression by virtue of its equation of motion,

$$\partial_\tau\mathcal{G}(\mathbf{k},\mathbf{k}';\tau)_{\alpha\beta} = -\delta(\tau)\sigma_{3,\alpha\beta}\delta_{\mathbf{k},\mathbf{k}'} - (\sigma_3\mathcal{H}_{\mathbf{k}})_{\alpha\gamma}\mathcal{G}(\mathbf{k},\mathbf{k}';\tau)_{\gamma\beta}, \tag{A.6}$$

where we used the relation

$$\partial_\tau \Psi_{\mathbf{k},\alpha}(\tau) = [H, \Psi_{\mathbf{k},\alpha}(\tau)] = -\frac{1}{2}(\sigma_3 \mathcal{H}_{\mathbf{k}})_{\alpha\gamma}\Psi_{\mathbf{k},\gamma} + \frac{i}{2}\Psi^\dagger_{-\mathbf{k},\gamma}(\mathcal{H}_{-\mathbf{k}}\sigma_2)_{\gamma\alpha} = -(\sigma_3\mathcal{H}_{\mathbf{k}})_{\alpha\gamma}\Psi_{\mathbf{k},\gamma} \tag{A.7}$$

The equation of motion [Eq. (A.6)] in matrix form reads

$$(\partial_\tau + \sigma_3\mathcal{H}_{\mathbf{k}})\mathcal{G}(\mathbf{k},\mathbf{k}';\tau) = -\sigma_3\delta(\tau)\delta_{\mathbf{k},\mathbf{k}'}, \tag{A.8}$$

so that $\mathcal{G}(\mathbf{k},\mathbf{k}';\tau) = \frac{-\sigma_3\delta(\tau)\delta_{\mathbf{k},\mathbf{k}'}}{\partial_\tau+\sigma_3\mathcal{H}_{\mathbf{k}}}$ and $\mathcal{G}(\mathbf{k},\mathbf{k}';ik_n) = \frac{\sigma_3}{ik_n-\sigma_3\mathcal{H}_{\mathbf{k}}}\delta_{\mathbf{k},\mathbf{k}'}$ in frequency-momentum space.

Now we show that the anomalous term in Eq. (A.4) can be alternatively expressed, with the help of particle-hole symmetry, in form of Green function

$$\begin{aligned}
\langle T_\tau \Psi^\dagger_{\mathbf{k},\alpha}(\tau)\Psi^\dagger_{\mathbf{k}',\rho}(0)\rangle &= \langle T_\tau \sigma_{1,\alpha\delta}\Psi_{-\mathbf{k},\delta}(\tau)\Psi^\dagger_{\mathbf{k}',\rho}(0)\rangle = -\sigma_{1,\alpha\delta}\mathcal{G}(-\mathbf{k},\mathbf{k}';\tau)_{\delta\rho}, \\
\langle T_\tau \Psi_{\mathbf{k}',\gamma}(\tau)\Psi_{\mathbf{k},\sigma}(0)\rangle &= \langle T_\tau \Psi_{\mathbf{k},\gamma}(\tau)\Psi^\dagger_{-\mathbf{k}',\mu}(0)\sigma_{1,\mu\sigma}\rangle = -\mathcal{G}(\mathbf{k},-\mathbf{k}';\tau)_{\gamma\mu}\sigma_{1,\mu\sigma}.
\end{aligned}$$

Therefore, Eq. (A.4) and the correlation tensor in Eq. (A.3) are rewritten in terms of Green function as

$$\begin{aligned}
&\langle T_\tau \Psi^\dagger_{\mathbf{k},\alpha}(\tau)\Psi_{\mathbf{k},\gamma}(\tau)\Psi^\dagger_{\mathbf{k}',\rho}(0)\Psi_{\mathbf{k}',\sigma}(0)\rangle \\
= \; &\mathcal{G}_{\sigma\alpha}(\mathbf{k}',\mathbf{k};-\tau)\mathcal{G}_{\gamma\rho}(\mathbf{k},\mathbf{k}';\tau) + [\sigma_1\mathcal{G}(-\mathbf{k},\mathbf{k}';\tau)]_{\alpha\rho}[\mathcal{G}(\mathbf{k},-\mathbf{k}';\tau)\sigma_1]_{\gamma\sigma},
\end{aligned} \tag{A.9}$$

and

$$\begin{aligned}
\Pi_{\mu\nu}(i\omega_m) = \; & -\frac{1}{V}\sum_{\mathbf{k},\mathbf{k}'}\int_0^\beta d\tau e^{i\omega_m\tau}(A_{\mu,\mathbf{k}})_{\alpha\gamma}(J^q_{\nu,\mathbf{k}'})_{\rho\sigma}\{\mathcal{G}_{\sigma\alpha}(\mathbf{k}',\mathbf{k};-\tau)\mathcal{G}_{\gamma\rho}(\mathbf{k},\mathbf{k}';\tau) \\
& +[\sigma_1\mathcal{G}(-\mathbf{k},\mathbf{k}';\tau)]_{\alpha\rho}[\mathcal{G}(\mathbf{k},-\mathbf{k}';\tau)\sigma_1]_{\gamma\sigma}\},
\end{aligned} \tag{A.10}$$

respectively. Furthermore, with the aid of the Green function relation $\mathcal{G}(-\mathbf{k},\tau) = -\sigma_1\mathcal{G}(\mathbf{k},-\tau)^T\sigma_1$, we can prove the equivalence of the first and second part on the right hand side of Eq. (A.10). As a result, the correlation function becomes

$$\Pi_{\mu\nu}(i\omega_m) = -\frac{2}{V}\sum_{\mathbf{k}}\int_0^\beta d\tau e^{i\omega_m\tau}\mathrm{tr}[A_{\mu,\mathbf{k}}\mathcal{G}(\mathbf{k},\tau)J^q_{\nu,\mathbf{k}}\mathcal{G}(\mathbf{k};-\tau)], \tag{A.11}$$

where $\mathcal{G}(\mathbf{k},\tau) = \frac{\sigma_3}{ik_n-\sigma_3\mathcal{H}_{\mathbf{k}}}$. Let's transform the Green function to frequency space with $\mathcal{G}(\mathbf{k};\tau) = \frac{1}{\beta}\sum\limits_{iq_n} e^{-iq_n\tau}\mathcal{G}(\mathbf{k};iq_n)$, then

$$\Pi_{\mu\nu}(i\omega_m) = \frac{2}{V}\sum_{\mathbf{k}}\int_{-\infty}^{+\infty}\frac{d\omega_1}{2\pi}\frac{d\omega_2}{2\pi}\mathrm{tr}[A_{\mu,\mathbf{k}}S(\mathbf{k},\omega_1)J^q_{\nu,\mathbf{k}}S(\mathbf{k},\omega_2)]\frac{n_{\mathrm{B}}(\omega_1)-n_{\mathrm{B}}(\omega_2)}{\omega_1-\omega_2-i\omega_m} \tag{A.12}$$

Here, we performed the Matsubara summation and utilized $\mathcal{G}(\mathbf{k};ik_n) = \int_{-\infty}^{+\infty}\frac{d\omega}{2\pi}\frac{S(\mathbf{k},\omega)}{ik_n-\omega}$, with $S(\mathbf{k},\omega)$ being the spectral function. Going back to the real time space and taking the zero frequency limit, we obtain the response tensor

$$\begin{aligned} K_{\mu\nu} &= -i\frac{\partial\Pi_{\mu\nu}(\omega+i0^+)}{\partial\omega}|_{\omega\to0} \\ &= \frac{2}{V}\sum_{\mathbf{k}}\int_{-\infty}^{+\infty}\frac{d\varepsilon}{2\pi}n_{\mathrm{B}}(\varepsilon)\mathrm{tr}[(G^R-G^A)(A_{\mu,\mathbf{k}}\frac{\partial G^R}{\partial\varepsilon}J^q_{\nu,\mathbf{k}} - J^q_{\nu,\mathbf{k}}\frac{\partial G^A}{\partial\varepsilon}A_{\mu,\mathbf{k}})] \end{aligned} \tag{A.13}$$

where we used the relation

$$\int_{-\infty}^{\infty}\frac{d\omega}{2\pi}\frac{S(k,\omega)}{(\varepsilon-\omega\pm i0^+)^2} = -\frac{\partial}{\partial\varepsilon}\int_{-\infty}^{\infty}\frac{d\omega}{2\pi}\frac{S(k,\omega)}{\varepsilon-\omega\pm i0^+} = -\frac{\partial G^{R/A}}{\partial\varepsilon} \tag{A.14}$$

and the expression $S(\mathbf{k},\varepsilon) = i(G^R-G^A)$.

A.0.2 In the eigenstate basis

To distinguish the intraband and interband contributions, we rewrite the response tensor in Eq. (A.13) in the eigenstate basis via the transformation $\Psi_{\mathbf{k}} = T_{\mathbf{k}}\Gamma_{\mathbf{k}}$. By definition, we have the Green function transformation $\mathcal{G}(\mathbf{k};\tau) = T_{\mathbf{k}} g(\mathbf{k},\tau) T^{\dagger}_{\mathbf{k}}$, where $g(\mathbf{k},\tau) = -\langle T_\tau \Gamma_{\mathbf{k}}(\tau)\Gamma^{\dagger}_{\mathbf{k}}(0)\rangle$ and $g^{R/A}(\mathbf{k},\varepsilon) = \frac{\sigma_3}{\varepsilon - \sigma_3 \mathcal{E}_{\mathbf{k}} \pm i0^+}$. After this transformation, we obtain

$$K_{\mu\nu} = \frac{2}{V}\sum_{\mathbf{k}}\int_{-\infty}^{+\infty}\frac{d\varepsilon}{2\pi} n_{\mathrm{B}}(\varepsilon)\mathrm{tr}[(g^R - g^A)(\mathcal{A}_{\mu,\mathbf{k}}\frac{\partial g^R}{\partial\varepsilon}\mathcal{J}_{\nu,\mathbf{k}} - \mathcal{J}_{\nu,\mathbf{k}}\frac{\partial g^A}{\partial\varepsilon}\mathcal{A}_{\mu,\mathbf{k}})], \tag{A.15}$$

where $\mathcal{J}_{\nu,\mathbf{k}} = T^{\dagger}_{\mathbf{k}} J^q_{\nu,\mathbf{k}} T_{\mathbf{k}}$ and $\mathcal{A}_{\mu,\mathbf{k}} = T^{\dagger}_{\mathbf{k}} A_{\mu,\mathbf{k}} T_{\mathbf{k}}$. We split the expression into two parts: intraband and interband contributions. Owing to the hermitian conjugate property of operators, we write the response tensor elements as

$$\begin{aligned} K_{\mu\nu} &= \frac{2}{V}\sum_{\mathbf{k}}\sum_{mn}\int_{-\infty}^{+\infty}\frac{d\varepsilon}{2\pi} n_{\mathrm{B}}(\varepsilon)[(g^R_m - g^A_m)((\mathcal{A}_{\mu,\mathbf{k}})_{mn}\frac{\partial g^R_n}{\partial\varepsilon}(\mathcal{J}_{\nu,\mathbf{k}})_{nm} - (\mathcal{J}_{\nu,\mathbf{k}})_{mn}\frac{\partial g^A_n}{\partial\varepsilon}(\mathcal{A}_{\mu,\mathbf{k}})_{nm})] \\ &= \frac{2i}{V}\sum_{\mathbf{k}}\sum_{mn}(\mathcal{A}_{\mu,\mathbf{k}})_{mn}(\mathcal{J}_{\nu,\mathbf{k}})_{nm}\frac{\sigma_{3,mm}\sigma_{3,nn}[n_{\mathrm{B}}((\sigma_3\mathcal{E}_{\mathbf{k}})_{mm}) - n_{\mathrm{B}}((\sigma_3\mathcal{E}_{\mathbf{k}})_{nn})]}{[(\sigma_3\mathcal{E}_{\mathbf{k}})_{mm} - (\sigma_3\mathcal{E}_{\mathbf{k}})_{nn} + i0^+]^2}, \end{aligned} \tag{A.16}$$

where we took the approximation $g^R_m - g^A_m = i2\mathrm{Im}(g^R_m) = -i2\pi\sigma_{3,mm}\delta[\varepsilon - (\sigma_3\mathcal{E}_{\mathbf{k}})_{mm}]$. If we incorporate the magnon spectrum broadening Γ_m into the Green function, i.e., $g^R_m(\varepsilon) = \frac{\sigma_{3,mm}}{\varepsilon - (\sigma_3\mathcal{E}_{\mathbf{k}})_{mm} + i\Gamma_m}$, the response tensor can be naturally divided into two parts, $K_{\mu\nu} = K^{\text{intra}}_{\mu\nu} + K^{\text{inter}}_{\mu\nu}$, where

$$K^{\text{intra}}_{\mu\nu} = \frac{1}{V}\sum_{\mathbf{k}}\sum_{n}\frac{1}{\Gamma_n}(\mathcal{J}_{\mathbf{k},\nu})_{nn}(\mathcal{A}_{\mu,\mathbf{k}})_{nn}\partial_\varepsilon n_{\mathrm{B}}[(\sigma_3\mathcal{E}_{\mathbf{k}})_{nn}], \tag{A.17}$$

and

$$K^{\text{inter}}_{\mu\nu} = \frac{2i}{V}\sum_{\mathbf{k}}\sum_{m\neq n}(\mathcal{A}_{\mu,\mathbf{k}})_{mn}(\mathcal{J}_{\nu,\mathbf{k}})_{nm}\frac{\sigma_{3,mm}\sigma_{3,nn}[n_{\mathrm{B}}((\sigma_3\mathcal{E}_{\mathbf{k}})_{mm}) - n_{\mathrm{B}}((\sigma_3\mathcal{E}_{\mathbf{k}})_{nn})]}{[(\sigma_3\mathcal{E}_{\mathbf{k}})_{mm} - (\sigma_3\mathcal{E}_{\mathbf{k}})_{nn}]^2} \tag{A.18}$$

The limit $\Gamma_n \to 0$ for $K^{\text{inter}}_{\mu\nu}$ is taken here. In consideration of $A^{\dagger}_{\mu} = A_\mu$ and $(J^q_\nu)^\dagger = J^q_\nu$, Eq. (A.18) can be transformed to

$$K^{\text{inter}}_{\mu\nu} = \frac{4}{V}\sum_{\mathbf{k}}\sum_{m\neq n}\frac{\mathrm{Im}[(\sigma_3\mathcal{A}_{\mu,\mathbf{k}})_{nm}(\sigma_3\mathcal{J}_{\mathbf{k},\nu})_{mn}]n_{\mathrm{B}}[(\sigma_3\mathcal{E}_{\mathbf{k}})_{nn}]}{[(\sigma_3\mathcal{E}_{\mathbf{k}})_{mm} - (\sigma_3\mathcal{E}_{\mathbf{k}})_{nn}]^2}. \tag{A.19}$$

The intraband response Eq. (4.10) in the main text can be recovered if we consider $\mathcal{J}_{\mathbf{k},\nu} = \frac{1}{4}(\mathcal{E}_{\mathbf{k}}\sigma_3\tilde{v}_{\mathbf{k},\nu} + \tilde{v}_{\mathbf{k},\nu}\sigma_3\mathcal{E}_{\mathbf{k}})$ whose diagonal components read

$$(\mathcal{J}_{\mathbf{k},\nu})_{nn} = \frac{1}{2}(\sigma_3\mathcal{E}_{\mathbf{k}})_{nn}(\tilde{v}_{\nu,\mathbf{k}})_{nn}, \tag{A.20}$$

where

$$\tilde{v}_{\mathbf{k},\nu} = \partial_{k_\nu}\mathcal{E}_{\mathbf{k}} - (\partial_{k_\nu}T^\dagger_{\mathbf{k}})\mathcal{H}_{\mathbf{k}}T_{\mathbf{k}} - T^\dagger_{\mathbf{k}}\mathcal{H}_{\mathbf{k}}(\partial_{k_\nu}T_{\mathbf{k}}). \tag{A.21}$$

From the paraunitary relation of $T_{\mathbf{k}}$ and $\partial_{k_\nu}(T_{\mathbf{k}}\sigma_3T^\dagger_{\mathbf{k}}) = 0$, we get $\partial_{k_\nu}T^\dagger_{\mathbf{k}} = -T_{\mathbf{k}}\sigma_3(\partial_{k_\nu}T_{\mathbf{k}})\sigma_3T^\dagger_{\mathbf{k}}$. From $T^\dagger_{\mathbf{k}}\mathcal{H}_{\mathbf{k}}T_{\mathbf{k}} = \mathcal{E}_{\mathbf{k}}$ and $(T_{\mathbf{k}})^{-1} = \sigma_3T^\dagger_{\mathbf{k}}\sigma_3$, we have $T^\dagger_{\mathbf{k}}\mathcal{H}_{\mathbf{k}} = \mathcal{E}_{\mathbf{k}}\sigma_3T^\dagger_{\mathbf{k}}\sigma_3$. Therefore, the diagonal elements of $\tilde{v}_{\mathbf{k},\nu}$ are shown to be

$$(\tilde{v}_{\mathbf{k},\nu})_{nn} = (\partial_{k_\nu}\mathcal{E}_{\mathbf{k}})_{nn} + (T^\dagger_{\mathbf{k}}\sigma_3\partial_{k_\nu}T_{\mathbf{k}}\sigma_3\mathcal{E}_{\mathbf{k}})_{nn} - (\mathcal{E}_{\mathbf{k}}\sigma_3T^\dagger_{\mathbf{k}}\sigma_3\partial_{k_\nu}T_{\mathbf{k}})_{nn} = (\partial_\nu\mathcal{E}_{\mathbf{k}})_{nn}; \tag{A.22}$$

thus,

$$(\mathcal{J}_{\mathbf{k},\nu})_{nn} = \frac{1}{2}(\sigma_3\mathcal{E}_{\mathbf{k}})_{nn}(\partial_{k_\nu}\mathcal{E}_{\mathbf{k}})_{nn}. \tag{A.23}$$

By inserting Eq. (A.23) into Eq. (A.17), we arrive at

$$K^{\text{intra}}_{\mu\nu} = \frac{1}{V}\sum_{\mathbf{k}}\sum_{n=1}^{2N}\frac{1}{2\Gamma_n}(\mathcal{A}_{\mu,\mathbf{k}})_{nn}\partial_{k_\nu}\mathcal{E}_{\mathbf{k},nn}(\sigma_3\mathcal{E}_{\mathbf{k}})_{nn}\partial_\varepsilon n_{\mathrm{B}}[(\sigma_3\mathcal{E}_{\mathbf{k}})_{nn}]. \tag{A.24}$$

Given the relation $n_{\mathrm{B}}(x) = -1 - n_{\mathrm{B}}(-x)$, the band index can be confined to the particle space, i.e., $1 \leq n \leq N$,

$$K^{\text{intra}}_{\mu\nu} = \frac{1}{V}\sum_{\mathbf{k}}\sum_{n=1}^{N}\frac{1}{2\Gamma_n}[(\mathcal{A}_{\mu,\mathbf{k}})_{nn} + (\mathcal{A}_{\mu,-\mathbf{k}})_{(n+N)(n+N)}]\partial_{k_\nu}\mathcal{E}_{\mathbf{k},nn}\mathcal{E}_{\mathbf{k},nn}\partial_\varepsilon n_{\mathrm{B}}[\mathcal{E}_{\mathbf{k},nn}]. \tag{A.25}$$

Applying particle-hole symmetry (PHS), $(\mathcal{A}_{\mu,\mathbf{k}})_{nn} = (\mathcal{A}_{\mu,-\mathbf{k}})_{(n+N)(n+N)}$, replacing $\mathcal{A}_{\mu,\mathbf{k}}$ by $\mathcal{S}_{\mu,\mathbf{k}}$ and taking $\nabla_\nu\phi = -\nabla_\nu T/T$ into account, we can obtain the intraband response

Eq. (4.10).

On the other hand, by plugging the expression of $\mathcal{J}_{\nu,\mathbf{k}}$ into Eqs. (A.18) or (A.19), the interband part can be reorganized as below

$$\begin{aligned} K^{\text{inter}}_{\mu\nu} &= \frac{1}{V}\sum_{\mathbf{k}}\sum_{m\neq n}\frac{i}{2}(\mathcal{A}_{\mu,\mathbf{k}})_{nm}[(\sigma_3\mathcal{E}_{\mathbf{k}})_{mm}(v_\nu)_{mn}+(v_\nu)_{mn}(\sigma_3\mathcal{E}_{\mathbf{k}})_{nn}] \\ &\times\frac{\sigma_{3,mm}\sigma_{3,nn}[n_{\mathrm{B}}((\sigma_3\mathcal{E}_{\mathbf{k}})_{nn})-n_{\mathrm{B}}((\sigma_3\mathcal{E}_{\mathbf{k}})_{mm})]}{[(\sigma_3\mathcal{E}_{\mathbf{k}})_{mm}-(\sigma_3\mathcal{E}_{\mathbf{k}})_{nn}]^2}, \\ &= \frac{1}{V}\sum_{\mathbf{k}}\sum_{n=1}^{2N}-(\Omega^A_{n,\mathbf{k}})_{\mu\nu}\bar{\varepsilon}_{n,\mathbf{k}}n_{\mathrm{B}}(\bar{\varepsilon}_{n,\mathbf{k}})-(m^A_{n,\mathbf{k}})_{\mu\nu}n_{\mathrm{B}}(\bar{\varepsilon}_{n,\mathbf{k}}), \end{aligned} \tag{A.26}$$

with

$$\begin{aligned} (\Omega^A_{n,\mathbf{k}})_{\mu\nu} &= \sum_{m(\neq n)}\frac{2\mathrm{Im}[(\sigma_3\mathcal{A}_{\mu,\mathbf{k}})_{nm}(\sigma_3\tilde{v}_{\nu,\mathbf{k}})_{mn}]}{(\bar{\varepsilon}_{n,\mathbf{k}}-\bar{\varepsilon}_{m,\mathbf{k}})^2}, \\ (m^A_{n,\mathbf{k}})_{\mu\nu} &= \sum_{m(\neq n)}\frac{-\mathrm{Im}[(\sigma_3\mathcal{A}_{\mu,\mathbf{k}})_{nm}(\sigma_3\tilde{v}_{\nu,\mathbf{k}})_{mn}]}{\bar{\varepsilon}_{n,\mathbf{k}}-\bar{\varepsilon}_{m,\mathbf{k}}}. \end{aligned} \tag{A.27}$$

Appendix B

Details of the models

B.0.1 Antiferromagnetic spin chain

We recapitulate that the Hamiltonian for the antiferromagnetic spin chain is

$$H = \sum_i \sum_{\delta=\pm1} [J(\gamma S^x_{1,i} S^x_{2,i+\nu} + S^y_{1,i} S^y_{2,i+\nu} + \lambda S^z_{1,i} S^z_{2,i+\nu}) + D^\nu_{12} \mathbf{e}_z \cdot (\mathbf{S}_{1,i} \times \mathbf{S}_{2,i+\nu})] \tag{B.1}$$

with exchange and DMI parameters as stated in the main text. After performing the Holstein-Primakoff transformation, the quadratic Hamiltonian written in the basis $\Psi_k = (a_{1,k}, a_{2,k}, a^\dagger_{1,-k}, a^\dagger_{2,-k})^T$ reads

$$\mathcal{H}_k = JS \begin{bmatrix} 2\lambda & 2\Delta_- \cos k & 0 & 2\Delta_+ \cos k + i\varrho_k \\ 2\Delta_- \cos k & 2\lambda & 2\Delta_+ \cos k + i\varrho_{-k} & 0 \\ 0 & 2\Delta_+ \cos k - i\varrho_k & 2\lambda & 2\Delta_- \cos k \\ 2\Delta_+ \cos k - i\varrho_{-k} & 0 & 2\Delta_- \cos k & 2\lambda \end{bmatrix}, \tag{B.2}$$

where $\Delta_\pm = \frac{1\pm\gamma}{2}$, $\varrho_k = \sum_\nu \delta D_\nu e^{ik\nu}/J = i2D_0 \sin k + 2\delta_D \cos k$, with $D_0 = \frac{D_1+D_2}{2J}$ and $\delta_D = \frac{D_1-D_2}{2J}$.

B.0.2 Non-coplanar Kagome antiferromagnet

We consider the non-coplanar kagome antiferromagnet discribed by

$$H = \sum_{\langle ij \rangle} J_1 \mathbf{S}_i \cdot \mathbf{S}_j + \mathbf{D}_{ij} \cdot (\mathbf{S}_i \times \mathbf{S}_j) + \sum_{\langle\langle ij \rangle\rangle} J_2 \mathbf{S}_i \cdot \mathbf{S}_j, \tag{B.3}$$

where $\mathbf{D}_{ij} = \mathbf{D}_{p,ij} + D_{z,ij}\hat{z}$. The spins cant out of the 2-D plane with a small angle η, and the spins' projection on the the $x - y$ plane form angles θ_i $(i = 1, 2, 3)$ with respect to x axis, specifically, $\theta_1 = -\pi/6$, $\theta_2 = \pi/2$ and $\theta_3 = 7\pi/6$. For each spin $\mathbf{S}_i$, we choose a local reference frame defined as follow

$$\begin{aligned} &\mathbf{e}_{i,x} = \{\sin\theta_i \ -\cos\theta_i, 0\}, \qquad \mathbf{e}_{i,y} = \{\sin\eta\cos\theta_i, \sin\eta\sin\theta_i, -\cos\eta\}, \\ &\mathbf{e}_{i,z} = \{\cos\eta\cos\theta_i, \cos\eta\sin\theta_i, \sin\eta\}. \end{aligned} \tag{B.4}$$

For a given spin $\mathbf{S}_i$, in the global frame, its components can be connected to the local frame expression $\tilde{\mathbf{S}}_i$ by

$$S_i^\alpha = \mathbf{e}_\alpha \cdot (\tilde{S}_i^\beta \mathbf{e}_{i,\beta}) = R_{i,\alpha\beta}\tilde{S}_i^\beta, \tag{B.5}$$

where $R_{i,\alpha\beta} = \mathbf{e}_\alpha \cdot \mathbf{e}_{i,\beta}$, or in matrix form,

$$R_i = \begin{pmatrix} \sin\theta_i & \sin\eta\cos\theta_i & \cos\eta\cos\theta_i \\ -\cos\theta_i & \sin\eta\sin\theta_i & \cos\eta\sin\theta_i \\ 0 & -\cos\eta & \sin\eta \end{pmatrix}. \tag{B.6}$$

For the general spin-spin interaction a correspondence between the two frames can be written as $S_i^\alpha \Gamma_{\alpha\beta}^{ij} S_j^\beta = \tilde{S}_i^\alpha (R_i^T \Gamma^{ij} R_j)_{\alpha\beta} \tilde{S}_j^\beta$. The interaction matrices are: $\Gamma_{\alpha\beta}^{ij} = J\delta_{\alpha\beta}$ for exchange and $\Gamma_{\alpha\beta}^{ij} = D_{ij}^\rho \epsilon^{\rho\alpha\beta}$ for DMI. Using these relations, we express the noninteracting magnon Hamiltonian in terms of the local reference frames as

$$\begin{aligned}
H_{J_1} &= J_1 \sum_{\langle ij\rangle} \cos\theta_{ij}\tilde{\mathbf{S}}_i\cdot\tilde{\mathbf{S}}_j + 2\sin^2(\theta_{ij}/2)(\cos^2\eta\tilde{S}_i^y\tilde{S}_j^y+\sin^2\eta\tilde{S}_i^z\tilde{S}_j^z)+\sin\eta\sin\theta_{ij}\hat{z}\cdot(\tilde{\mathbf{S}}_i\times\tilde{\mathbf{S}}_j),\\
H_{J_2} &= J_2 \sum_{\langle\langle ij\rangle\rangle} \cos\theta_{ij}\tilde{\mathbf{S}}_i\cdot\tilde{\mathbf{S}}_j + 2\sin^2(\theta_{ij}/2)(\cos^2\eta\tilde{S}_i^y\tilde{S}_j^y+\sin^2\eta\tilde{S}_i^z\tilde{S}_j^z)+\sin\eta\sin\theta_{ij}\hat{z}\cdot(\tilde{\mathbf{S}}_i\times\tilde{\mathbf{S}}_j),\\
H_{D_z} &= \sum_{\langle ij\rangle} -s_{ij}D_z[\sin\theta_{ij}(\tilde{S}_i^x\tilde{S}_j^x+\sin^2\eta\tilde{S}_i^y\tilde{S}_j^y+\cos^2\eta\tilde{S}_i^z\tilde{S}_j^z)-\sin\eta\cos\theta_{ij}\hat{z}\cdot(\tilde{\mathbf{S}}_i\times\tilde{\mathbf{S}}_j)],\\
H_{D_p} &= \sum_{\langle ij\rangle} -s_{ij}D_p[\sin(2\eta)\sin(\frac{\theta_{ij}}{2})(\tilde{S}_i^z\tilde{S}_j^z-\tilde{S}_i^y\tilde{S}_j^y)+\cos\eta\cos(\frac{\theta_{ij}}{2})\hat{z}\cdot(\tilde{\mathbf{S}}_i\times\tilde{\mathbf{S}}_j)],\\
H_{D_R} &= \sum_{\langle ij\rangle} -s_{ij}\nu_{ij}D_R[\sin(2\eta)\sin(\frac{\theta_{ij}}{2})(\tilde{S}_i^z\tilde{S}_j^z-\tilde{S}_i^y\tilde{S}_j^y)+\cos\eta\cos(\frac{\theta_{ij}}{2})\hat{z}\cdot(\tilde{\mathbf{S}}_i\times\tilde{\mathbf{S}}_j)].
\end{aligned} \tag{B.7}$$

Here we used the notation that $\theta_{ij} = \theta_i - \theta_j = -s_{ij}\frac{2\pi}{3}$, $D_{z,ij} = D_z s_{ij}$ and $\mathbf{D}_{p,ij} = -s_{ij}D_p[\cos(\frac{\theta_i+\theta_j}{2})\hat{x}+\sin(\frac{\theta_i+\theta_j}{2})\hat{y}]$, where s_{ij} is used to express the sign convention: $s_{ij} = 1$ as the indices i, j run clockwise around the triangle loop and $s_{ij} = -1$ when they run counter-clockwise. The notation ν_{ij} takes care of the opposite convention for Rashba-DMI in upward and downward triangles with $\nu_{ij} = \pm 1$ for $(ij) \in \triangle/\bigtriangledown$. Plugging in the expression of θ_{ij} and performing the Holstein-Primakoff transformation $\tilde{S}_i^x = \sqrt{\frac{S}{2}}(b_i^\dagger + b_i)$, $\tilde{S}_i^y = i\sqrt{\frac{S}{2}}(b_i^\dagger - b_i)$, $\tilde{S}_i^z = (S - b_i^\dagger b_i)$, we can obtain nearest neighbor interaction

$$\begin{aligned}
H_{\text{NN}} &= \frac{1}{2}S\sum_{\langle ij\rangle}[(\Delta_1^{(0)}+\nu_{ij}\Delta_R^{(0)})(b_i^\dagger b_i + b_j^\dagger b_j) + (\Delta_{1,ij}+\nu_{ij}\Delta_{R,ij})b_i^\dagger b_j + h.c.\\
&+(\Delta_1'+\nu_{ij}\Delta_R')b_i^\dagger b_j^\dagger + h.c.]
\end{aligned} \tag{B.8}$$

with

$$\begin{aligned}
\Delta_1^{(0)} &= J_1(1-3\sin^2\eta) - \sqrt{3}(D_z\cos^2\eta + D_p\sin(2\eta)),\\
\Delta_{1,ij} &= \Delta_1^{re} + is_{ij}\Delta_1^{im},\\
\Delta_1^{re} &= \frac{1}{2}[(1-3\sin^2\eta)J_1 + \sqrt{3}(1+\sin^2\eta)D_z - \sqrt{3}\sin(2\eta)D_p],\\
\Delta_1^{im} &= \cos\eta D_p + \sin\eta(D_z + \sqrt{3}J_1),\\
\Delta_1' &= \frac{1}{2}[\cos^2\eta(\sqrt{3}D_z - 3J_1) + \sqrt{3}\sin(2\eta)D_p],
\end{aligned} \tag{B.9}$$

and

$$\begin{aligned}
\Delta_R^{(0)} &= -\sqrt{3}D_R\sin 2\eta,\\
\Delta_{R,ij} &= -\frac{\sqrt{3}}{2}D_R\sin(2\eta) + is_{ij}D_R\cos\eta,\\
\Delta_R' &= \frac{\sqrt{3}}{2}\sin(2\eta)D_R.
\end{aligned} \tag{B.10}$$

In a similar way, we get second-nearest neighbor interaction, i.e. the second-nearest exchange, as

$$H_{\text{NNN}} = \frac{1}{2}S\sum_{\langle\langle ij\rangle\rangle}[\Delta_2^{(0)}(b_i^\dagger b_i + b_j^\dagger b_j) + \Delta_{2,ij}b_i^\dagger b_j + h.c. + \Delta_2' b_i^\dagger b_j^\dagger + h.c.] \tag{B.11}$$

with

$$\begin{aligned}
\Delta_2^{(0)} &= J_2(1-3\sin^2\eta),\\
\Delta_{2,ij} &= \Delta_2^{re} + is_{ij}\Delta_2^{im},\\
\Delta_2^{re} &= \frac{1}{2}(1-3\sin^2\eta)J_2,\\
\Delta_2^{im} &= \sqrt{3}\sin\eta J_2,\\
\Delta_2' &= -\frac{3}{2}\cos^2\eta J_2.
\end{aligned} \tag{B.12}$$

Let's denote $H_{\rm NN}$ and $H_{\rm NNN}$ by H_1 and H_2, respectively. The total Hamiltonian can be written as $H = H_1 + H_2 + H_R$. By performing Fourier transformation, H_m ($m = 1, 2$) becomes

$$\begin{aligned} H_m \quad &= \frac{S}{2}\sum_{\mathbf{r},\alpha\beta}\sum_{\lambda=\pm1}\frac{1}{2}\{\Delta_m^{(0)}[b_\alpha^\dagger(\mathbf{r})b_\alpha(\mathbf{r}) + b_\beta^\dagger(\mathbf{r}+\lambda\boldsymbol{\delta}_{\alpha\beta}^{(m)})b_\beta(\mathbf{r}+\lambda\boldsymbol{\delta}_{\alpha\beta}^{(m)})] \\ &+\Delta_{m,\alpha\beta}b_\alpha^\dagger(\mathbf{r})b_\beta(\mathbf{r}+\lambda\boldsymbol{\delta}_{\alpha\beta}^{(m)}) + h.c. + \Delta'_m b_\alpha^\dagger(\mathbf{r})b_\beta^\dagger(\mathbf{r}+\lambda\boldsymbol{\delta}_{\alpha\beta}^{(m)}) + h.c.\} \\ &= \frac{S}{2}\sum_{\mathbf{k},\alpha\beta}[4\Delta_m^{(0)}\delta_{\alpha\beta} + 2\Delta_{m,\alpha\beta}\cos(\mathbf{k}\cdot\delta_{\alpha\beta}^{(m)})]b_{\alpha,\mathbf{k}}^\dagger b_{\beta,\mathbf{k}} + \Delta'_m\cos(\mathbf{k}\cdot\delta_{\alpha\beta}^{(m)}) \\ &\times(b_{\alpha,\mathbf{k}}^\dagger b_{\beta,-\mathbf{k}}^\dagger + b_{\alpha,\mathbf{k}}b_{\beta,-\mathbf{k}}). \end{aligned} \tag{B.13}$$

Here $\boldsymbol{\delta}_{12}^{(1)} = \mathbf{e}_3$, $\boldsymbol{\delta}_{23}^{(1)} = \mathbf{e}_1$, $\boldsymbol{\delta}_{31}^{(1)} = \mathbf{e}_2$ and $\boldsymbol{\delta}_{12}^{(2)} = \mathbf{e}'_3$, $\boldsymbol{\delta}_{23}^{(2)} = \mathbf{e}'_1$, $\boldsymbol{\delta}_{31}^{(2)} = \mathbf{e}'_2$. We choose $\boldsymbol{\delta}_{\alpha\beta}^{(m)} = -\boldsymbol{\delta}_{\beta\alpha}^{(m)}$ and $\mathbf{e}_1 = (-\frac{1}{2}, -\frac{\sqrt{3}}{2})$, $\mathbf{e}_2 = (1, 0)$, $\mathbf{e}_3 = (-\frac{1}{2}, \frac{\sqrt{3}}{2})$, $\mathbf{e}'_1 = \mathbf{e}_2 - \mathbf{e}_3$, $\mathbf{e}'_2 = \mathbf{e}_3 - \mathbf{e}_1$, $\mathbf{e}'_3 = \mathbf{e}_1 - \mathbf{e}_2$. In a similar way, we can show

$$H_R = \frac{S}{2}\sum_{\mathbf{k},\alpha\beta} i2\Delta_{R,\alpha\beta}\sin(\mathbf{k}\cdot\delta_{\alpha\beta}^{(1)})b_{\alpha,\mathbf{k}}^\dagger b_{\beta,\mathbf{k}} + i\Delta'_m\sin(\mathbf{k}\cdot\delta_{\alpha\beta}^{(1)})(b_{\alpha,\mathbf{k}}^\dagger b_{\beta,-\mathbf{k}}^\dagger + b_{\alpha,\mathbf{k}}b_{\beta,-\mathbf{k}}) \tag{B.14}$$

Finally, the Hamiltonian is expressed in the basis $\Psi_{\mathbf{k}} = (b_{1,\mathbf{k}}, b_{2,\mathbf{k}}, b_{3,\mathbf{k}}, b_{1,-\mathbf{k}}^\dagger, b_{2,-\mathbf{k}}^\dagger, b_{3,-\mathbf{k}}^\dagger)^T$ as $H = \frac{S}{2}\sum_{\mathbf{k}}\Psi_{\mathbf{k}}\mathcal{H}_{\mathbf{k}}\Psi_{\mathbf{k}}$ with

$$\mathcal{H}_{\mathbf{k}} = \begin{pmatrix} A_0 + A_{\mathbf{k}} & B_{\mathbf{k}} \\ B_{\mathbf{k}} & A_0 + A_{\mathbf{k}}^* \end{pmatrix}. \tag{B.15}$$

Here, $A_0 = 2(\Delta_1^{(0)} + \Delta_2^{(0)})\mathbb{1}_{3\times 3}$ and

$$
\begin{aligned}
A_{\mathbf{k}} &= \begin{pmatrix} 0 & \cos k_3 \Delta_1 & \cos k_2 \Delta_1^* \\ \cos k_3 \Delta_1^* & 0 & \cos k_1 \Delta_1 \\ \cos k_2 \Delta_1 & \cos k_1 \Delta_1^* & 0 \end{pmatrix} + \begin{pmatrix} 0 & \cos p_3 \Delta_2 & \cos p_2 \Delta_2^* \\ \cos p_3 \Delta_2^* & 0 & \cos p_1 \Delta_2 \\ \cos p_2 \Delta_2 & \cos p_1 \Delta_2^* & 0 \end{pmatrix} \\
&+ \begin{pmatrix} 0 & i \sin k_3 \Delta_R & -i \sin k_2 \Delta_R^* \\ -i \sin k_3 \Delta_R^* & 0 & i \sin k_1 \Delta_R \\ i \sin k_2 \Delta_R & -i \sin k_1 \Delta_R^* & 0 \end{pmatrix}, \\
B_{\mathbf{k}} &= \Delta_1' \begin{pmatrix} 0 & \cos k_3 & \cos k_2 \\ \cos k_3 & 0 & \cos k_1 \\ \cos k_2 & \cos k_1 & 0 \end{pmatrix} + \Delta_2' \begin{pmatrix} 0 & \cos p_3 & \cos p_2 \\ \cos p_3 & 0 & \cos p_1 \\ \cos p_2 & \cos p_1 & 0 \end{pmatrix} \\
&+ \Delta_R' \begin{pmatrix} 0 & i \sin k_3 & -i \sin k_2 \\ -i \sin k_3 & 0 & i \sin k_1 \\ i \sin k_2 & -i \sin k_1 & 0 \end{pmatrix}.
\end{aligned}
\tag{B.16}
$$

We abbreviated the notations: $k_i = \mathbf{k} \cdot \mathbf{e}_i$, $p_i = \mathbf{k} \cdot \mathbf{e}_i'$, $\Delta_m = \Delta_m^{re} + i\Delta_m^{im}$ $(m = 1, 2)$, $\Delta_R = -\frac{\sqrt{3}}{2} D_R \sin(2\eta) + i D_R \cos \eta$ and considered the convention that $s_{12} = s_{23} = s_{31} = 1$ and $s_{ij} = -s_{ji}$.

B.0.3 Breathing pyrochlore antiferromagnet

We consider the model

$$
H = J \sum_{\langle ij \rangle \in u} \mathbf{S}_{\mathbf{r}_i} \cdot \mathbf{S}_{\mathbf{r}_j} + J' \sum_{\langle ij \rangle \in d} \mathbf{S}_{\mathbf{r}_i} \cdot \mathbf{S}_{\mathbf{r}_j} + D \sum_i (\mathbf{S}_{\mathbf{r}_i} \cdot \hat{z}_i)^2. \tag{B.17}
$$

Similar to the two-dimensional model, the magnon excitation is represented via the local Holstein-Primakoff transformation as $\mathbf{S}_\mu = (S - a_\mu^\dagger a_\mu)\hat{z}_\mu + \sqrt{\frac{S}{2}}(a_\mu + a_\mu^\dagger)\hat{x}_\mu - i\sqrt{\frac{S}{2}}(a_\mu -$

$a^\dagger_\mu)\hat{y}_\mu$. Therefore, the exchange interaction between two neighboring spins is expressed as

$$\mathbf{S}_\mu \cdot \mathbf{S}_\nu = S^c_\mu S^d_\nu \Lambda^{cd}_{\mu\nu} = S^2 \Lambda^{zz}_{\mu\nu} - S(a^\dagger_\mu a_\mu + a^\dagger_\nu a_\nu)\Lambda^{zz}_{\mu\nu} + \frac{S}{2}[a^\dagger_\mu a_\nu \Gamma_{\mu\nu} + a_\mu a_\nu \Omega_{\mu\nu} + \text{H.c.}] \tag{B.18}$$

where $\Gamma_{\mu\nu} = \Lambda^{xx}_{\mu\nu} + \Lambda^{yy}_{\mu\nu} - i\Lambda^{xy}_{\mu\nu} + i\Lambda^{yx}_{\mu\nu}$ and $\Omega_{\mu\nu} = \Lambda^{xx}_{\mu\nu} - \Lambda^{yy}_{\mu\nu} - i\Lambda^{xy}_{\mu\nu} - i\Lambda^{yx}_{\mu\nu}$. Here $\Lambda^{cd}_{\mu\nu} = \hat{c}_\mu \cdot \hat{d}_\nu$ with $\hat{c}_\mu$, $\hat{d}_\nu$ being the c, d axis of the local frame of μ and ν atoms, respectively, i.e., $c, d = x, y, z$ and $\mu, \nu \in (0, 1, 2, 3)$ with $\mu \neq \nu$. We choose local frames as shown in Table B.1. It can be shown by straightforward calculation that $\Lambda^{zz}_{\mu\nu} = -\frac{1}{3}$, $\Gamma_{\mu\nu} = -\frac{2}{3}$ and $\Omega_{\mu\nu} = \frac{4}{3}e^{i\phi_{\mu\nu}}$ where $\phi_{01} = \phi_{23} = -\frac{\pi}{3}$, $\phi_{02} = \phi_{13} = \frac{\pi}{3}$, $\phi_{03} = \phi_{12} = \pi$ and other terms can be generated by $\phi_{\mu\nu} = \phi_{\nu\mu}$ $(\mu \neq \nu)$. By substituting the magnon representation of spin-spin interaction Eq. (B.18) into Eq. (B.17) and performing Fourier transformation, we obtain the noninteracting magnon Hamiltonian

$$\begin{aligned} H = \quad & \sum_{\mathbf{k},\mu\nu} S[(J + J' - 2D)\delta_{\mu\nu} - \frac{1}{3}(J + J'e^{-i\mathbf{k}\cdot\mathbf{d}_{\mu\nu}})]a^\dagger_{\mu,\mathbf{k}} a_{\nu,\mathbf{k}} \\ & + S\frac{1}{3}(J + J'e^{-i\mathbf{k}\cdot\mathbf{d}_{\mu\nu}})e^{i\phi_{\mu\nu}} a_{\mu,-\mathbf{k}} a_{\nu,\mathbf{k}} + h.c. \end{aligned} \tag{B.19}$$

where $\mathbf{d}_{\mu\nu} = \mathbf{a}_\nu - \mathbf{a}_\mu$ with $\mathbf{a}_0 = (0, 0, 0)$, $\mathbf{a}_1 = \frac{1}{2}(0, 1, 1)$, $\mathbf{a}_2 = \frac{1}{2}(1, 0, 1)$, and $\mathbf{a}_3 = \frac{1}{2}(1, 1, 0)$.

μ	$\hat{x}_\mu$	$\hat{y}_\mu$	$\hat{z}_\mu$
0	$\frac{1}{\sqrt{2}}(-1, 1, 0)$	$\frac{1}{\sqrt{6}}(-1, -1, 2)$	$\frac{1}{\sqrt{3}}(1, 1, 1)$
1	$\frac{1}{\sqrt{2}}(-1, -1, 0)$	$\frac{1}{\sqrt{6}}(-1, 1, -2)$	$\frac{1}{\sqrt{3}}(1, -1, -1)$
2	$\frac{1}{\sqrt{2}}(1, 1, 0)$	$\frac{1}{\sqrt{6}}(1, -1, -2)$	$\frac{1}{\sqrt{3}}(-1, 1, -1)$
3	$\frac{1}{\sqrt{2}}(1, -1, 0)$	$\frac{1}{\sqrt{6}}(1, 1, 2)$	$\frac{1}{\sqrt{3}}(-1, -1, 1)$

Table B.1: Local coordinates of AIAO breathing pyrochlore.

Appendix C

Spin Nernst calculation

C.1 Squeezed cone phase

To intuitively understand the squeezed cone phase, we extract an ansatz depicting the profile of both spiral and squeezed cone phases from the numerical simulation. Without loss of generality, assuming these two types of spin texture vary along the x-direction, the spin texture can be approximately captured by

$$\boldsymbol{n} = N(a_1 \sin\frac{x}{L}, a_2, a_3 + \cos\frac{x}{L}). \tag{C.1}$$

Here, N is a normalization factor, L is the spatial period of spin texture, a_1, a_2, a_3 are varying parameters. When $a_2 = 0$, the ansatz delineates a spiral structure with Néel field lying in $x - z$ plane. Otherwise, it describes a squeezed cone structure with an elliptic cone cross-section which is captured by a_1, a_3. Next, we substitute the ansatz into the free energy (the spatial integration of Eq. (5.1)) and minimize it with respect to a_1, a_2, a_3, $\mathcal{K}$, and $\mathcal{H}_s$. The ground state at each point in the parameter manifold can be determined by comparing the minimized free energy resulting from a different ansatz. In a collinear phase, $\mathcal{F} = \mathcal{K}(n_z - \frac{\mathcal{H}_s}{2\mathcal{K}})^2 + \frac{\mathcal{H}_s^2}{4\mathcal{K}}$, which favors a tilted collinear phase with $n_z = \frac{\mathcal{H}_s}{2\mathcal{K}} < 1$ when $\mathcal{H}_s < 2\mathcal{K}$. The free energy in this tilted phase is minimized to $\mathcal{F}_{tilted} = \frac{\mathcal{H}_s^2}{4\mathcal{K}}$. The minimization process based on ansatz Eq. (C.1) shows that , at $\mathcal{H}_s = 0$, the spiral and squeezed cone phase meet at $\mathcal{K}\mathcal{J}/\mathcal{D}^2 = 1$, and the squeezed cone phase turns to the tilted collinear phase at $\mathcal{K}\mathcal{J}/\mathcal{D}^2 = 2$. This is consistent with the phase diagram in the main text. Furthermore, when $\mathcal{H}_s > 0$, the minimization shows that the critical $\mathcal{K}$ value between the squeezed cone and tilted phase slowly shifts to the left along with increasing the value of $\mathcal{H}_s$, which again confirms an oblique-line boundary between two phases in the phase diagram.

C.2 Spin current operator

In antiferromagnets, the local magnon spin density is $S_z(\vec{r}) = \mathcal{S}(\boldsymbol{m}_A + \boldsymbol{m}_B) \cdot \hat{z} \simeq \frac{\mathcal{S}}{2} \cos\theta(\vec{r})(\psi_B^* \psi_B - \psi_A^* \psi_A)$, which can be written in subspace up to a constant as

$$S_z^\chi(\vec{r}) = -\frac{\mathcal{S}}{2} \eta_\chi^\dagger \cos\theta(\vec{r}) \tau_3 \eta_\chi. \tag{C.2}$$

According to the spin density definition and Schrödinger-like equation (5.17), the time evolution of spin density reads

$$\begin{aligned}
\partial_t S_z^\chi &= -\frac{\mathcal{S}}{2} \cos\theta(\partial_t \eta_\chi^\dagger \tau_3 \eta_\chi + \eta_\chi^\dagger \tau_3 \partial_t \eta_\chi) = -i\chi \cos\theta \eta_\chi^\dagger (\overleftarrow{\mathcal{H}_\chi^*} - \overrightarrow{\mathcal{H}}_\chi)\eta_\chi \\
&= -i\chi \frac{\mathcal{J}}{8} \cos\theta \eta_\chi^\dagger [(\overleftarrow{\partial}_i + i\chi a_i)^2 - (\overrightarrow{\partial}_i - i\chi a_i)^2](\tau_1 - \mathbb{1})\eta_\chi \\
&= -i\chi \frac{\mathcal{J}}{8} \cos\theta \eta_\chi^\dagger [(\overleftarrow{\partial}_i^2 - \overrightarrow{\partial}_i^2) + i\chi 2(\overleftarrow{\partial}_i a_i + a_i \overrightarrow{\partial_i})](\tau_1 - \mathbb{1})\eta_\chi \\
&= -\chi \frac{i\mathcal{J}}{8} \partial_i \{\cos\theta [\eta_\chi^\dagger (\overleftarrow{\partial_i} - \overrightarrow{\partial_i})(\tau_1 - \mathbb{1})\eta_\chi]\} - \frac{i\mathcal{J}}{8} \partial_i (i2a_i \cos\theta \eta_\chi^\dagger (\tau_1 - \mathbb{1})\eta_\chi) \\
&\quad + \chi \frac{i\mathcal{J}}{8} (\partial_i \cos\theta) \eta_\chi^\dagger (\overleftarrow{\partial_i} - \overrightarrow{\partial_i})(\tau_1 - \mathbb{1})\eta_\chi + \cdots
\end{aligned} \tag{C.3}$$

Here, "$\cdots$" refers to higher order of spin texture derivative. We can identify a spin current as

$$\begin{aligned} j^{\chi}_{s,i} &= \chi\frac{i\mathcal{J}}{8}\cos\theta[\eta^{\dagger}_{\chi}(\overleftarrow{\partial_i} - \overrightarrow{\partial_i})(\tau_1 - \mathbb{1})\eta_{\chi} + i\chi 2a_i\eta^{\dagger}_{\chi}(\tau_1 - \mathbb{1})\eta_{\chi}] \\ &= \chi\frac{\mathcal{J}}{8}\cos\{\theta\eta^{\dagger}[(i\overleftarrow{\partial}_i - \chi a_i) + (-i\overrightarrow{\partial}_i - \chi a_i)](\tau_1 - \mathbb{1})\eta\} \\ &= \chi\frac{\mathcal{J}}{8}\eta^{\dagger}(\overleftarrow{\mathcal{D}}^{\chi *}_i\cos\theta + \cos\theta\overrightarrow{\mathcal{D}}^{\chi}_i)(\tau_1 - \mathbb{1})\eta, \end{aligned} \tag{C.4}$$

where $\mathcal{D}^{\chi}_i = -i\partial_i - \chi a_i$. The left term is regarded as a torque contribution for z-component spin density, i.e.,

$$\tau^{\chi}_z = \chi\frac{i\mathcal{J}}{8}(\partial_i\cos\theta)\eta^{\dagger}_{\chi}(\overleftarrow{\partial_i} - \overrightarrow{\partial_i})(\tau_1 - \mathbb{1})\eta_{\chi}. \tag{C.5}$$

So far, the derivation is performed in subspace for each chirality, while it's straightforward to recover the full basis representation. Take the spin current as an example,

$$j_{s,i} = \frac{1}{2}\psi^{\dagger}(\hat{j}^{+}_{s,i} \oplus \hat{j}^{-}_{s,i})\psi \tag{C.6}$$

where $\hat{j}^{\chi}_{s,i} = \chi\frac{\mathcal{J}}{8}(\overleftarrow{\mathcal{D}}^{\chi *}_i\cos\theta + \cos\theta\overrightarrow{\mathcal{D}}^{\chi}_i)(\tau_1 - \mathbb{1})$, the prefactor $1/2$ compensates for the double counting effect. Note that this result is block diagonalized as a result of the leading order approximation. When all higher-order terms are taken into account, there could be components mixing two chiralities.

C.3 Spin Nernst effect calculation based on the Landau levels

Since the spin current density operator $\hat{j}_{s,i}$ breaks translational symmetry in both directions, there is no ready-made formula for calculating the spin Nernst response. However, in a skyrmion lattice (SkX), $\hat{j}_{s,i}$ takes the same form in each skyrmion unit cell, which allows us to use the result for a periodic system. Consider a triangle SkX with basis vectors $\vec{a}_1 = a\hat{x}$ and $\vec{a}_2 = a/2\hat{x} + \sqrt{3}/2a\hat{y}$, where $a = 2R$ and R is the radius of a single skyrmion. In the two subspaces, as a result of two magnetic flux per unit cell, i.e., $B\hat{z} \cdot (\vec{a}_1 \times \vec{a}_2)/(2\pi) = 2$ (the sign of the flux depends on the chirality), magnetic translational operators are defined as

$$T_{\vec{a}_1} = e^{i\vec{a}_1 \cdot \hat{\boldsymbol{p}}}, \qquad T_{\vec{a}_2} = e^{-i\chi\frac{4\pi}{a}x} e^{i\vec{a}_2 \cdot \hat{\boldsymbol{p}}}, \tag{C.7}$$

where $\hat{\boldsymbol{p}} = -i\vec{\nabla}$. We are able to construct a basis based on the Landau level solution, which is composed of a scalar and a spinor part. The periodic condition is imposed on the spatial variable dependent scalar part. Suppose the periodic basis takes the form $\varphi^{\chi}_{n_s,m} = \bar{\Phi}^s_{\chi,n}\rho^{\chi}_{n,m}(\vec{r})$ in the full space, where $\bar{\Phi}_{+,n} = (1,0)^T \otimes \Phi^s_{+,n}$, $\bar{\Phi}_{-,n} = (0,1)^T \otimes \Phi^s_{-,n}$. Translational invariance requires $\rho^{\chi}_{n,m}(\vec{r})$ to satisfy

$$T_{\vec{a}_1}\rho^{\chi}_{n_s,m} = e^{ik_1 a}\rho^{\chi}_{n_s,m}, \qquad T_{\vec{a}_2}\rho^{\chi}_{n_s,m} = e^{ik_2 a}\rho^{\chi}_{n_s,m}, \tag{C.8}$$

where $\vec{k} = k_1\hat{b}_1 + k_2\hat{b}_2$ with $\hat{b}_1 = \frac{2\pi}{a}(\hat{x} - \hat{y}/\sqrt{3})$ and $\hat{b}_2 = \frac{2\pi}{a}\frac{2}{\sqrt{3}}\hat{y}$, $m = 0, 1$ refers to a degeneracy index for each Landau level. The basis scalar part is constructed as [235, 256]

$$\rho^{\chi}_{n_s,m} = \sum_{l=-\infty}^{\infty} (-1)^{(l+\frac{m}{2})(l+\frac{m}{2}-1)} e^{-i\chi(l+\frac{m}{2})(\frac{k_1}{2}-k_2)a} \xi^{\chi}_{n,-k_1-(l+\frac{m}{2})\frac{4\pi}{a}}. \tag{C.9}$$

To include all possible terms neglected in the leading-order-derivative approximation and uniform magnetic field assumption, we go back to work in the full space $\psi = (\psi_A, \psi_B^*, \psi_A^*, \psi_B)^T$. The Fourier components of this field can be expanded in the periodic basis

$$\psi_{\boldsymbol{k}} = \sum_{n,m,\chi,s} a_{n_s,m,\chi}(\boldsymbol{k})\bar{\Phi}^s_{\chi,n}\rho^{\chi}_{n,m}(\boldsymbol{k}). \tag{C.10}$$

Here, $\{\rho^{\chi}_{n,m}(\boldsymbol{k})\}$ is a set of complete orthogonal basis with $\int d\vec{r}\rho^{\chi *}_{n,m}(\boldsymbol{k})\rho^{\chi}_{n',m'}(\boldsymbol{k}) = \delta_{nn'}\delta_{mm'}$ and $\sum_{n,m}\rho^{\chi}_{n,m}(\boldsymbol{k})\rho^{\chi *}_{n,m}(\boldsymbol{k}) = \mathbb{1}_{LL}$ with $\mathbb{1}_{LL}$ being the unitary matrix in the Landau-level space. In second quantization language, regard $a_{n_s,m,\chi}$ ($a^{\dagger}_{n_s,m,\chi}$) as annihilation (creation) operator. Therefore,

$$[\psi_{\boldsymbol{k}}, \psi^{\dagger}_{\boldsymbol{k}}] = \sum_{n,m,\chi,s}\sum_{n',m',\chi',s'} \rho^{\chi}_{n,m}\rho^{\chi',*}_{n',m'}\bar{\Phi}^{s}_{\chi,n}(\bar{\Phi}^{s'}_{\chi',n'})^{T}[a_{n_s,m,\chi}, a^{\dagger}_{n'_{s'},m',\chi'}] = \sigma_3 \otimes \tau_3, \quad \text{(C.11)}$$

with σ_3, τ_3 being the Pauli matrix acting on chirality (or particle-hole) and sublattice space, respectively. This requires

$$[a_{n_s,m,\chi}, a^{\dagger}_{n'_{s'},m',\chi'}] = \delta_{n,n'}\delta_{m,m'}\delta_{\chi,\chi'}(\tau_3)_{ss'}, \quad \text{(C.12)}$$

where we used

$$\sum_{\chi,s}\bar{\Phi}^{s}_{\chi,n}(\bar{\Phi}^{s}_{\chi,n})^{T}(\tau_3)_{ss} = \sigma_3 \otimes \tau_3. \quad \text{(C.13)}$$

On the other hand, the original basis satisfies particle-hole symmetry, $\psi^{T}_{\boldsymbol{k}} = \psi^{\dagger}_{-\boldsymbol{k}}\sigma_1 \otimes \tau_0$ with σ_1 being the Pauli matrix in chirality space, and this property will also be reflected in the new basis. Apply the particle-hole symmetry relation

$$\begin{aligned}
\psi^{T}_{\boldsymbol{k}} &= \psi^{\dagger}_{-\boldsymbol{k}}\sigma_1 \otimes \tau_0 = \sum_{n,m,\chi,s} a^{\dagger}_{n_s,m,\chi}(-\boldsymbol{k})[(\bar{\Phi}^{s}_{\chi,n})^{T}\sigma_1 \otimes \tau_0]\rho^{\chi *}_{n,m}(-\boldsymbol{k}) \\
&= \sum_{n,m,\chi,s} a^{\dagger}_{n_s,m,\chi}(-\boldsymbol{k})(\bar{\Phi}^{-s}_{-\chi,n})^{T}\rho^{-\chi}_{n,m}(\boldsymbol{k}) \\
&= \sum_{n,m,\chi,s} a^{\dagger}_{n_{-s},m,-\chi}(-\boldsymbol{k})(\bar{\Phi}^{s}_{\chi,n})^{T}\rho^{\chi}_{n,m}(\boldsymbol{k}), \quad \text{(C.14)}
\end{aligned}$$

which suggests

$$a_{n_s,m,\chi}(\boldsymbol{k}) = a^{\dagger}_{n_{-s},m,-\chi}(-\boldsymbol{k}). \quad \text{(C.15)}$$

Here, we used the relations $(\bar{\Phi}^{s}_{\chi,n})^{T}\sigma_1 \otimes \tau_0 = (\bar{\Phi}^{-s}_{-\chi,n})^{T}$ and $\rho^{\chi}_{n,m}(\boldsymbol{k}) = \rho^{-\chi*}_{n,m}(-\boldsymbol{k})$. The relations in Eq. (C.12) and (C.15) guarantee that a Hamiltonian expressed in the new basis can be also diagonalized by a paraunitary matrix, as we shall discuss below. Actually, Eq. (C.12) is a natural result of Eq. (C.15).

To describe the magnon excitation in a real skyrmion lattice based on the Landau-level expansion, one can divide the magnon Hamiltonian in a SkX into two parts: $\mathcal{H} = \mathcal{H}_0 + \mathcal{H}'$. Here, $\mathcal{H}_0$ is the Hamiltonian leading to the Landau levels, $\mathcal{H}'$ is regarded as a perturbation, which contains all possible terms dropped in the Landau level analysis. These perturbations include anisotropy, staggered Zeeman term, and those containing higher orders of the spin-texture spatial derivative, and especially the emergent gauge field lost in the average process, i.e., $\boldsymbol{a}' = \boldsymbol{a} - \boldsymbol{a}_0$. In principle, the spin texture induced emergent vector potential, especially the part corresponding to a nonuniform magnetic field, $\boldsymbol{a}'$, acts as a periodic potential that confines magnons in a lattice. In total, the full Hamiltonian can be represented as a matrix under the periodic basis Eq. (C.9)

$$(H_{\boldsymbol{k}})_{n_s m\chi, n'_{s'}, m'\chi'} = \varepsilon_n \delta_{ss'}\delta_{n,n'}\delta_{m,m'}\delta_{\chi\chi'} + (H'_{\boldsymbol{k}})_{n_s m\chi, n'_{s'}, m'\chi'}, \tag{C.16}$$

where $\langle \varphi^{\chi}_{n_s,m}|\hat{\mathcal{H}}_0|\varphi^{\chi'}_{n'_{s'},m'}\rangle = \varepsilon_n \delta_{ss'}\delta_{n,n'}\delta_{m,m'}\delta_{\chi\chi'}$ and $(H'_{\boldsymbol{k}})_{n_s m\chi, n'_{s'}, m'\chi'} = \langle \varphi^{\chi}_{n_s,m}|\hat{\mathcal{H}}'|\varphi^{\chi'}_{n'_{s'},m'}\rangle$. Here, $\langle \varphi^{\chi}_{n_s,m}|\hat{\mathcal{O}}|\varphi^{\chi^{\chi}}_{n'_{s'},m'}\rangle = \int_{u.c.} d\vec{r}[\varphi^{\chi}_{n_s,m}(\vec{r})]^{*T}\hat{\mathcal{O}}\varphi^{\chi'}_{n'_{s'},m'}(\vec{r})$, with $u.c.$ standing for the "unit cell" and $\hat{\mathcal{O}} = \hat{\mathcal{H}}_0, \hat{\mathcal{H}}'$. If we number the element of the Hamiltonian matrix by arranging the indexes in the order $s \to n \to m \to \chi$, the Hamiltonian matrix can be diagonalized by a paraunitary matrix $T_{\boldsymbol{k}}$

$$T^{\dagger}_{\boldsymbol{k}} H_{\boldsymbol{k}} T_{\boldsymbol{k}} = \mathrm{Diag}\{\varepsilon_{1,\boldsymbol{k}}, \cdots, \varepsilon_{4N,\boldsymbol{k}}, \varepsilon_{1,-\boldsymbol{k}}, \cdots, \varepsilon_{4N,-\boldsymbol{k}}\}. \tag{C.17}$$

Here, N counts the Landau levels which are truncated to an energy comparable with the dominant scale J, and $T^{\dagger}_{\boldsymbol{k}}\tilde{\sigma}_3 T_{\boldsymbol{k}} = \tilde{\sigma}_3$, where $\tilde{\sigma}_3 = \sigma_3 \otimes \mathbb{1}_N \otimes \mathbb{1}_2 \otimes \mathbb{1}_2$ with four matrices on the right acting in particle-hole, Landau level, degeneracy freedom, and chirality space, individually. The Bloch wave function is expressed as

$$|u_{j,\boldsymbol{k}}(\vec{r})\rangle = \sum_{n,s,m,\chi} (T_{\boldsymbol{k}})_{n_s m\chi,j} |u^{\chi}_{n_s,m}(\vec{r})\rangle. \tag{C.18}$$

Here, $u^{\chi}_{n_s,m}(\vec{r}) = \varphi^{\chi}_{n_s,m}(\vec{r}-\vec{R})$ with $\vec{R} = p\vec{a}_1 + q\vec{a}_2$ ($p, q \in$ integer) and $\vec{r} \in V_{\vec{R}}$, the “unit cell" at $\vec{R}$. This is a result of the periodic property of $\varphi^{\chi}_{n_s,m}$: $\varphi^{\chi}_{n_s,m}(\vec{r}) = e^{i\vec{k}\cdot\vec{R}} u^{\chi}_{n_s,m}(\vec{r})$.

Finally, the spin Nernst current is calculated as

$$J_{s,y} = \frac{2k_B}{V} \sum_{n,\boldsymbol{k}} (\Omega_n)^{j_{s,y}}_{v_x} c_1[g(\varepsilon_{n,\boldsymbol{k}})] \partial_x T \tag{C.19}$$

with

$$(\Omega_n)^{j_{s,y}}_{v_x} = \sum_{m \neq n} (\tilde{\sigma}_3)_{nn} (\tilde{\sigma}_3)_{mm} \frac{2\mathrm{Im}[(j_{s,y})_{nm}(v_x)_{mn}]}{(\bar{\varepsilon}_{n,\boldsymbol{k}} - \bar{\varepsilon}_{m,\boldsymbol{k}})^2}. \tag{C.20}$$

Here, $\mathcal{O}_{mn} = \langle \psi_{m\boldsymbol{k}} | \hat{\mathcal{O}} | \psi_{n\boldsymbol{k}} \rangle = \int_{u.c.} d\vec{r} [u^*_{m\boldsymbol{k}}(\vec{r})]^T \hat{\mathcal{O}}_{\boldsymbol{k}} u_{n\boldsymbol{k}}(\vec{r})$ with $\hat{\mathcal{O}}_{\boldsymbol{k}} = e^{-i\boldsymbol{k}\cdot\vec{R}} \hat{\mathcal{O}} e^{i\boldsymbol{k}\cdot\vec{R}}$, $\mathcal{O} = j_{s,y}, v_x$, and $\bar{\varepsilon}_{n,\boldsymbol{k}} = \varepsilon_{n,\boldsymbol{k}}$ ($-\varepsilon_{n,-\boldsymbol{k}}$) for $n \leq \mathcal{N}$ ($\mathcal{N} < n \leq 2\mathcal{N}$) with $\mathcal{N} = 4N$ being the total number of bands. Note that the result calculated in this way is correct to the leading order of spin-texture spatial gradient as the spin current operator is derived to this order.